THE PENNSYLVANIA STATE UNIVERSITY
SCHREYER HONORS COLLEGE

DEPARTMENT OF BIOENGINEERING

A FLUID DYNAMIC STUDY OF THE EFFECT OF HEMATOCRIT IN THE 12 CC PENN STATE PEDIATRIC VENTRICULAR ASSIST DEVICE

JEREMY M. SILVER
FALL 2014

A thesis
submitted in partial fulfillment
of the requirements
for a baccalaureate degree
in Bioengineering
with honors in Bioengineering

Reviewed and approved* by the following

Keefe B. Manning
Associate Professor of Biomedical Engineering and Surgery
Thesis Supervisor/Honors Adviser

William O. Hancock
Professor of Biomedical Engineering
Faculty Reader

Peter J. Butler
Professor of Biomedical Engineering
Faculty Reader

*Signatures are on file in the Schreyer Honors College.

ABSTRACT

As part of the continuing development of the Penn State 12 cc pulsatile pediatric ventricular assist device (PVAD), this study focused on examining the effect of hematocrit on the fluid dynamics within the device. Hematocrit is defined as the ratio of the volume of packed red blood cells to total blood volume. Changes in hematocrit have a considerable effect on the viscoelastic properties of blood and can alter the fluid dynamics throughout circulatory support devices like the PVAD. Unlike adults that generally have a more consistent hematocrit, the pediatric population has been shown to have a more varied hematocrit range anywhere from 20%-60%. Additionally, the animals used for PVAD testing tend to have a comparatively low hematocrit in the 20%-30% range. For this study, three different non-Newtonian blood analogs were created to match the viscoelastic properties of 20%, 40% and 60% hematocrit pediatric blood. These fluids were then used in an *in vitro* mock circulatory loop designed to mimic the pediatric circulatory system. In order to examine the effect of hematocrit on the flow through the PVAD, planar particle image velocimetry (PIV) was used to develop whole field velocity profiles. These fluid dynamic measurements helped to describe the flow both quantitatively and qualitatively throughout the cardiac cycle. The changes observed in the flow field of the different hematocrit blood analogs are important because flow characteristics like stagnation and turbulent flow have the potential to increase the chances of clot formation, cause blood damage, and disrupt flow. While the general flow pattern within the PVAD was similar, the varying blood analogs created distinct inlet/outlet jets and rotational flow patterns. Specifically, the 20% hematocrit blood

analog created a slightly higher peak velocity inlet jet that penetrated deeper into the blood sac earlier in the cardiac cycle. The more viscoelastic fluid, the 60% hematocrit blood analog, created an inlet jet that developed later and was maintained longer into the cardiac cycle, resulting in a more delayed rotational flow pattern. This delay continued into systole and resulted in a lower velocity outlet jet in the more viscoelastic fluids. It is clear that changes in hematocrit alter the fluid dynamics in the PVAD. Understanding the exact effect of hematocrit on the PVAD flow helps to understand animal testing data and guide future use of the device in pediatric patients in a hematocrit range of 20%-60%.

TABLE OF CONTENTS

LIST OF FIGURES

LIST OF TABLES

ACKNOWLEDGEMENTS

This study was supported by NIH NHLBI HL 108123.

First and foremost, I would like to thank my research and thesis advisor Dr. Keefe Manning. Through the many ups and downs of my research, he was always there to talk to. Without his support and guidance, this thesis would not have been possible. I would also like to thank the other members of my thesis committee, Dr. Peter Butler and Dr. William Hancock. I appreciate their generosity, flexibility, and willingness to go out of their way to help me complete this work.

I would also like to thank all of my peers in the Artificial Heart Lab. Josh Taylor, Bryan Good, Kenny Aycock, Kory Witmer, and many other students were always supportive when I needed assistance or guidance. I am thankful to have had their support over the years.

Finally, I would like to thank my family. Their unconditional love and support has helped me get through many long hours in lab, and I am forever grateful for them.

Chapter 1 INTRODUCTION

1.1 Clinical Need

In the United States, an estimated 600,000 adults over the age of 20 die from cardiovascular disease (CVD) each year [1]. This makes CVD the leading cause of death among all Americans. Because of this widespread problem, much advancement has been made to treat CVD in adults. Pacemakers, arterial stents, and heart transplantations have become commonplace. What has lagged behind, however, is the advancement in treatments for pediatric patients with CVD.

Congenital cardiovascular defects are the most common cause of infant death due to birth defects [2]. It is estimated that 32,000 children are born with congenital cardiovascular heart defects each year [2]. Of those children, around 25% require invasive treatment in the first year of life [2]. Of those infants under one year of age, nearly 50% die waiting for a donor heart [3]. There simply are not enough donor hearts to meet the needs of all the children. This shortage is the reason why children listed for heart transplantation face the highest waiting list mortality in solid-organ transplantation [4]. Additionally, the median heart transplant waiting list time for infants is 119 days [5]. These statistics demonstrate the need for a successful bridge-to-transplant solution for children waiting for a heart.

1.2 Current Pediatric Circulatory Support Devices

Presently, extracorporeal membrane oxygenation (ECMO) is the most widespread form of circulatory support to treat pediatrics on the heart transplant waiting list. ECMO, as shown in **Figure 1-1**, consists of a pump, a membrane oxygenator, and a heat exchanger that work in combination to provide oxygen to a patient that has a severely diseased heart and/or lungs. ECMO, however, only provides effective support for up to two weeks [6]. After this time period, the incidence of negative cardiovascular effects, like blood damage and hemolysis, increases [7]. Given that the median waiting list time for pediatric heart transplantation is only 119 days, ECMO is often not an effective bridge-to-transplant solution. This poor long-term effectiveness means that only about 40%-60% of children treated with ECMO survive until transplantation [8].

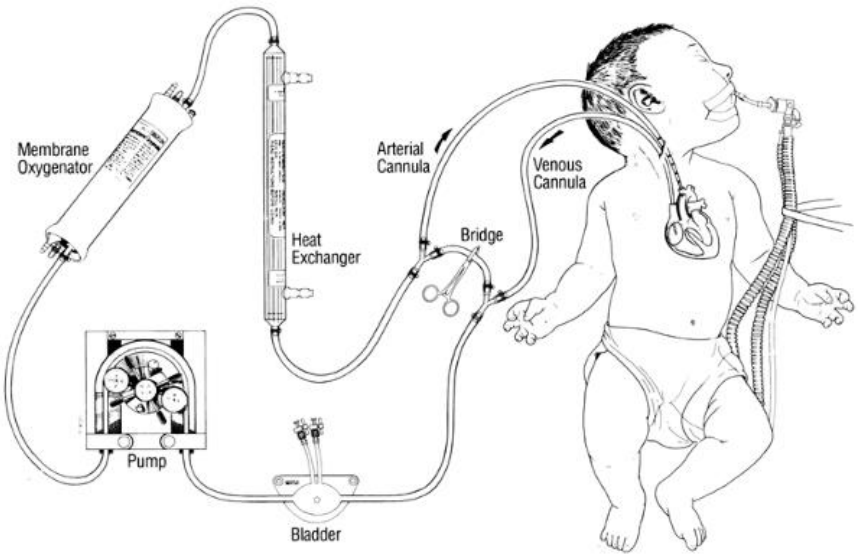

Figure 1-1. Diagram of a venoarterial ECMO system [9].

Another method of circulatory support as a bridge-to-transplant solution for pediatrics is the use of ventricular assist devices (VADs). VADs provide mechanical support to damaged or weakened hearts with poor cardiac output. They are used in conjunction with the native heart to improve blood flow to the body. VADs have been effective as bridge-to-transplant devices in adults since the FDA approved them for such in 1994 [10]. The use of VADs as a bridge-to-transplant solution is a short-term one, which has been shown to normalize hemodynamics, improve end-organ dysfunction, and increase exercise tolerance [10]. VADs have also been successfully used to treat adults that are ineligible for cardiac transplantation [10].

The success of VADs to treat end-stage heart failure in adults has led to the development of VADs for use in children. While some adult-sized VADs were initially used to treat pediatrics, they were simply too large for most children [11]. It was not until December 16, 2011, that the FDA approved a pediatric VAD (PVAD), the Berlin Heart EXCOR, for clinical use in the United States. The Berlin Heart EXCOR is a pneumatically driven, extracorporeal device. As shown in **Figure 1-2**, the Berlin Heart is made in sizes from 10 cc to 60 cc and can be implanted as a left ventricular assist device (LVAD), a right ventricular assist device (RVAD), or two pumps can be used as a bi-ventricular assist device (BiVAD).

A) 

B) 

C) 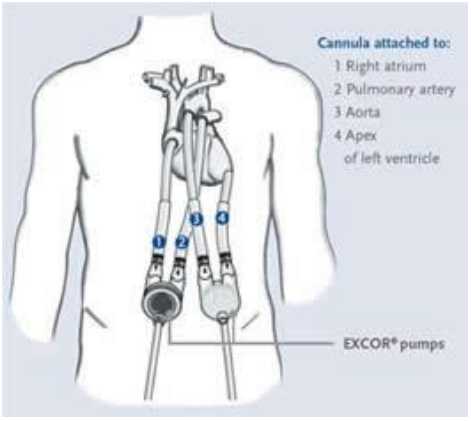

Figure 1-2. A) The Berlin Heart EXCOR pulsatile device. B) The Berlin Heart EXCOR is made in sizes from 10 cc to 60 cc [12]. C) The device can be implanted as a left or a right VAD or a bi-VAD (BiVAD). The BiVAD connection is shown and is where two EXCOR pumps are used, one connected to each side of the heart [13].

The first clinical trial completed in the United States showed that 70% of patients survived to cardiac transplantation and 7% were successfully weaned from the device and ultimately did not need transplantation [14]. Another study was done to compare the effectiveness of ECMO to the Berlin Heart EXCOR to treat pediatrics waiting for a heart transplant. The median survival time for patients on ECMO was just 13 days whereas the median survival time for patients on the Berlin Heart EXCOR was 174 days [15]. Given that the median time spent on the pediatric heart transplant waiting list is 119 days, these studies demonstrate the effectiveness of PVADs as a bridge-to-transplant solution.

However, complications associated with thrombosis and hemolysis remain significant challenges in designing pediatric VADs [16].

1.3 The 12 cc Penn State Pediatric Ventricular Assist Device

In response to the high incidence of infection, bleeding, and thromboembolism found in short-term extracorporeal devices for pediatric patients, the National Heart, Lung and Blood Institute started the Pediatric Circulatory Support Program in 2006 [17]. As part of this program, Penn State continued the development of its 12 cc, pneumatically driven PVAD. The pediatric device is modeled after the successful 70 cc Pierce-Donachy VAD, shown in **Figure 1-3**, which was also developed at Penn State. The Pierce-Donachy VAD had a success rate of over 90% [18].

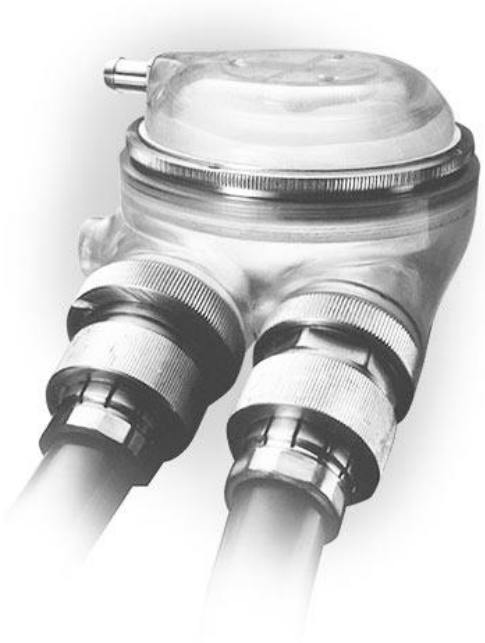

Figure 1-3. Model of the Pierce-Donachy 70 cc VAD. This VAD was first FDA-approved in 1980. Two VADs used in unison could serve as a total artificial heart [19].

Penn State's PVAD was created by scaling down the linear dimensions of the 70 cc Pierce-Donachy VAD by the cube root of the ratio of volumes [20]. It was designed for patients ranging from 2-25 kg [16]. The mechanical heart valves at the inlet and outlet ports are Bjork-Shiley Monostrut (BSM) tilting disk valves. A previous study conducted by *Cooper et al.* showed that BSM valves were better suited than bi-leaflet valves in order to minimize the potential for thrombosis in the PVAD [21].

The PVAD also has a segmented poly(ether urethane) urea (SPEUU) blood sac and a diaphragm. Negative and positive pressures drive the pulsatility of the device. Negative pressures contract the diaphragm and allow the blood sac to fill, and positive pressures expand the diaphragm and expel the blood through the outlet of the device. This rhythmic motion of the diaphragm creates the pulsatility of the device that mimics the mechanics of the native heart. As shown in **Figure 1-4**, the PVAD is often not fully implanted inside of the patient's body like the adult VAD is. Depending on the size of the patient, the PVAD can be implanted or used as an extracorporeal device.

A) 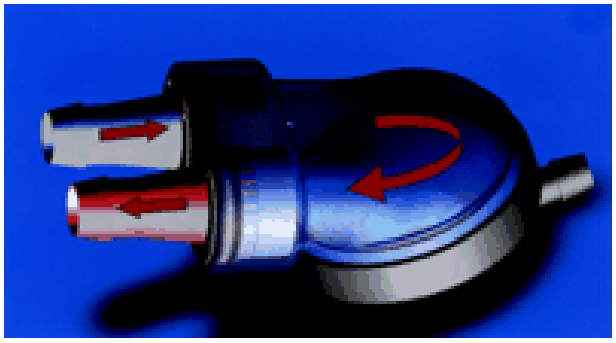 B) 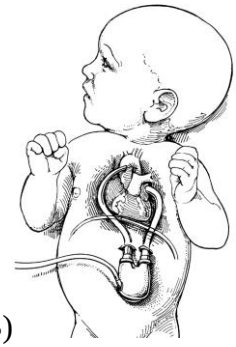

Figure 1-4. A) The Penn State 12 cc PVAD. The arrows indicate the direction of the flow. B) An artist's rendition of how the Penn State PVAD would be implanted in a child as an LVAD [17].

1.4 Fluid Mechanics within the Ventricular Assist Device

Thromboembolic events are a major concern with any device that interacts with blood. The implantation of a foreign material will always evoke a response from the host. When blood interacts with an artificial surface, the surface adsorbs proteins and starts platelet activation. Platelets begin to aggregate in a positive feedback loop, which may lead to thrombus formation [22]. The presence of thrombi not only disrupts the flow field but also have the potential to detach and cause strokes or ischemia.

In VADs, thrombus attached to the blood sac is of particular concern because of the long-term use and complex flow patterns of the blood along the polyurethane surface [23]. Additionally, it has been shown that clot formation correlates to areas of low wall shear rate and stagnation [24]. For segmented polyurethane, a material that is very similar to that used in the Penn State PVAD, Hubbell and McIntire found that the minimum wall shear rate to prevent clot formation is 500 s^{-1} [25]. Preliminary animal tests done on a 15 cc Penn State PVAD showed extensive thrombus formation on the blood sac that was not present in the adult VAD [26]. Because of this finding, it was determined that scaling down the device changed the fluid dynamics in the VAD. This was confirmed by *in vitro* experiments that showed the wall shear rate of the PVAD was much lower than the 500 s^{-1} threshold needed to prevent clot formation [27].

The PVAD has reduced valve effective orifice area and more highly angled valve ports than the adult VAD [28]. The more highly angled valve ports have been shown to

increase wall shear rates, which would potentially reduce the chance of thrombus formation inside the PVAD [29]. As previously mentioned, BSM tilting disk valves produce a stronger inlet jet and a better rotational flow pattern [21]. Strong inlet jets and rotational washing patterns are desirable flow attributes in a VAD because they tend to produce higher wall shear stresses and diminish the residence time of blood. Both of these characteristics have been shown to prevent thrombosis [28] [21].

Further studies associated with the operating conditions of the PVAD have been performed. The PVAD has a higher degree of three-dimensionality than the larger VADs [30]. Previous studies have been conducted in order to understand this three-dimensional flow, which is important in diagnosing the potential for thrombus formation in the smaller device [30]. Stroke volume reduction studies associated with weaning have also been analyzed in the Penn State PVAD [31]. Flow rate reduction that is associated during device weaning and myocardial recovery was shown to significantly alter PVAD flow [31]. End-diastolic delay, defined as the time between the end of diastole and the start of systole, has also been shown to significantly alter PVAD flow [32]. The results of these studies highlight the importance of understanding the PVAD flow in order to improve device functionality in different applications.

1.5 Viscoelasticity of Blood

Hematocrit (HCT) is defined as the ratio of the volume of packed red blood cells to the total volume of whole blood. Hematocrit has been shown to vary more so in pediatric patients than in adults. Pediatric blood hematocrit usually varies anywhere from 20%-60% [33]. Additionally, animal hematocrit tends to be lower, which is important because the PVAD is tested in sheep that usually have a hematocrit of around 27% [34]. The viscoelastic properties of blood change in accordance with the hematocrit [35]. Generally, lower hematocrit blood has both a lower viscosity and elasticity than higher hematocrit blood [35]. It has been shown that changes in the viscoelasticity of blood can have a dramatic effect on the fluid dynamics within medical devices [33]. The fluid dynamics associated with such devices directly impact the potential for thrombus formation and blood damage, both of which can lead to device failure or more serious adverse events like strokes [23]. Because changes in hematocrit affect the fluid dynamics and can impact the efficacy of mechanical circulatory support devices, it is important to understand exactly how hematocrit alters the flow in the PVAD.

1.6 Purpose

This study will focus on the effect of hematocrit on the fluid dynamics in the PVAD. Three different non-Newtonian blood analogs were created to match the known viscoelastic properties of 20%, 40%, and 60% hematocrit pediatric blood. Particle image velocimetry (PIV), a flow visualization technique, was used to quantify the flow of each of these fluids through the PVAD. Using an *in vitro* flow loop designed to mimic the pediatric circulatory support system, whole field velocity maps of the flow through the PVAD were developed under physiological conditions. This study aims at identifying the differences in the flow of the three different hematocrit analogs. By understanding this phenomenon, it will be easier to make sense of animal testing data and improve the efficacy of the PVAD in patients where hematocrit could have a large range.

Chapter 2 PARTICLE IMAGE VELOCIMETRY THEORY

2.1 PIV Setup

Several non-invasive flow measurement techniques have previously been used to study the flow in VADs. Generally, these techniques use either a LaGrangian or Eulerian method of characterizing the fluid dynamics associated within a device. A common example of a LaGrangian technique is laser Doppler velocimetry (LDV), which is used to collect velocity and other fluid dynamic data at a point. An example of an Eulerian method would be particle image velocimetry (PIV), which allows for the characterization of an entire flow field at one time. For this particular application, PIV is beneficial because it offers a global perspective of the flow through the PVAD. Two-dimensional planar PIV, which was used in this study, involves a dual-pulsed laser, optics, and a high speed camera. The optics condition the laser light into a sheet that illuminates the flow field of interest while the camera records the movement, as shown in **Figure 2-1**.

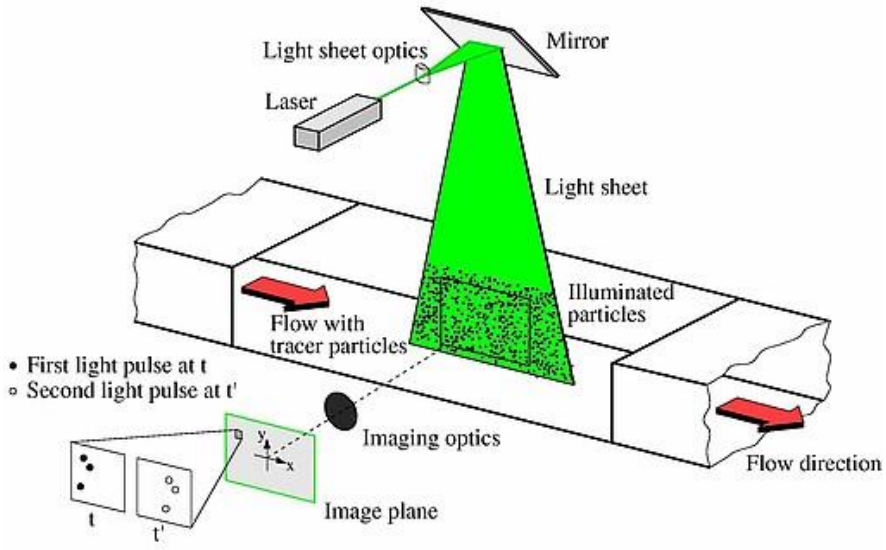

Figure 2-1. An example PIV setup [36].

2.2 Tracer Particles

In order to use PIV, the fluid needs to be seeded with tracer particles. The laser light is conditioned by optics into a thin light sheet that illuminates the particles in the fluid. The laser sends two pulses separated by a known time (ΔT) while the high speed camera captures two images of the illuminated particles. The location of the particles and the change in time between the image pair are then used to calculate the velocity of the particles in both the x and y directions using **Equations 1a and 1b:**

$$u = \frac{\Delta x}{\Delta T} \qquad (1a)$$

$$v = \frac{\Delta y}{\Delta T} \qquad (1b)$$

A modified Stokes number is calculated in order to ensure that the particles travel with the streamlines of a flow field and are an accurate representation of the flow [37]. The Stokes number is a dimensionless parameter that characterizes the flow of particles suspended in a fluid. The modified Stokes number is the particle relaxation time (τ_s) divided by the laser pulse delay (ΔT). This number needs to be much less than 1 to guarantee that the particle movement represents the bulk flow [37]. The mathematical representations of the particle relaxation time (τ_s) and the modified Stokes number are shown in **Equations 2a and 2b**:

$$\tau_s = \frac{\rho_p d_p^2}{18\mu_f} \qquad (2a)$$

$$\frac{\tau_s}{\Delta T} \ll 1 \qquad (2b)$$

The particle relaxation time is a function of the particle density (ρ_p), particle diameter (d_p), and the viscosity of the fluid (μ_f). As long as the modified Stokes number shown in **Equation 2b** is much less than 1, the particle path will be an accurate representation of the bulk fluid path [37].

2.3 Cross-Correlation

In order to develop the velocity maps using PIV, each image is broken into smaller interrogation regions. Cross-correlation of each interrogation region is achieved by using pattern recognition to identify the group particle displacement shift between images. This displacement corresponds to a peak in the cross-correlation pattern, which results in representative group particle displacement for that interrogation region. **Equations 1a and 1b** are then used to calculate the velocity vectors based upon the displacement of the particles and the change in time between images. An example of a cross-correlation peak is shown in **Figure 2-2**.

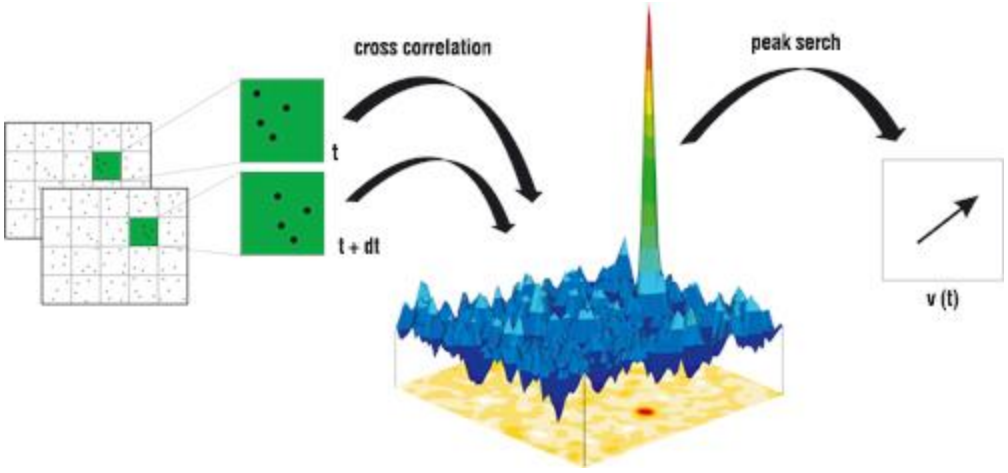

Figure 2-2. Sample cross-correlation peak [38].

2.4 Potential Error

There are several potential errors associated with PIV as a fluid measurement technique. There is inherently some thickness associated with the laser light sheet used in two-dimensional planar PIV. While the thickness is almost negligible (~500 μm), the laser light can illuminate particles that are not exactly in the same two-dimensional plane. Additionally, particles can move into and out of the plane between successive images, especially in highly three-dimensional flows [37]. Other errors are related to particle diameter, pixel size, and the size of the interrogation region [24] [37].

Chapter 3 MATERIALS AND METHODS

3.1 The 12 cc Penn State PVAD

In order to use PIV, an acrylic model of the 12 cc Penn State PVAD was manufactured. This model allows the laser light to illuminate a plane of particles that can then be acquired by a high-speed camera placed perpendicular to the light sheet. A polyurethane diaphragm was placed into the model and connected to an air line controlled by a pneumatic driver. This driver controlled the motion of the diaphragm by rhythmically pulsing air into and vacuuming air out of the chamber to expand and contract the diaphragm. Two 17 mm BSM tilting disc valves are placed in the inlet and outlet ports of the device and are rotated 15^{o} in order to increase wall shear rates, which aid in the reduction of thrombus formation [29]. The 12 cc PVAD is shown in **Figure 3-1.**

A) 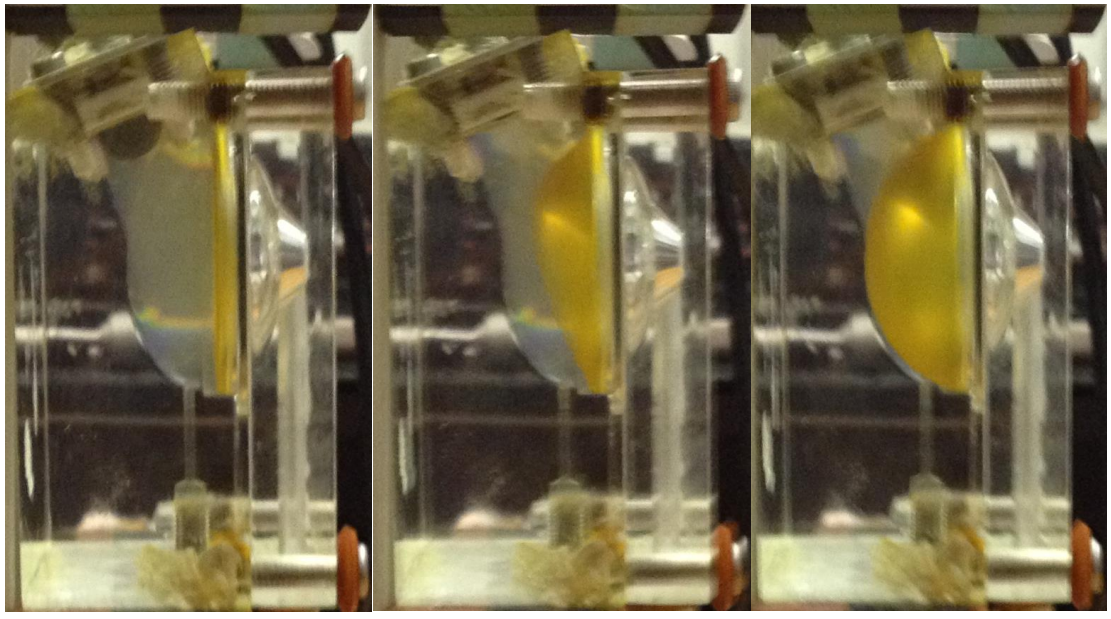

B) 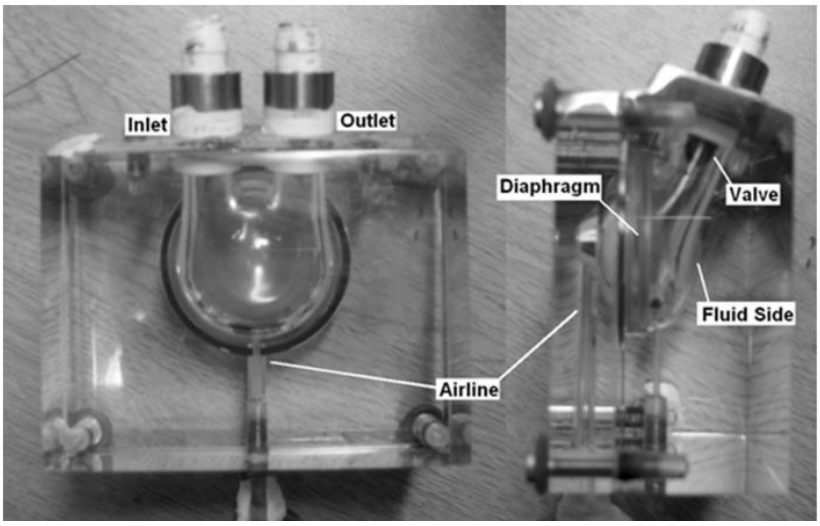

Figure 3-1. A) PVAD at various stages of the cardiac cycle. B) Labeled PVAD [29].

3.2 The Mock Circulatory System

To mimic physiologically relevant conditions, a pediatric mock circulatory loop was assembled. This loop was based upon the loop developed by *Rosenberg et al.* [39]. Because that loop was assembled for an adult, the loop was adapted for a pediatric application by reducing the overall volume and increasing the resistance. The loop consists of the acrylic PVAD, two compliance chambers, a venous reservoir, and a resistance element. Each component was connected using flexible Tygon 3603 tubing (Saint-Gobain Performance Plastics, Aurora, OH) ranging from ¼" to ½" in diameter depending on the connection. A diagram of the mock circulatory loop is shown in **Figure 3-2.**

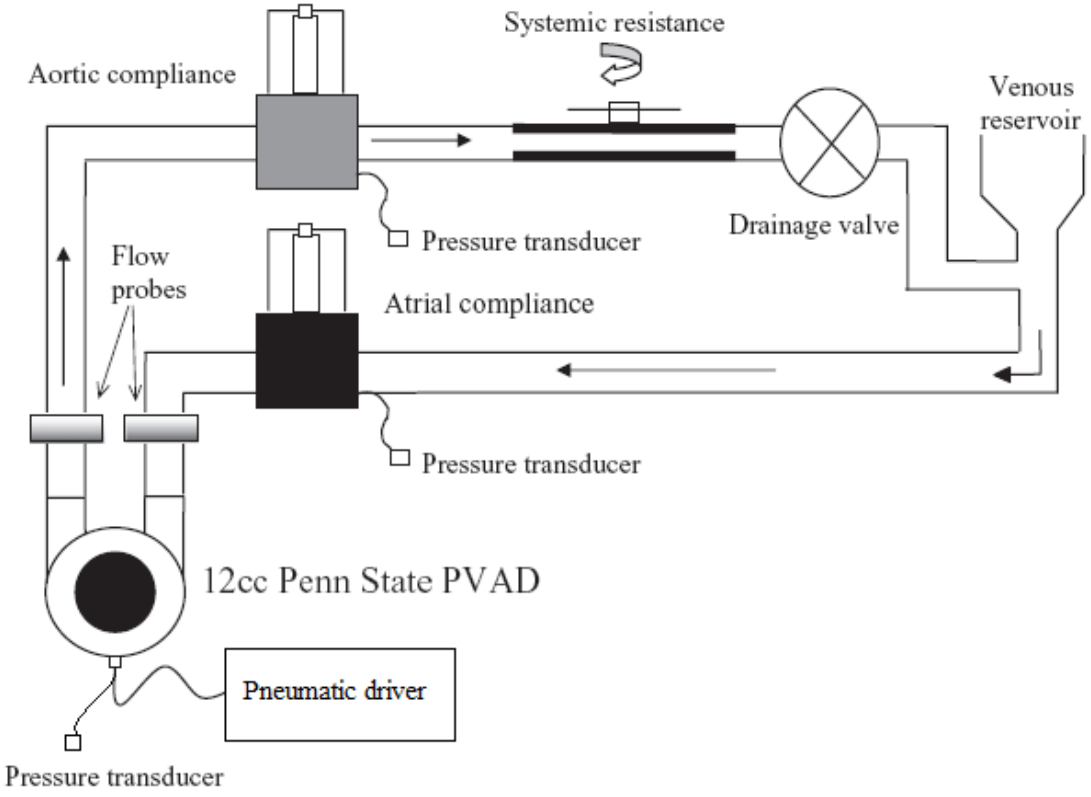

Figure 3-2. Schematic of the pediatric mock circulatory loop [28].

The mock circulatory system can be thought of as an electrical circuit with resistance and capacitance. The resistive element consists of two rectangular plates that clamp down a section of tubing downstream of the VAD. This component can be adjusted in order to raise or lower the magnitude of the aortic pressure.

There are two capacitance components, one on the atrial side and one on the aortic side. These components are meant to account for the natural compliance of the atrium and aorta and are labeled as compliance chambers, which are piston-spring devices with a

dynamic volume that changes linearly with pressure. The atrial chamber precedes the inflow to the VAD while the aortic chamber is on the outlet side of the VAD. These components can be adjusted so as to change the atrial and aortic pressure waveforms.

In order to drive the VAD, a pneumatic driver is used. The driver controls the beat rate, systolic duration, and systolic/diastolic pressures for the PVAD. Air is vacuumed out of the VAD to contract the diaphragm and allow atrial filling. Then air is pushed into the VAD in order to expand the diaphragm and eject the fluid into the aorta. This expansion and contraction of the VAD occurs rhythmically based upon the desired beat rate and systolic duration. For all PIV experiments in this study, the beat rate was set to 75 beats/min and the systolic duration was 340 ms. A picture of the pneumatic driver is shown in **Figure 3-3.**

A) 

B) 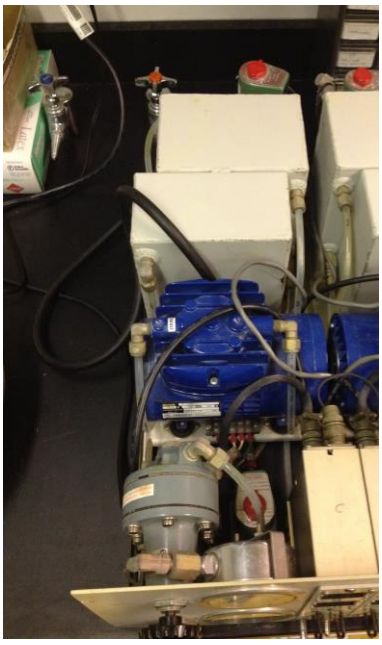

Figure 3-3. A) Front and B) top views of the pneumatic driver that controls the PVAD. The driver is connected to an air line and controls the beat rate and systolic duration of the pump.

3.3 Fluid Preparation

The three different non-Newtonian blood analogs were created using a mixture of water, sodium iodide, glycerin, and Xanthan gum. Each fluid was designed to match the viscoelastic properties of 20%, 40%, and 60% hematocrit pediatric blood. **Table 3-1** shows the percentage by weight of each ingredient for the three different blood analogs. Because the fluids are non-Newtonian, the viscoelasticity is a function of the shear rate. The Vilastic-3 Viscometer (Austin, TX) was used to calculate the viscoelasticity of the analogs and blood sample. **Figure 3-4** shows the viscoelastic curves of each blood analog compared to a sample of 40% hematocrit pediatric blood. Both the viscosity and elasticity values increase for increasing hematocrit.

Table 3-1. Blood analog composition by weight.

Ingredient	20% HCT	40% HCT	60% HCT
Sodium Iodide	50%	50%	50%
Water	34.991%	33.97%	27.95%
Glycerin	15%	16%	22%
Xanthan Gum	0.009%	0.03%	0.05%

A)

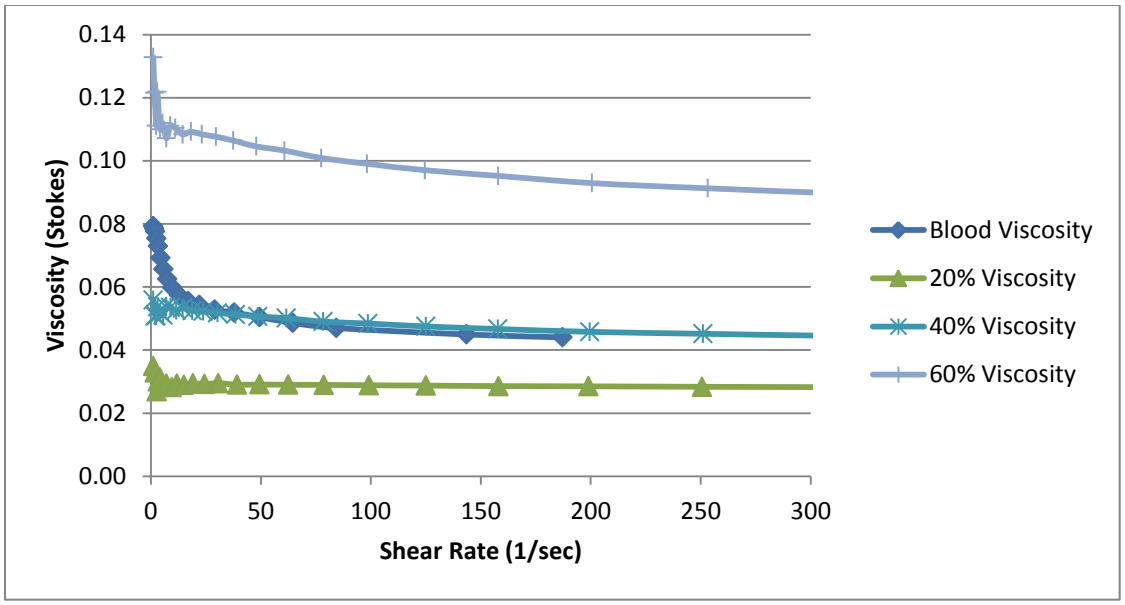

B)

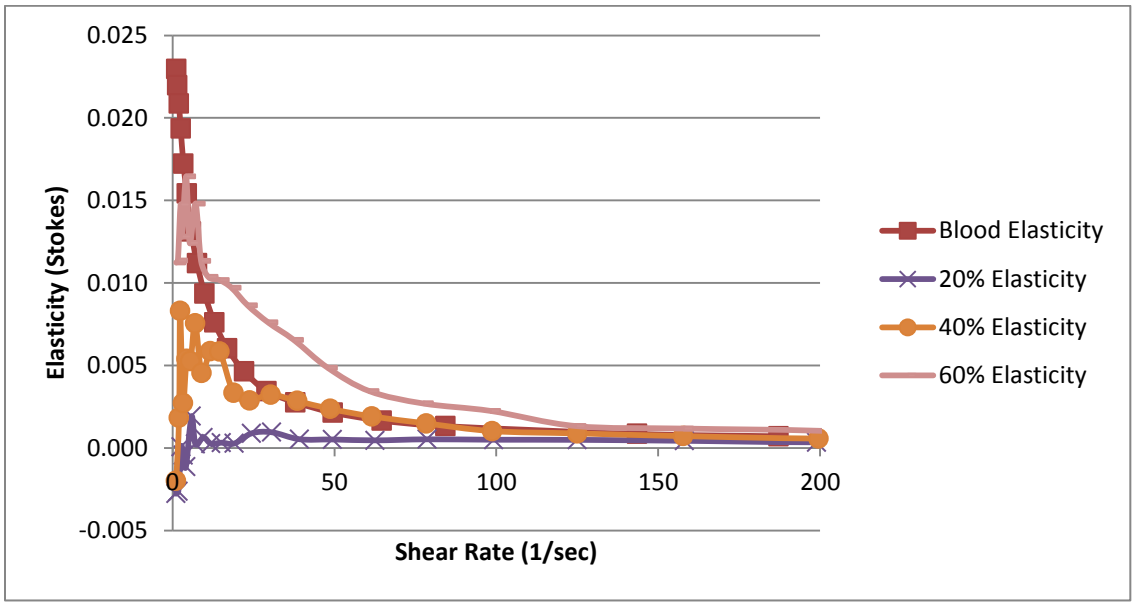

Figure 3-4. All three blood analogs are non-Newtonian so the viscoelasticity is shown as a function of shear rate. All values are shown in Stokes. A) Viscosity and B) elasticity comparison of the three blood analogs with the 40% HCT pediatric blood sample.

In order to use PIV, the refractive index of the fluid was adjusted to 1.49 to match the refractive index of the acrylic model. Additionally, the fluids were seeded with tracer particles, which is a necessary component of PIV. After creating the fluids, the tracer

particles were added to the reservoir in the loop in order to attain the proper seeding density for use in PIV. Ten μm glass beads were used as the tracer particles. The beads had a density of 205 g/cm^3, which corresponds to a modified Stokes number of 3.47 x 10^{-7}, which is much less than 1 as desired by **Equation 2b**.

3.4 Operating Conditions

In order to determine the effect of hematocrit on the fluid dynamics in the PVAD, the operating conditions of the loop were consistently maintained throughout all of the experiments. The PVAD was operated at 75 beats/min with a systolic duration of 340 ms. The flow rate for all three fluids was 1.4 L/min while the outlet pressure was 90/60 mmHg. One of the key operating conditions for the PVAD is the end diastolic delay, which is defined as the time between the end of diastole and the start of systole. On the waveforms, the end of diastole was considered when the inflow waveform goes to zero, and the start of systole is the positive spike in the drive pressure. Based upon previous studies, an end diastolic delay of 10 ms ensures complete filling of the PVAD while minimizing the potential for thrombus formation throughout the cardiac cycle [32]. For these experiments, the end diastolic delay was kept between 0 and 10 ms. A summary of the operating conditions is shown in **Table 3-2.**

Table 3-2. Operating conditions for the pediatric mock circulatory loop.

Parameter	Value
Beat Rate	75 beats/min
Systolic Duration	340 ms
Flow Rate	1.4 L/min
Aortic Pressure	90/60 mmHg
End Diastolic Delay	<10 ms

For each experiment, waveforms were captured to monitor the pressures and velocities at various points in the flow loop. A WaveBook data acquisition device (IOtech, Inc., Cleveland, OH) was used to monitor the pertinent values and display them in real time on a computer. An ultrasonic flow probe system (Transonic Systems, Inc., Cleveland, OH) was used to capture the inflow and outflow waveforms. Pressure transducers (Maxxim Medical, Athens, OH) were also used to monitor the inlet and outlet pressures at both compliance chambers and the drive pressure. A Waverunner oscilloscope (Teledyne Lecroy, Chestnut Ridge, NY) was used in conjunction with the data acquisition device to trigger the system at known points in the cardiac cycle. This triggering mechanism, shown in **Figure 3-5**, allowed for data to be collected at the same point in the cardiac cycle so as to capture data throughout an entire beat. For each fluid, the waveforms were almost identical. The only minor difference is the development of the inflow waveforms. The 20% HCT blood analog spikes at a higher velocity earlier in the cardiac cycle than both the 40% and 60% HCT blood analogs. The outflow waveforms and driveline pressure waveforms are extremely similar for all three fluids. **Figure 3-6** shows a sample waveform for each fluid.

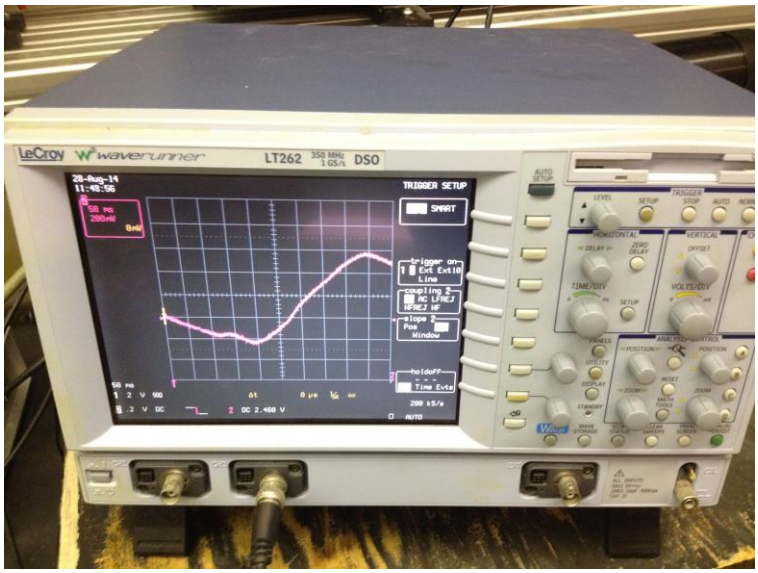

Figure 3-5. Oscilloscope used for triggering off of the outlet pressure waveform.

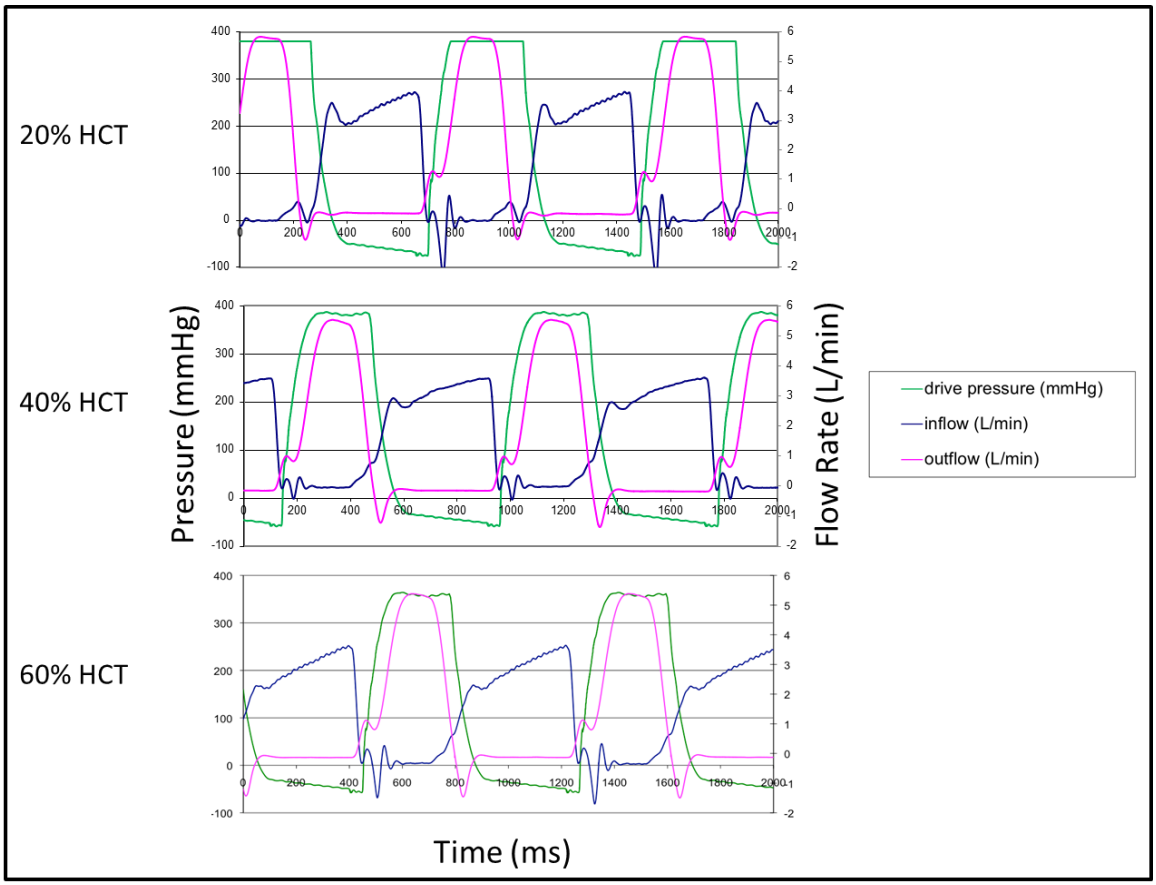

Figure 3-6. Sample waveforms for the 20%, 40%, and 60% HCT blood analogs.

3.5 Particle Image Velocimetry

Two-dimensional planar particle image velocimetry was used to measure the flow in this study. Whole field velocity flow maps were developed using PIV and were used to characterize the flow through the PVAD for all three blood analogs. The PIV parameters were consistent for all experiments.

3.5.1 PIV System & Setup

A Gemini PIV 15 system (New Wave Research, Inc., Fremont, CA) was used for the experiments and consisted of dual Nd:YAG lasers that produced a 6 mm diameter beam as the light source. The beam was transformed into a 500 μm thick light sheet using a -25 mm cylindrical lens coupled with a 25 mm diameter high-energy mirror and a 500 mm spherical lens. The light sheet illuminated the plane of interest, and images of the flow field were captured with a two-megapixel charge-coupled device (CCD) camera (TSI, Inc., Shoreview, MN) with a Micro-Nikkor 60 mm F1.8 lens (Nikon Corporation, Tokyo, Japan). A LaserPulse Synchronizer (TSI, Inc., Shoreview, MN) controlled the laser pulsing through Insight 3G^{TM} software (TSI, Inc., Shoreview, MN) that synchronized the laser pulse emissions with the camera exposure in order to capture image pairs separated by a known change in time. A picture of the PIV setup is shown in **Figure 3-7**.

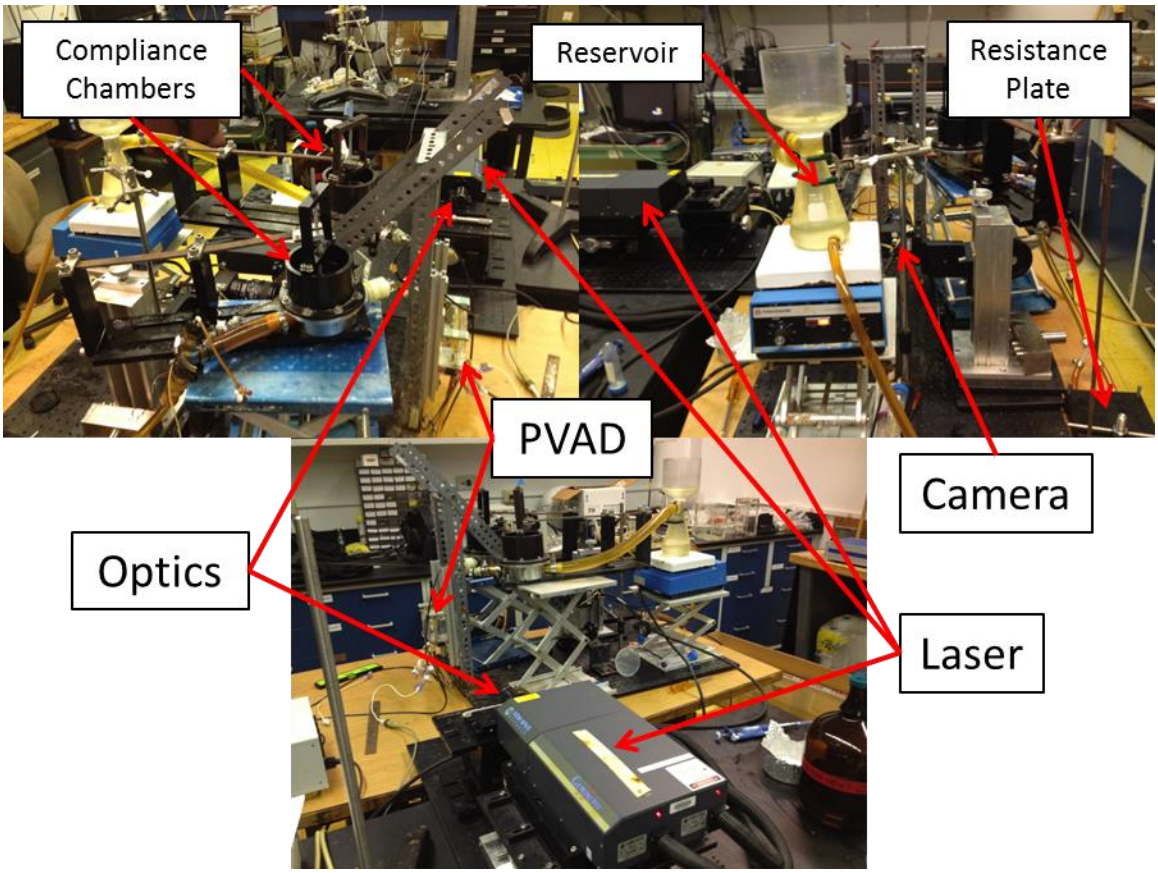

Figure 3-7. Laser and camera positioning for the PIV experiments.

3.5.2 Data Acquisition

PIV data was collected at four different planes for each of the three different blood analogs. The planes are all located parallel to the diaphragm and are measured by the distance they are located from the edge of inlet/outlet port boundary. In order to obtain sufficient vector counts needed for reliable data, 200 image pairs were collected every 50 ms of the cardiac cycle for all fluids and all planes. **Figure 3-8** shows the location of the parallel planes.

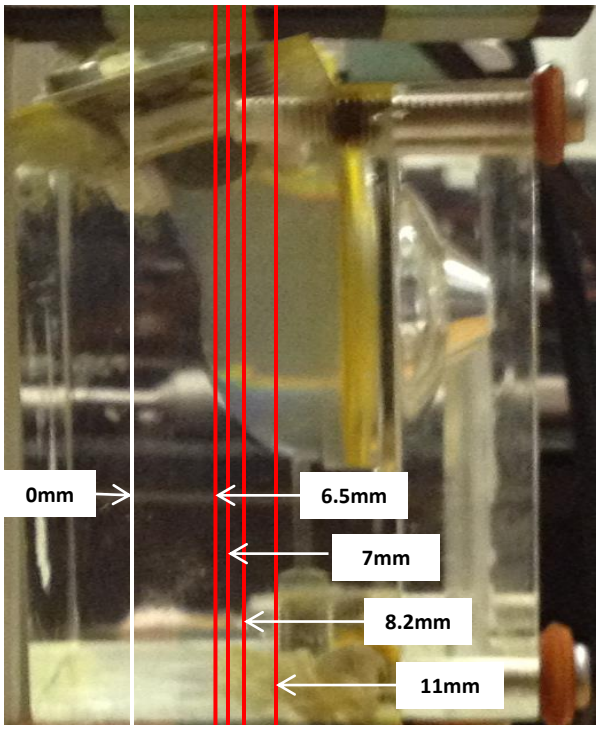

Figure 3-8. Location of the parallel planes where data was collected.

Insight 3G^{TM} software (TSI, Inc., Shoreview, MN) was used to obtain the velocity vectors during the PIV experiments. **Table 3-3** and **Figure 3-9** show imaging parameters used for the experiments.

Table 3-3. Imaging parameters for the PIV experiments.

Parameter	Value
PIV Frame Mode	Straddle
Pulse Repetition Rate	14.50 Hz
Laser Pulse Delay	400 µs
Delta T (ΔT)	100-300 µs
PIV Exposure	405 µs

A) 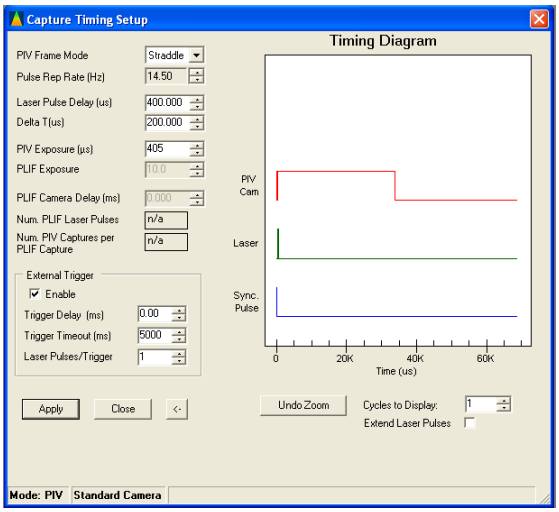

B) 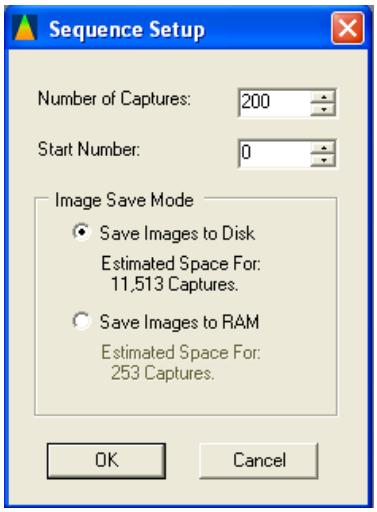

Figure 3-9. Image of the A) timing setup and B) sequence setup in Insight 3G™.

The laser control panels shown in **Figure 3-10** were used to control the intensity of the lasers. The laser intensity was of particular importance for obtaining sufficient vector counts. Because dual lasers were used, the intensity of each image in an image pair needed to be matched as closely as possible in order to properly track the movement of the particles. Differences in laser intensity between two images in a pair would result in poor particle tracking [37].

Figure 3-10. Control panels for the two lasers, and the laser synchronizer.

3.5.3 Processing

After collecting the raw data, the images were post-processed through an in-house Matlab® 7.1 (The MathWorks, Inc., Natick, MA) program that identified the fluid boundary and masked out the background portion of the image. An example of an image being masked in Matlab is shown in **Figure 3-11.**

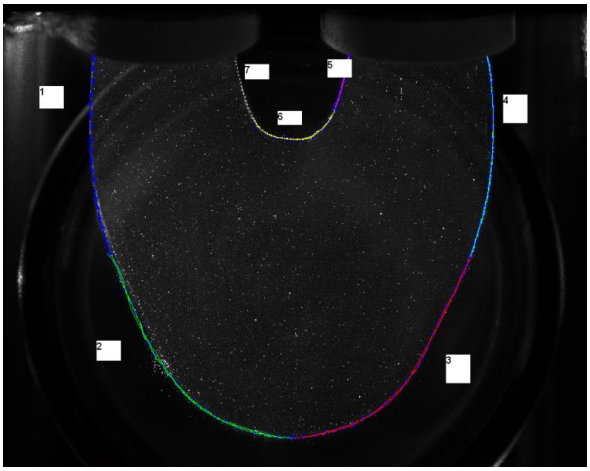

Figure 3-11. Sample image being masked.

After masking, the images were processed using Insight 3G™ software (TSI, Inc., Shoreview, MN), which separated each image pair into 32 x 32 pixel interrogation regions. The displacement of the tracer particles was analyzed using a cross-correlation method to detect particle movement between image pairs. The time difference between the images in a pair, called the laser pulse delay, was adjusted from 100 μs to 300 μs to optimize particle displacements. Displacement vectors for the particles were developed using a recursive Nyquist grid, a fast Fourier transform, and a Gaussian peak algorithm. The vectors were then divided by the laser pulse delay to obtain fluid velocities. Two-

dimensional velocity flow maps were then produced by averaging the two hundred image pairs. **Table 3-4** and **Figure 3-12** show the processing parameters used in order to develop the velocity vectors.

Table 3-4. Processing parameters for PIV experiments.

Parameter	**Value**
Grid Engine	Recursive Nyquist
Correlation Engine	Hart Correlator
Peak Engine	Bilinear Peak
Starting Spot Dimensions	32
Final Spot Dimensions	16
Width of Image	1600 pixels
Height of Image	1192 pixels
Calibration	45.12 µm/pixel

A) 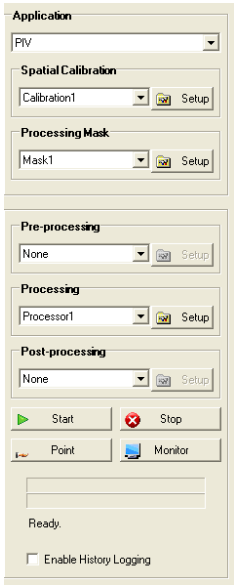

B) 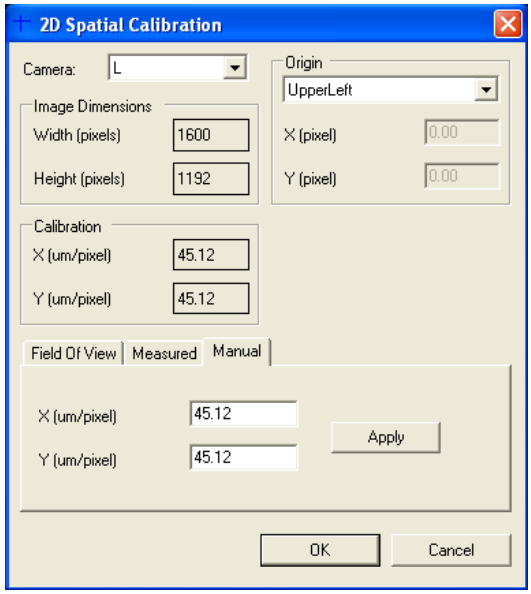

C) 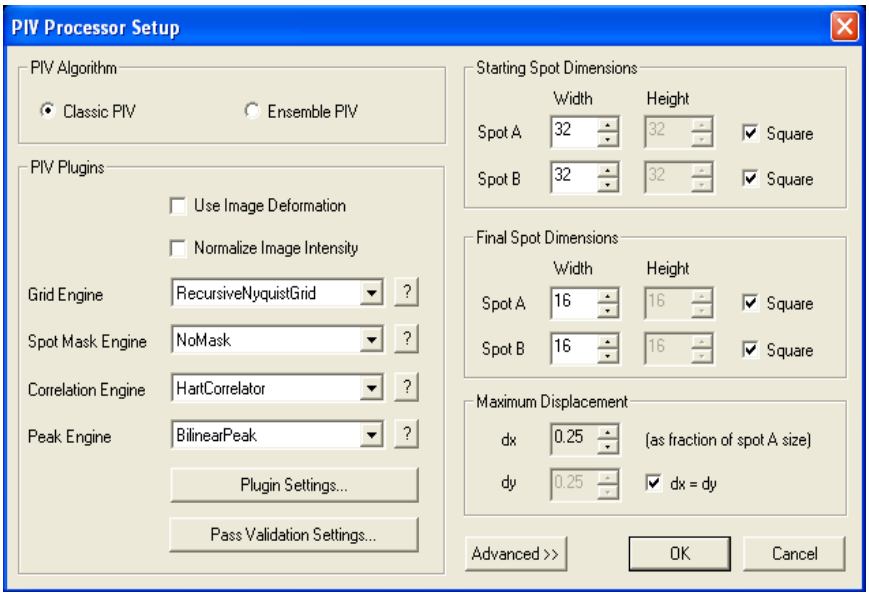

Figure 3-12. A) Processing tab, B) spatial calibration, and C) PIV processor setup in Insight 3G™.

Chapter 4 RESULTS

Using PIV, whole field velocity maps were developed for each of the three different blood analogs at all four parallel planes. The velocity maps show representative flow fields at 50 ms intervals throughout the cardiac cycle. The PVAD was operated at 75 beats/min, which resulted in an 800 ms cardiac cycle. The beginning of diastole was considered the beginning of the cycle and lasted the first 460 ms, while systole lasted for the remaining 340 ms. PIV data was taken throughout the cardiac cycle except early in diastole and late in systole when the movement of the diaphragm interfered with the laser sheet. This interference was most pronounced in the 11 mm plane because of its proximity to the diaphragm. However, data were collected at all points during the cardiac cycle where the diaphragm did not interfere with the plane of interest.

4.1 20% Hematocrit

The 20% HCT blood analog was the least viscoelastic of the three fluids. A strong inlet jet was observed early in diastole that developed into a solid body rotation before washing the walls toward the outlet port during systole.

4.1.1 Diastole

At the beginning of diastole, a strong inlet jet developed along the outer wall of the inlet port. A secondary inlet jet from the minor orifice of the BSM valve was created along the inner portion of the inlet port with a peak velocity of 0.75 m/s at 100 ms. This flow pattern was consistent with the three dimensional flow associated with the device. The secondary jet diminished as diastole continued and the primary inlet jet along the outer

wall strengthened. The primary jet peaked at 0.8 m/s and penetrated into the bottom of the device, which initiated a rotational flow pattern at 200 ms in the 7 mm plane, shown in **Figure 4-1**.

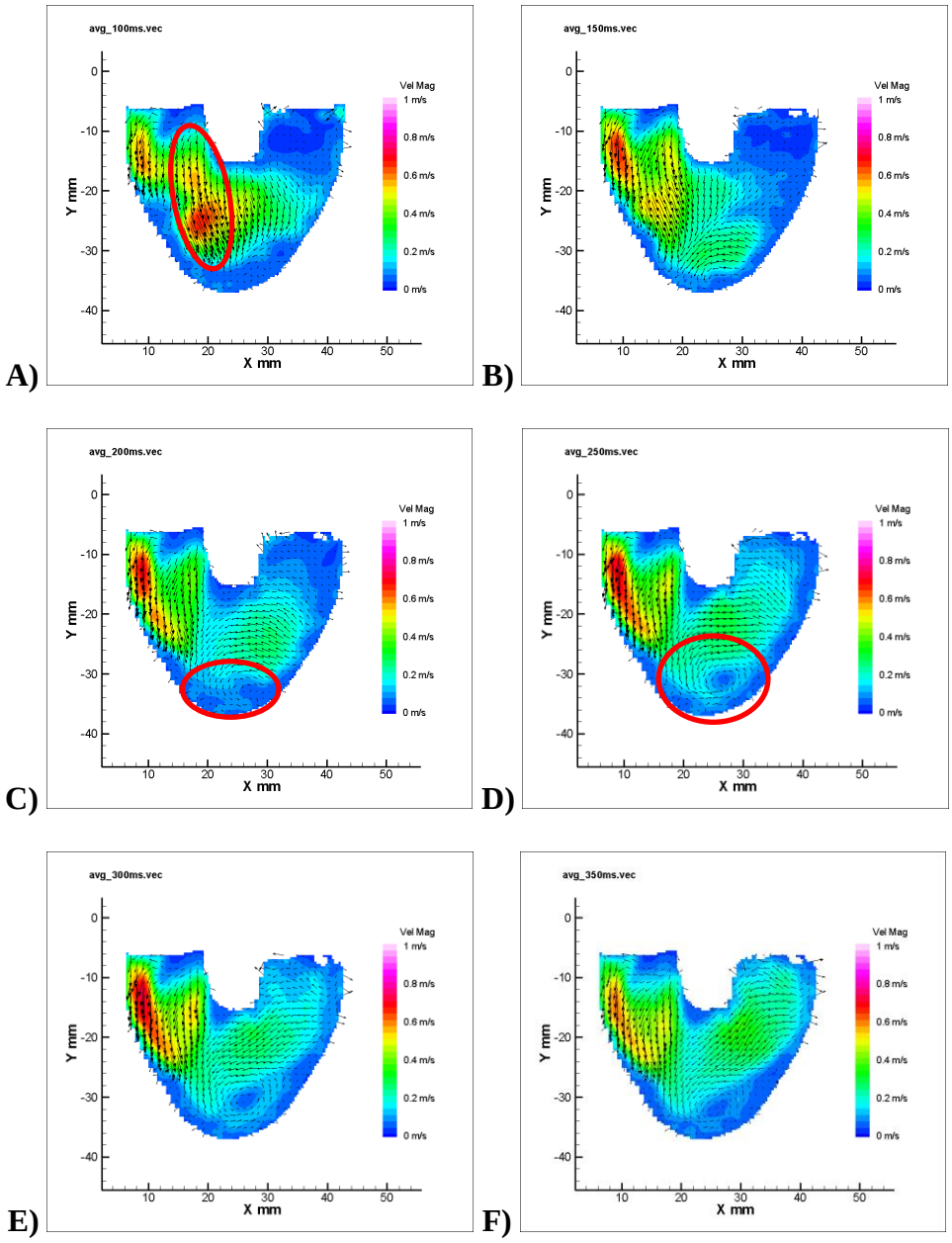

Figure 4-1. 7 mm plane at A) 100 ms, B) 150 ms, C) 200 ms, D) 250 ms, E) 300 ms, and F) 350 ms. The red circle in image A highlights evidence of three-dimensionality. The two circles in images C and D highlight the development of the rotational flow at the apex of the PVAD.

In contrast to the 7 mm plane, the rotational flow pattern was evident earlier in diastole in the 8.2 mm plane, shown in **Figure 4-2**. There was some evidence of a secondary inlet jet but the velocity peaked at 0.5 m/s, which was less than the peak velocity of the primary inlet jet along the outside wall of 0.8 m/s. The primary inlet jet maintained flow throughout diastole, setting up the solid body rotation that persisted through the entirety of diastole. The inlet jet velocity increased from 0.6 m/s at 150 ms to 0.8 m/s at 300 ms while maintaining coherence through 350 ms.

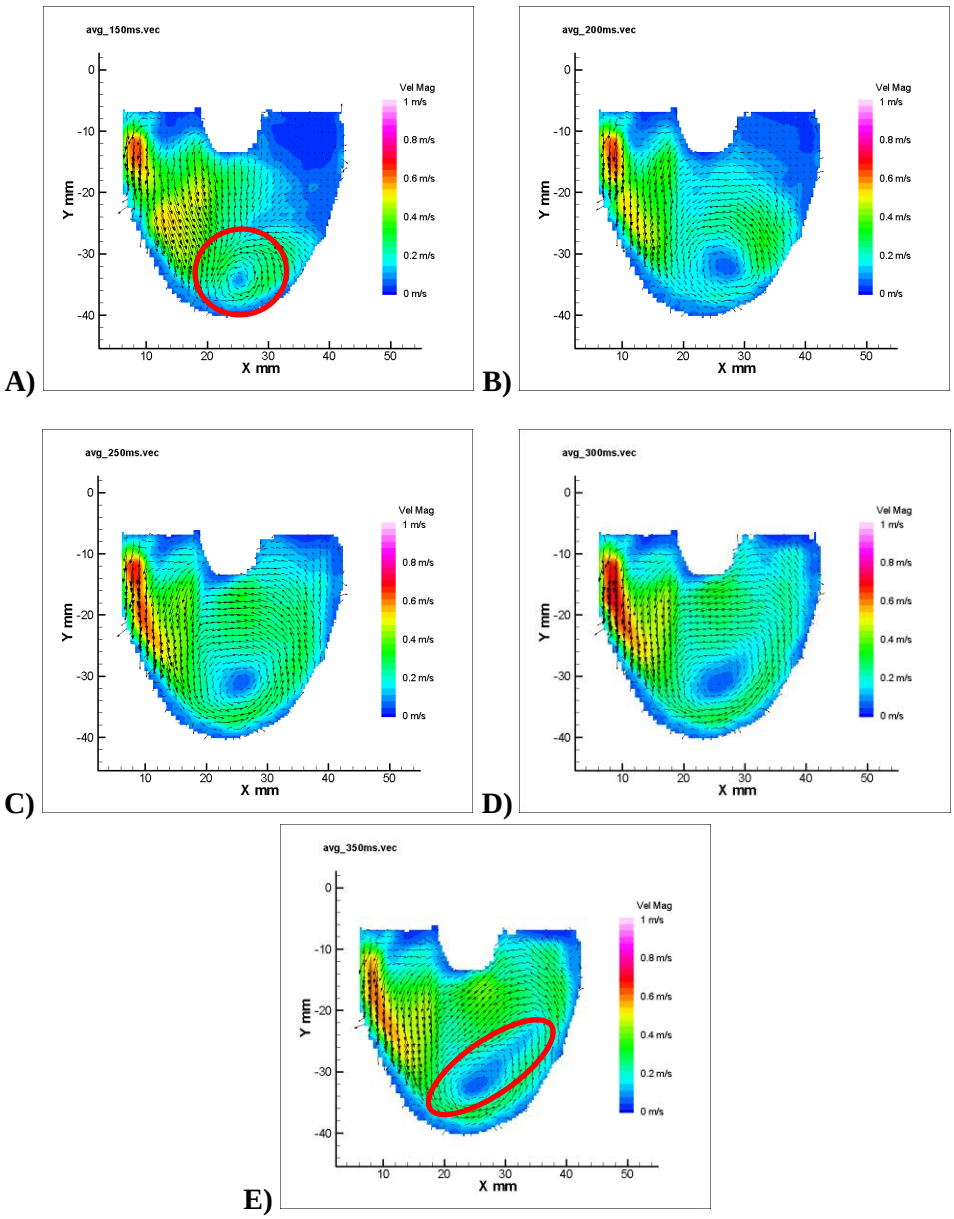

Figure 4-2. 8.2 mm plane at A) 150 ms, B) 200 ms, C) 250 ms, D) 300 ms, and E) 350 ms. The red circles highlight the formation of the solid body rotation. The 20% HCT blood analog begins to penetrate higher up on the outlet side later in diastole, as shown in image E.

A similar pattern was evident in the 11 mm plane. The solid body rotation began even earlier in this plane and was evident at 200 ms. The inlet jet continued to increase in velocity through diastole while peaking at 0.6 m/s at 350 ms, as shown in **Figure 4-3**.

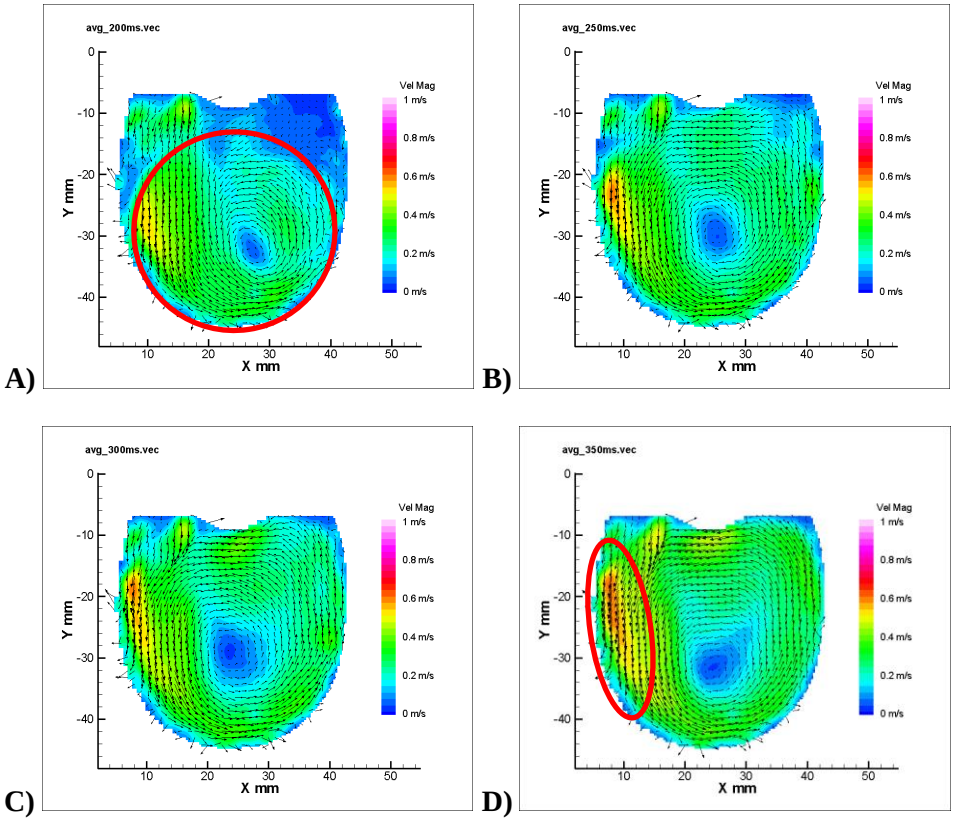

Figure 4-3. 11 mm plane at A) 200 ms, B) 250 ms, C) 300 ms, and D) 350 ms. The red circle in image A highlights the rotational flow pattern that is beginning to develop. The inlet jet at 350 ms is highlighted in image D.

After 350 ms, the primary inlet jet began to dissipate while the solid body rotation continued to develop. This fluid dynamic pattern served to wash the walls along the outer edge of the device. The rotational flow was maintained throughout the remainder of diastole as the flow prepared to be ejected from the device. This phenomenon is depicted in **Figure 4-4**.

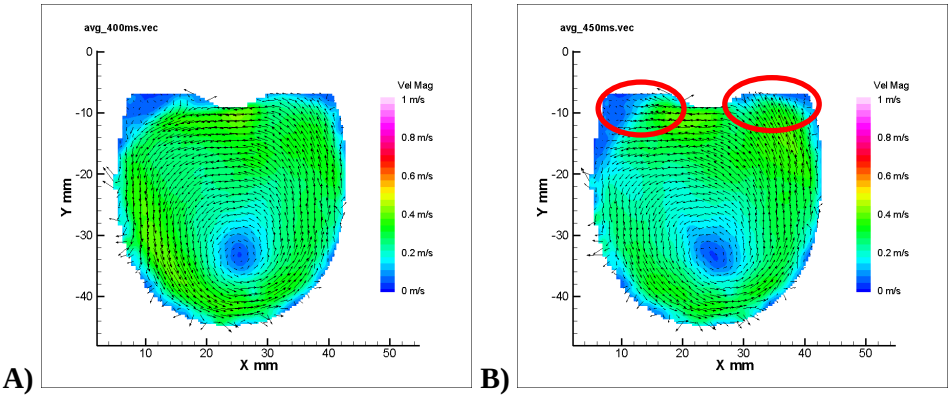

Figure 4-4. 11 mm plane at A) 400 ms and B) 450 ms. The red circles highlight the dissipation of the inlet jet as the 20% HCT blood analog prepares to leave the outlet side.

4.1.2 Systole

The first sign of systole in the PIV data occurred at 500 ms when the outlet jet began to form. The development of the outlet jet was consistent with the operating conditions of the PVAD where systole began at 460 ms into the cardiac cycle. At this point, the inlet valve closed and the outlet valve opened, beginning systole. The outlet jet encompassed the entire outlet port at the 500 ms and 550 ms time points as it began to increase in velocity. At 600 ms and 650 ms, however, the outlet jet split into two jets on the inside and outside of the port walls. In addition, higher velocity flow moving toward the outlet was seen lower in the device before being split as it moved closer to the outlet valve. The

peak velocity of the outlet jet increased from 0.55 m/s at 500 ms to 1.1 m/s at 650 ms. These phenomena are shown in the 6.5 mm plane in **Figure 4-5**.

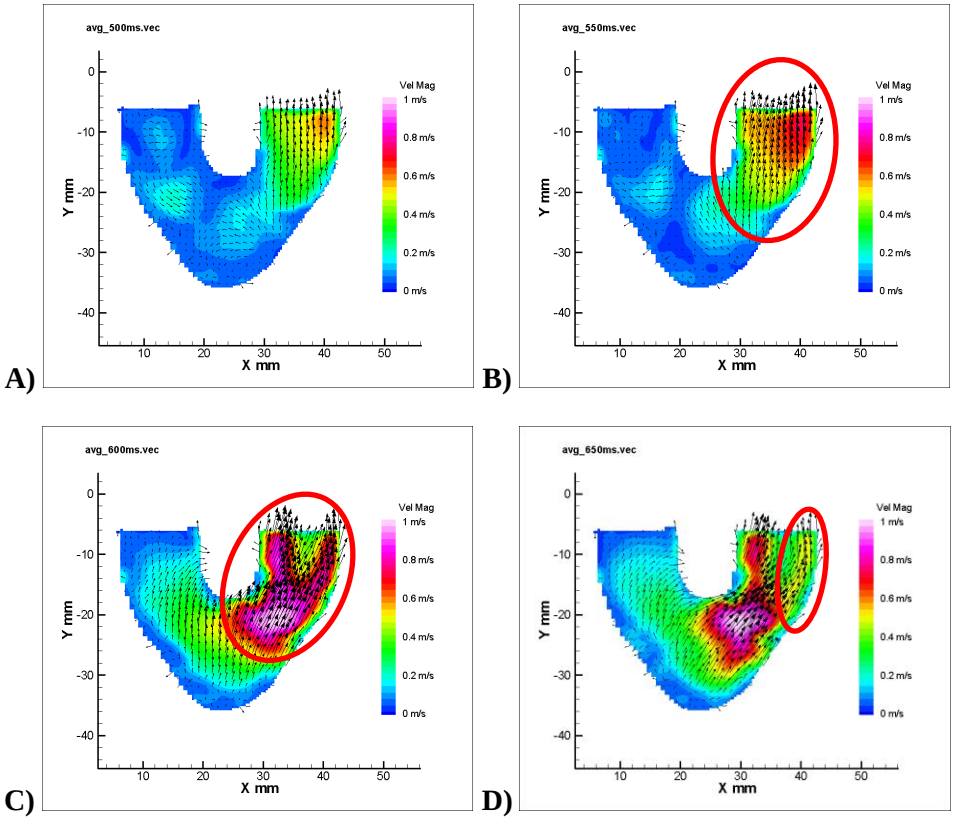

Figure 4-5. 6.5 mm plane at A) 500 ms, B) 550 ms, C) 600 ms, and D) 650 ms. The red circles highlight the development of a coherent outlet jet in image B and the flow blockage evident upstream of the outlet valve occluder in images C and D.

A similar flow pattern was developed in the 7 mm and 8.2 mm planes. The outlet jet began to form at 500 ms and continued throughout the remainder of the cardiac cycle. The outlet flow splitting was also evident at 600 ms and 650 ms in both planes. In the 8.2 mm plane, there was evidence of the solid body rotation pattern dissipating at 500 ms and

starting to give way to the outlet flow that followed. The 7 mm and 8.2 mm outlet data is shown in **Figure 4-6** and **Figure 4-7**, respectively.

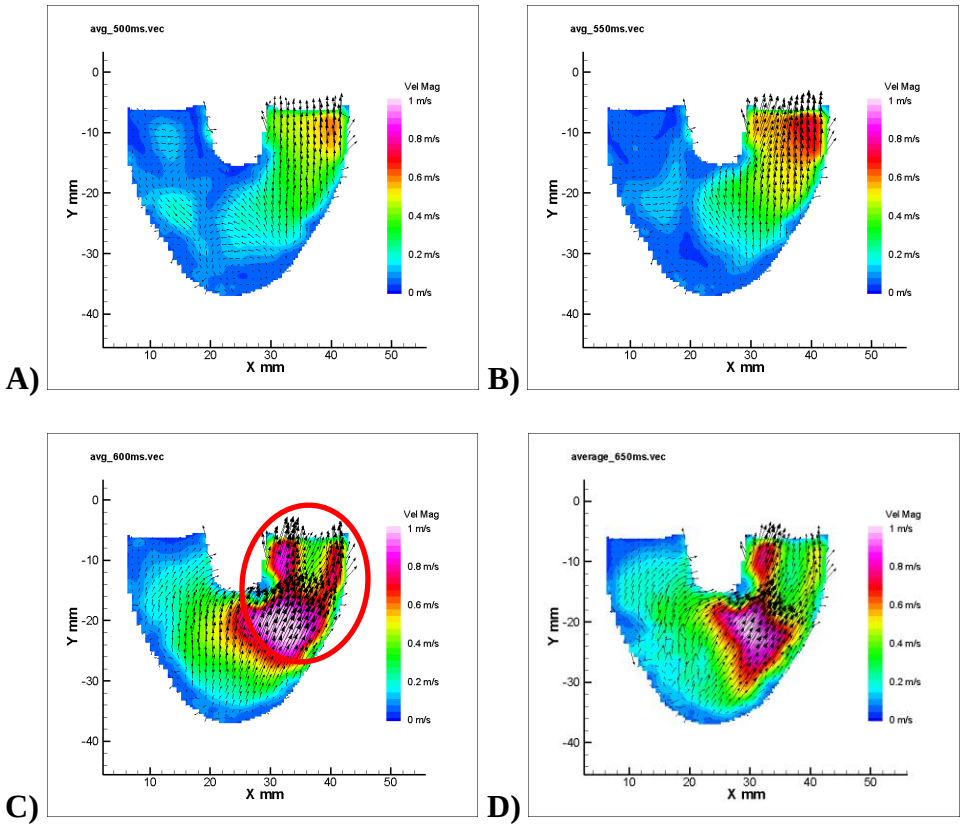

Figure 4-6. 7 mm plane at A) 500 ms, B) 550 ms, C) 600 ms, and D) 650 ms. The red circle highlights the outlet flow blockage that develops at 600 ms.

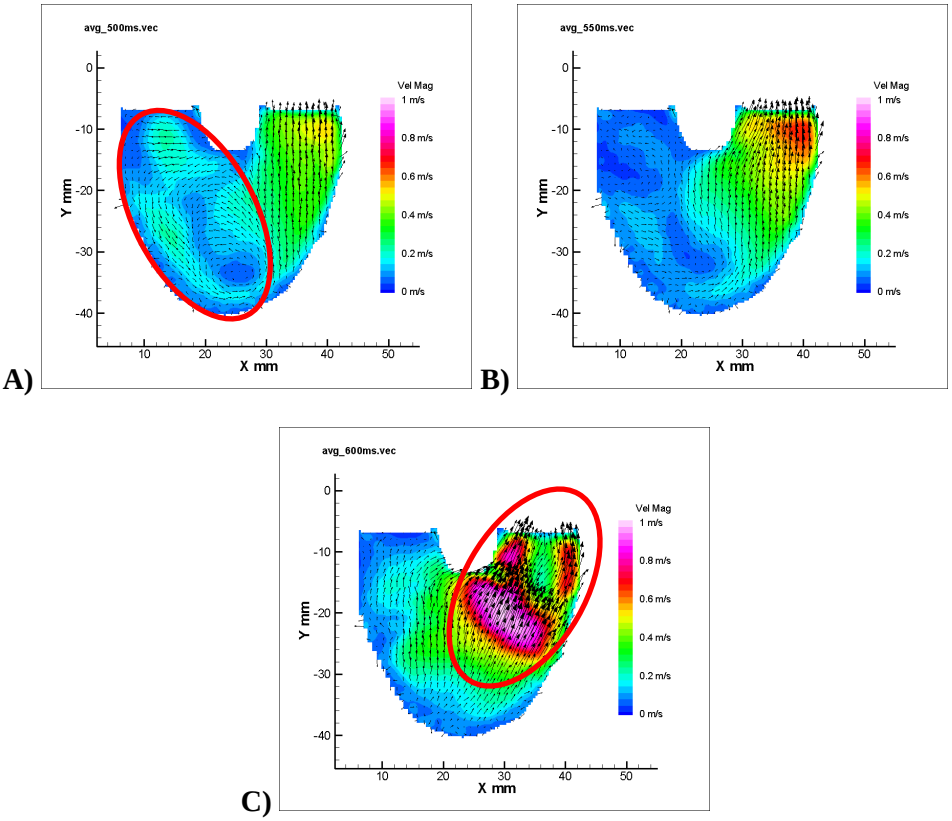

Figure 4-7. 8.2 mm plane at A) 500 ms, B) 550 ms, and C) 600 ms. The red circle in image A highlights the dissipation of the rotational flow pattern as the outlet flow begins to develop. The flow blockage is again highlighted in image C.

4.2 40% Hematocrit

The 40% HCT blood analog had a slightly higher viscosity and elasticity than the 20% HCT blood analog. The flow patterns were similar to the 20% HCT blood analog as an inlet jet formed early in diastole giving way to a rotational flow pattern later in diastole, which transitioned into the outlet flow during systole.

4.2.1 Diastole

A primary inlet jet formed along the outside wall of the device as a result from the BSM major orifice that persisted and slightly increased in velocity from 0.5 m/s at 100 ms to 0.7 m/s at 300 ms. There was evidence of a secondary inlet jet that formed on the inner portion of the inlet port at 100 ms but diminished in velocity from 0.5 m/s at 100 ms to 0.3 m/s after that point. As solid body rotation began to develop around 200 ms but was never fully maintained in the 7 mm plane, as shown in **Figure 4-8**.

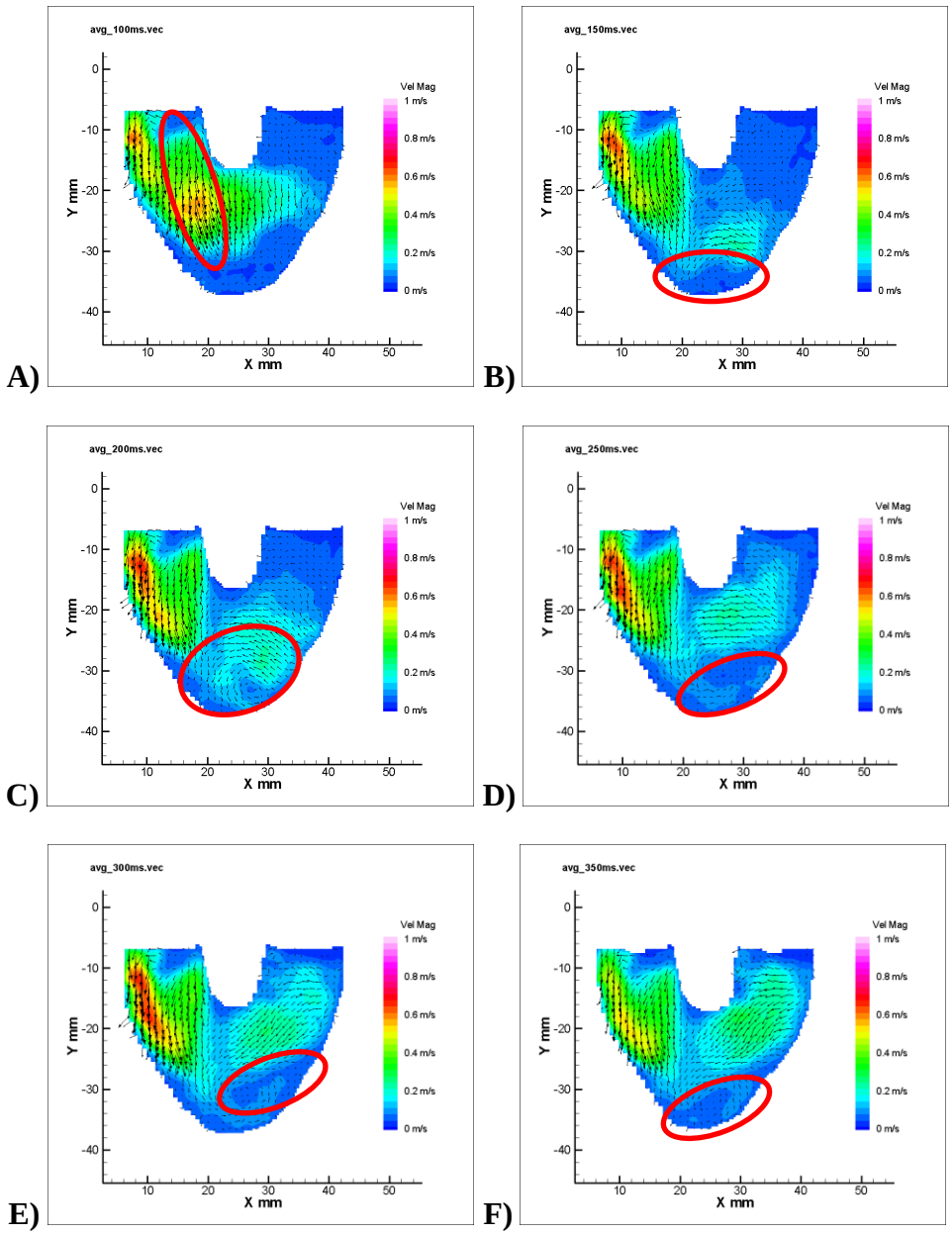

Figure 4-8. 7 mm plane at A) 100 ms, B) 150 ms, C) 200 ms, D) 250 ms, E) 300 ms, and F) 350 ms. Three-dimensional flow is highlight in image A. The red circles in images B through F show the inability of the inlet jet to coherently penetrate into the apex of the device.

The flow was similar in the 8.2 mm parallel plane as the inlet jet set up the rotational flow pattern around 200 ms. The rotational flow was greater in velocity and more consistently formed in the 8.2 mm plane, shown in **Figure 4-9**.

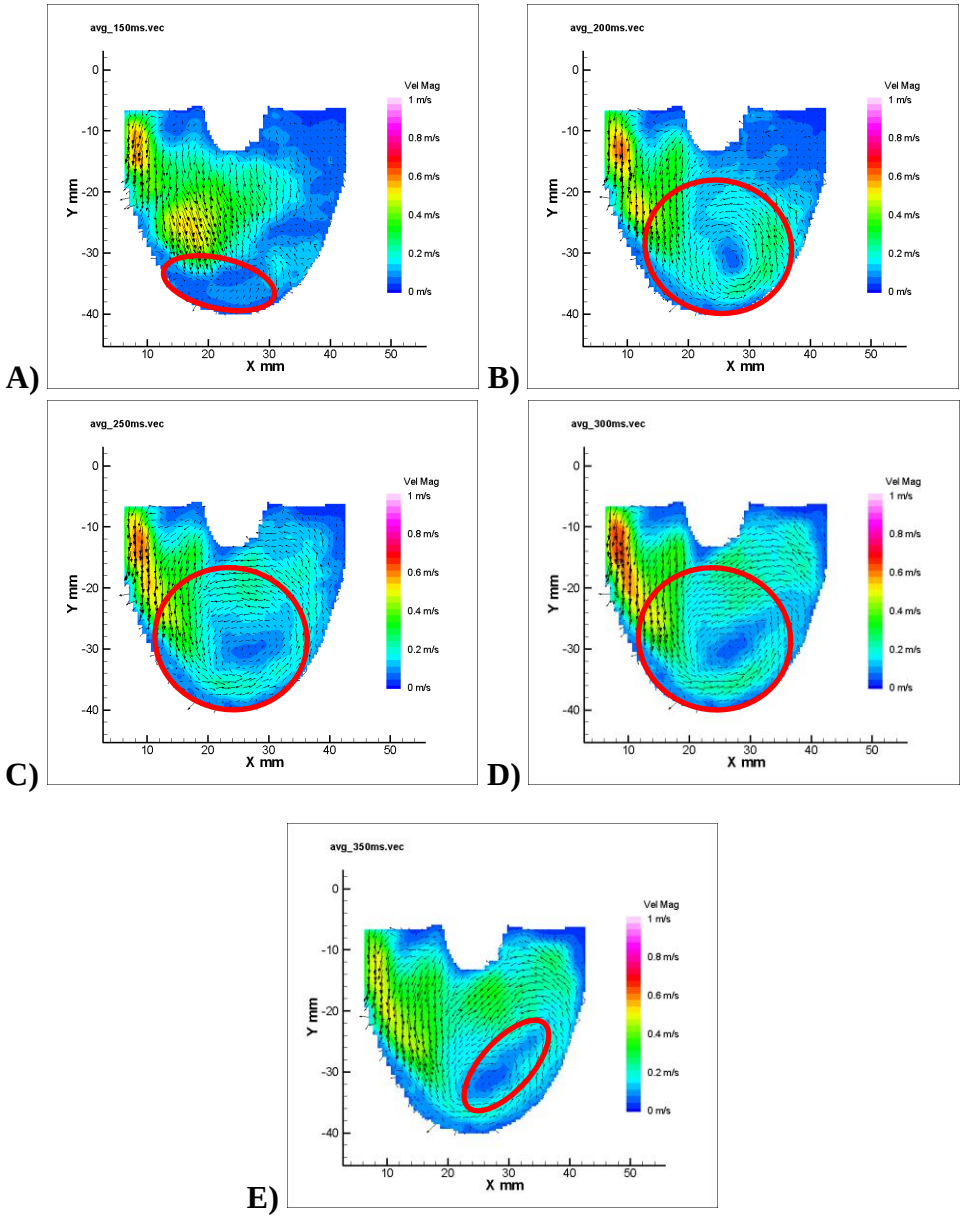

Figure 4-9. 8.2 mm plane at A) 150 ms, B) 200 ms, C) 250 ms, D) 300 ms, and E) 350 ms. The red circles highlight the formation of the rotational flow pattern that was not seen in the 7 mm plane. The 40% HCT blood analog penetrates higher up the outlet side wall later in diastole.

Towards the end of diastole, the inlet jet started to dissipate at 400 ms while the solid body rotation persisted. There was evidence of some regurgitation on the inlet side at 450 ms. The rotational flow started the transition to the outlet flow at the end of diastole and into systole. **Figure 4-10** shows the 8.2 mm plane data in late diastole.

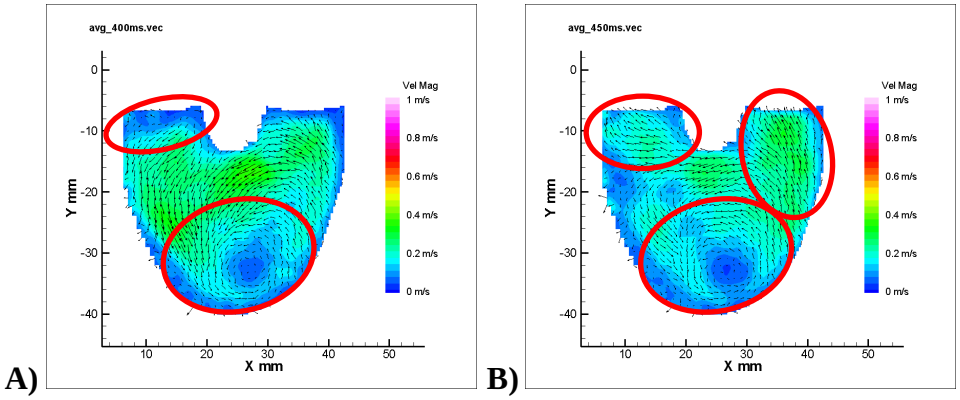

Figure 4-10. 8.2 mm plane at A) 400 ms and B) 450 ms. The red circles highlight regurgitant flow on the inlet side and the rotational flow beginning to transition into the outlet jet.

4.2.2 Systole

Systole began with the formation of an outlet jet evident at 500 ms. The outlet flow peak velocity increased from 0.45 m/s at 500 ms to 0.7 m/s at 650 ms. The outlet flow encompassed the entirety of the outlet port at 500 ms and 550 ms but an outlet flow blockage developed at 600 ms that forced most of the outlet flow to the edges of the port walls upstream of the outlet valve. This flow blockage was maintained at 650 ms and is shown in the 6.5 mm plane data in **Figure 4-11**.

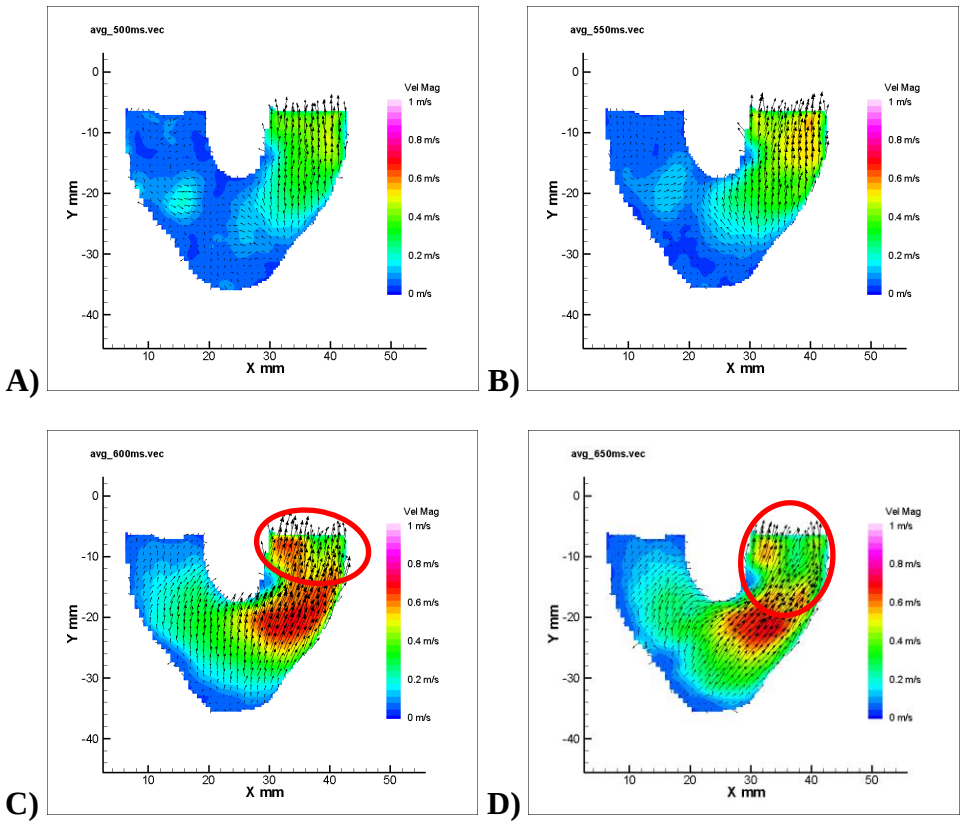

Figure 4-11. 6.5 mm parallel plane data at A) 500 ms, B) 550 ms, C) 600 ms, and D) 650 ms. The red circles highlight the outlet flow blockage upstream of the outlet valve occluder.

A similar flow pattern with comparable velocities was seen in the 8.2 mm plane. The solid body rotation dissolved at 500 ms and gave way to the outlet jet. Similarly to the 6.5 mm plane, the outlet jet split at 600 ms, as shown in **Figure 4-12**.

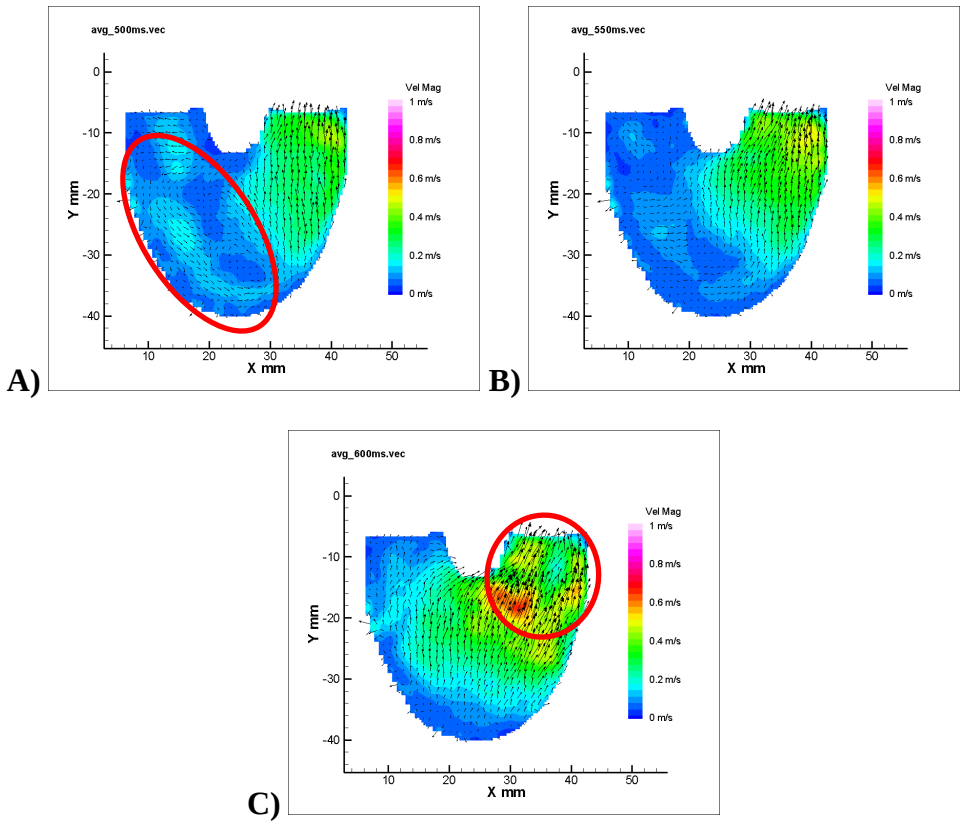

Figure 4-12. 8.2 mm plane at A) 500 ms, B) 550 ms, and C) 600 ms. The red circles highlight the dissipation of the rotational flow in image A and the outlet flow blockage in image C.

4.3 60% Hematocrit

The 60% HCT blood analog was the most viscoelastic fluid of the three analogs. An inlet jet developed early in diastole that set up a similar rotational flow pattern, leading to the outlet flow during systole.

4.3.1 Diastole

A strong inlet jet developed along the outside wall of the inlet port and increased in velocity from 0.5 m/s at 100 ms to 0.75 m/s at 350 ms. This jet set up the rotational flow pattern that began around 200 ms and was loosely maintained throughout the remainder of diastole in the 7 mm parallel plane. This phenomenon is shown in **Figure 4-13**.

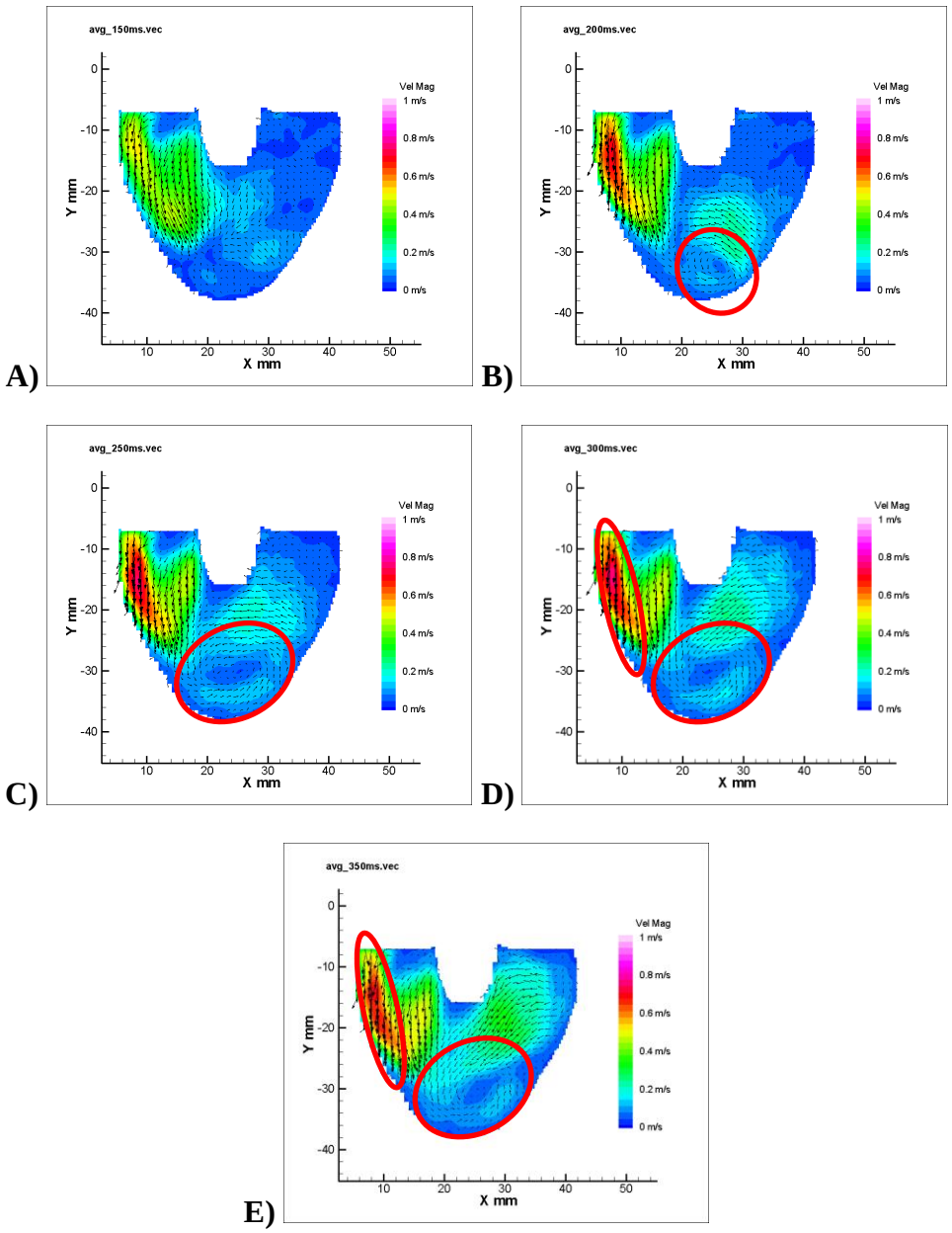

Figure 4-13. 7 mm plane at A) 150 ms, B) 200 ms, C) 250 ms, D) 300 ms, and E) 350 ms. The red circles highlight the rotational flow development at the apex of the device and the sustained inlet jet that forms form the major orifice of the inlet valve.

A similar pattern was evident in the 8.2 mm parallel plane. The inlet jet developed the rotational flow pattern that was more consistent and higher in average velocity than that of the 7 mm plane. The solid body rotation began to develop at 200 ms and was maintained throughout the remainder of diastole, as shown in **Figure 4-14**.

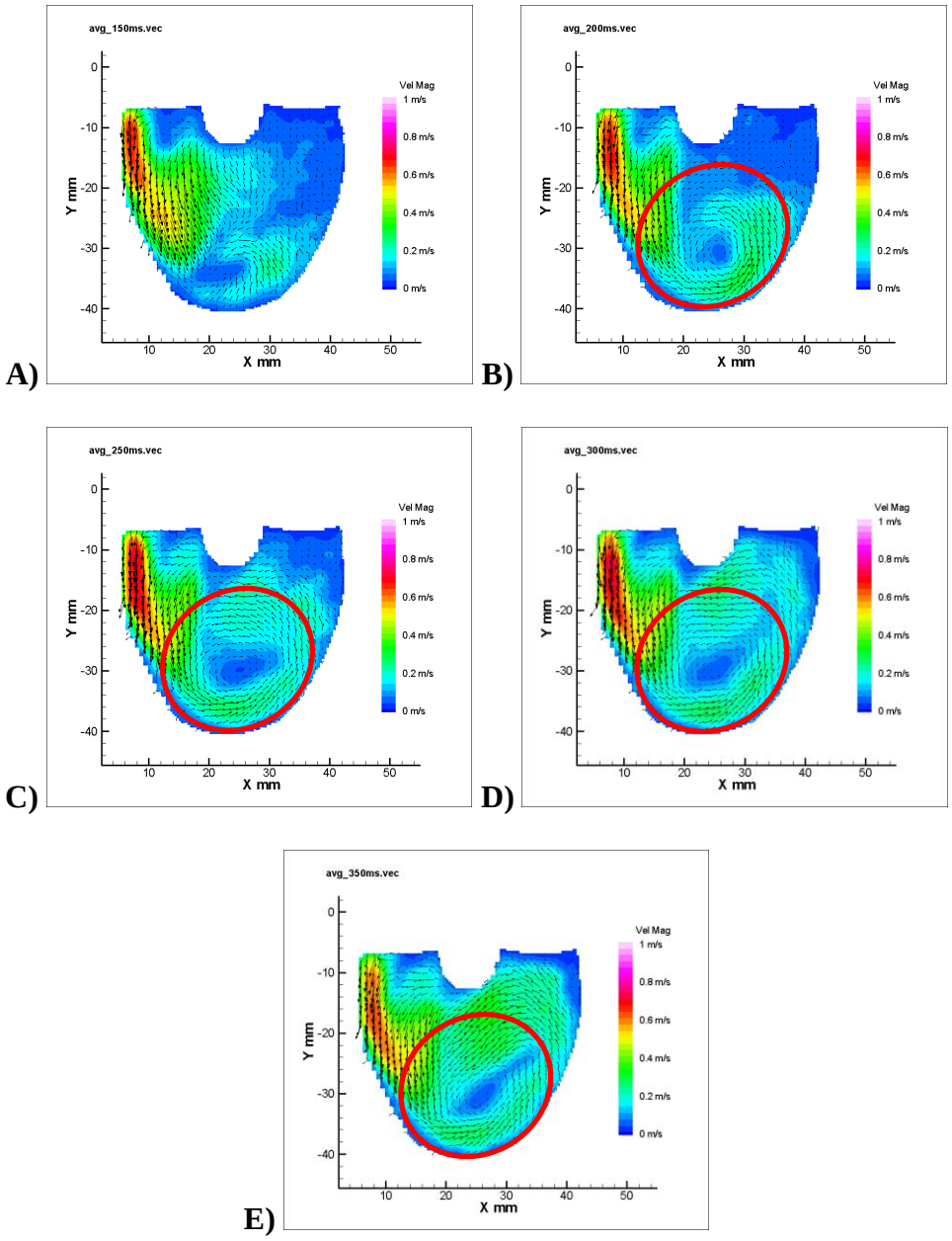

Figure 4-14. 8.2 mm plane at A) 150 ms, B) 200 ms, C) 250 ms, D) 300 ms, and E) 350 ms. The red circles highlight the progression of the rotational flow throughout diastole.

The inlet jet began to dissipate at 400 ms while the rotational flow pattern was maintained until the end of diastole at 450 ms. There was some evidence of regurgitation at 450 ms, as shown in **Figure 4-15**.

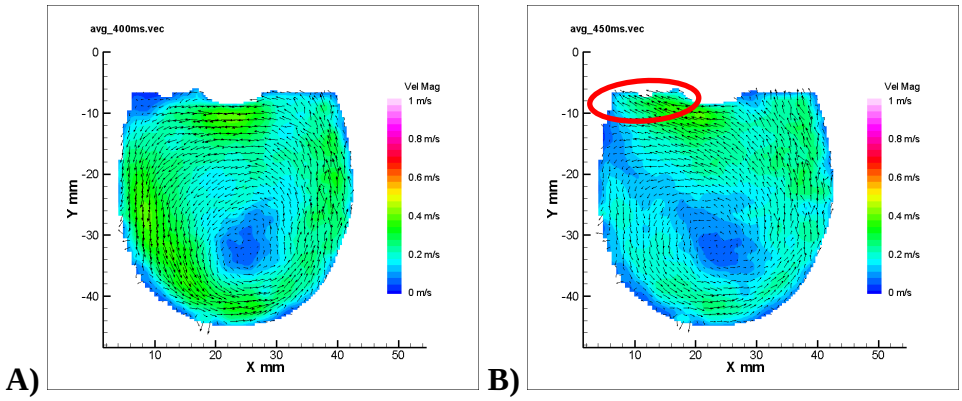

Figure 4-15. 11 mm plane at A) 400 ms and B) 450 ms. The red circle highlights the regurgitation on the inlet side late in diastole.

4.3.2 Systole

Systole began at 500 ms with the development of an outlet jet that encompassed the entire outlet port. Evidence of the rotational flow pattern dissipating was seen at 500 ms in the 8.2 mm plane. The outlet jet increased in velocity from 0.45 m/s at 500 ms to 0.7 m/s at 650 ms. Outlet flow blockage formed upstream of the outlet valve occluder at 650 ms in both the 7 mm and 8.2 mm planes. This phenomenon is shown in **Figure 4-16** and **Figure 4-17**.

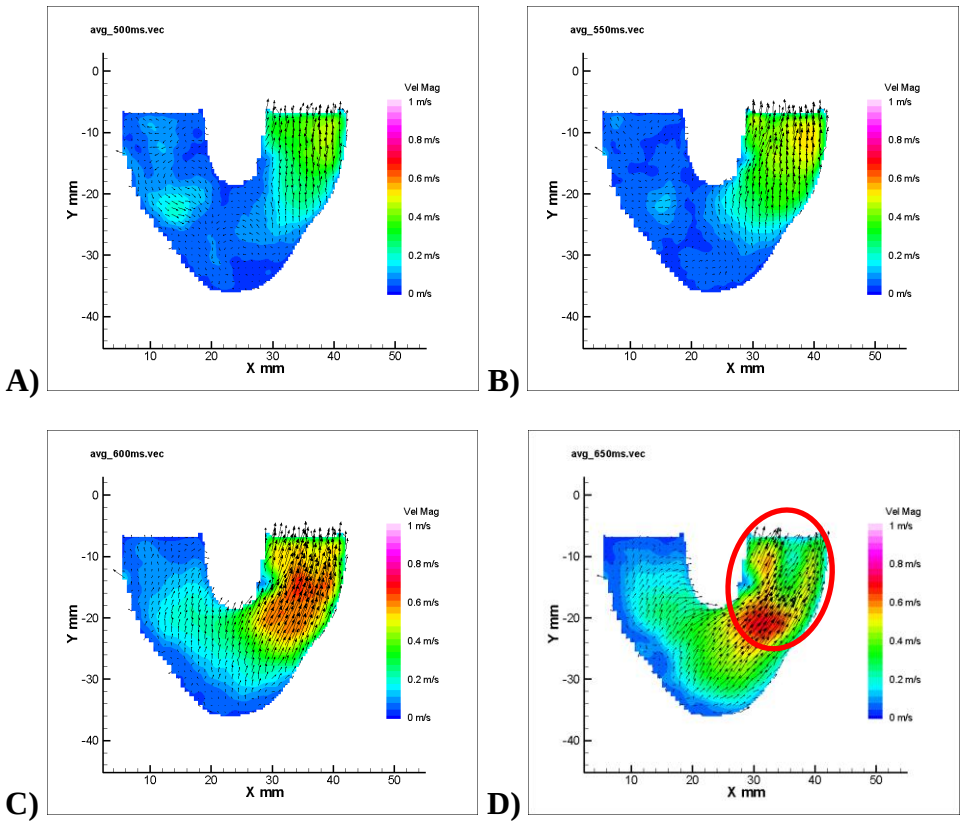

Figure 4-16. 6.5 mm plane at A) 500 ms, B) 550 ms, C) 600 ms, and D) 650 ms. The red circle highlights the outlet flow blockage that develops at 650 ms.

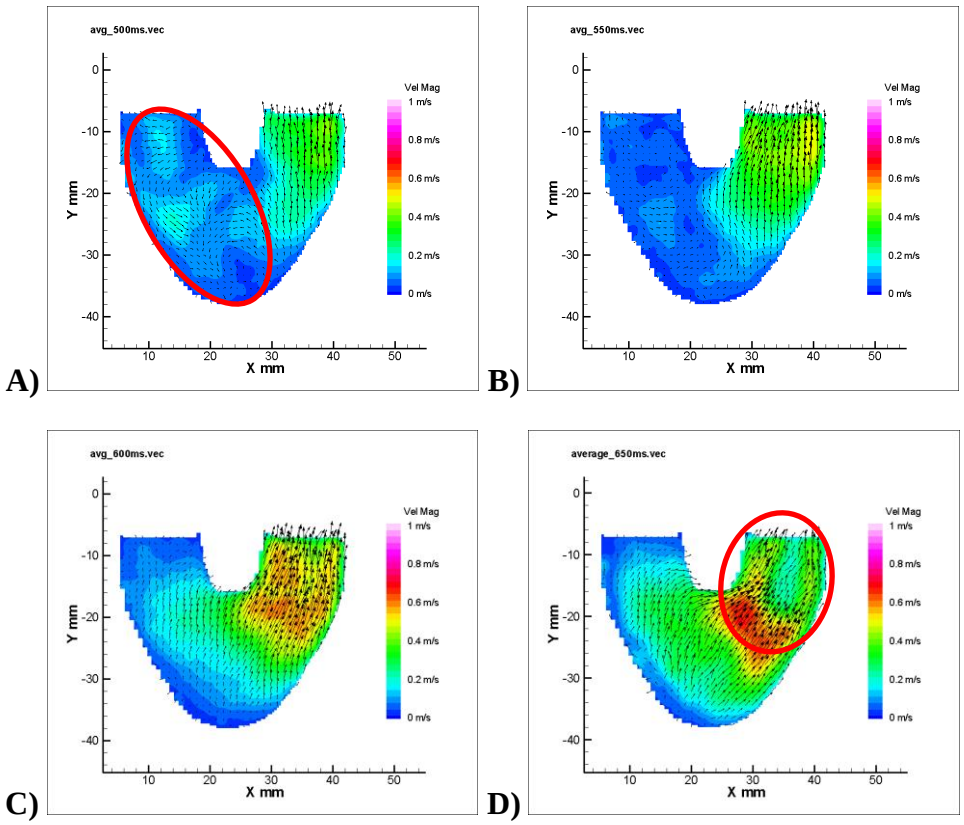

Figure 4-17. 7 mm plane at A) 500 ms, B) 550 ms, C) 600 ms, and D) 650 ms. The red circle highlights the dissipation of the rotational flow in image A and the outlet flow blockage in image D.

Chapter 5 DISCUSSION

Despite the differences in the viscoelasticity of the three blood analogs, a similar flow pattern was developed for all three throughout the cardiac cycle. In general, inlet jets developed early in diastole and increased in velocity as diastole continued. This jet formation evolved into a solid body rotation throughout the body of the device that lasted the remainder of diastole. As diastole transitioned to systole, the rotational flow morphed into an outlet jet flow that ejected the fluid from the device. There was a flow blockage that developed late in systole and was evident in the data for all three fluids, resulting in the splitting of the outlet jet into two distinct jets along the outer edges of the outlet port. This general flow pattern was present in all of the data and was consistent with the fluid dynamics of the PVAD presented in previous studies [21] [28] [32].

While there are certainly similarities between the flow patterns of the three different blood analogs, there were also key fluid dynamic differences. In general, the more viscoelastic fluids tended to resist movement more than the less viscoelastic fluids. This resistance resulted in a general delay of the development of flow. The specific characteristics that resulted from this phenomenon are highlighted in the following sections.

5.1 Diastole

One of the key differences between the fluid dynamics of the three different blood analogs was the timing of the inlet jet formation. The 20% HCT blood analog tended to create an inlet jet that developed earlier in the cardiac cycle while the 40% and 60% HCT

blood analogs displayed a delayed jet formation. This delayed inlet jet formation was consistent with the slight differences in the waveforms of the three fluids shown in **Figure 3-7**. The 20% HCT blood analog resulted in an inflow waveform of higher velocity earlier in the cycle compared to the more viscoelastic blood analogs. This timing difference is highlighted in **Figure 5-1** and **Figure 5-2**, which shows the 150 ms time point of the 7 mm plane for all three fluids. At 150 ms into the cardiac cycle, the 20% HCT blood analog has already penetrated into the bottom of the device and begun to set up the solid body rotation that follows later in diastole. In contrast, the 60% HCT blood analog has yet to reach the bottom of the device while the 40% HCT blood analog is in between the others. Additionally, at 150 ms in the 7 mm plane, the 20% HCT blood analog had a peak inlet jet velocity of 0.7 m/s compared to 0.6 m/s and 0.5 m/s in the 40% and 60% HCT blood analogs, respectively. This velocity difference was consistent with the idea that the 20% HCT blood analog developed a higher velocity inlet jet earlier in the cardiac cycle.

A – 20% HCT **B – 40% HCT** **C – 60% HCT**

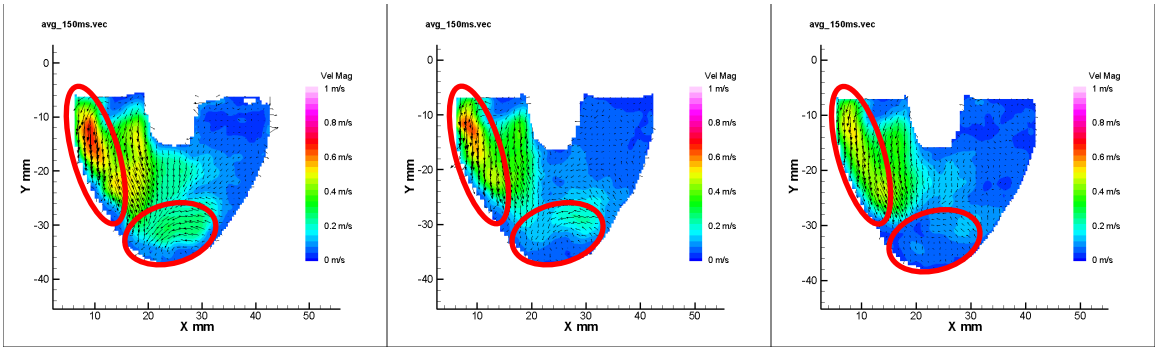

Figure 5-1. 7 mm plane at 150 ms with the A) 20%, B) 40%, and C) 60% HCT blood analogs. The red circles highlight the differences in the inlet jet formation between the fluids. The 20% HCT blood analog has a higher velocity inlet jet that has penetrated further into the device than the more viscoelastic blood analogs. Additionally, evidence of three-dimensional flow is observed as flow is wrapping around from another plane.

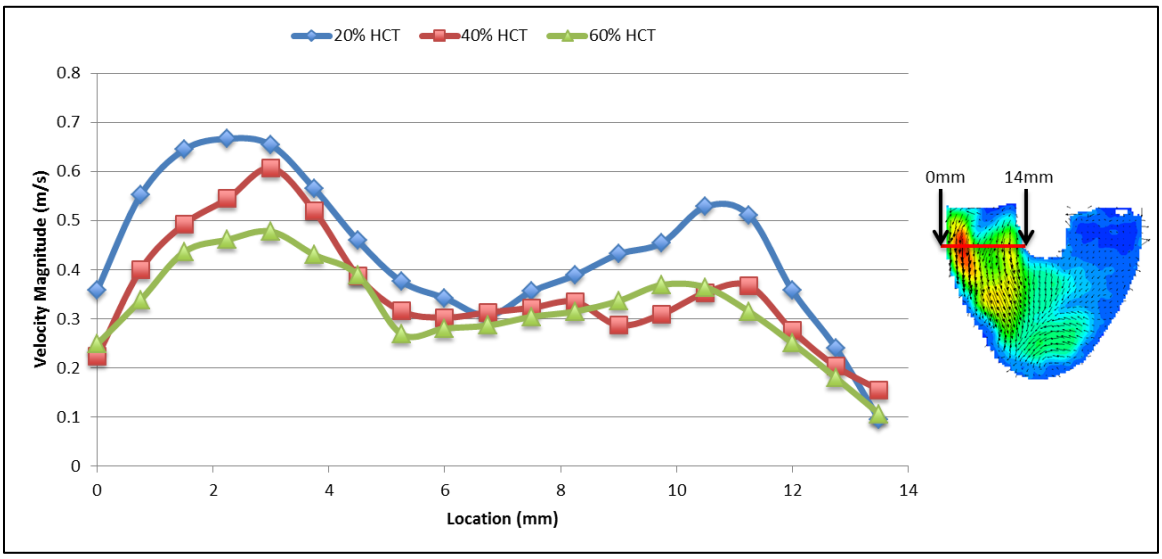

Figure 5-2. Inlet velocity data for the 7 mm plane at 150 ms. This graph further highlights the trend that the 20% HCT blood analog develops a higher velocity inlet jet earlier in diastole than the more viscoelastic blood analogs. The primary inlet jet that forms from the major orifice of the BSM valve is located from about 0 to 5 mm on the x-axis while the secondary inlet jet is located in the 9 to 12 mm range.

This phenomenon is further illustrated in the 8.2 mm plane shown in **Figure 5-3**. The 40% and 60% HCT blood analogs lag behind the 20% HCT blood analog in all three of the time points shown. At 150 ms, 200 ms, and 250 ms, the development of the solid body rotation in the 20% HCT blood analog precedes the same development in the more viscoelastic blood analogs. However, the peak velocity of the inlet jets in this plane is 0.7 m/s for all fluids.

A – 20% HCT **B – 40% HCT** **C – 60% HCT**

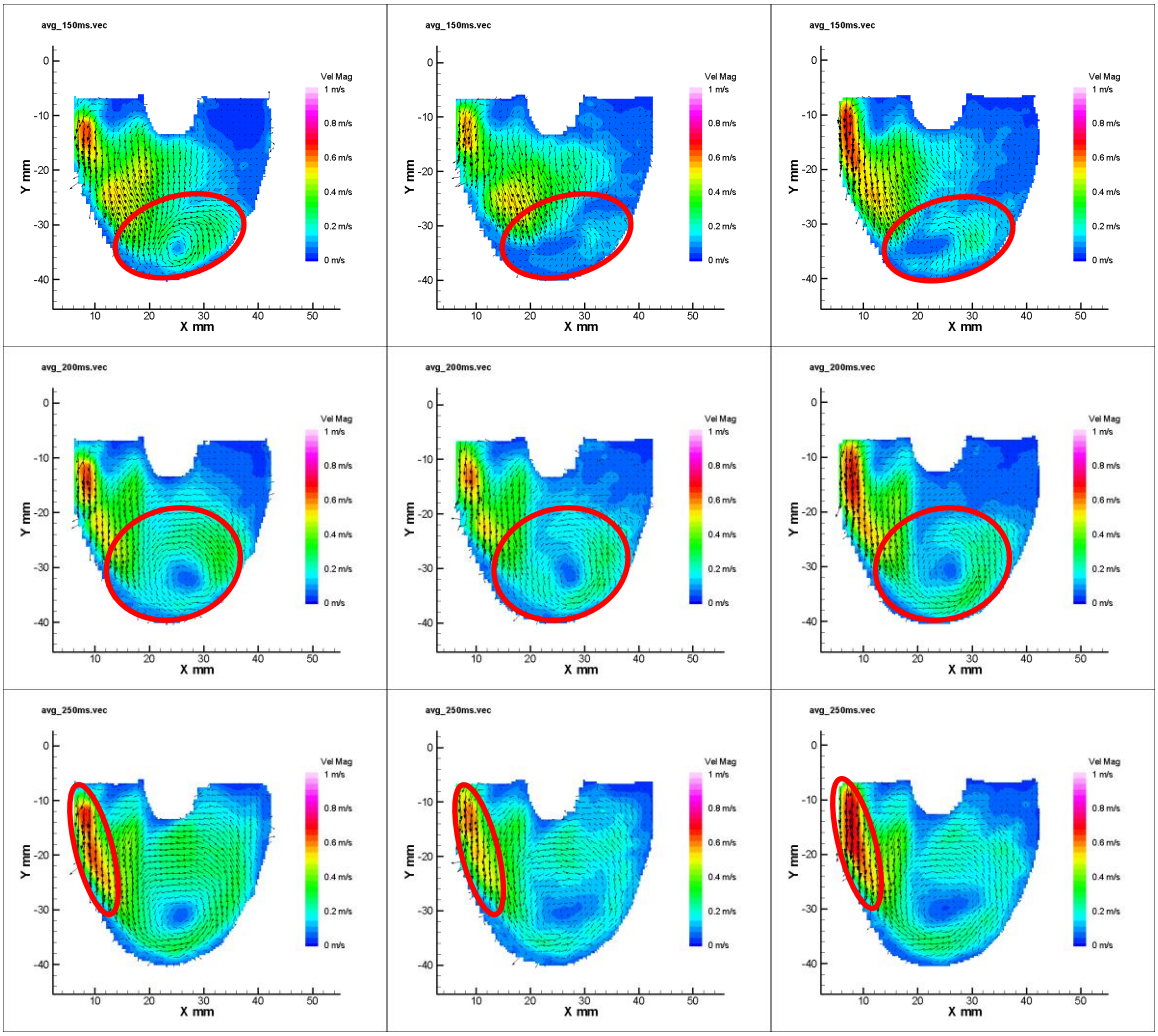

Figure 5-3. 8.2 mm plane at 150 ms, 200 ms, and 250 ms with the A) 20%, B) 40%, and C) 60% HCT blood analogs. The red circles highlight the delay in the progression of the inlet jet and subsequent rotational flow pattern in the 40% and 60% HCT blood analogs.

Similarly, in the 11 mm plane, the solid body rotation developed later in the cardiac cycle in the 60% HCT blood analog. At 200 ms, the 20% HCT blood analog was almost entirely set up in solid body rotation while the 60% inlet jet was just beginning to penetrate to the bottom of the device and turn against the bottom wall. This delayed development is further confirmed by the presence of a higher velocity inlet jet later in

diastole in the 60% HCT blood analog. At 300 ms, the 60% HCT blood analog had a peak inlet jet velocity of 0.7 m/s while the peak velocity of the less viscoelastic blood analogs was 0.6 m/s. **Figure 5-4** highlights this difference.

A – 20% HCT **B – 40% HCT** **C – 60% HCT**

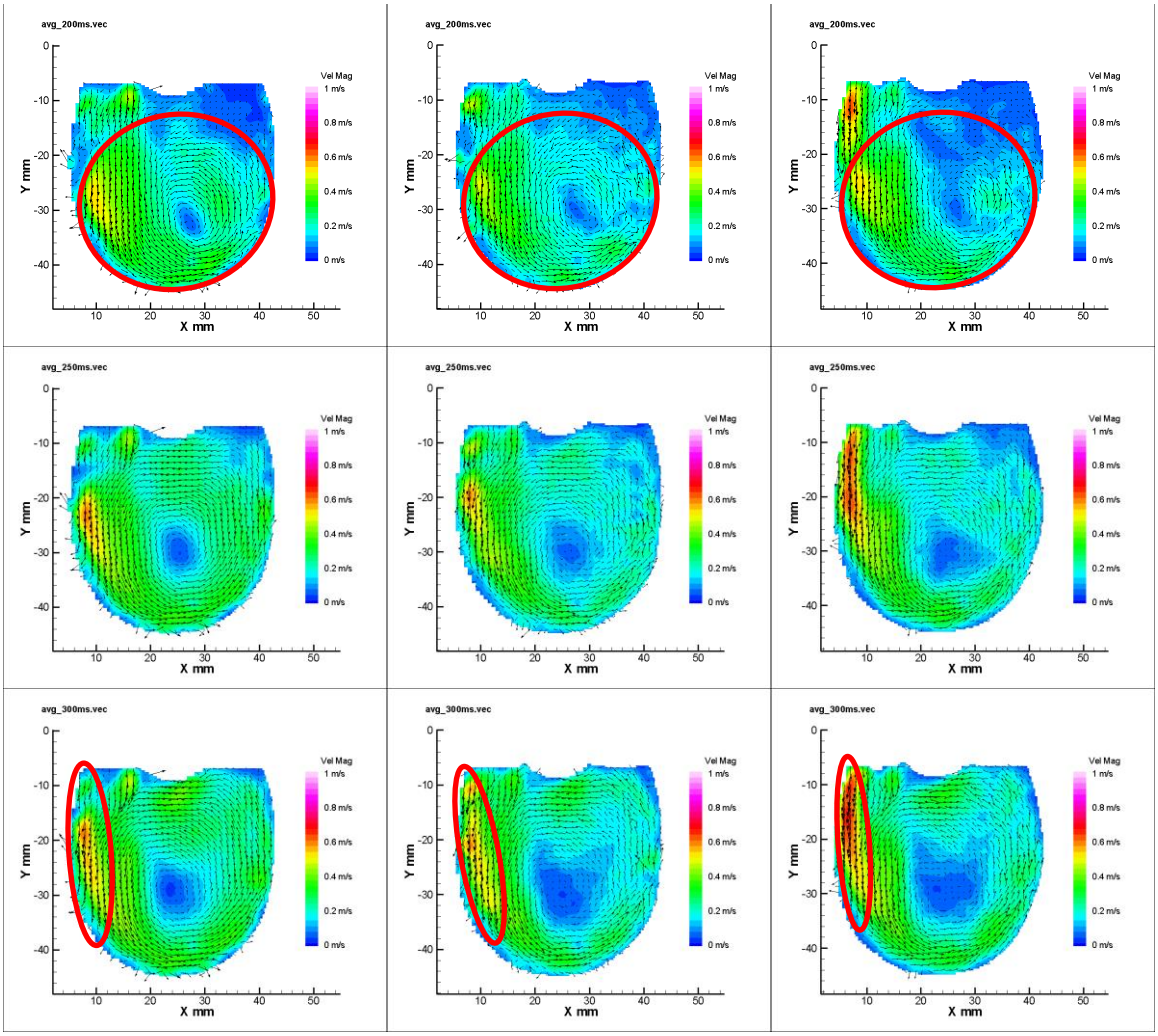

Figure 5-4. 11 mm plane at 200 ms, 250 ms, and 300 ms with the A) 20%, B) 40%, and C) 60% HCT blood analogs. The red circles highlight the delay in the rotational flow pattern seen in the more viscoelastic blood analogs.

The 6.5 mm plane shows similar peak velocities for the inlet jets of all three fluids. However, the 20% HCT blood analog penetrates deeper into the device than the 40% and 60% HCT blood analogs. This penetration sets up a rotational flow with higher velocity in the apex of the device earlier on in the cardiac cycle. This phenomenon is highlighted in **Figure 5-5**.

A – 20% HCT **B – 40% HCT** **C – 60% HCT**

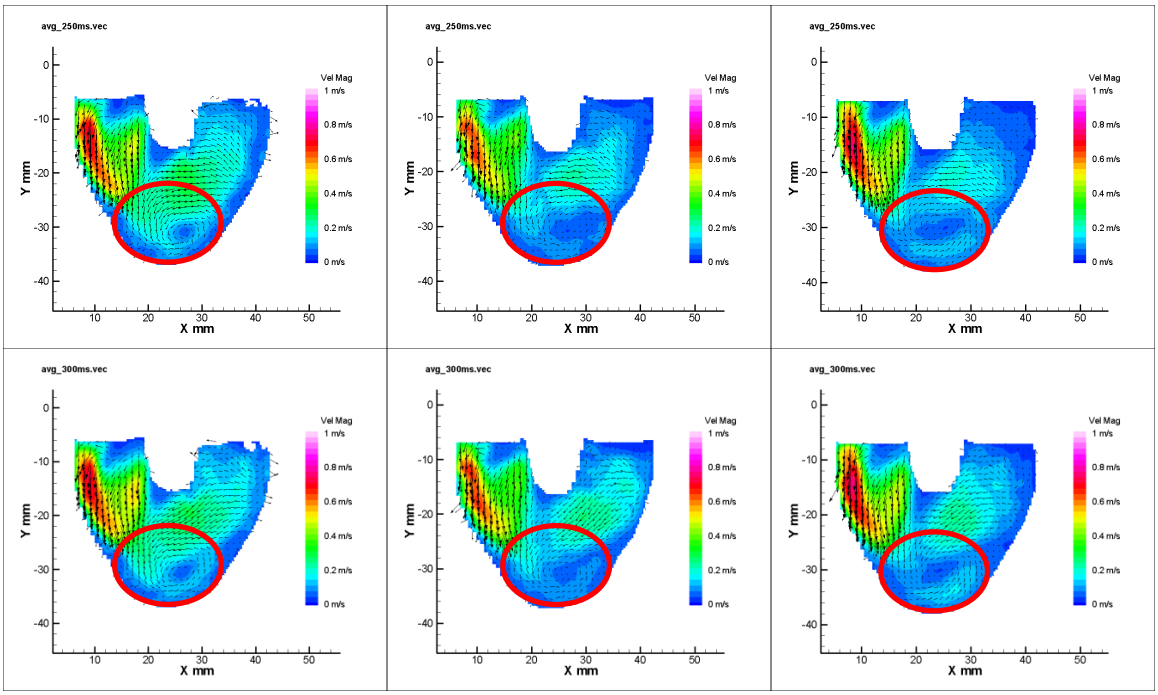

Figure 5-5. 6.5 mm parallel plane at 250 ms and 300 ms with the A) 20%, B) 40%, and C) 60% HCT blood analogs. The red circles highlight the fact that the inlet jet of the 20% HCT blood analog penetrates deeper into the device earlier in diastole than the 40% and 60% HCT blood analogs.

5.2 Systole

The PVAD was operated at 75 beats/min, which resulted in an 800 ms cardiac cycle. By convention, the start of diastole began a new cycle and was referred to as 0 ms. Because the systolic duration was set at 340 ms, systole began at 460 ms. As diastole turned into systole at 460 ms into the cardiac cycle, the solid body rotation shifted to an outlet jet flow. As expected, this outlet jet began to appear in the data at 500 ms and continued throughout the remainder of systole. One of the main differences that was evident throughout systole was that the 20% HCT blood analog resulted in the highest velocity outlet jet. In the 6.5 mm plane, the peak velocity of the outlet jet was 1.1 m/s in the 20% HCT blood analog compared to 0.7 m/s in both the 40% and 60% HCT blood analogs. Additionally, a flow blockage develops upstream of the outlet valve occluder late in systole. This flow pattern is unique to the PVAD and is consistent with previous studies on the device [21] [28] [30]. **Figure 5-6**, **Figure 5-7**, and **Figure 5-8** highlight these phenomena.

A – 20% HCT **B – 40% HCT** **C – 60% HCT**

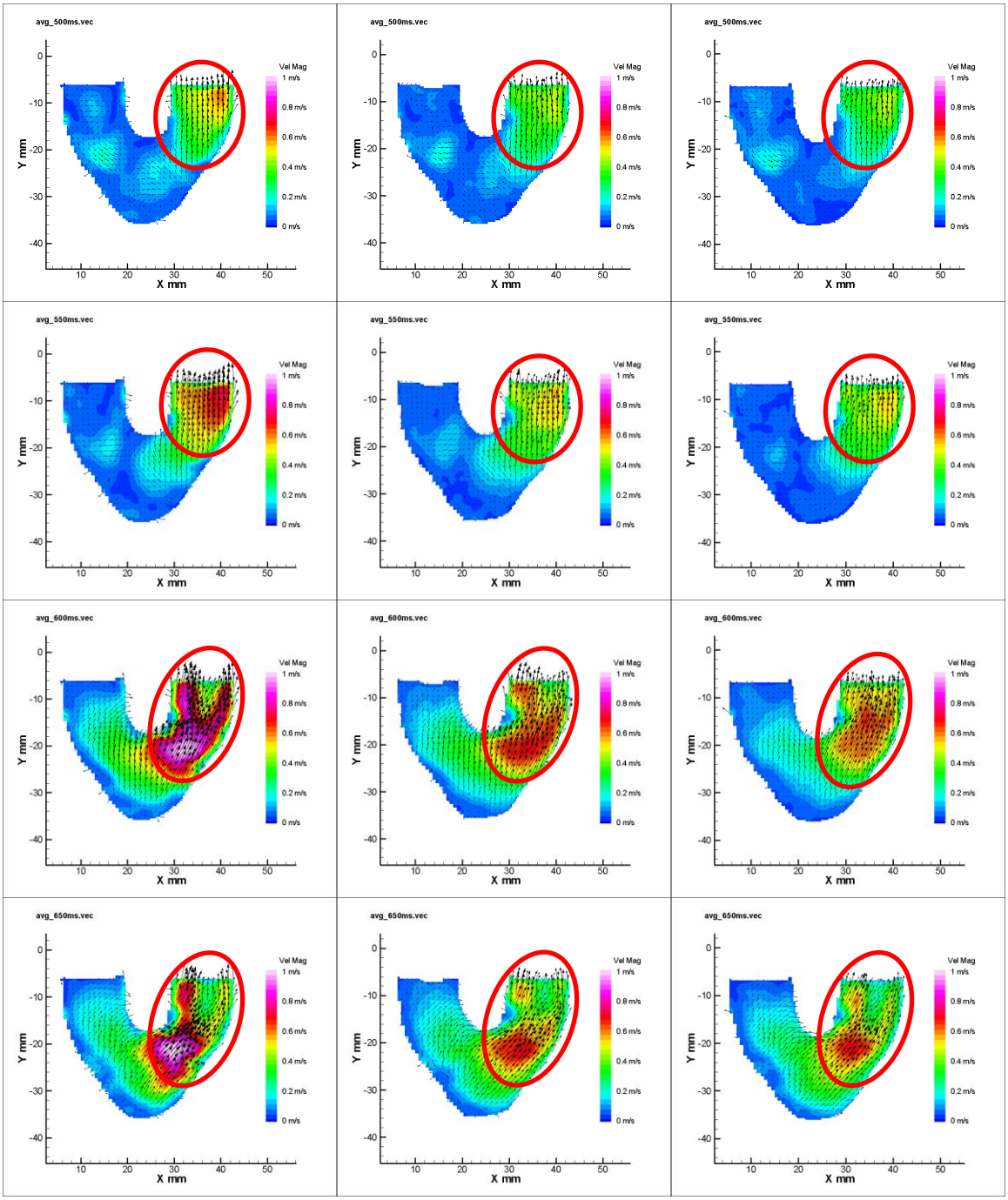

Figure 5-6. 6.5 mm plane at 500 ms, 550 ms, 600 ms, and 650 ms with the A) 20%, B) 40%, and C) 60% HCT blood analogs. The red circles highlight the delay in the development of the outlet jet seen across the three fluids. At 600 ms, the outlet flow blockage is seen in both the 20% and 40% HCT blood analogs while the blockage does not appear in the 60% HCT blood analog until 650 ms.

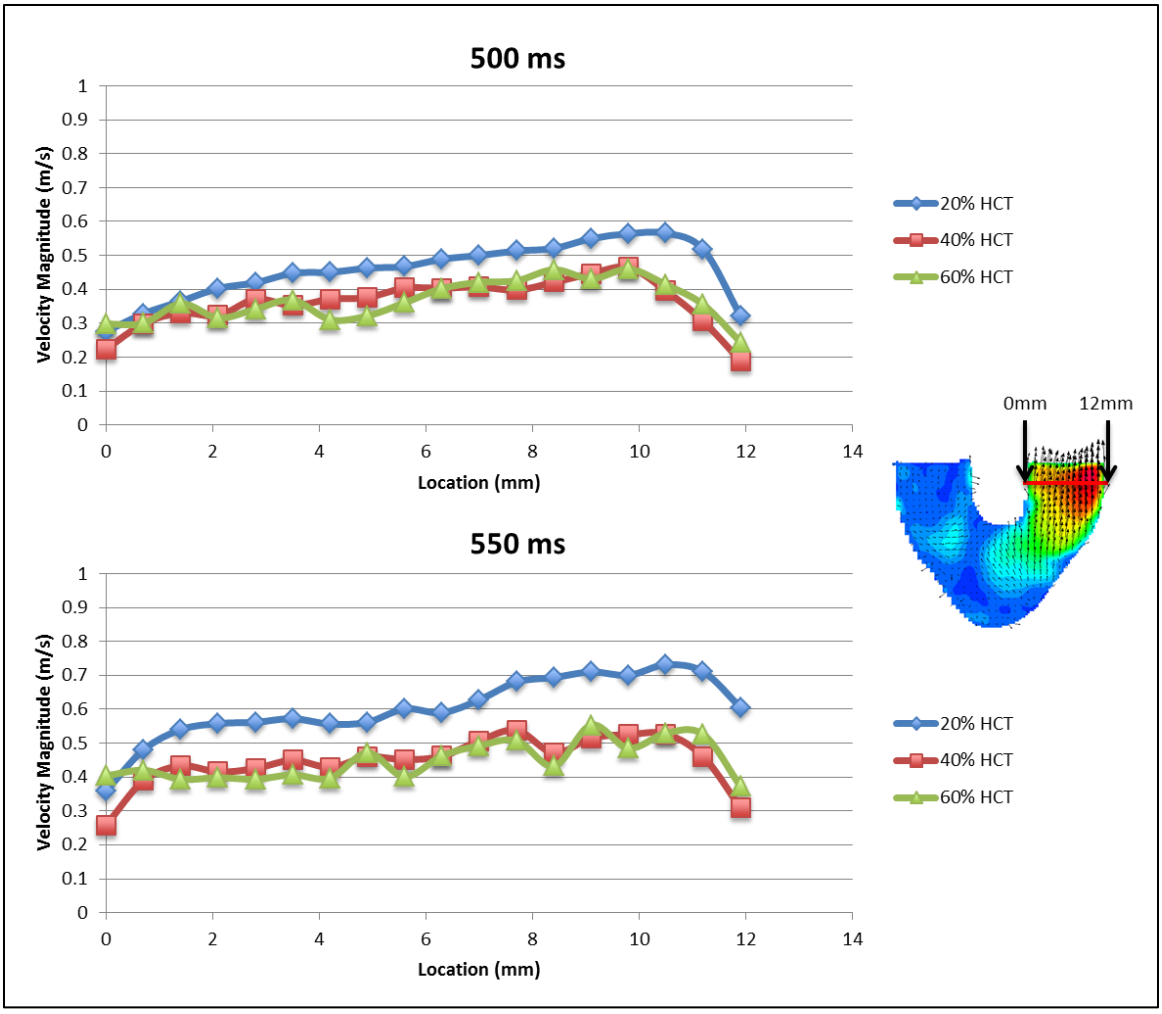

Figure 5-7. Outlet jet velocity data for the 6.5 mm plane at 500 ms and 550 ms. This figure highlights the difference in the velocity of the outlet jet across the three fluids. The 20% HCT blood analog has developed a higher velocity outlet jet earlier in systole than the 40% and 60% HCT blood analogs.

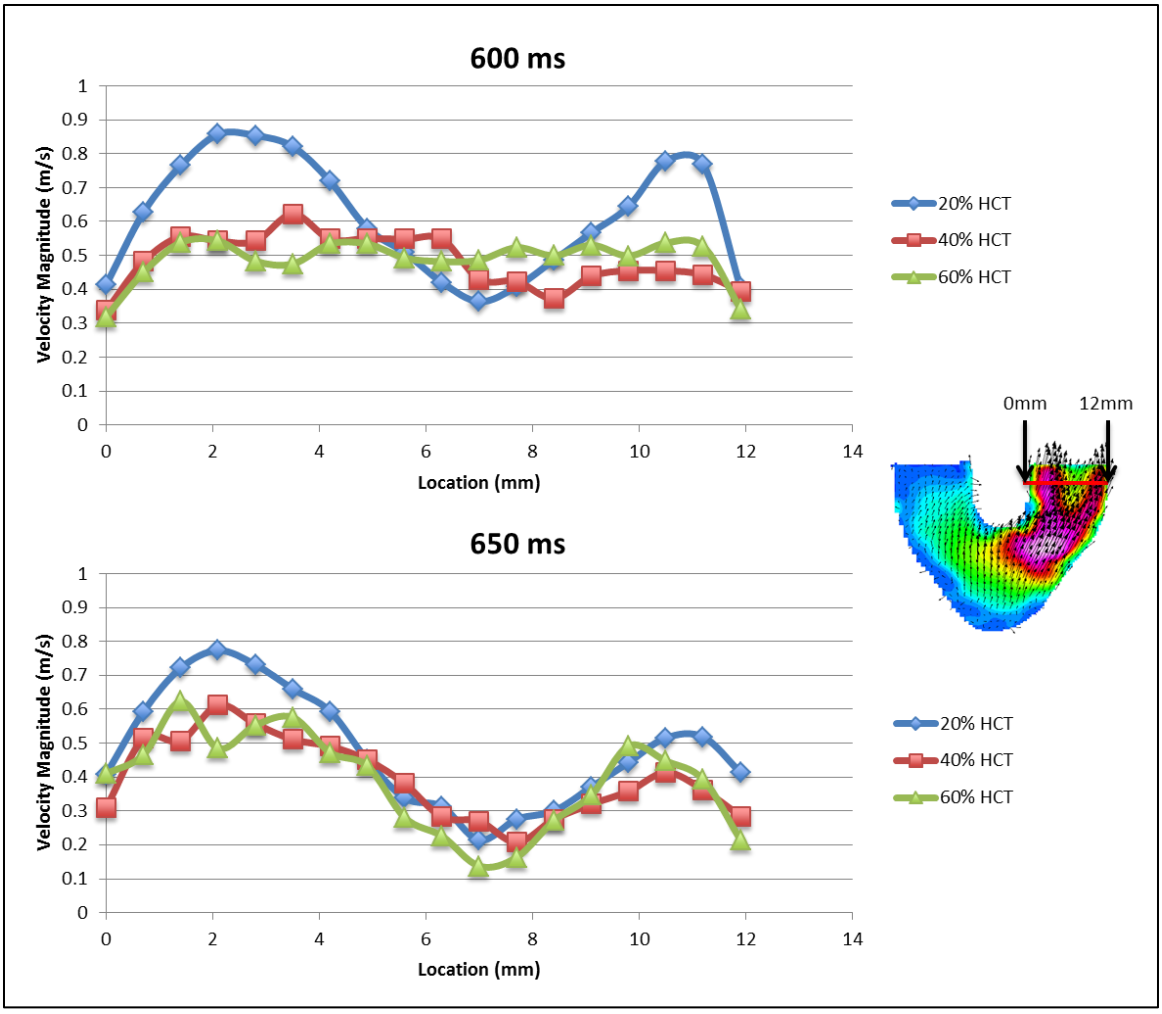

Figure 5-8. Outlet jet velocity data for the 6.5 mm plane at 600 ms and 650 ms. This figure further highlights the delay in the outlet jet formation of the 40% and 60% HCT blood analogs. The outlet flow blockage is clearly evident at 600 ms in the 20% HCT blood analog but has not yet developed in the more viscoelastic fluids.

This same fluid dynamic trend was shown in both the 7 mm and 8.2 mm planes. The flow blockage was evident as was the higher outlet jet velocity in the 20% HCT blood analog. However, a relative delay in the development of the splitting pattern was observed in the more viscoelastic blood analogs. While the blockage is evident across all fluids at 650 ms in **Figure 5-9** and **Figure 5-10** that depict the 7 mm plane, it is not as pronounced in the 40% and 60% HCT blood analogs at 600 ms. This delay confirmed

that the delay of the inlet jet formation seen in the more viscoelastic blood analogs during diastole was carried over into systole.

A – 20% HCT **B – 40% HCT** **C – 60% HCT**

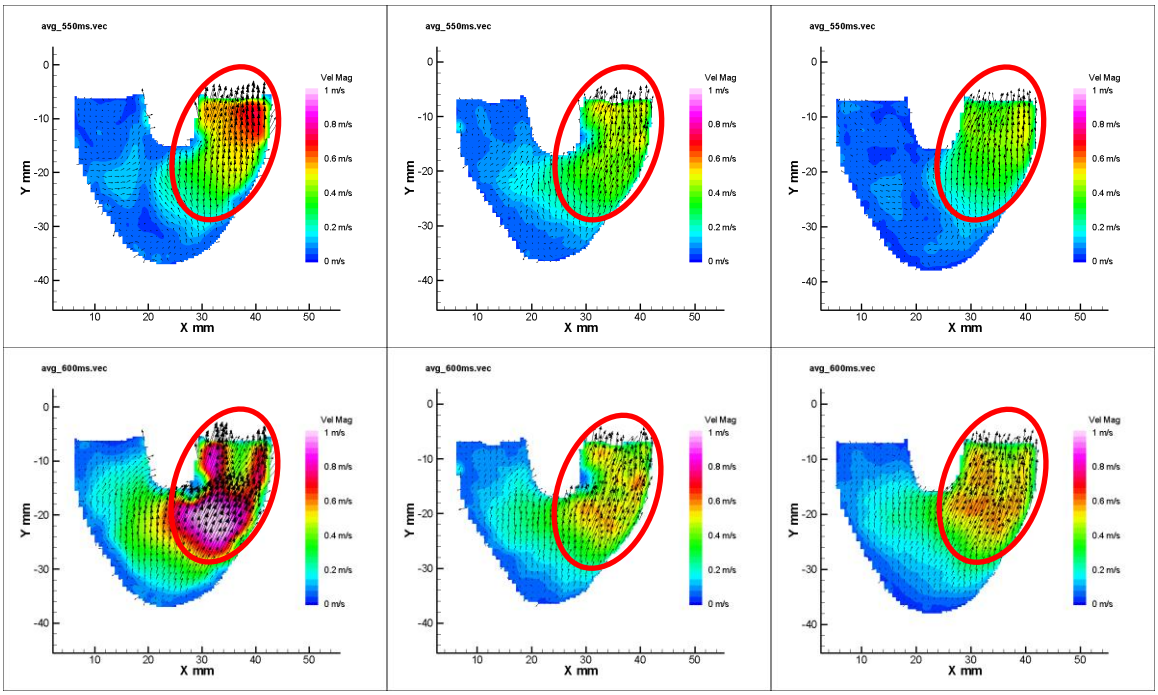

Figure 5-9. 7 mm parallel plane at 550 ms and 600 ms with the A) 20%, B) 40%, and C) 60% HCT blood analogs. The red circles highlight the delay in the development of the outlet jet in the more viscoelastic blood analogs.

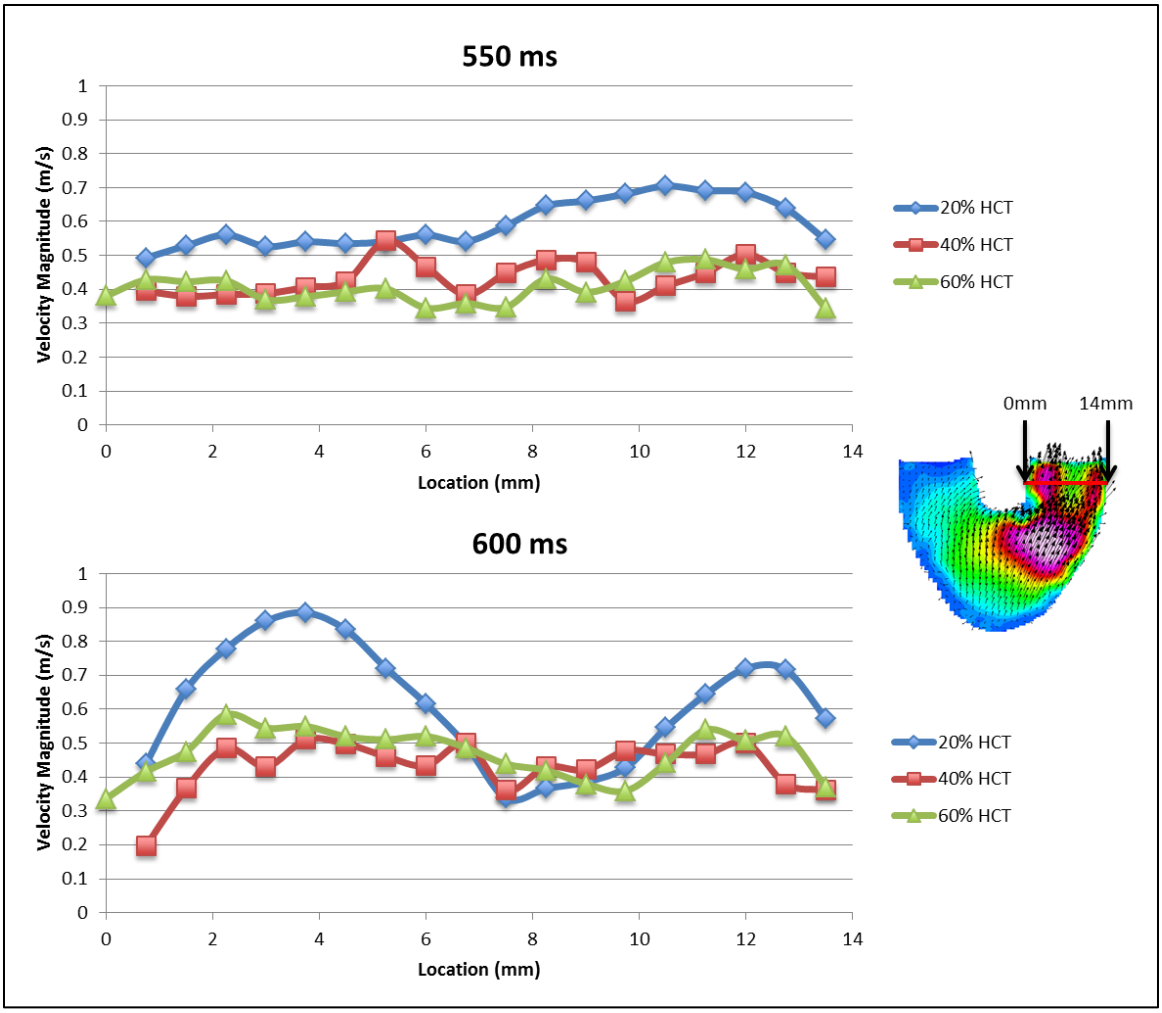

Figure 5-10. Outlet jet velocity data for the 7 mm plane at 550 ms and 600 ms. The delay in the development of the 40% and 60% HCT blood analogs is evident as the outlet flow blockage has not yet developed at 600 ms but has developed in the 20% HCT blood analog.

Figure 5-11 depicts a comparison of the fluids at the end of systole in the 8.2 mm plane. The flow blockage is evident at 600 ms for all three fluids but is much more pronounced in the 20% HCT blood analog. Additionally, the peak outlet flow velocity was 1.1 m/s in the 20% HCT blood analog compared to 0.7 m/s in the 40% HCT blood analog and 0.6 m/s in the 60% HCT blood analog.

A – 20% HCT **B – 40% HCT** **C – 60% HCT**

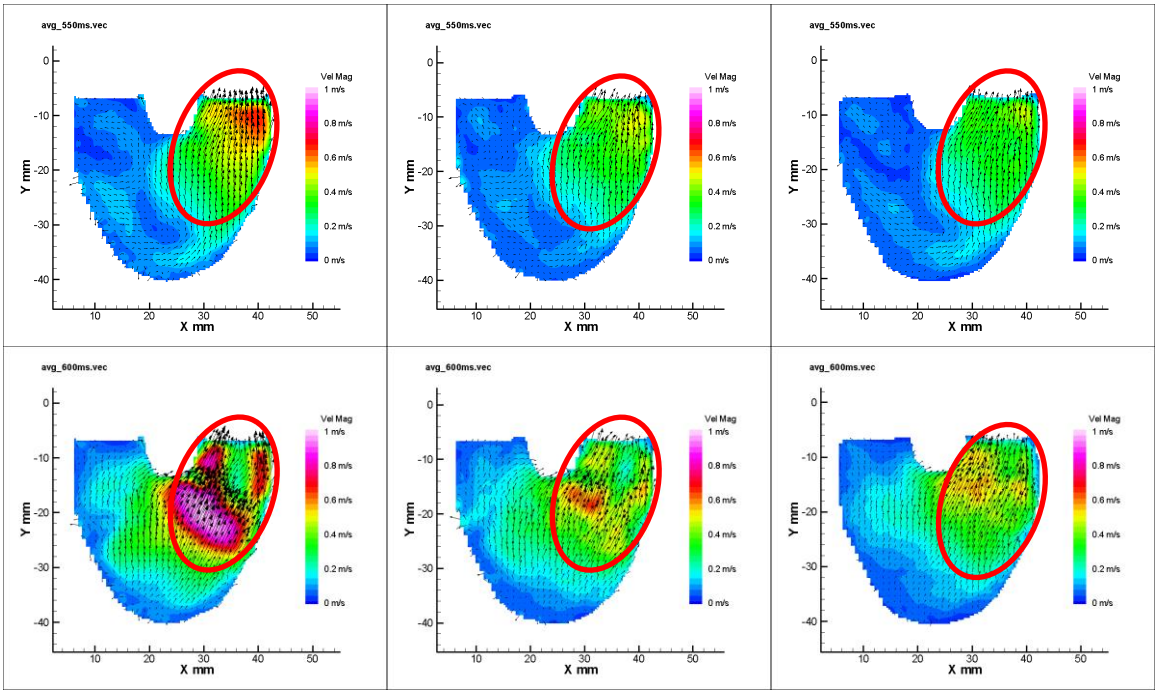

Figure 5-11. 8.2 mm parallel plane at 550 ms and 600 ms with the A) 20%, B) 40%, and C) 60% HCT blood analogs. The red circles highlight the outlet jet that forms earlier and at a higher velocity in the 20% HCT blood analog.

The delayed development of the inlet jet formation seen in diastole was similarly evident into systole. All three fluids produced similar flow patterns consistent with previous fluid dynamic studies of the PVAD [21] [28] [29]. The main difference between the three fluids was the development of the flow patterns. The more viscoelastic blood analogs were delayed in setting up the PVAD flow throughout the entirety of the cardiac cycle.

5.3 Limitations

While this data identifies many of the fundamental differences in the fluid dynamics of the three different blood analogs, there is one limitation that hinders the study of the complete cardiac cycle. As discussed earlier, diaphragm interference did not allow for the collection of data at the very beginning of diastole and end of systole. This lack of data hinders the study of the initial development of the inlet jet formation, which is very influential in setting up the flow field moving deeper into the cardiac cycle [21] [28] [29] [30]. Additionally, the lack of data at the end of systole makes it difficult to see if the flow blockage that was seen near the outlet resolves at all before the end of systole. Areas of flow blockage near the valve can cause increased pressure drops across the valves and induce blood damage, so it is important to have a complete understanding of this flow phenomenon [30].

Chapter 6 CONCLUSIONS

6.1 Conclusions

This study was performed in order to analyze the effect of hematocrit on the fluid dynamics within the 12 cc Penn State PVAD. Because pediatric patients can have a large hematocrit range anywhere from 20%-60%, it is important to understand how these variations impact the PVAD flow. Two-dimensional planar PIV was used to characterize this flow for three blood analogs that matched the viscoelastic properties of 20%, 40%, and 60% pediatric blood.

The 20%, 40%, and 60% HCT blood analogs created distinct fluid dynamic patterns within the 12 cc Penn State PVAD. While the general flow throughout the device was similar, there were several key differences including the duration and alignment of jet formation and the development of the solid body rotational flow. Specifically, the more viscoelastic blood analogs resulted in a delayed development of inlet jets that correlated to a delay in the development of the solid body rotation. The formation of the outlet jet was similarly delayed and resulted in a lower peak velocity outlet flow during systole. Additionally, an outlet flow blockage upstream of the outlet valve occluder was evident late in systole. This pattern was observed in all of the fluids but slightly later in systole for the more viscoelastic analogs. Changes in these fluid dynamic characteristics have the potential to impact the likelihood of blood damage and thromboembolic events in mechanical circulatory support devices like the PVAD. This study demonstrated that hematocrit variations do, in fact, alter the fluid dynamics within the PVAD and can ultimately affect the efficacy of the device. Care must be taken to ensure that the fluid

dynamics within the PVAD minimize the probability of hazardous events like thrombosis.

6.2 Future Studies

Further studies are necessary to more completely define the effect of hematocrit on the fluid dynamics within the PVAD. For example, planar PIV could be used to take data on planes normal to the diaphragm. Fluid dynamic data taken in this orientation would provide valuable information as to the three-dimensionality of the flow created by the three different blood analogs. Wall shear rate is another important metric for evaluating the potential for thrombus formation. Calculating the wall shear rate for the three different blood analogs for both the parallel and normal orientation PIV data would be helpful in order to further characterize how hematocrit affects the likelihood of thromboembolic events. It is extremely important to understand exactly how changes in viscoelasticity affect the fluid dynamics in the device. Identifying the exact mechanism will allow researchers to more adequately understand data collected while testing on animals with lower hematocrit. Additionally, a further understanding of this phenomenon will allow doctors to tailor the use of the PVAD and other mechanical circulatory support devices to suit pediatric patients that are within the 20%-60% hematocrit range.

Appendix A 20% HEMATOCRIT

Appendix A-1. 6.5 mm Parallel Plane

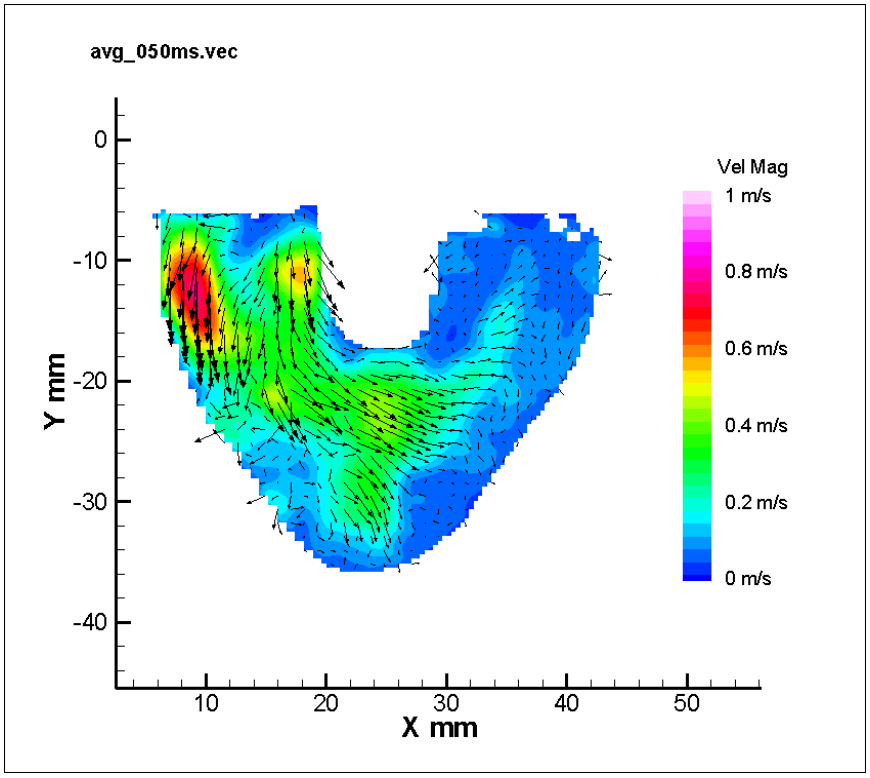

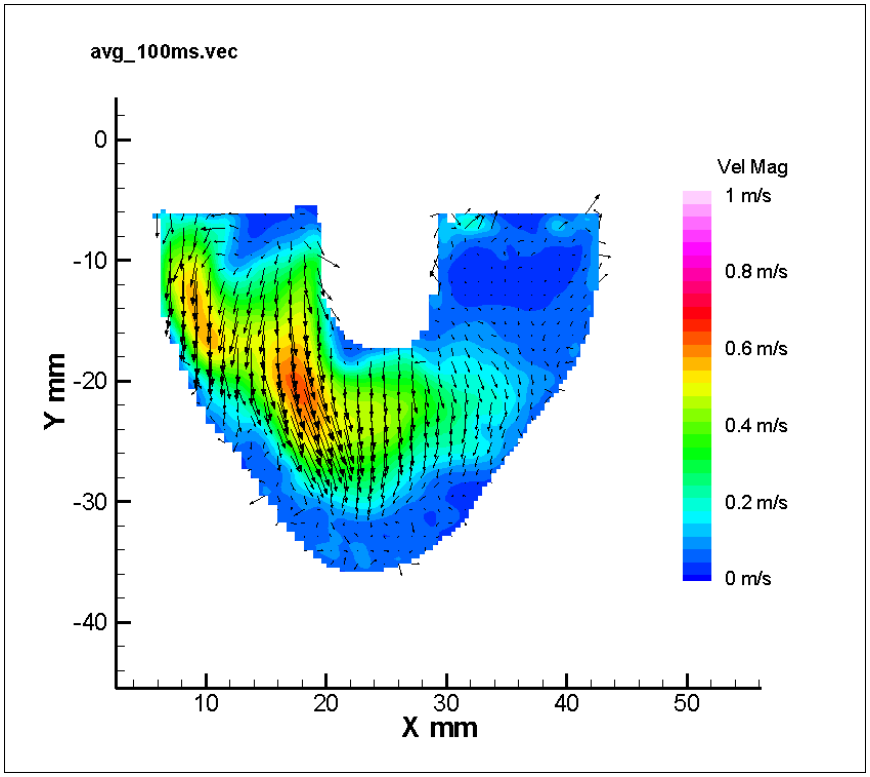

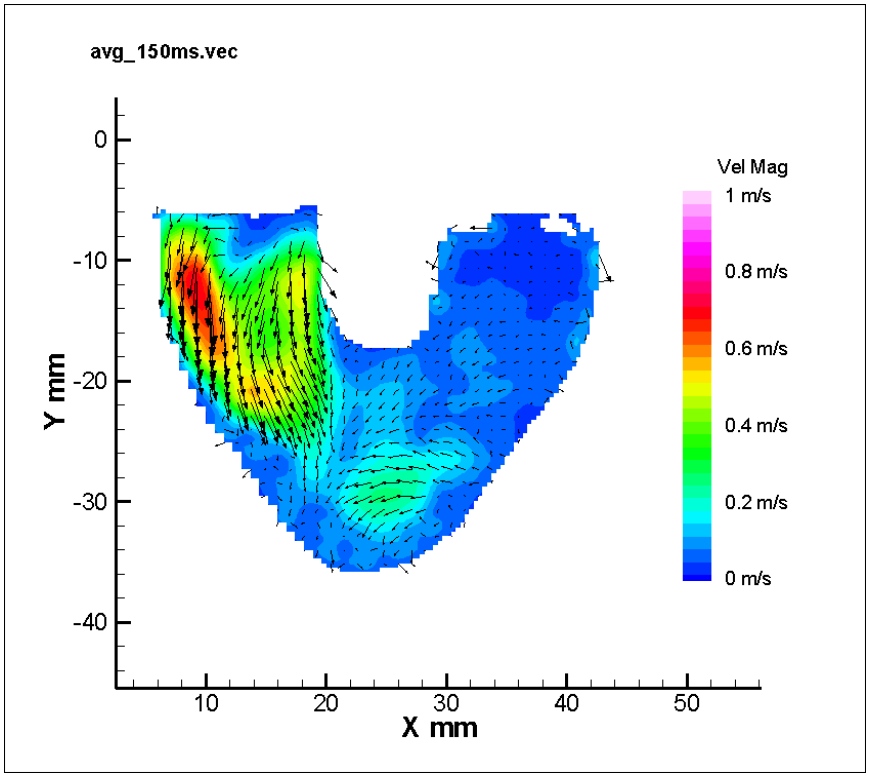
avg_150ms.vec
0
-10
-20
-30
-40
Y mm
10
20
30
40
50
X mm
Vel Mag
1 m/s
0.8 m/s
0.6 m/s
0.4 m/s
0.2 m/s
0 m/s

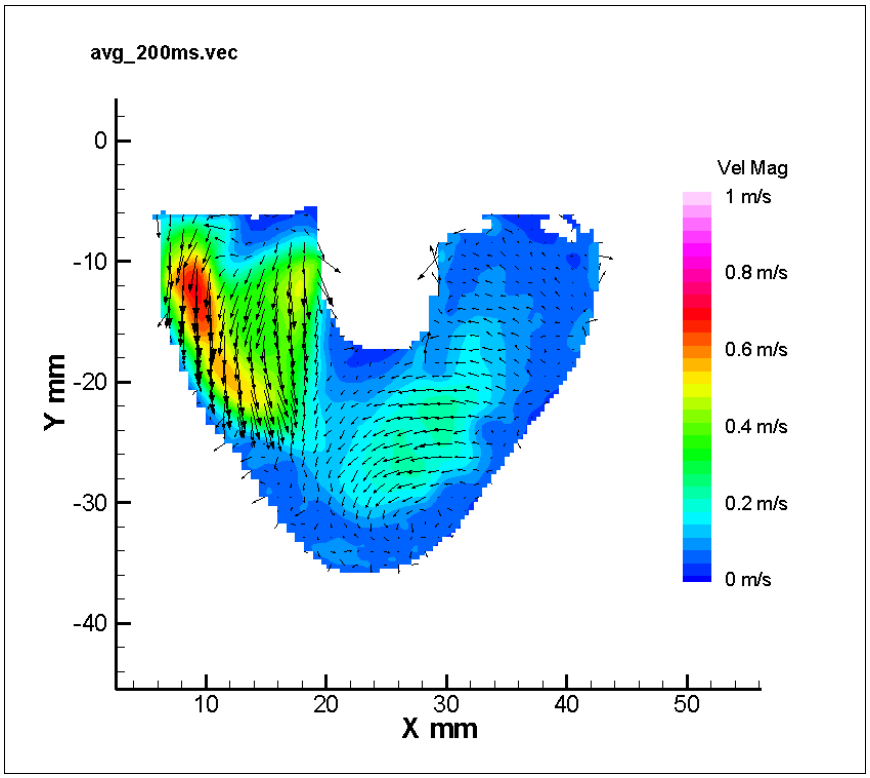
avg_200ms.vec
0
-10
-20
-30
-40
Y mm
10
20
30
40
50
X mm
Vel Mag
1 m/s
0.8 m/s
0.6 m/s
0.4 m/s
0.2 m/s
0 m/s

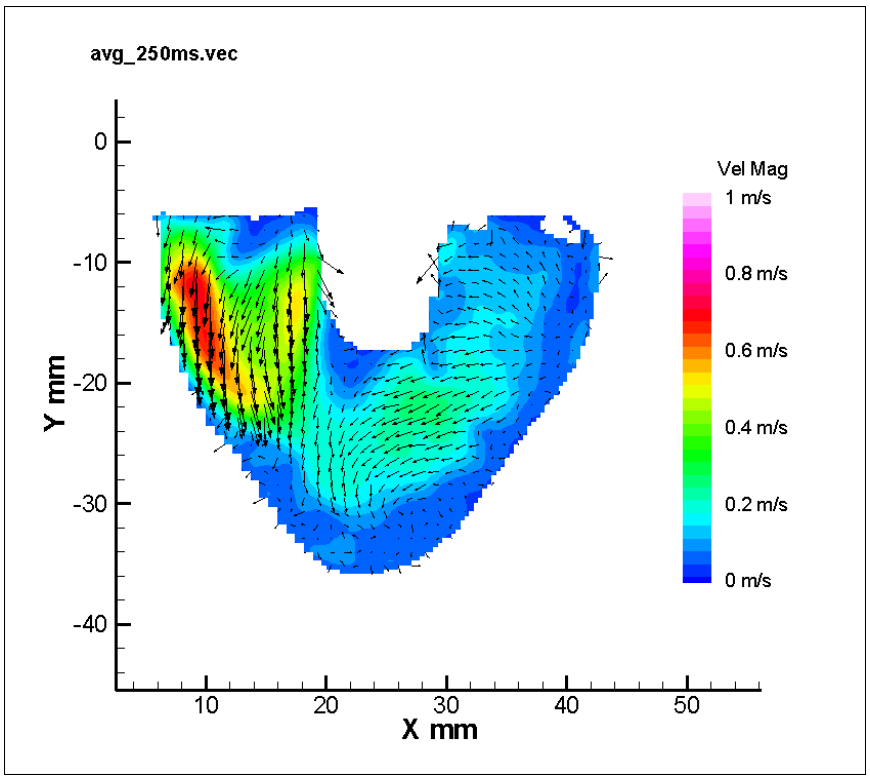
avg_250ms.vec
0
-10
-20
-30
-40
Y mm
10
20
30
40
50
X mm
Vel Mag
1 m/s
0.8 m/s
0.6 m/s
0.4 m/s
0.2 m/s
0 m/s

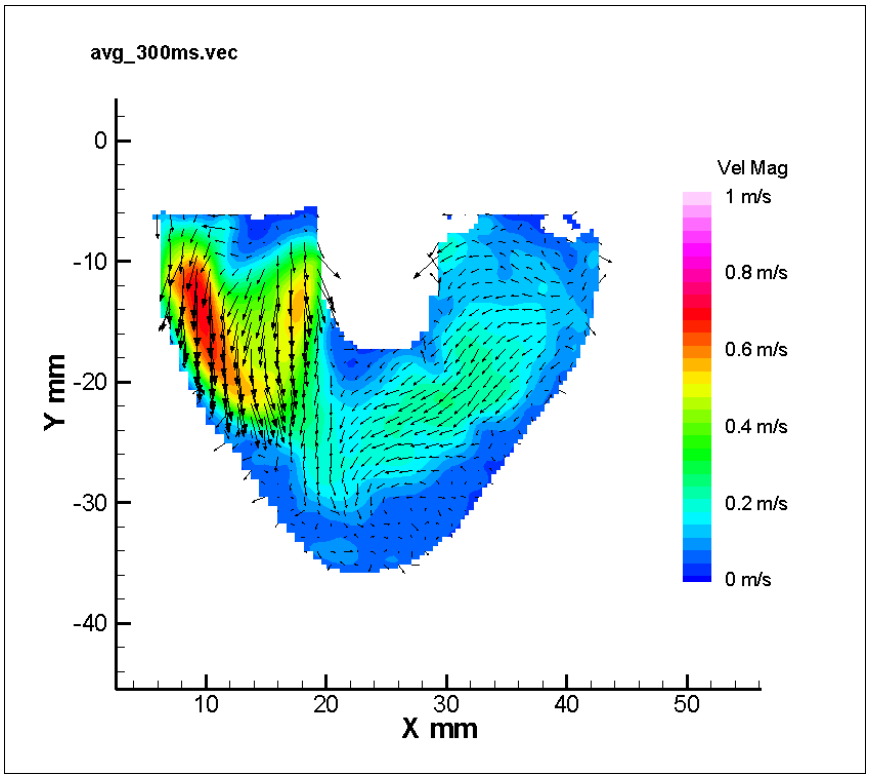
avg_300ms.vec
0
-10
-20
-30
-40
Y mm
10
20
30
40
50
X mm
Vel Mag
1 m/s
0.8 m/s
0.6 m/s
0.4 m/s
0.2 m/s
0 m/s

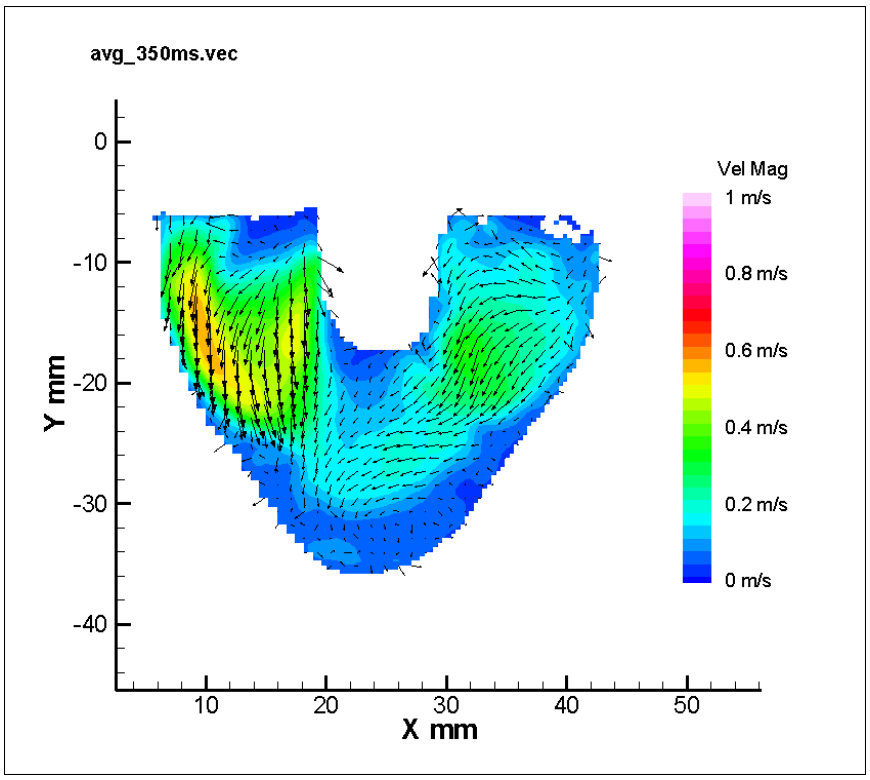
avg_350ms.vec
0
-10
-20
-30
-40
Y mm
10
20
30
40
50
X mm
Vel Mag
1 m/s
0.8 m/s
0.6 m/s
0.4 m/s
0.2 m/s
0 m/s

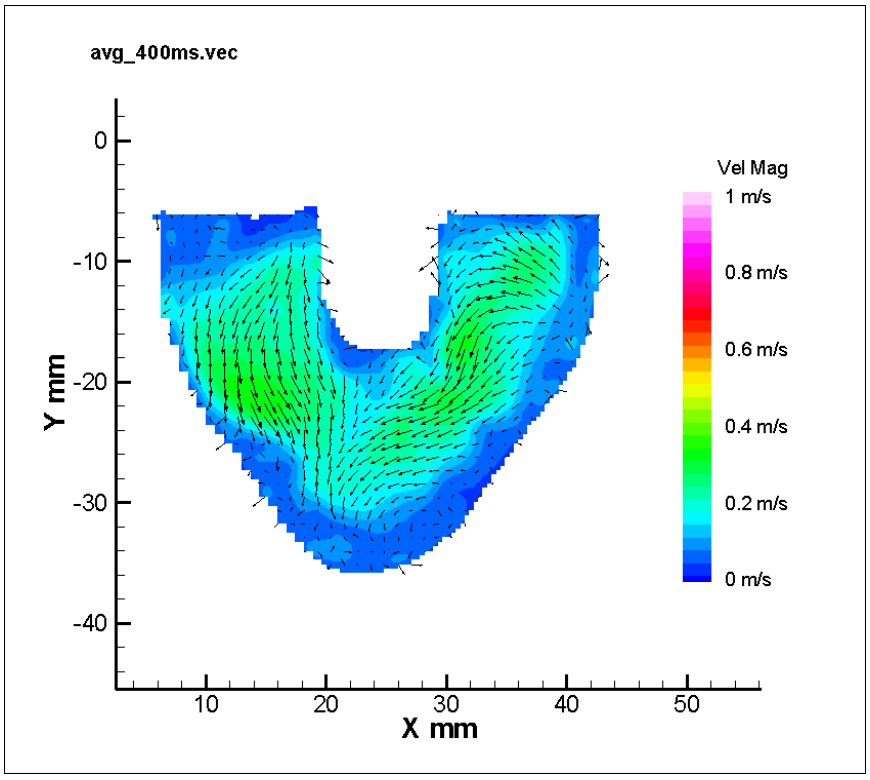
avg_400ms.vec
0
-10
-20
-30
-40
Y mm
10
20
30
40
50
X mm
Vel Mag
1 m/s
0.8 m/s
0.6 m/s
0.4 m/s
0.2 m/s
0 m/s

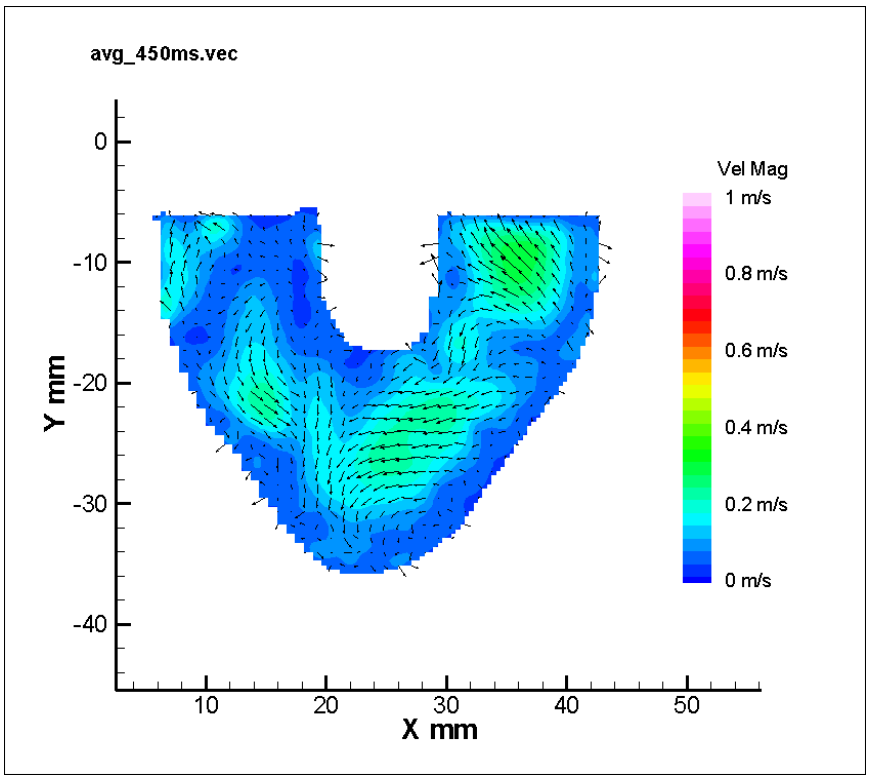
avg_450ms.vec
0
-10
-20
-30
-40
Y mm
10
20
30
40
50
X mm
Vel Mag
1 m/s
0.8 m/s
0.6 m/s
0.4 m/s
0.2 m/s
0 m/s

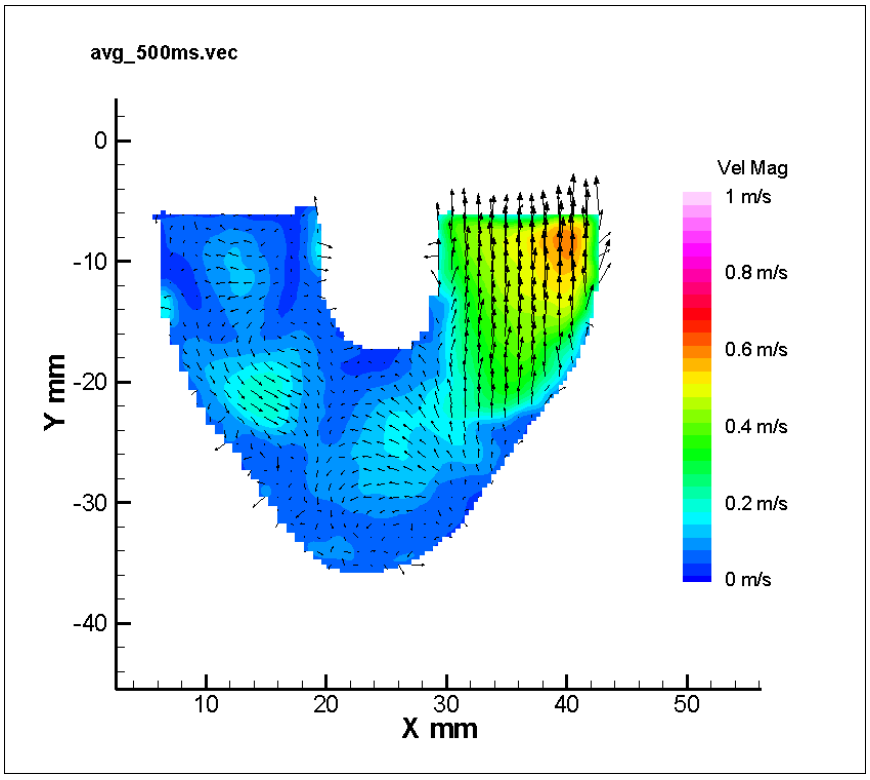
avg_500ms.vec
0
-10
-20
-30
-40
Y mm
10
20
30
40
50
X mm
Vel Mag
1 m/s
0.8 m/s
0.6 m/s
0.4 m/s
0.2 m/s
0 m/s

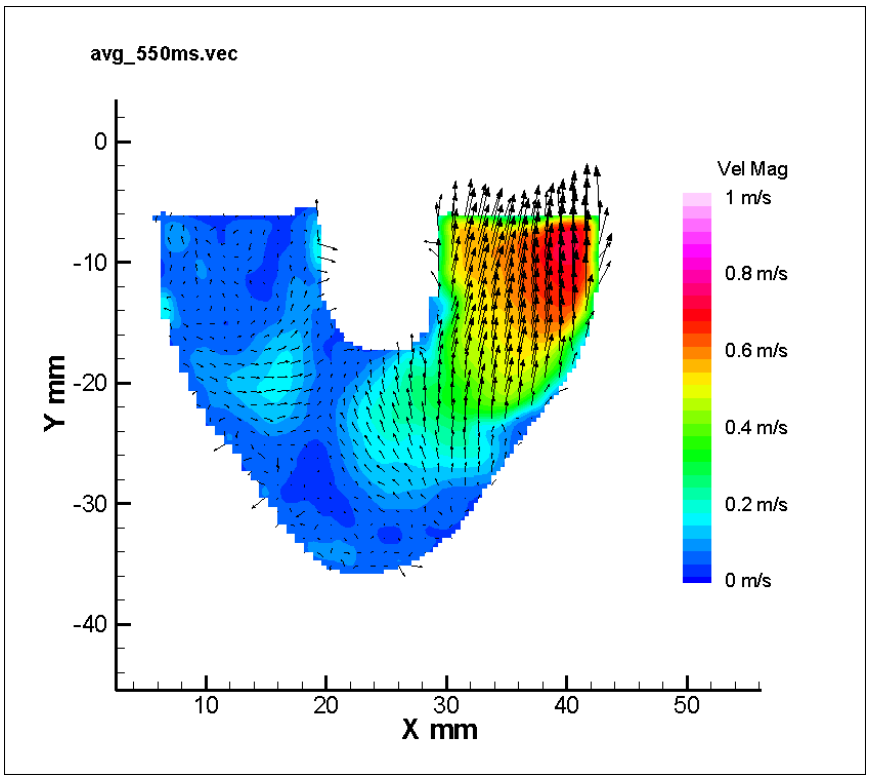
avg_550ms.vec
0
-10
-20
-30
-40
Y mm
10
20
30
40
50
X mm
Vel Mag
1 m/s
0.8 m/s
0.6 m/s
0.4 m/s
0.2 m/s
0 m/s

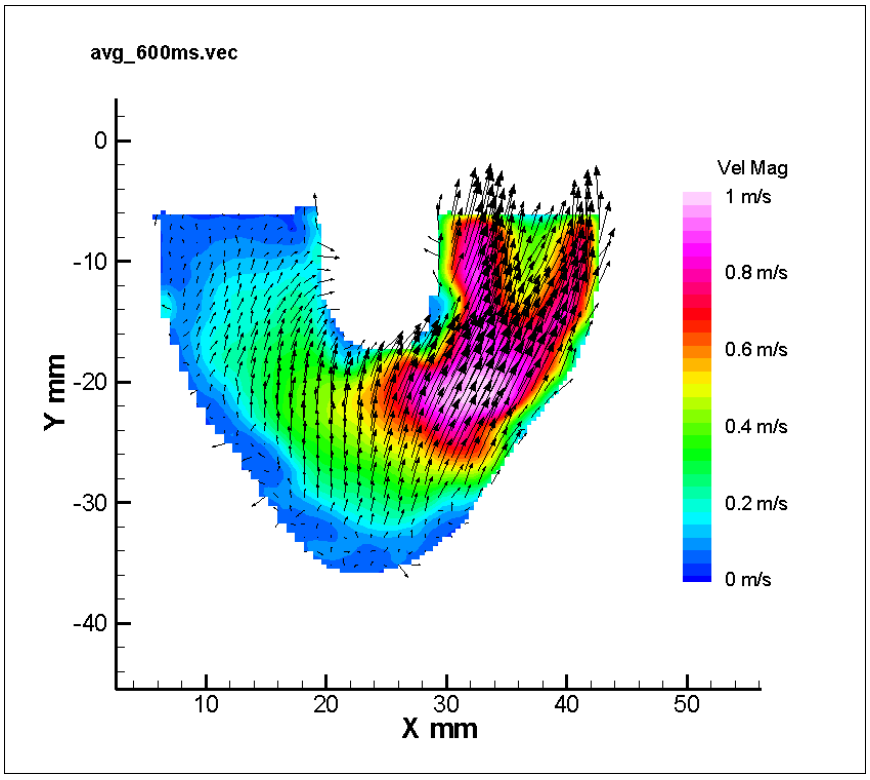
avg_600ms.vec
0
-10
-20
-30
-40
Y mm
10
20
30
40
50
X mm
Vel Mag
1 m/s
0.8 m/s
0.6 m/s
0.4 m/s
0.2 m/s
0 m/s

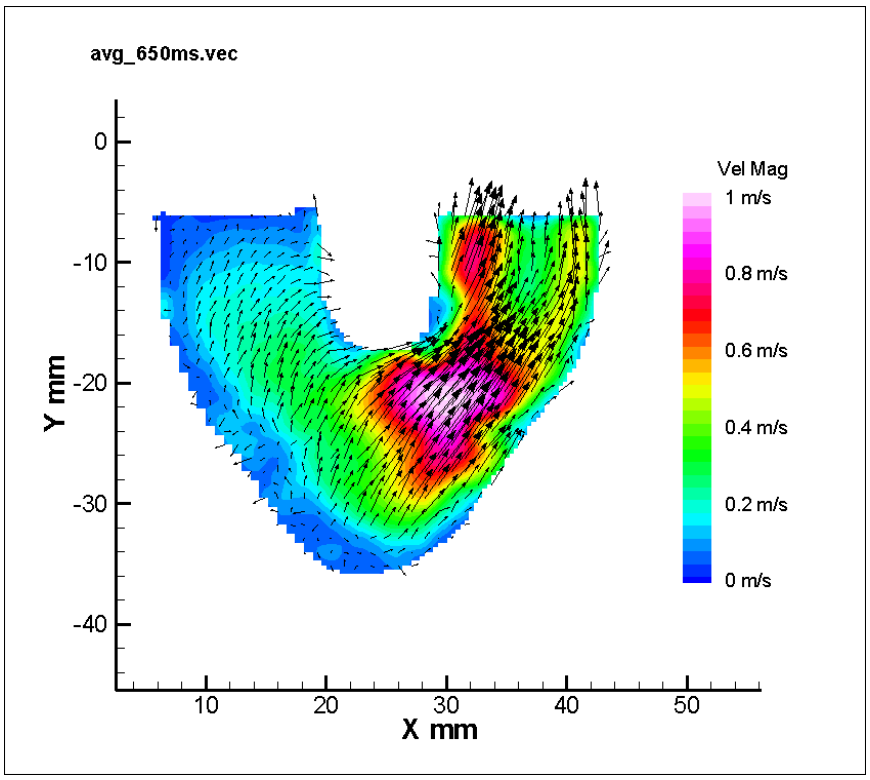
avg_650ms.vec
0
-10
-20
-30
-40
Y mm
10
20
30
40
50
X mm
Vel Mag
1 m/s
0.8 m/s
0.6 m/s
0.4 m/s
0.2 m/s
0 m/s

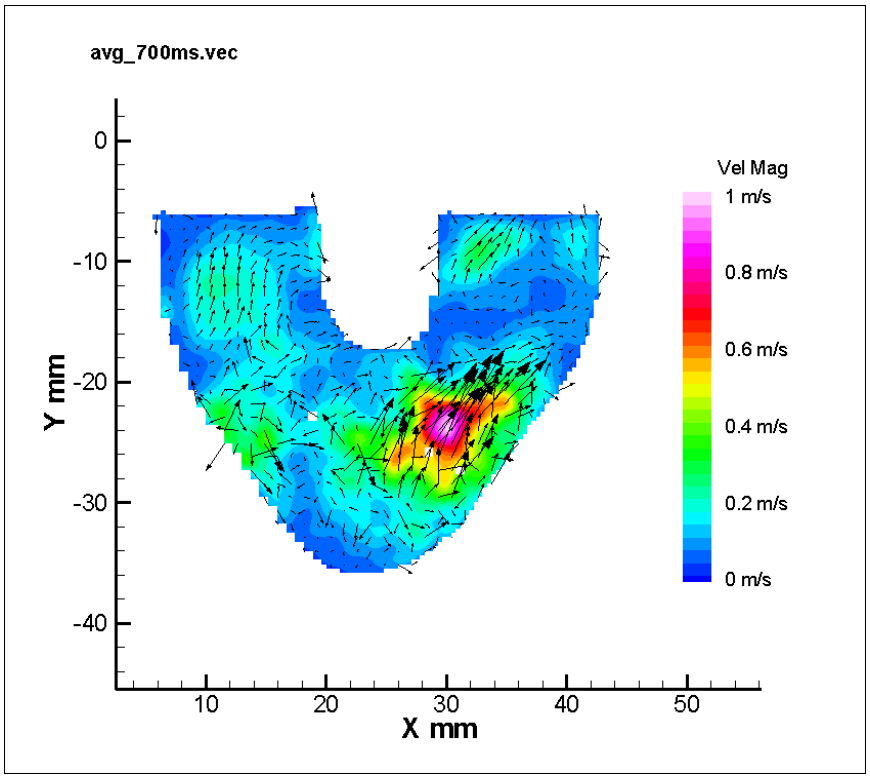
avg_700ms.vec
0
-10
-20
-30
-40
Y mm
10
20
30
40
50
X mm
Vel Mag
1 m/s
0.8 m/s
0.6 m/s
0.4 m/s
0.2 m/s
0 m/s

Appendix A-2. 7 mm Parallel Plane

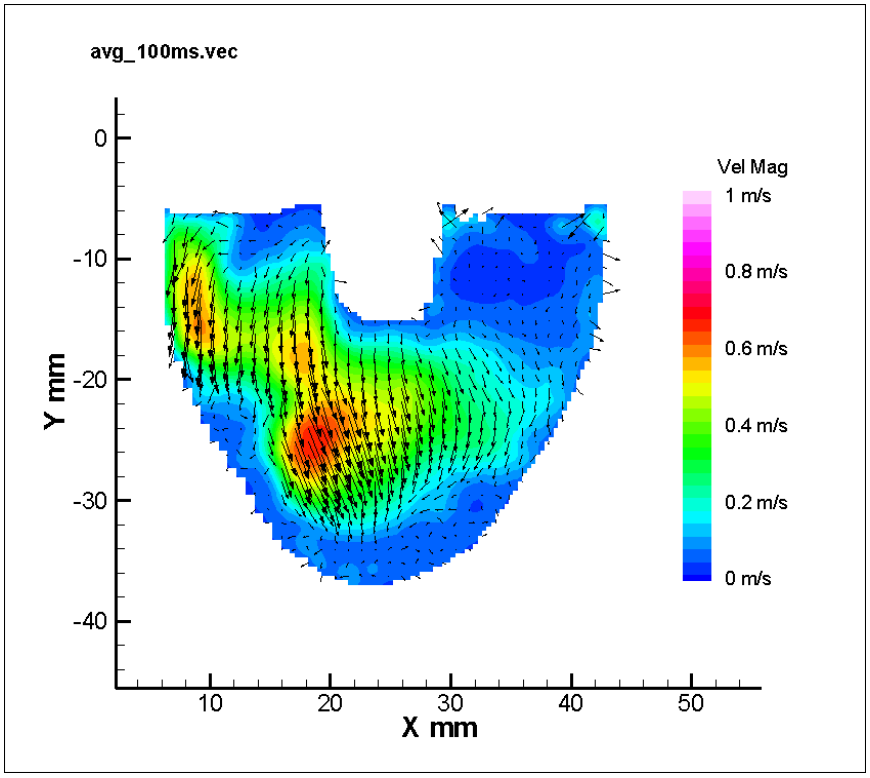

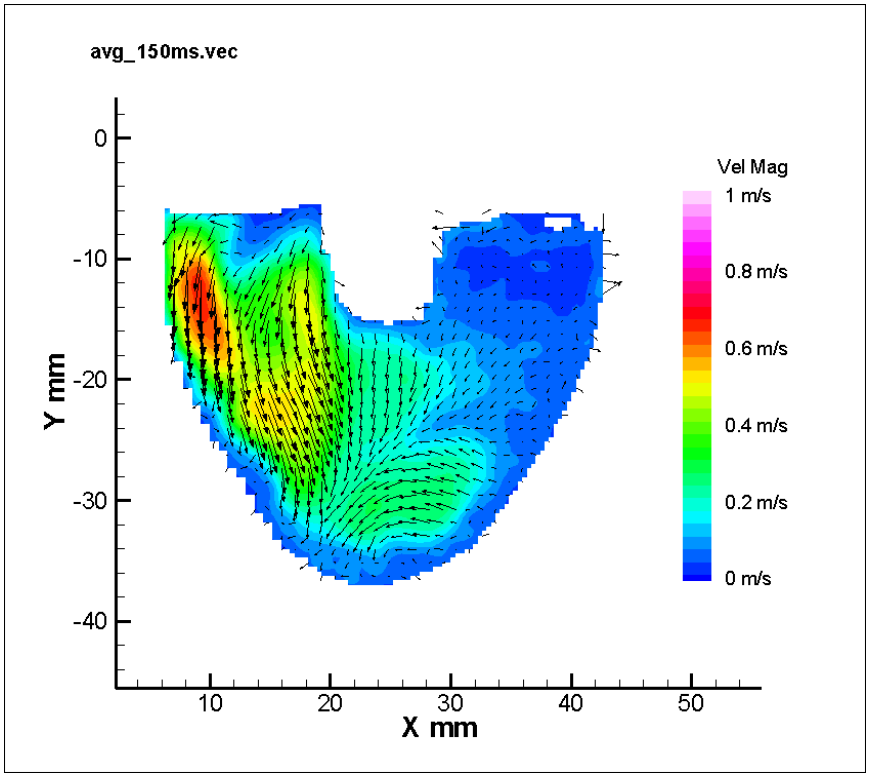

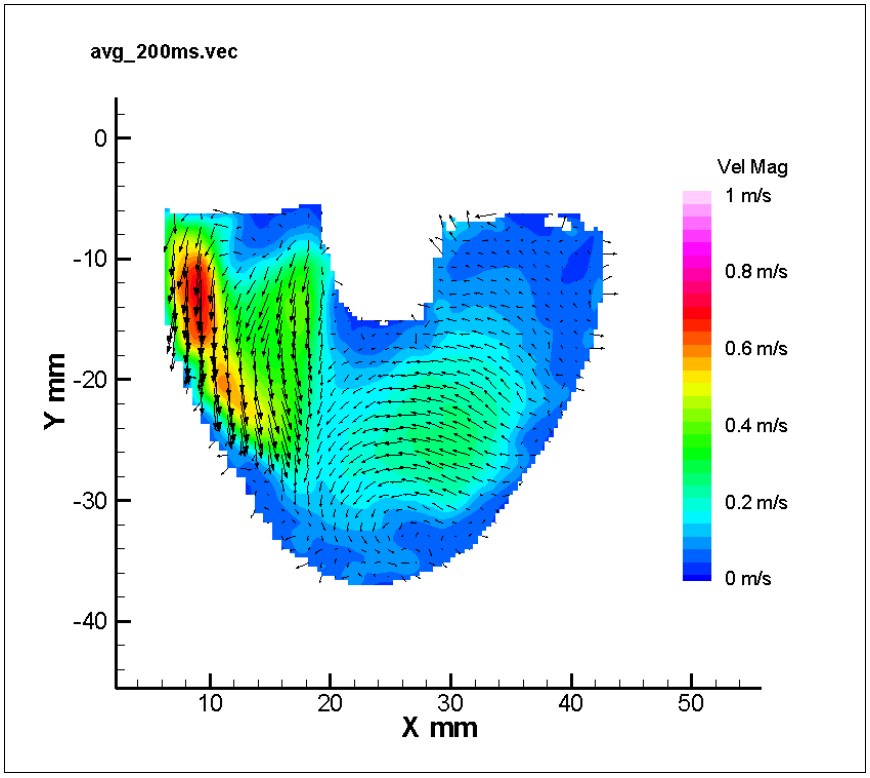
avg_200ms.vec
0
-10
-20
-30
-40
Y mm
10
20
30
40
50
X mm
Vel Mag
1 m/s
0.8 m/s
0.6 m/s
0.4 m/s
0.2 m/s
0 m/s

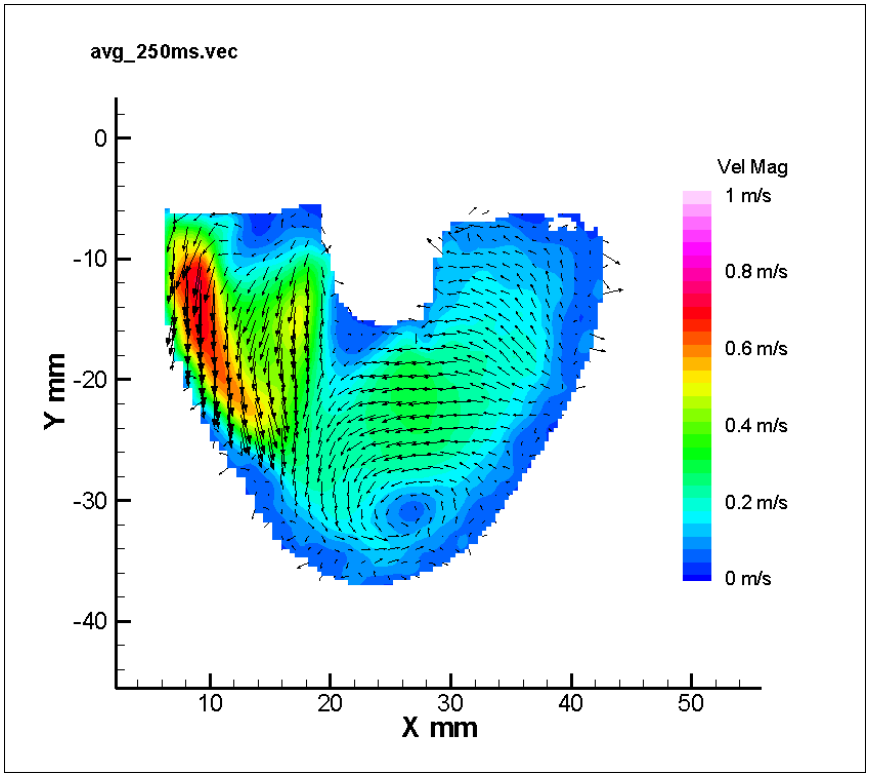
avg_250ms.vec
0
-10
-20
-30
-40
Y mm
10
20
30
40
50
X mm
Vel Mag
1 m/s
0.8 m/s
0.6 m/s
0.4 m/s
0.2 m/s
0 m/s

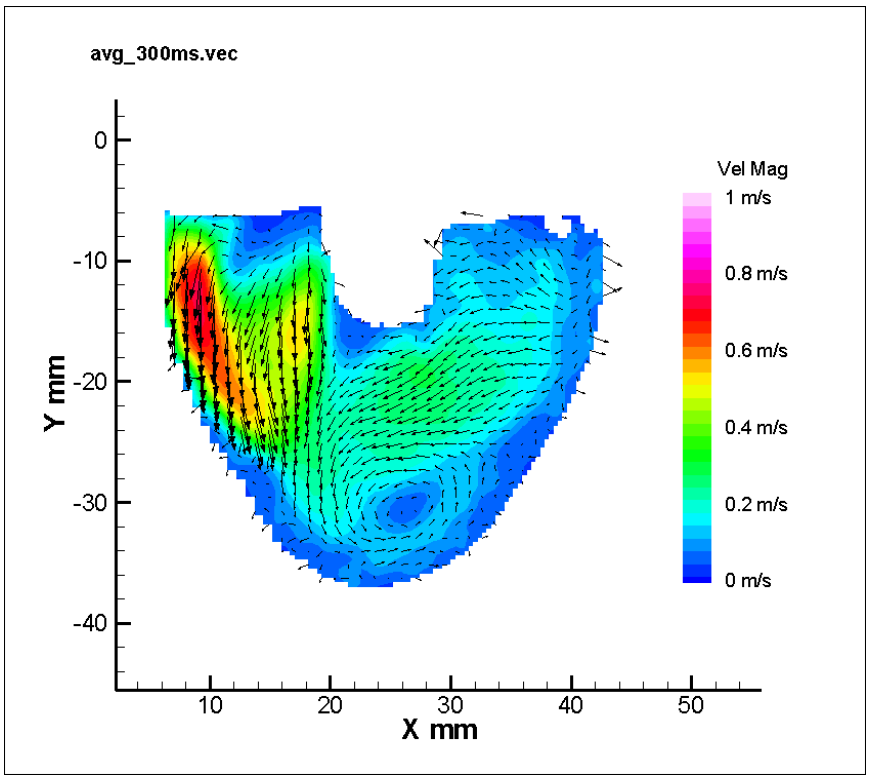
avg_300ms.vec
0
-10
-20
-30
-40
Y mm
10
20
30
40
50
X mm
Vel Mag
1 m/s
0.8 m/s
0.6 m/s
0.4 m/s
0.2 m/s
0 m/s

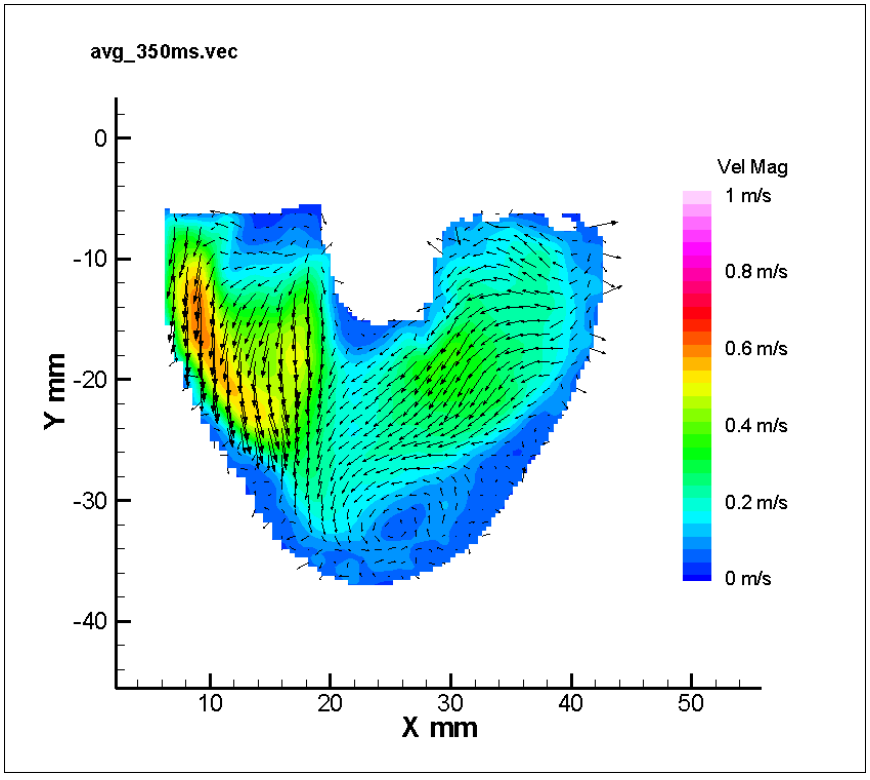
avg_350ms.vec
0
-10
-20
-30
-40
Y mm
10
20
30
40
50
X mm
Vel Mag
1 m/s
0.8 m/s
0.6 m/s
0.4 m/s
0.2 m/s
0 m/s

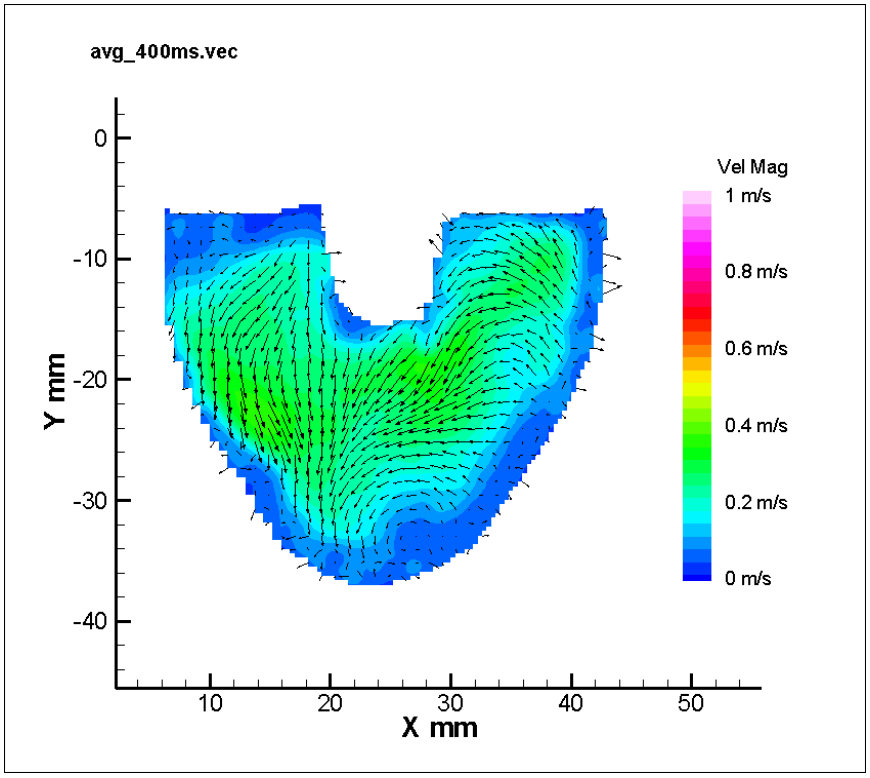
avg_400ms.vec
0
-10
-20
-30
-40
Y mm
10
20
30
40
50
X mm
Vel Mag
1 m/s
0.8 m/s
0.6 m/s
0.4 m/s
0.2 m/s
0 m/s

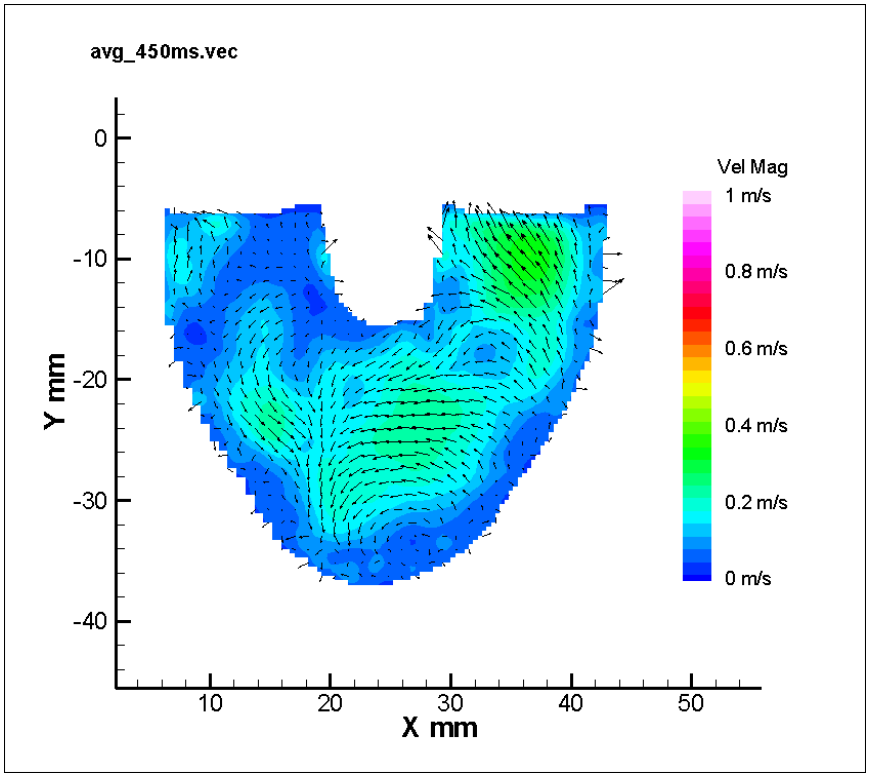
avg_450ms.vec
0
-10
-20
-30
-40
Y mm
10
20
30
40
50
X mm
Vel Mag
1 m/s
0.8 m/s
0.6 m/s
0.4 m/s
0.2 m/s
0 m/s

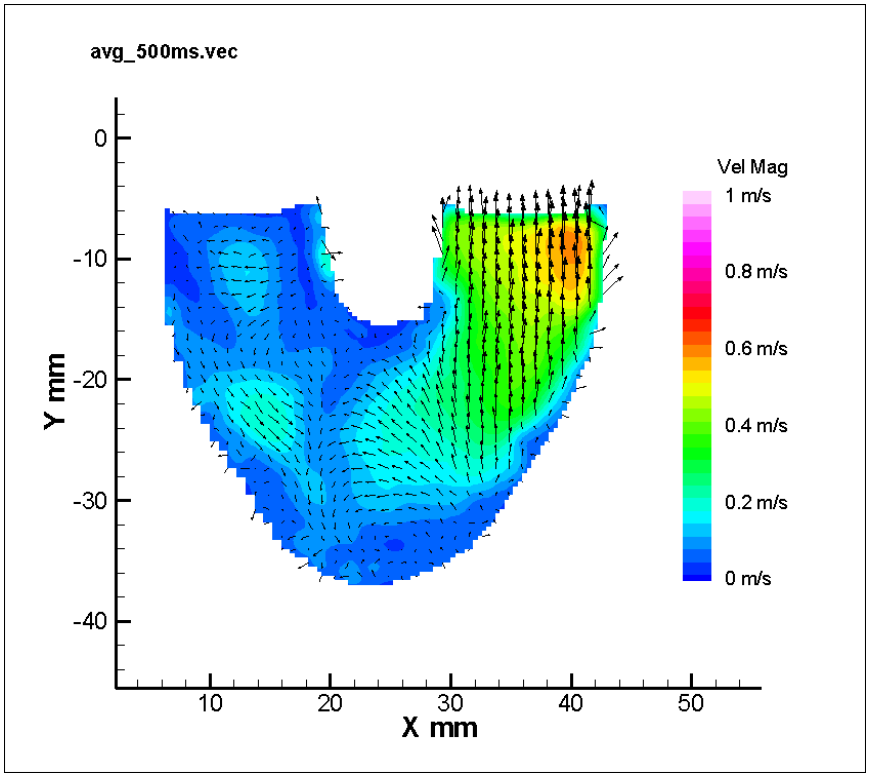
avg_500ms.vec
0
-10
-20
-30
-40
Y mm
10
20
30
40
50
X mm
Vel Mag
1 m/s
0.8 m/s
0.6 m/s
0.4 m/s
0.2 m/s
0 m/s

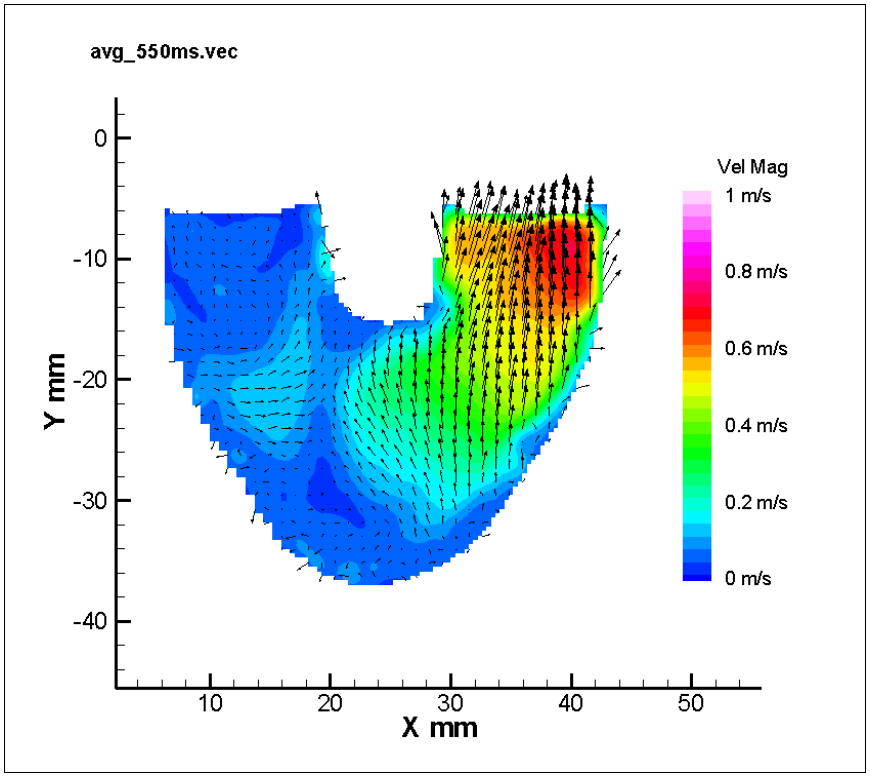
avg_550ms.vec
0
-10
-20
-30
-40
Y mm
10
20
30
40
50
X mm
Vel Mag
1 m/s
0.8 m/s
0.6 m/s
0.4 m/s
0.2 m/s
0 m/s

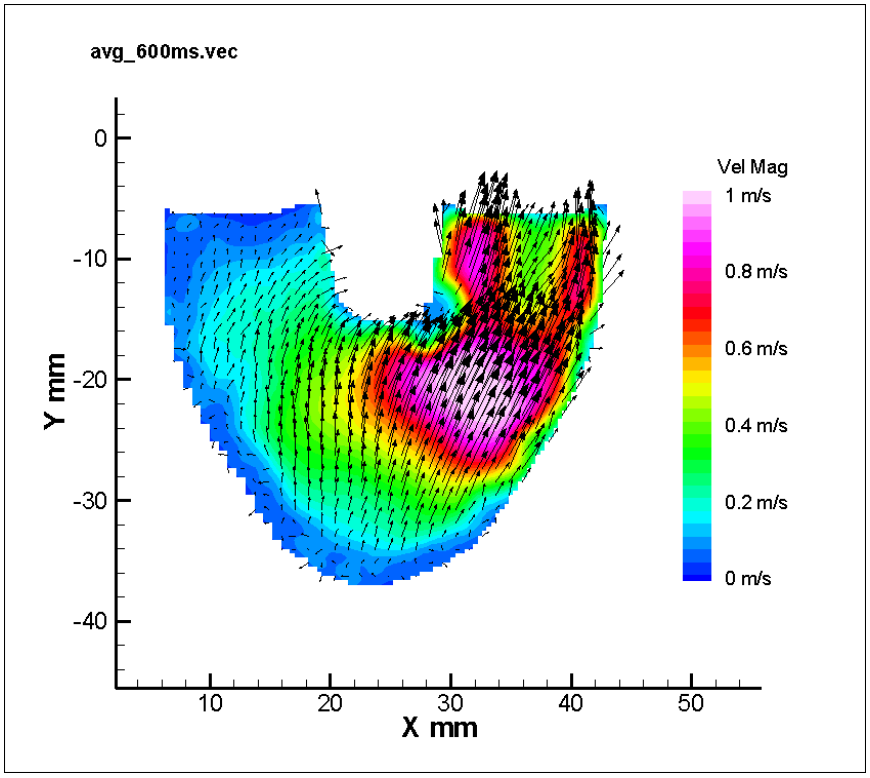
avg_600ms.vec
0
-10
-20
-30
-40
Y mm
10
20
30
40
50
X mm
Vel Mag
1 m/s
0.8 m/s
0.6 m/s
0.4 m/s
0.2 m/s
0 m/s

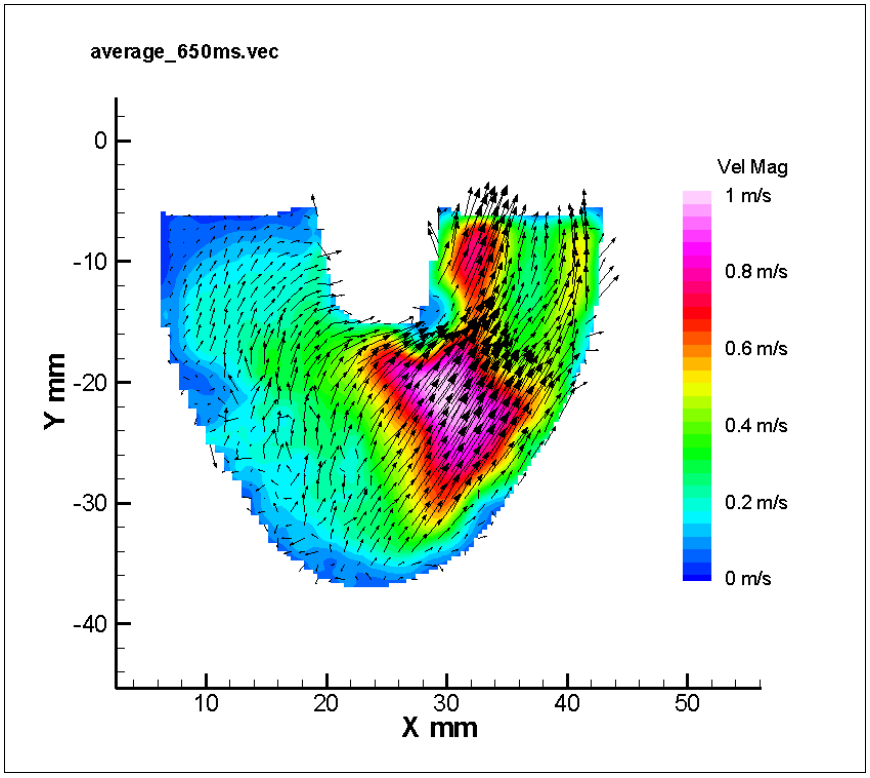
average_650ms.vec
0
-10
-20
-30
-40
Y mm
10
20
30
40
50
X mm
Vel Mag
1 m/s
0.8 m/s
0.6 m/s
0.4 m/s
0.2 m/s
0 m/s

Appendix A-3. 8.2 mm Parallel Plane

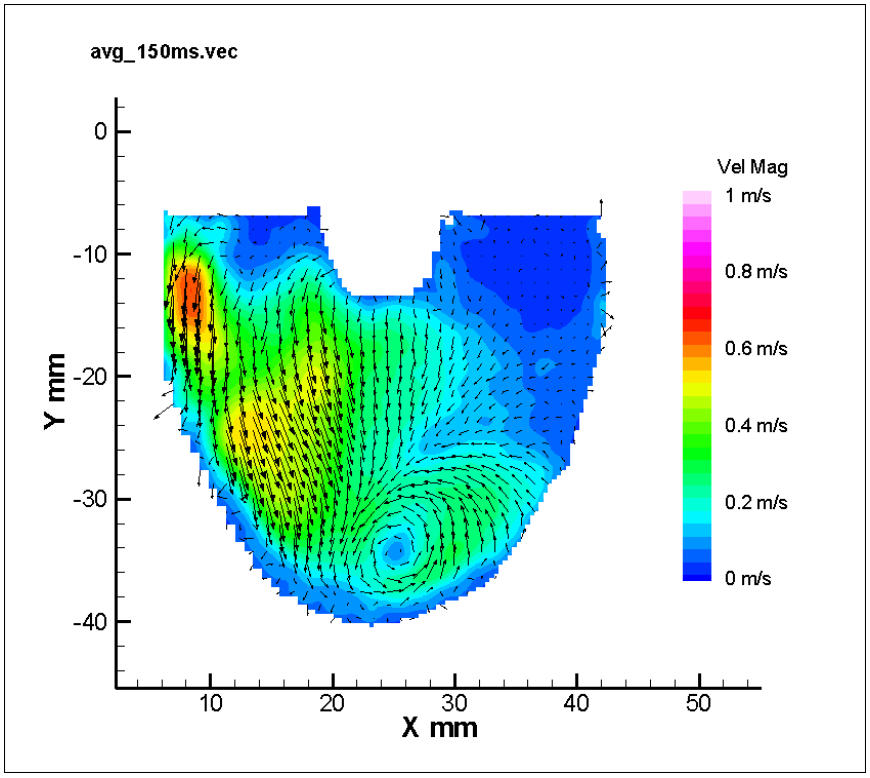

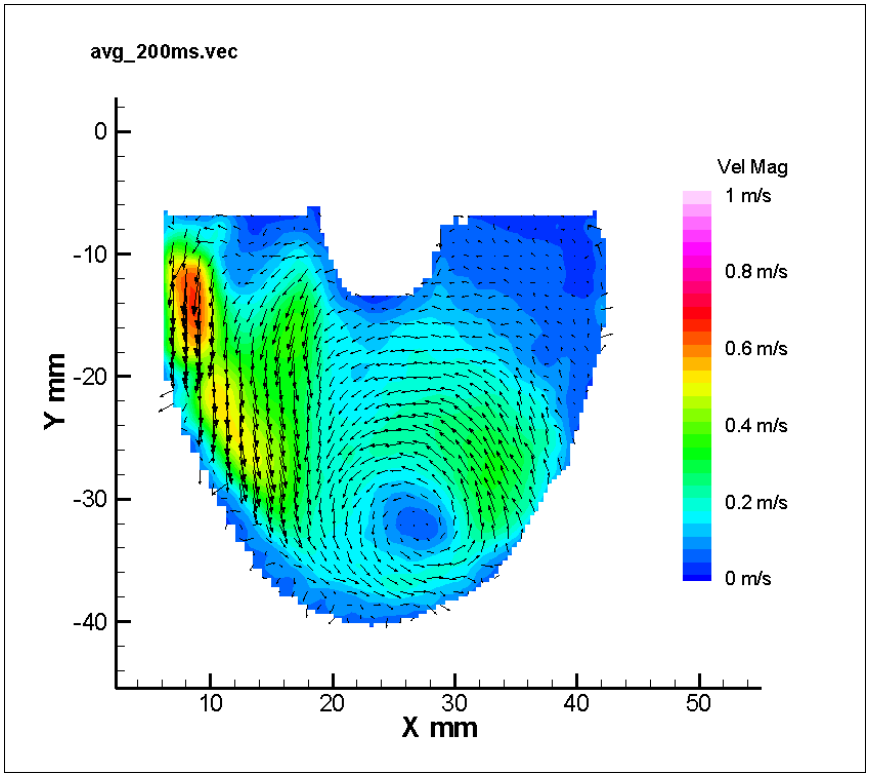

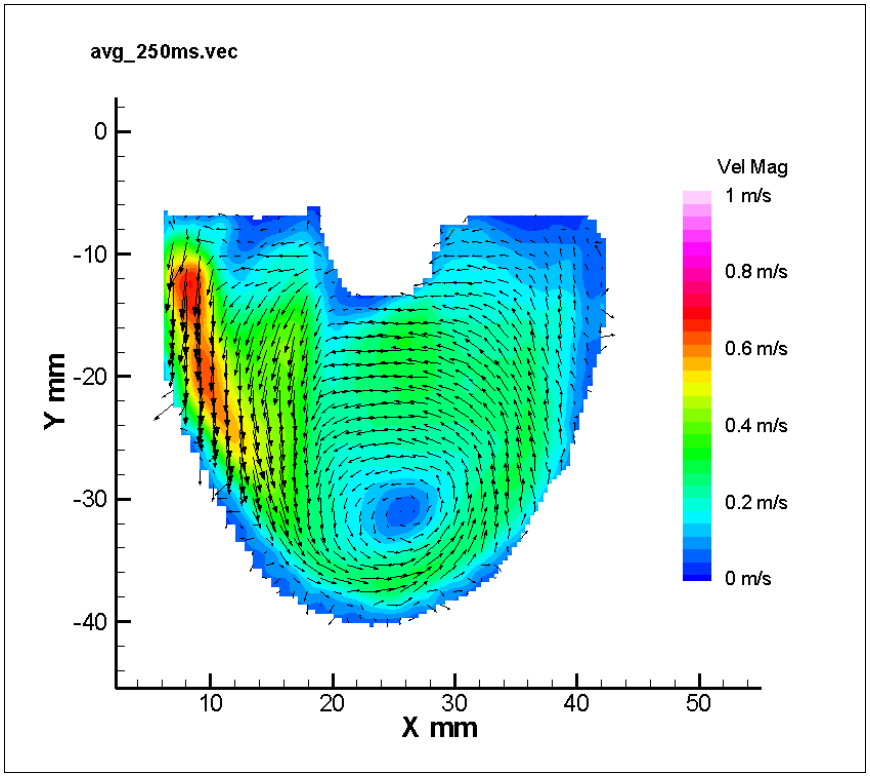
avg_250ms.vec
0
-10
-20
-30
-40
Y mm
10
20
30
40
50
X mm
Vel Mag
1 m/s
0.8 m/s
0.6 m/s
0.4 m/s
0.2 m/s
0 m/s

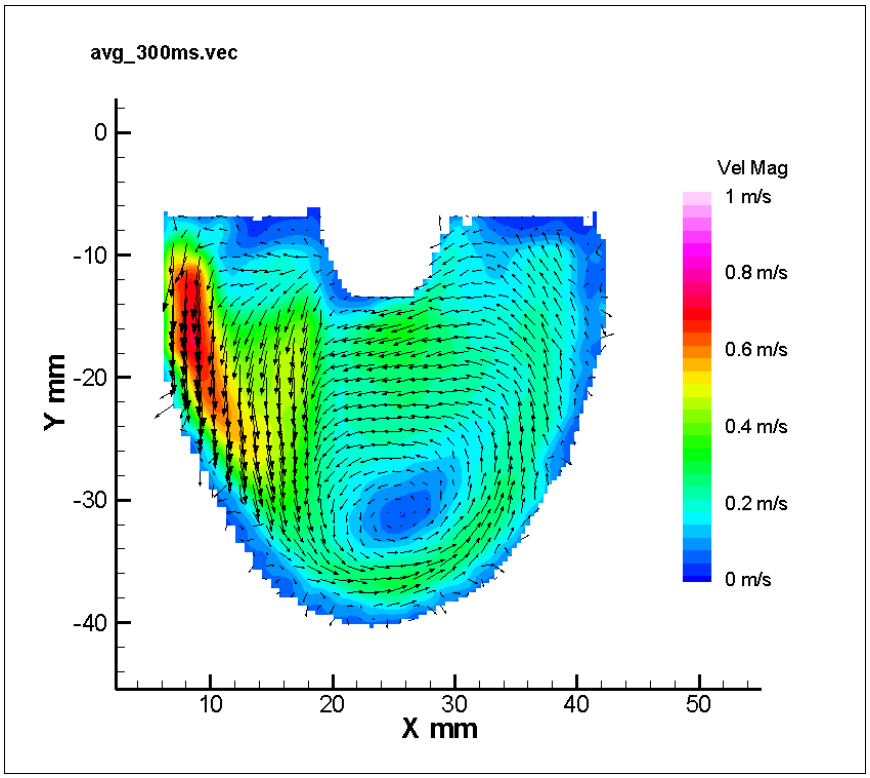
avg_300ms.vec
0
-10
-20
-30
-40
Y mm
10
20
30
40
50
X mm
Vel Mag
1 m/s
0.8 m/s
0.6 m/s
0.4 m/s
0.2 m/s
0 m/s

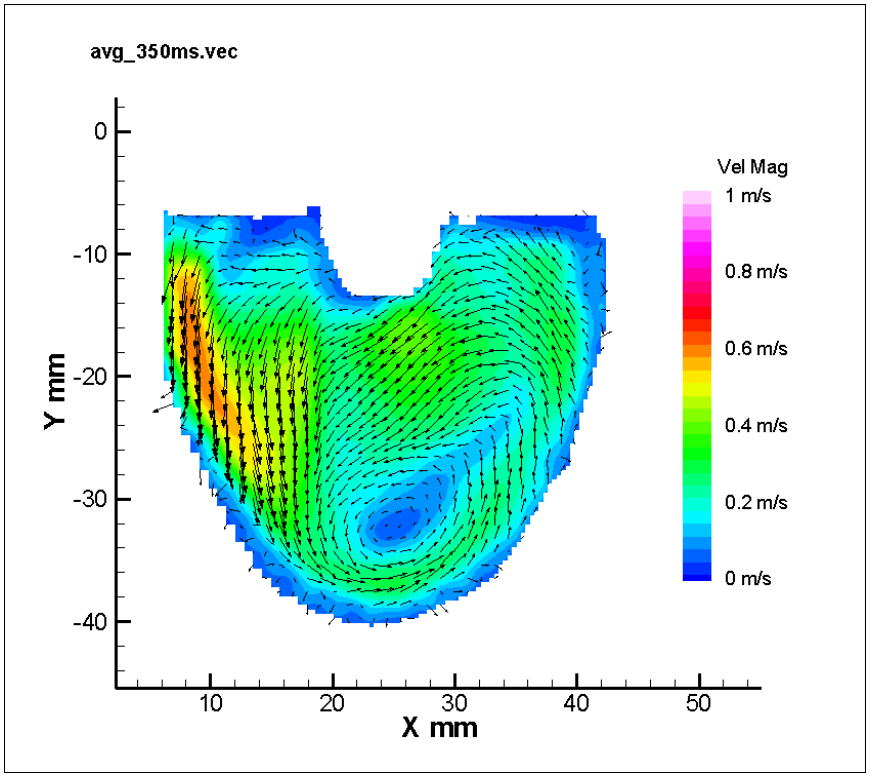
avg_350ms.vec
0
-10
-20
-30
-40
Y mm
10
20
30
40
50
X mm
Vel Mag
1 m/s
0.8 m/s
0.6 m/s
0.4 m/s
0.2 m/s
0 m/s

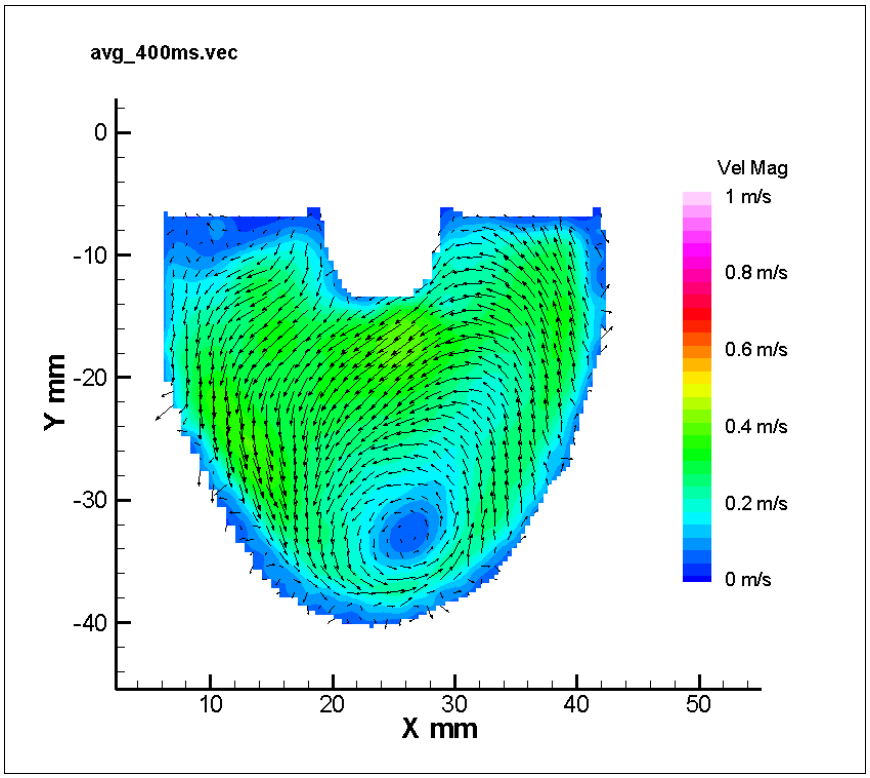
avg_400ms.vec
0
-10
-20
-30
-40
Y mm
10
20
30
40
50
X mm
Vel Mag
1 m/s
0.8 m/s
0.6 m/s
0.4 m/s
0.2 m/s
0 m/s

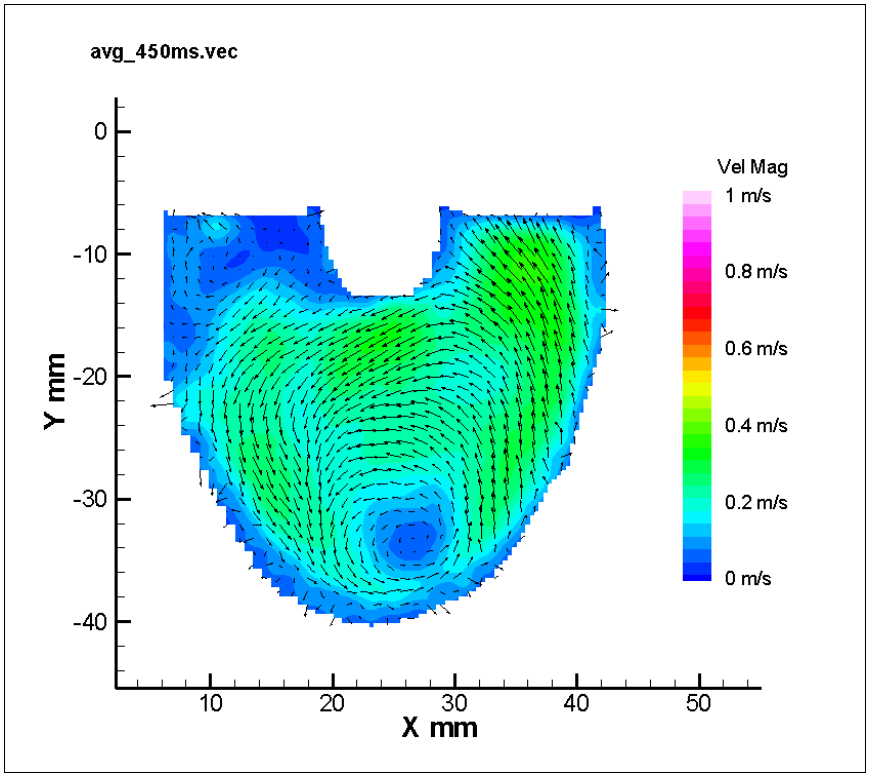
avg_450ms.vec
0
-10
-20
-30
-40
Y mm
10
20
30
40
50
X mm
Vel Mag
1 m/s
0.8 m/s
0.6 m/s
0.4 m/s
0.2 m/s
0 m/s

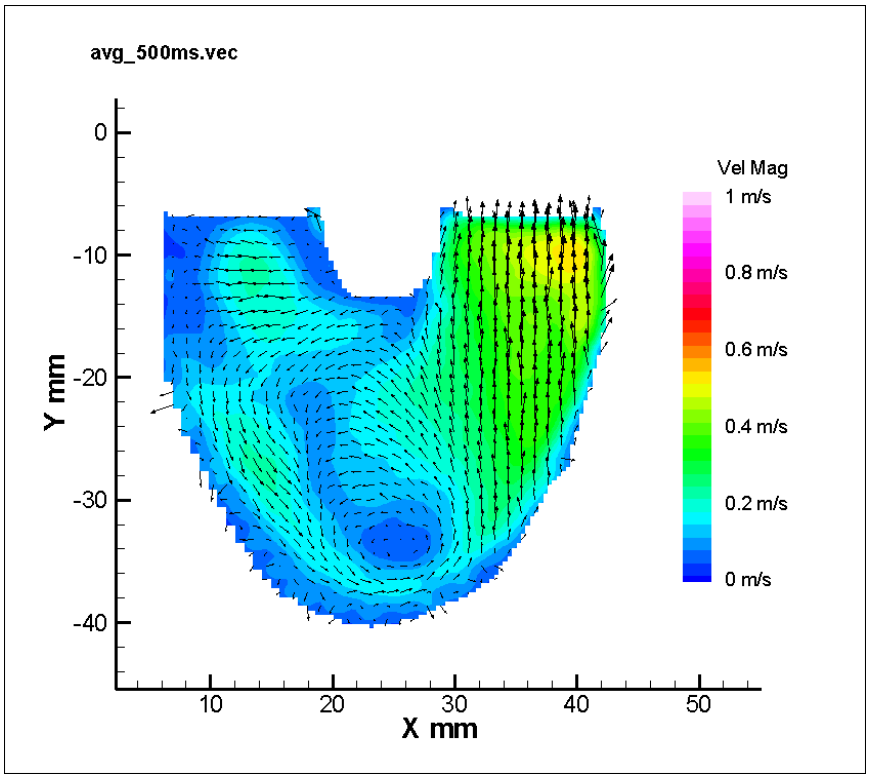
avg_500ms.vec
0
-10
-20
-30
-40
Y mm
10
20
30
40
50
X mm
Vel Mag
1 m/s
0.8 m/s
0.6 m/s
0.4 m/s
0.2 m/s
0 m/s

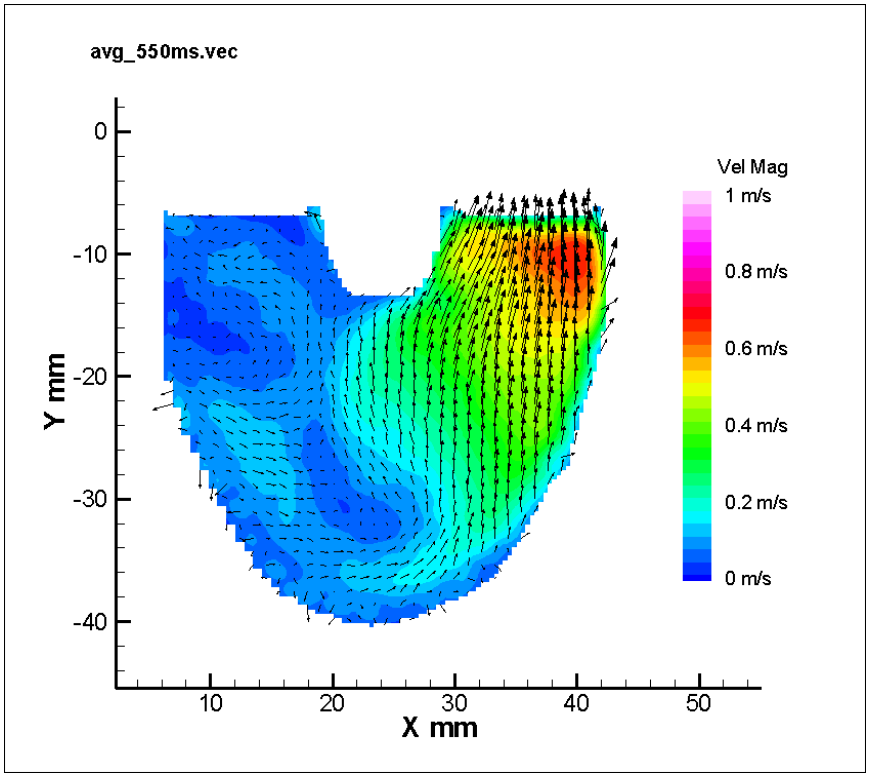
avg_550ms.vec
0
-10
-20
-30
-40
Y mm
10
20
30
40
50
X mm
Vel Mag
1 m/s
0.8 m/s
0.6 m/s
0.4 m/s
0.2 m/s
0 m/s

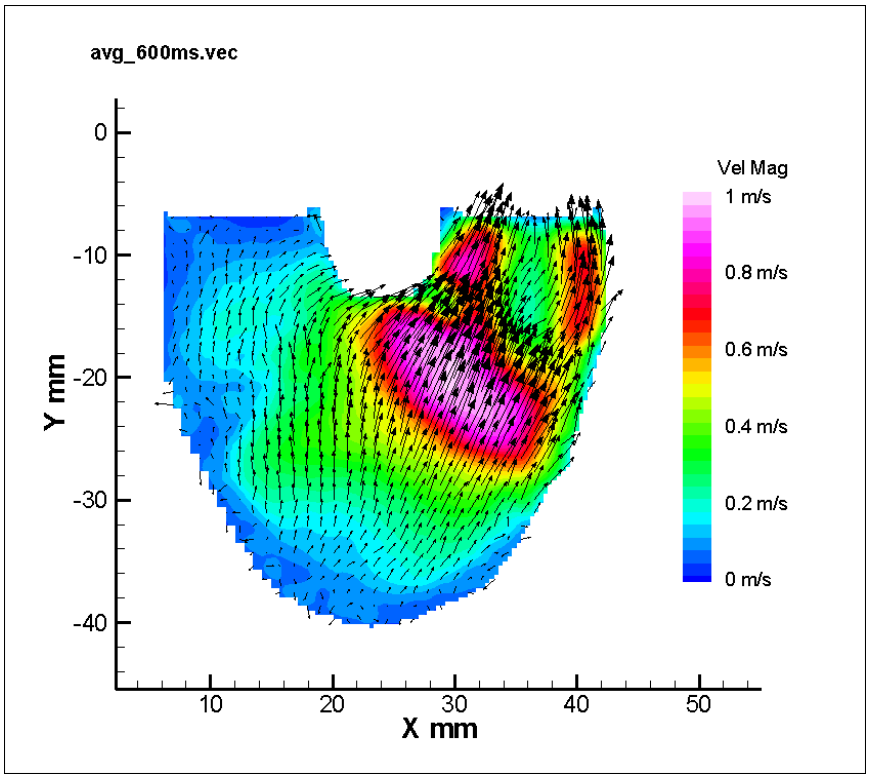
avg_600ms.vec
0
-10
-20
-30
-40
Y mm
10
20
30
40
50
X mm
Vel Mag
1 m/s
0.8 m/s
0.6 m/s
0.4 m/s
0.2 m/s
0 m/s

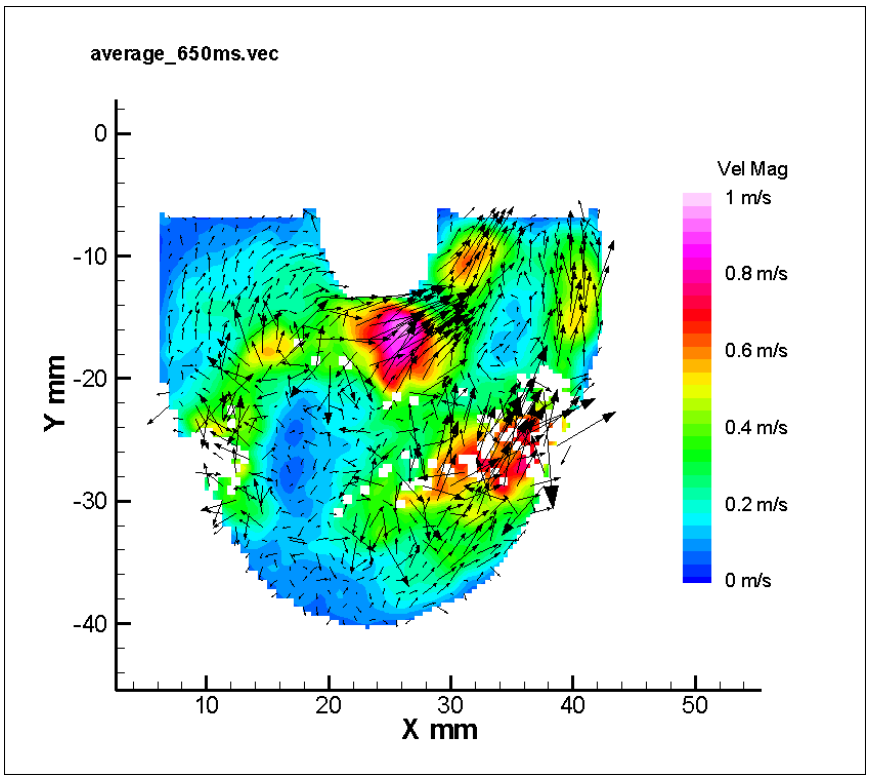
average_650ms.vec
0
-10
-20
-30
-40
Y mm
10
20
30
40
50
X mm
Vel Mag
1 m/s
0.8 m/s
0.6 m/s
0.4 m/s
0.2 m/s
0 m/s

Appendix A-4. 11 mm Parallel Plane

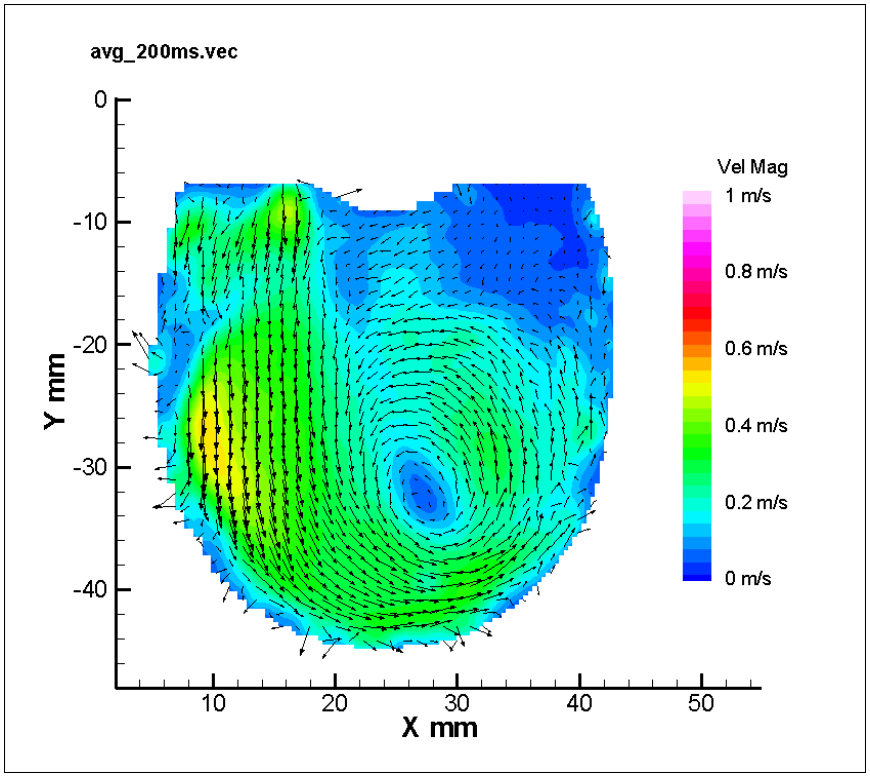

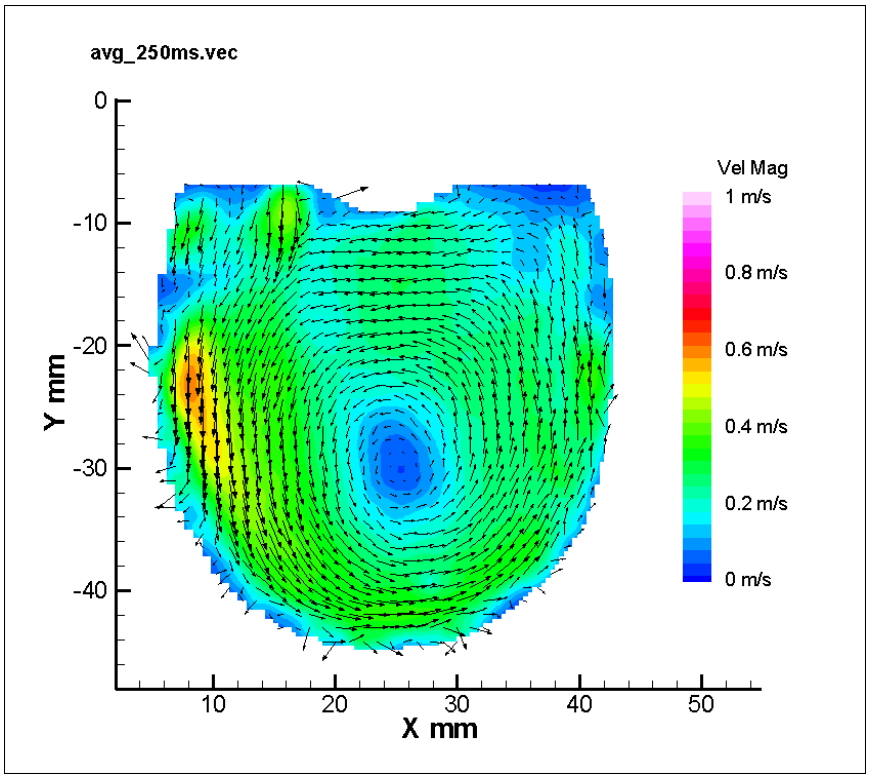

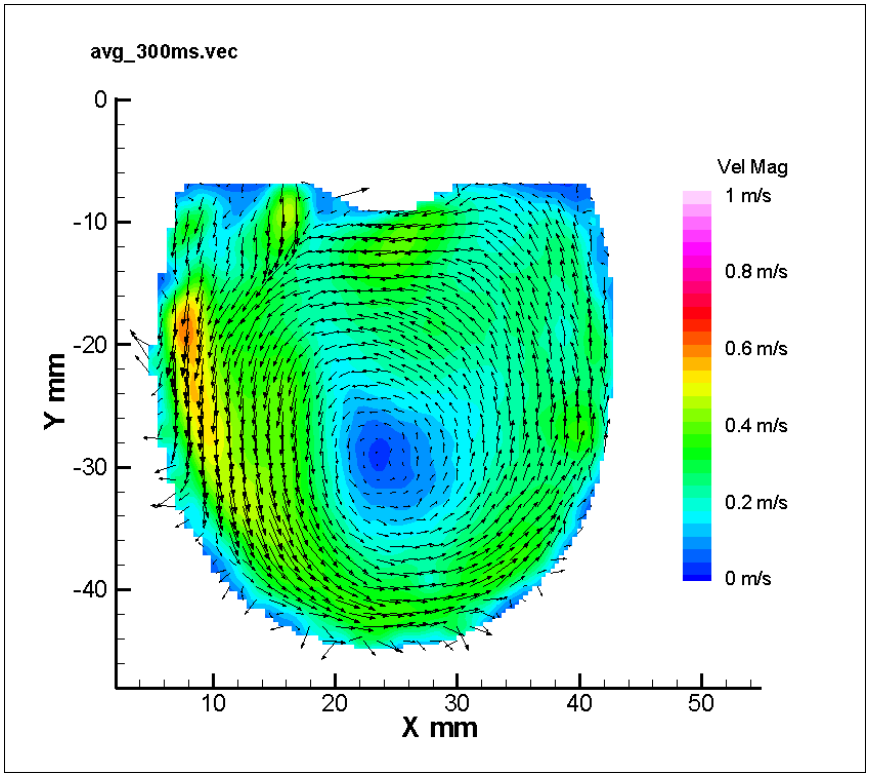
avg_300ms.vec
0
-10
-20
-30
-40
Y mm
10
20
30
40
50
X mm
Vel Mag
1 m/s
0.8 m/s
0.6 m/s
0.4 m/s
0.2 m/s
0 m/s

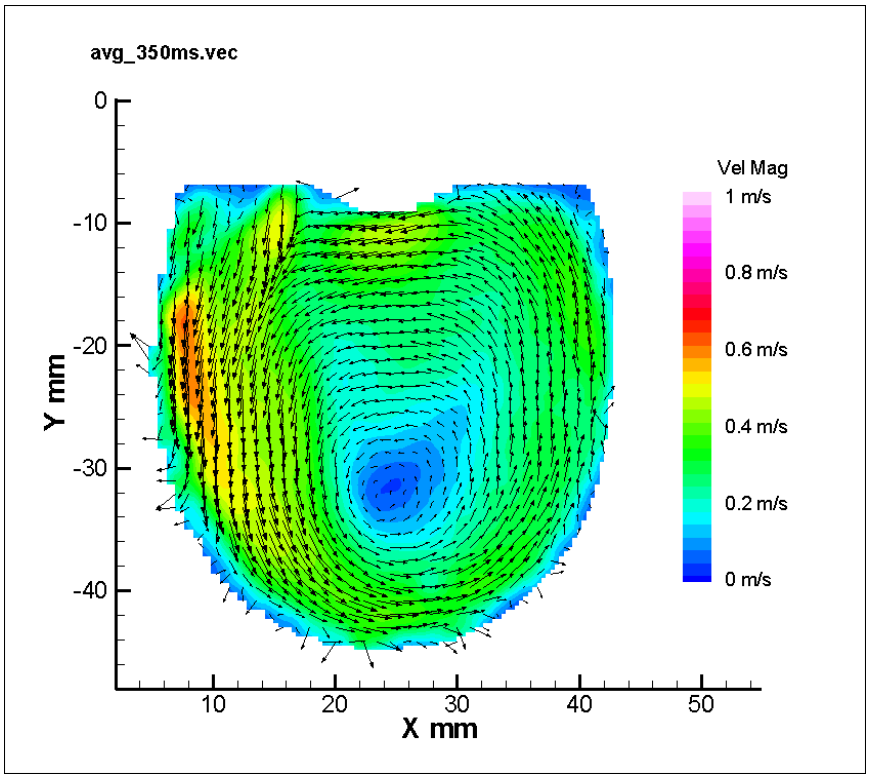
avg_350ms.vec
0
-10
-20
-30
-40
Y mm
10
20
30
40
50
X mm
Vel Mag
1 m/s
0.8 m/s
0.6 m/s
0.4 m/s
0.2 m/s
0 m/s

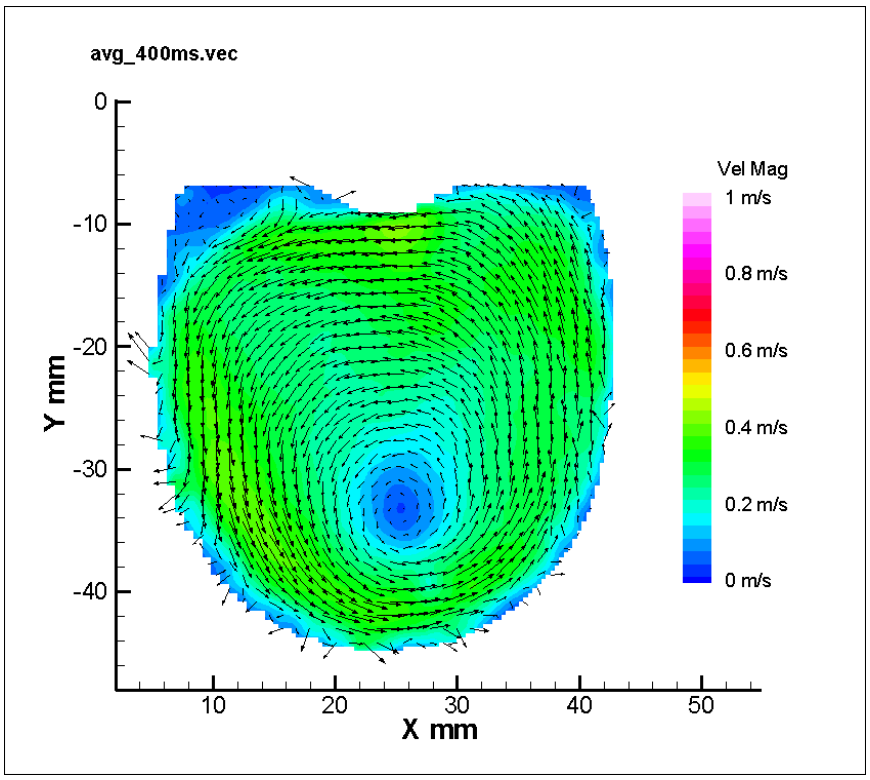
avg_400ms.vec
0
-10
-20
-30
-40
Y mm
10
20
30
40
50
X mm
Vel Mag
1 m/s
0.8 m/s
0.6 m/s
0.4 m/s
0.2 m/s
0 m/s

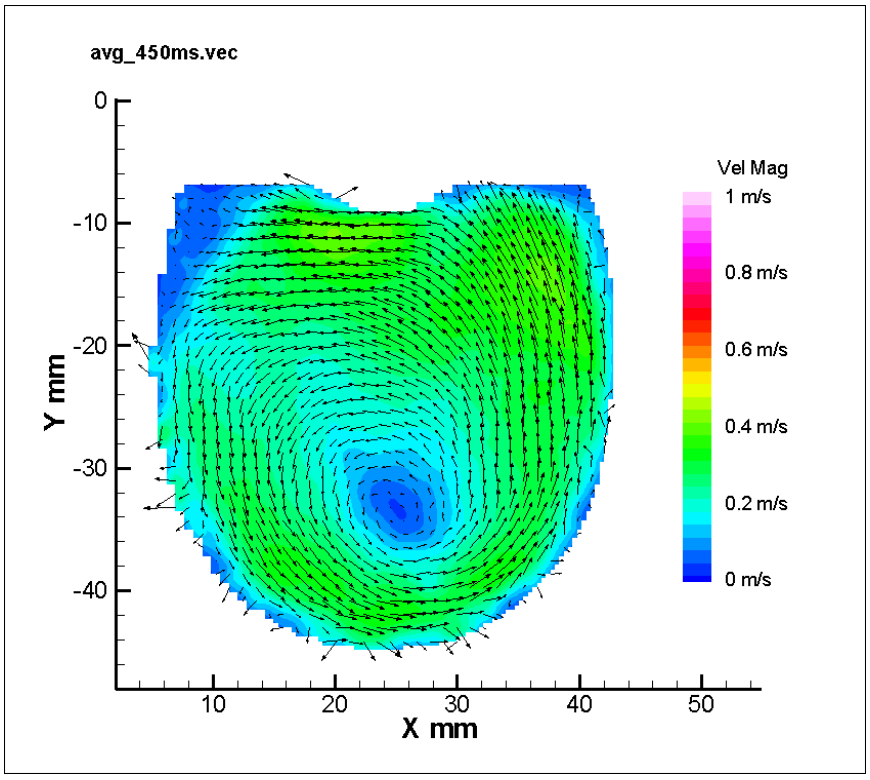
avg_450ms.vec
0
-10
-20
-30
-40
Y mm
10
20
30
40
50
X mm
Vel Mag
1 m/s
0.8 m/s
0.6 m/s
0.4 m/s
0.2 m/s
0 m/s

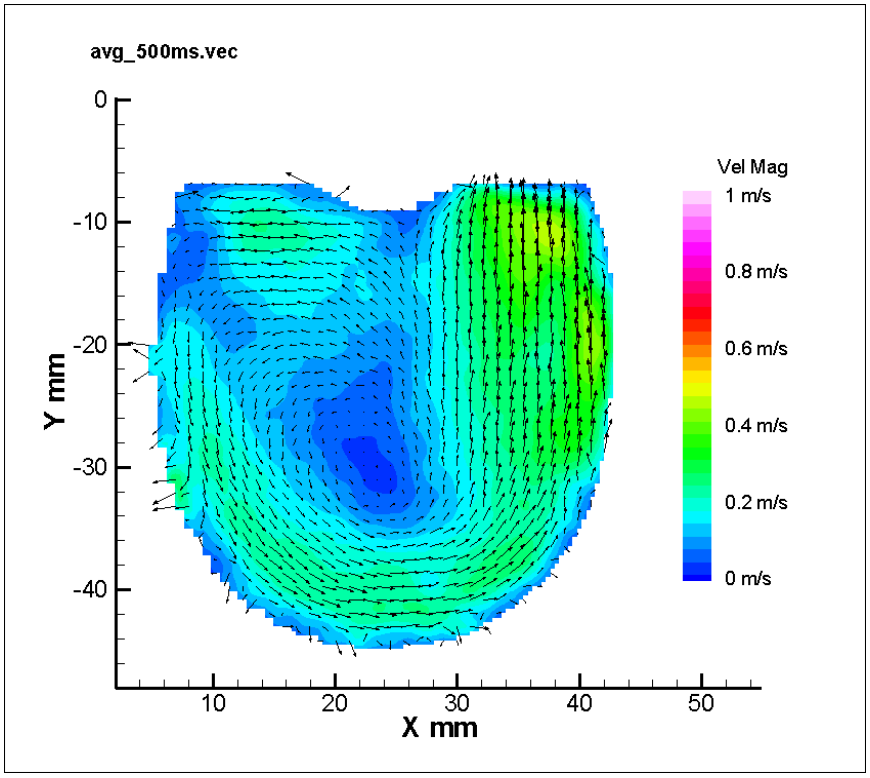
avg_500ms.vec
0
-10
-20
-30
-40
Y mm
10
20
30
40
50
X mm
Vel Mag
1 m/s
0.8 m/s
0.6 m/s
0.4 m/s
0.2 m/s
0 m/s

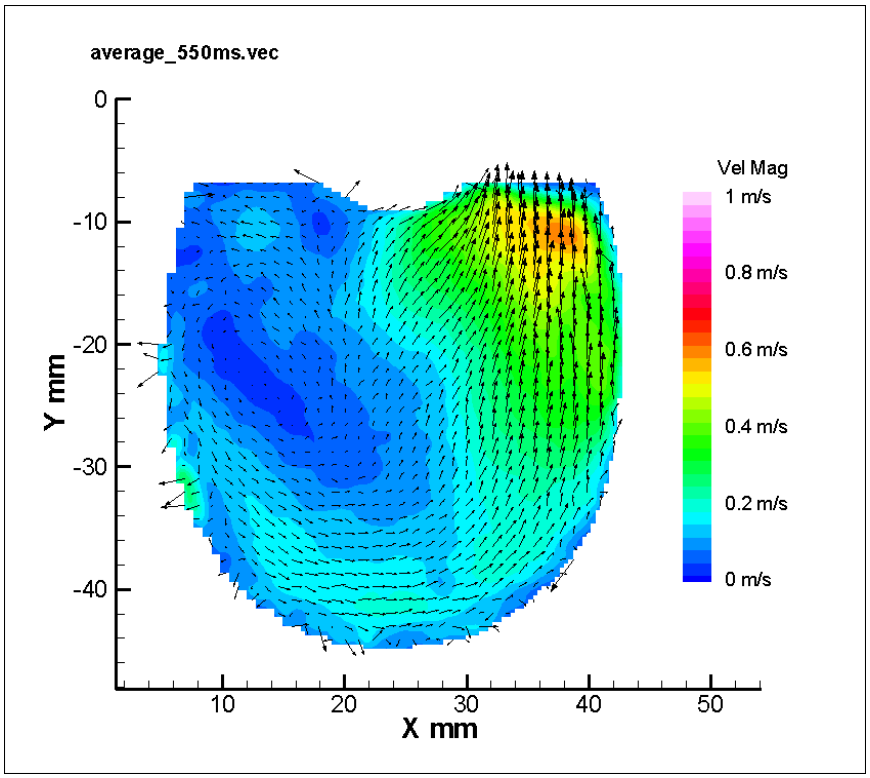
average_550ms.vec
0
-10
-20
-30
-40
Y mm
10
20
30
40
50
X mm
Vel Mag
1 m/s
0.8 m/s
0.6 m/s
0.4 m/s
0.2 m/s
0 m/s

Appendix B 40% HEMATOCRIT

Appendix B-1. 6.5 mm Parallel Plane

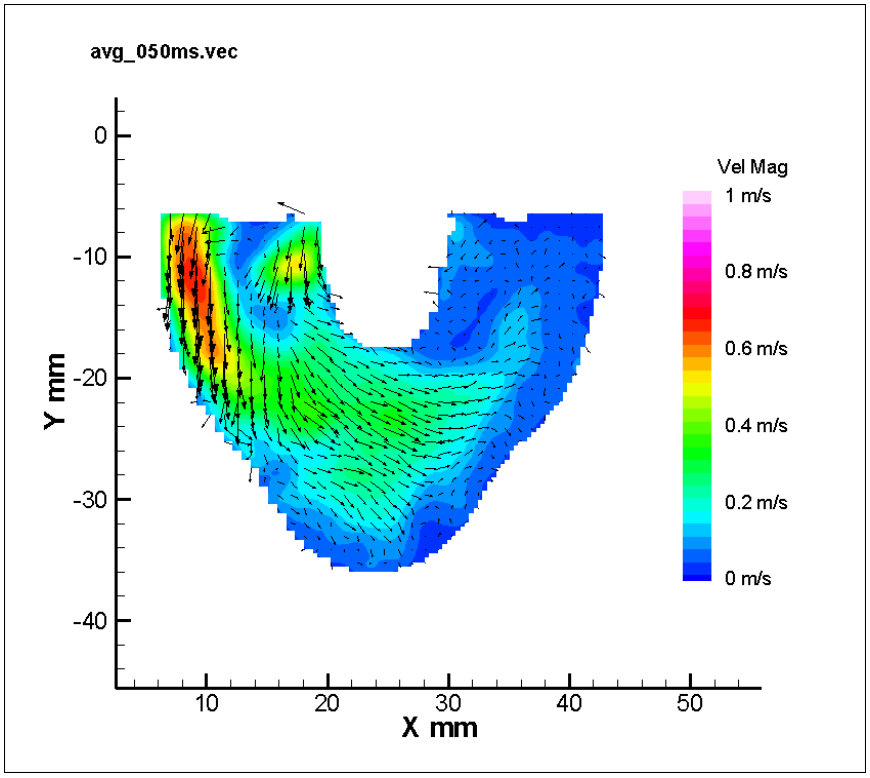

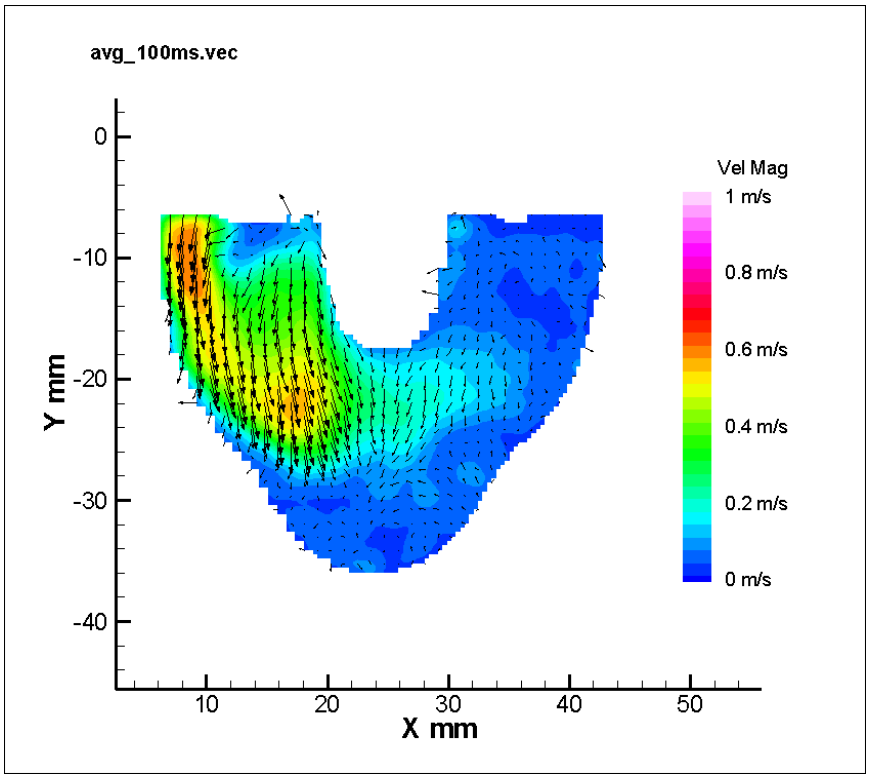

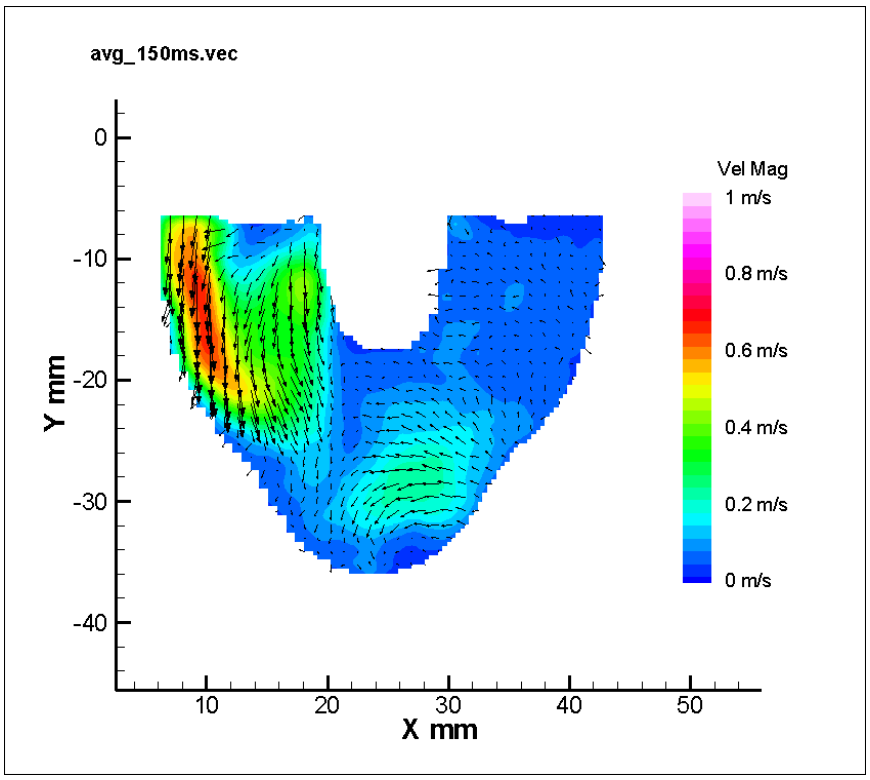
avg_150ms.vec
0
-10
-20
-30
-40
Y mm
10
20
30
40
50
X mm
Vel Mag
1 m/s
0.8 m/s
0.6 m/s
0.4 m/s
0.2 m/s
0 m/s

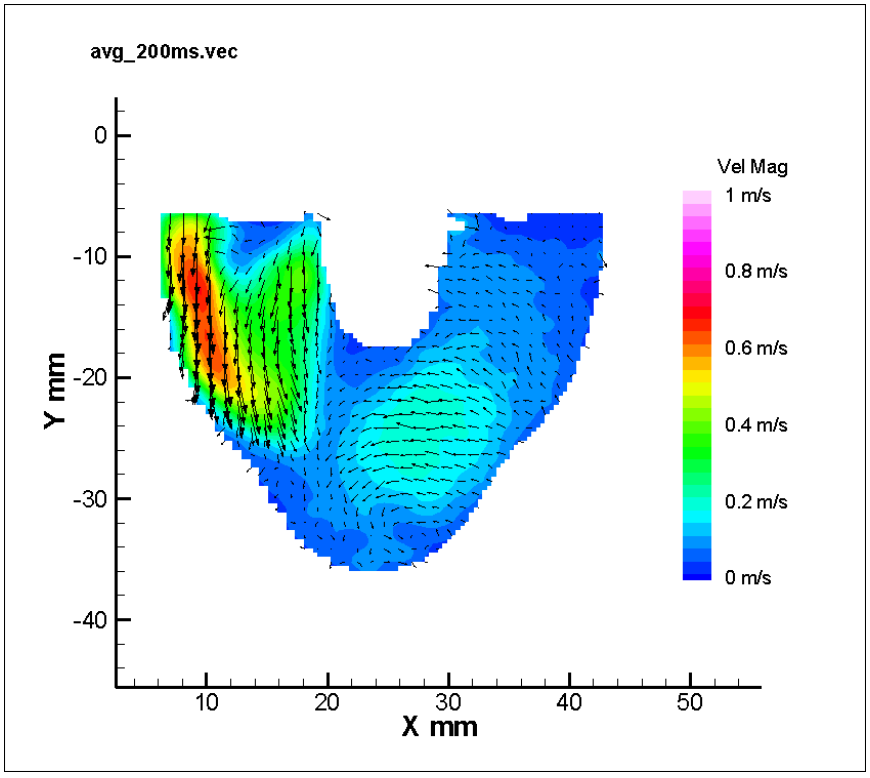
avg_200ms.vec
0
-10
-20
-30
-40
Y mm
10
20
30
40
50
X mm
Vel Mag
1 m/s
0.8 m/s
0.6 m/s
0.4 m/s
0.2 m/s
0 m/s

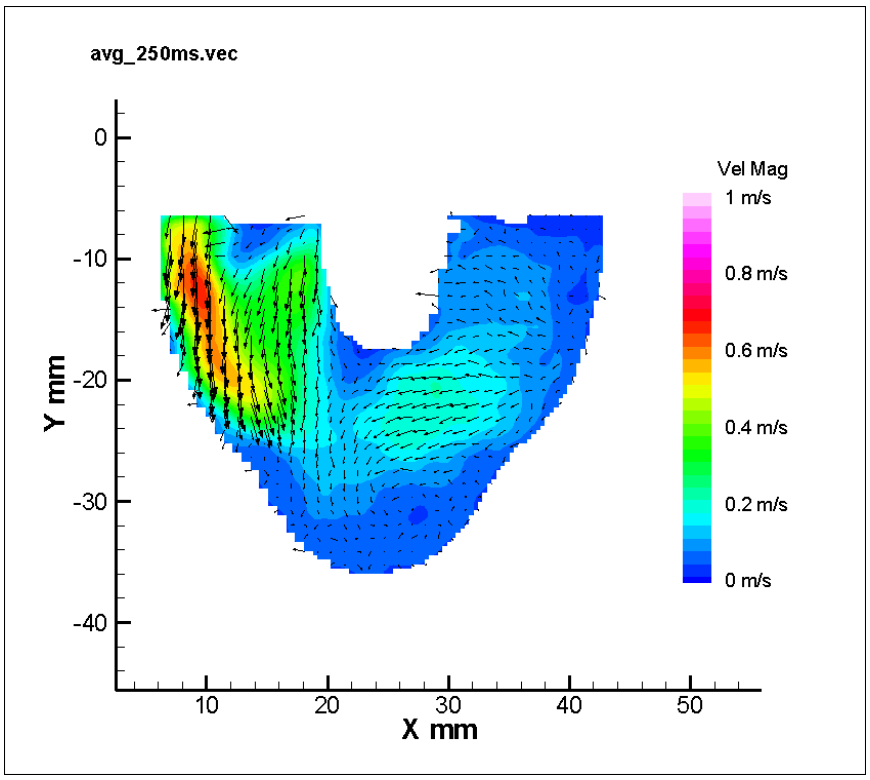
avg_250ms.vec
0
-10
-20
-30
-40
Y mm
10
20
30
40
50
X mm
Vel Mag
1 m/s
0.8 m/s
0.6 m/s
0.4 m/s
0.2 m/s
0 m/s

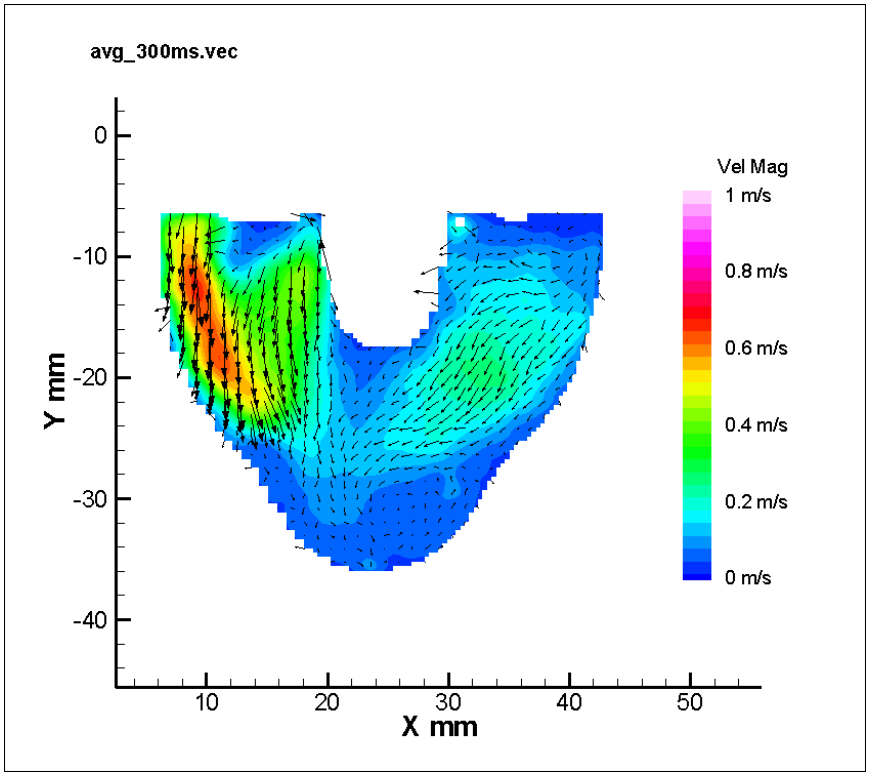
avg_300ms.vec
0
-10
-20
-30
-40
Y mm
10
20
30
40
50
X mm
Vel Mag
1 m/s
0.8 m/s
0.6 m/s
0.4 m/s
0.2 m/s
0 m/s

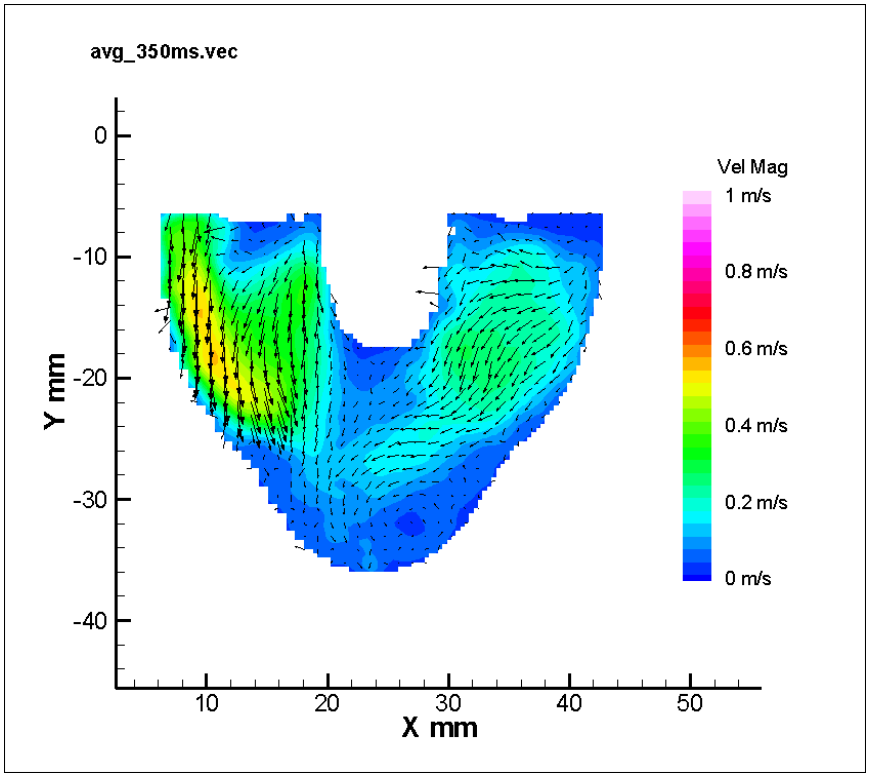
avg_350ms.vec
0
-10
-20
-30
-40
Y mm
10
20
30
40
50
X mm
Vel Mag
1 m/s
0.8 m/s
0.6 m/s
0.4 m/s
0.2 m/s
0 m/s

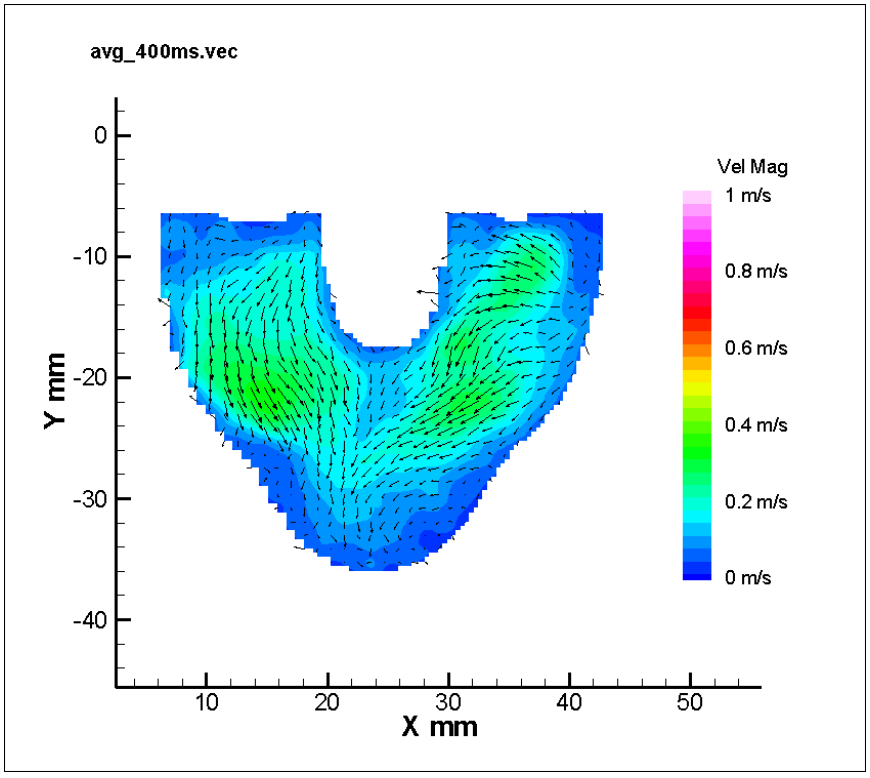
avg_400ms.vec
0
-10
-20
-30
-40
Y mm
10
20
30
40
50
X mm
Vel Mag
1 m/s
0.8 m/s
0.6 m/s
0.4 m/s
0.2 m/s
0 m/s

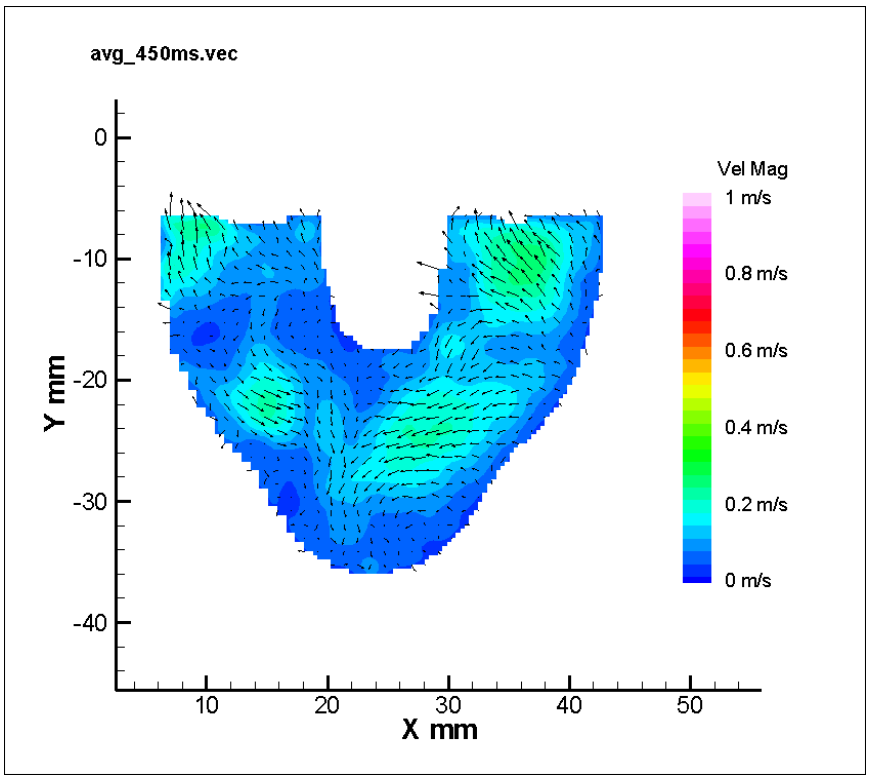
avg_450ms.vec
0
-10
-20
-30
-40
Y mm
10
20
30
40
50
X mm
Vel Mag
1 m/s
0.8 m/s
0.6 m/s
0.4 m/s
0.2 m/s
0 m/s

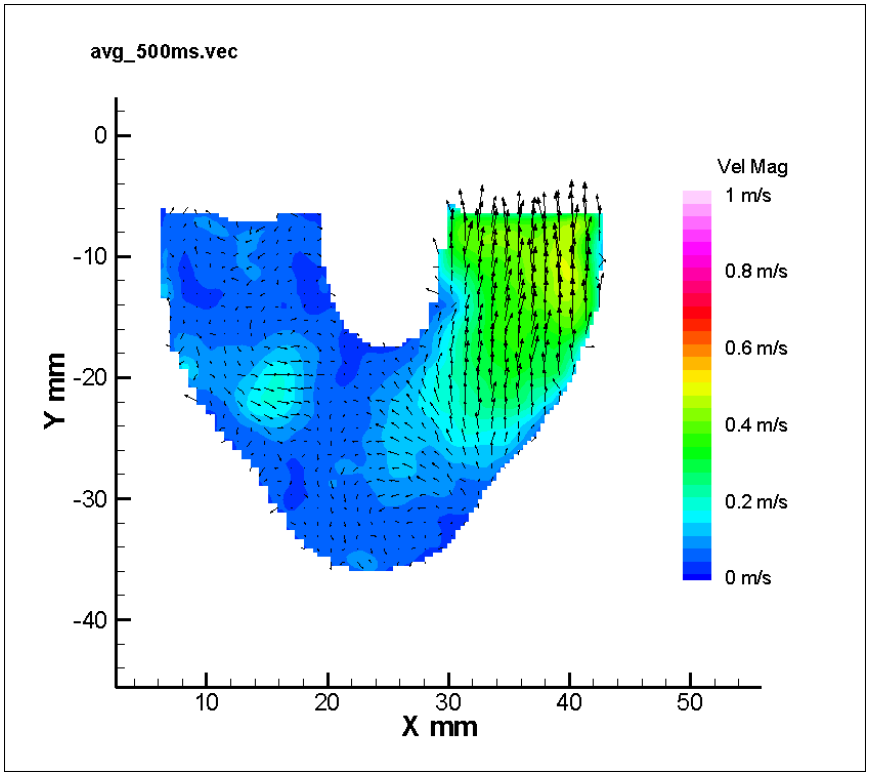
avg_500ms.vec
0
-10
-20
-30
-40
Y mm
10
20
30
40
50
X mm
Vel Mag
1 m/s
0.8 m/s
0.6 m/s
0.4 m/s
0.2 m/s
0 m/s

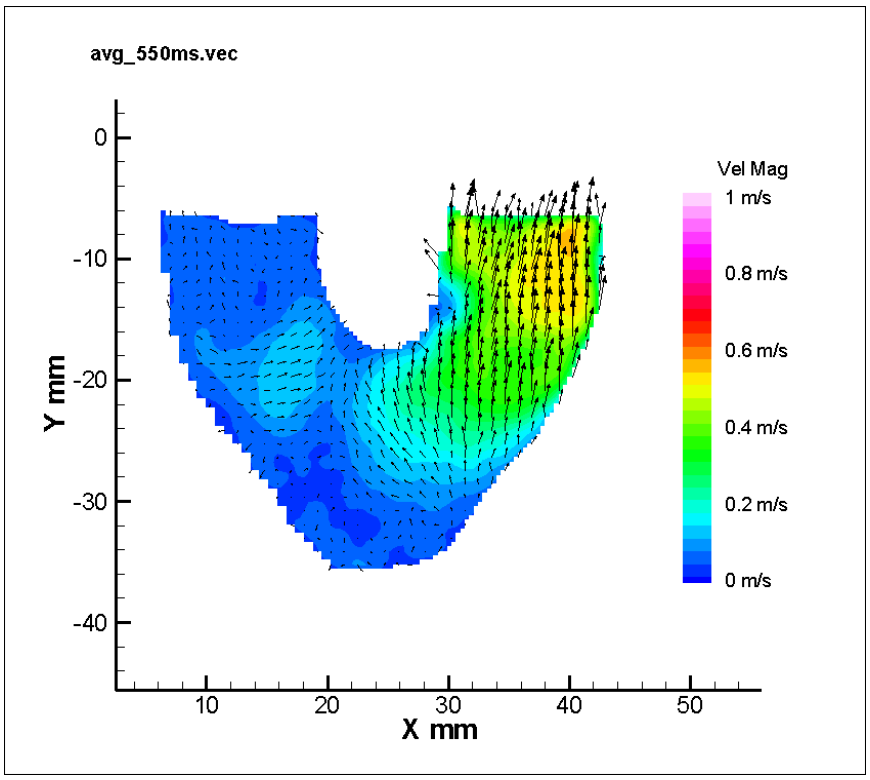
avg_550ms.vec
0
-10
-20
-30
-40
Y mm
10
20
30
40
50
X mm
Vel Mag
1 m/s
0.8 m/s
0.6 m/s
0.4 m/s
0.2 m/s
0 m/s

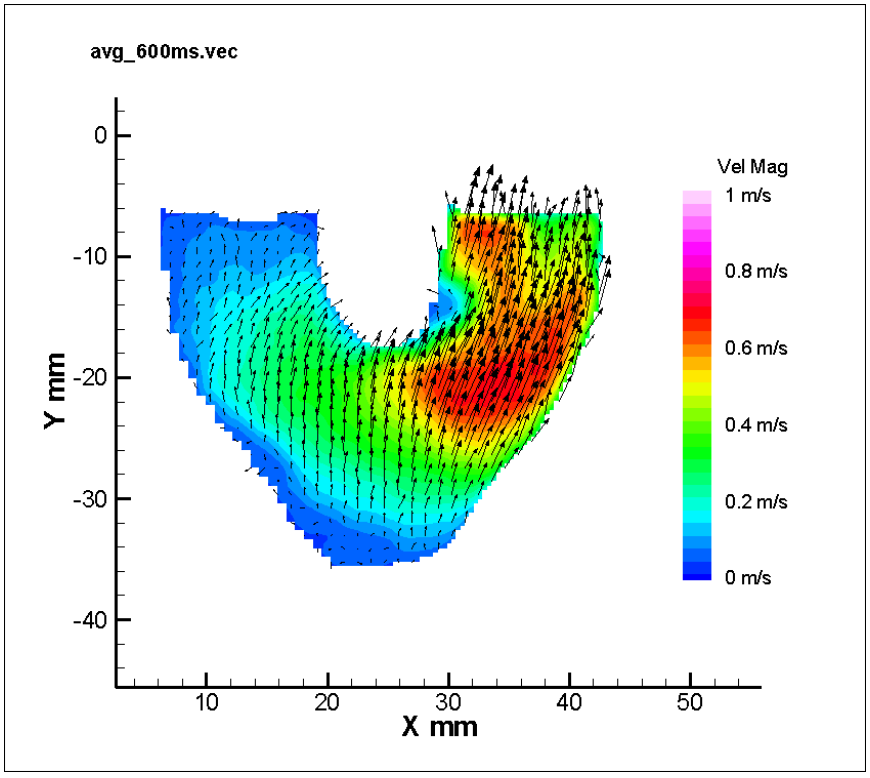
avg_600ms.vec
0
-10
-20
-30
-40
Y mm
10
20
30
40
50
X mm
Vel Mag
1 m/s
0.8 m/s
0.6 m/s
0.4 m/s
0.2 m/s
0 m/s

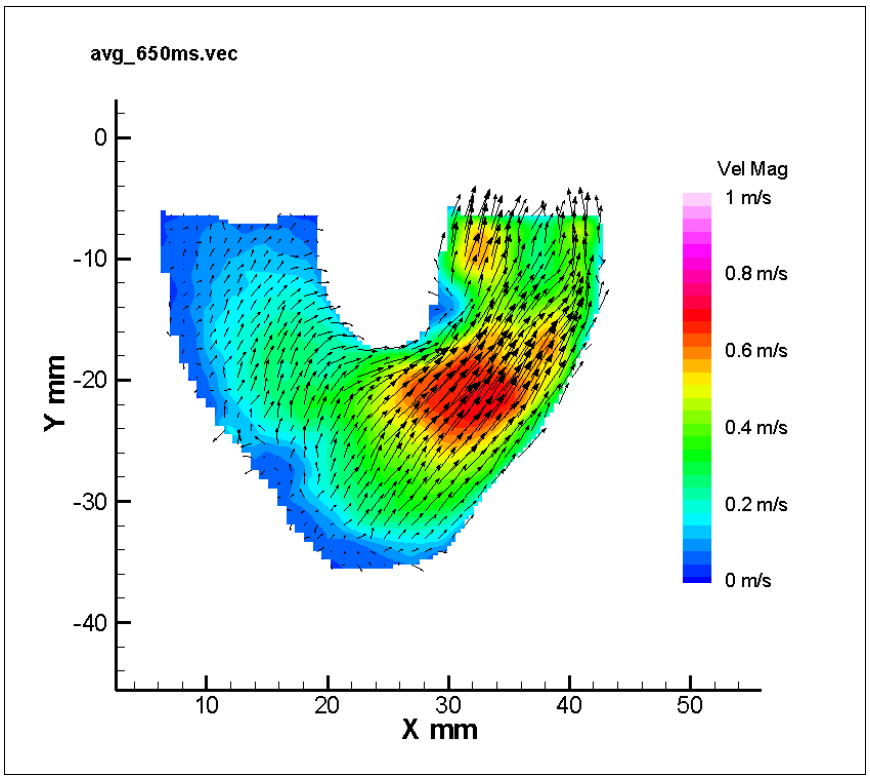
avg_650ms.vec
0
-10
-20
-30
-40
Y mm
10
20
30
40
50
X mm
Vel Mag
1 m/s
0.8 m/s
0.6 m/s
0.4 m/s
0.2 m/s
0 m/s

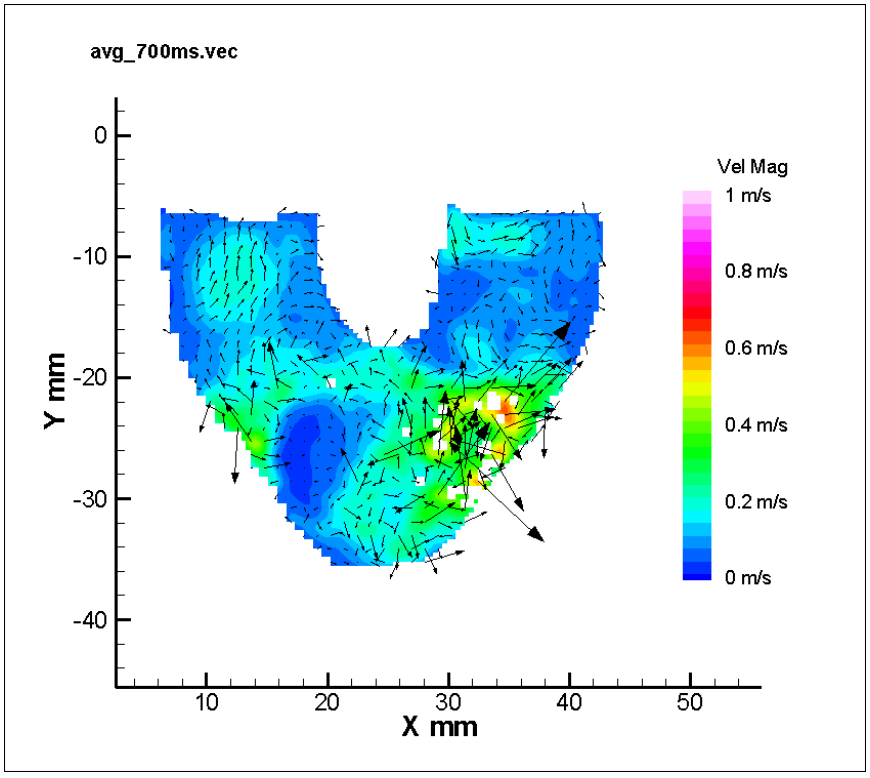
avg_700ms.vec
0
-10
-20
-30
-40
Y mm
10
20
30
40
50
X mm
Vel Mag
1 m/s
0.8 m/s
0.6 m/s
0.4 m/s
0.2 m/s
0 m/s

Appendix B-2. 7 mm Parallel Plane

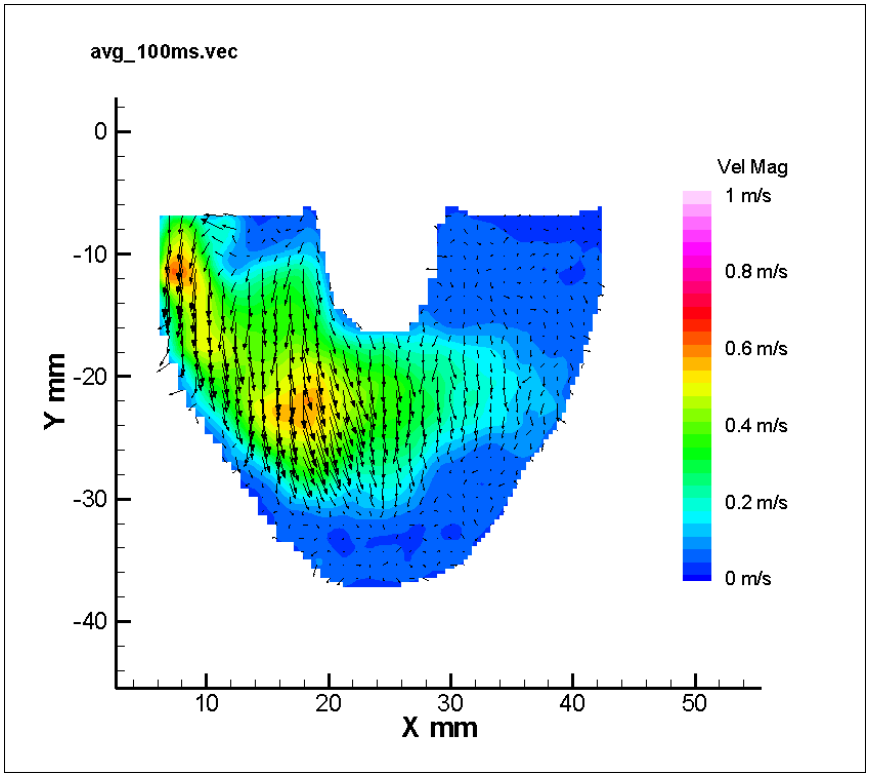

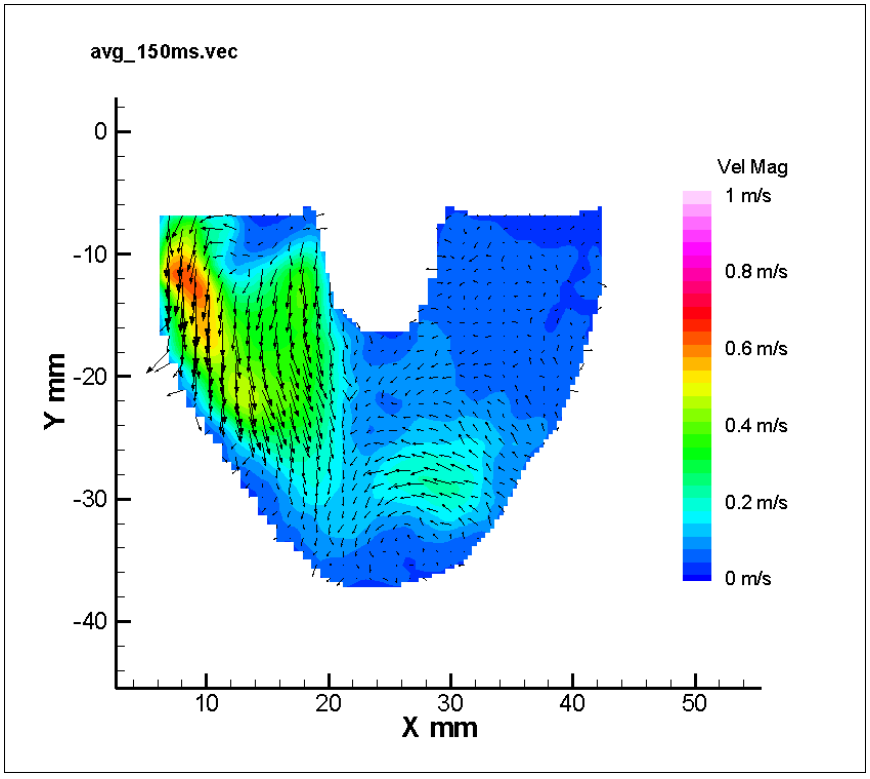

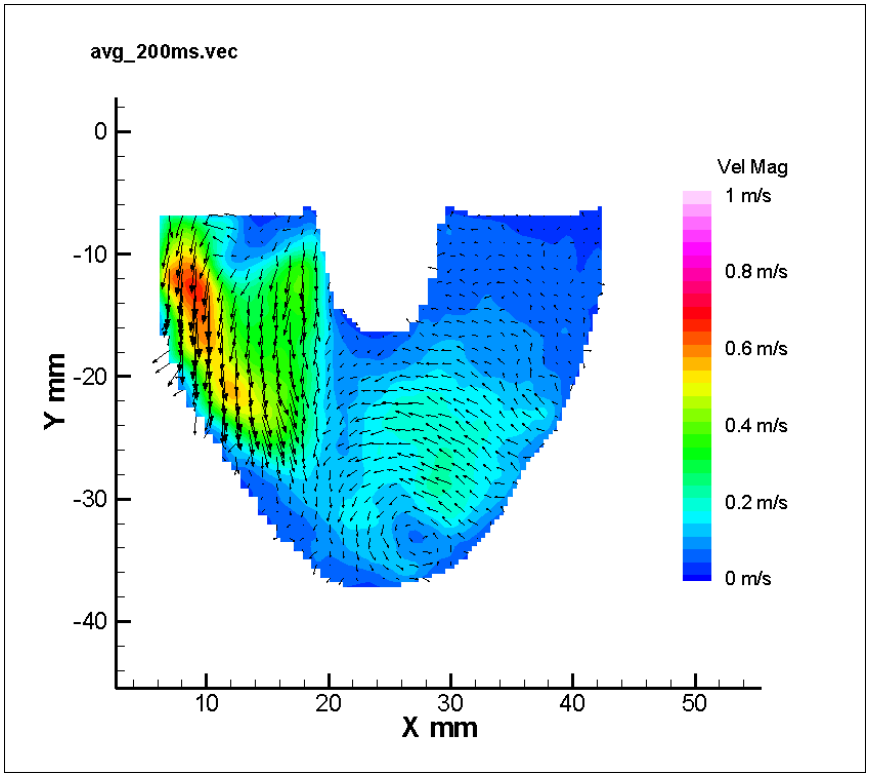
avg_200ms.vec
0
-10
-20
-30
-40
Y mm
10
20
30
40
50
X mm
Vel Mag
1 m/s
0.8 m/s
0.6 m/s
0.4 m/s
0.2 m/s
0 m/s

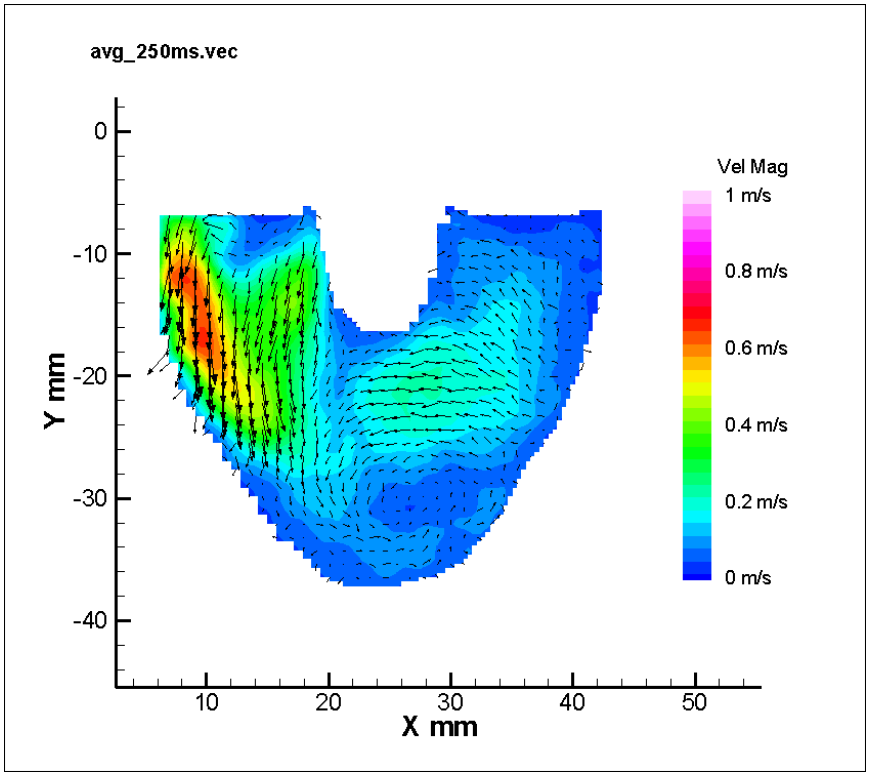
avg_250ms.vec
0
-10
-20
-30
-40
Y mm
10
20
30
40
50
X mm
Vel Mag
1 m/s
0.8 m/s
0.6 m/s
0.4 m/s
0.2 m/s
0 m/s

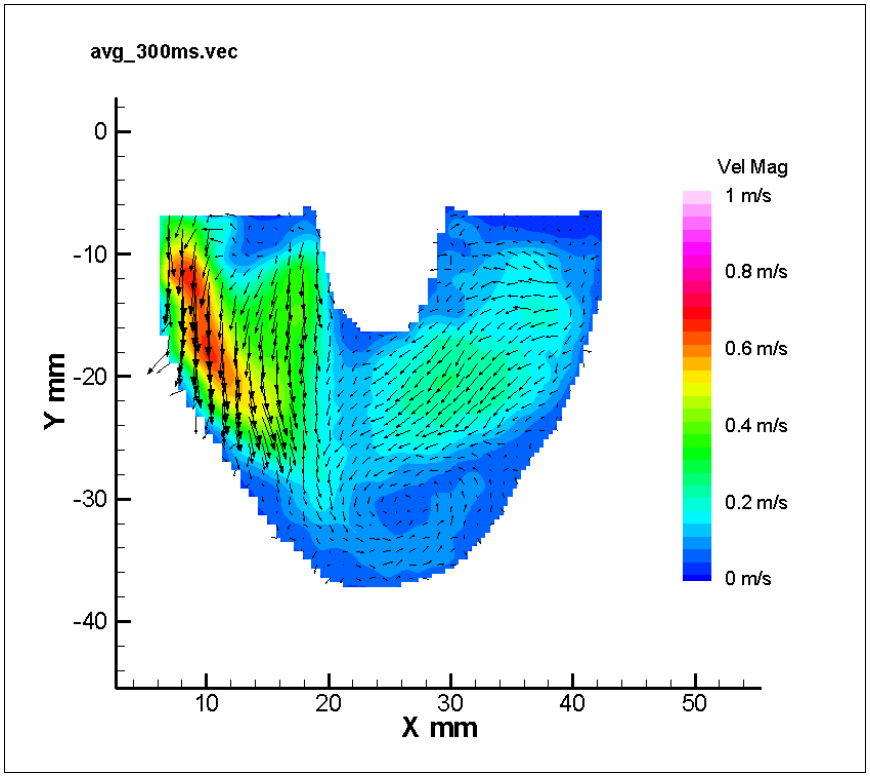
avg_300ms.vec
0
-10
-20
-30
-40
Y mm
10
20
30
40
50
X mm
Vel Mag
1 m/s
0.8 m/s
0.6 m/s
0.4 m/s
0.2 m/s
0 m/s

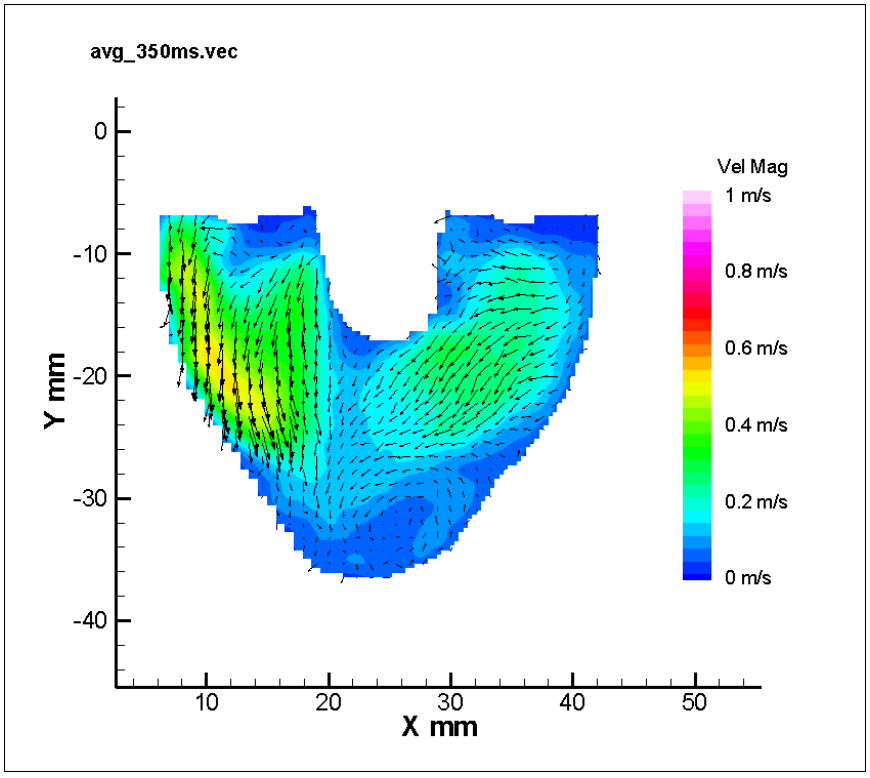
avg_350ms.vec
0
-10
-20
-30
-40
Y mm
10
20
30
40
50
X mm
Vel Mag
1 m/s
0.8 m/s
0.6 m/s
0.4 m/s
0.2 m/s
0 m/s

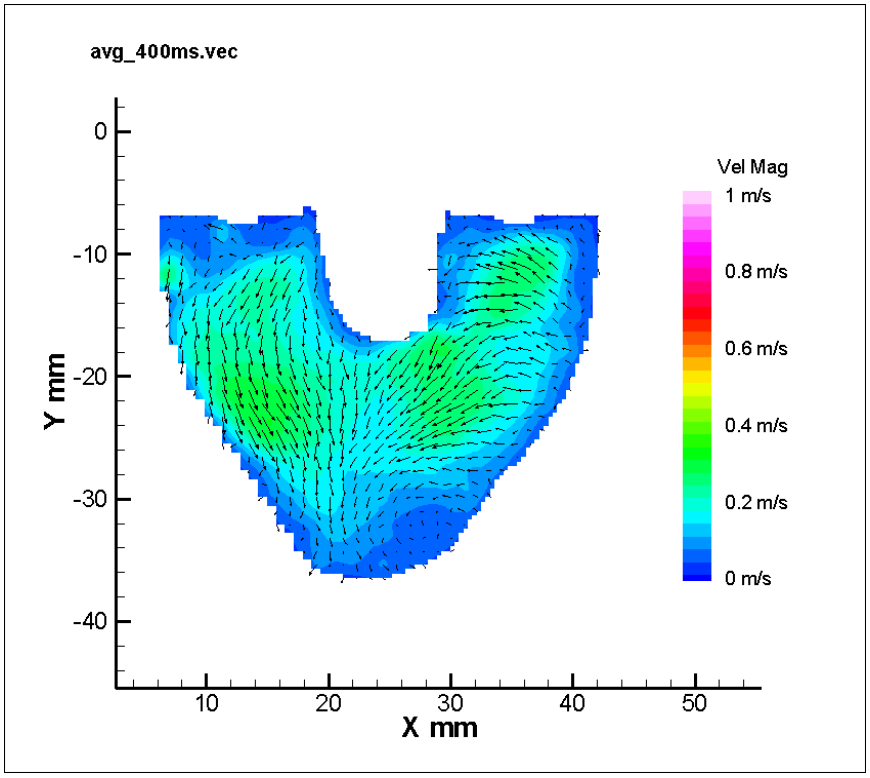
avg_400ms.vec
0
-10
-20
-30
-40
Y mm
10
20
30
40
50
X mm
Vel Mag
1 m/s
0.8 m/s
0.6 m/s
0.4 m/s
0.2 m/s
0 m/s

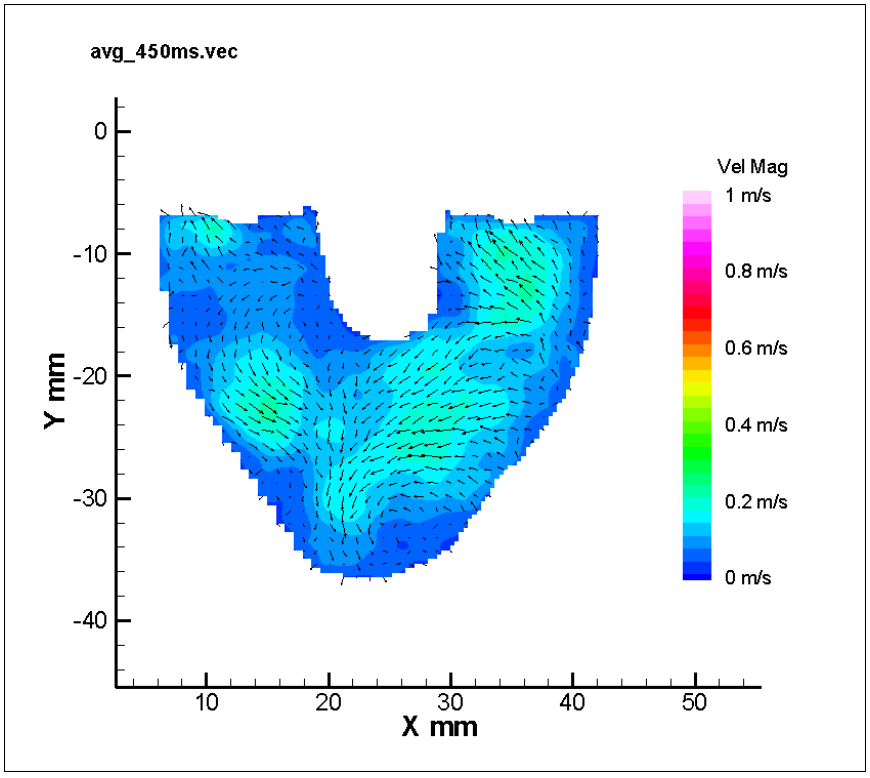
avg_450ms.vec
0
-10
-20
-30
-40
Y mm
10
20
30
40
50
X mm
Vel Mag
1 m/s
0.8 m/s
0.6 m/s
0.4 m/s
0.2 m/s
0 m/s

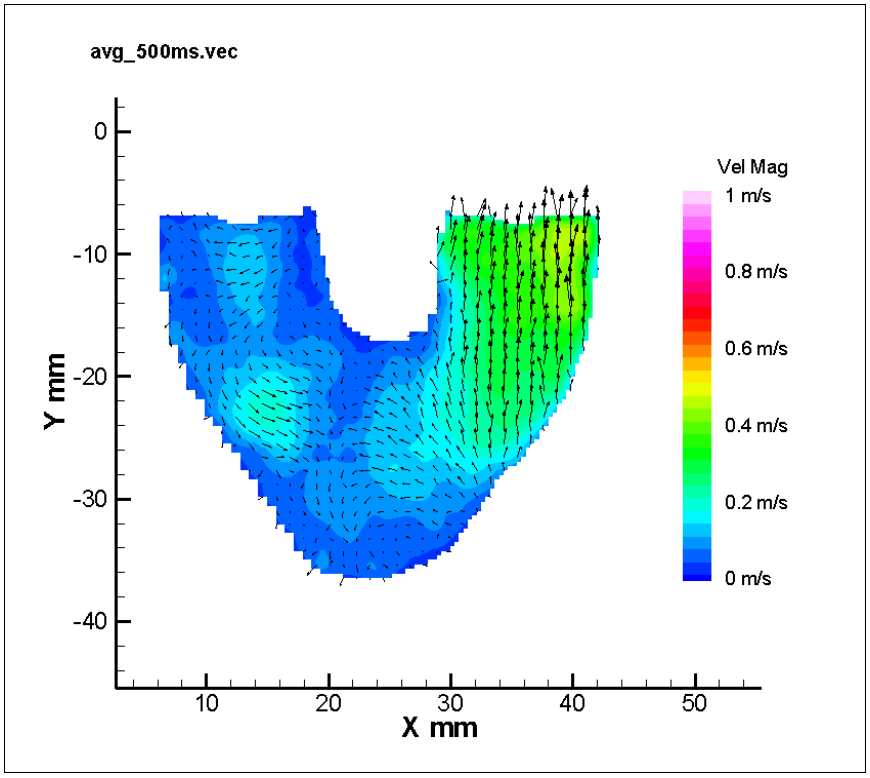
avg_500ms.vec
0
-10
-20
-30
-40
Y mm
10
20
30
40
50
X mm
Vel Mag
1 m/s
0.8 m/s
0.6 m/s
0.4 m/s
0.2 m/s
0 m/s

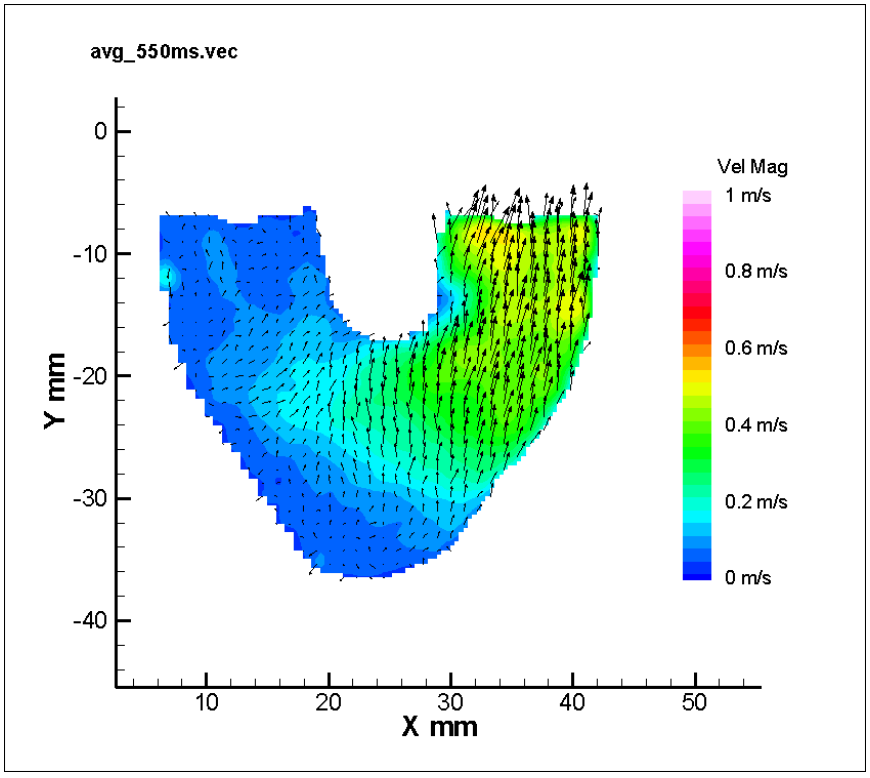
avg_550ms.vec
0
-10
-20
-30
-40
Y mm
10
20
30
40
50
X mm
Vel Mag
1 m/s
0.8 m/s
0.6 m/s
0.4 m/s
0.2 m/s
0 m/s

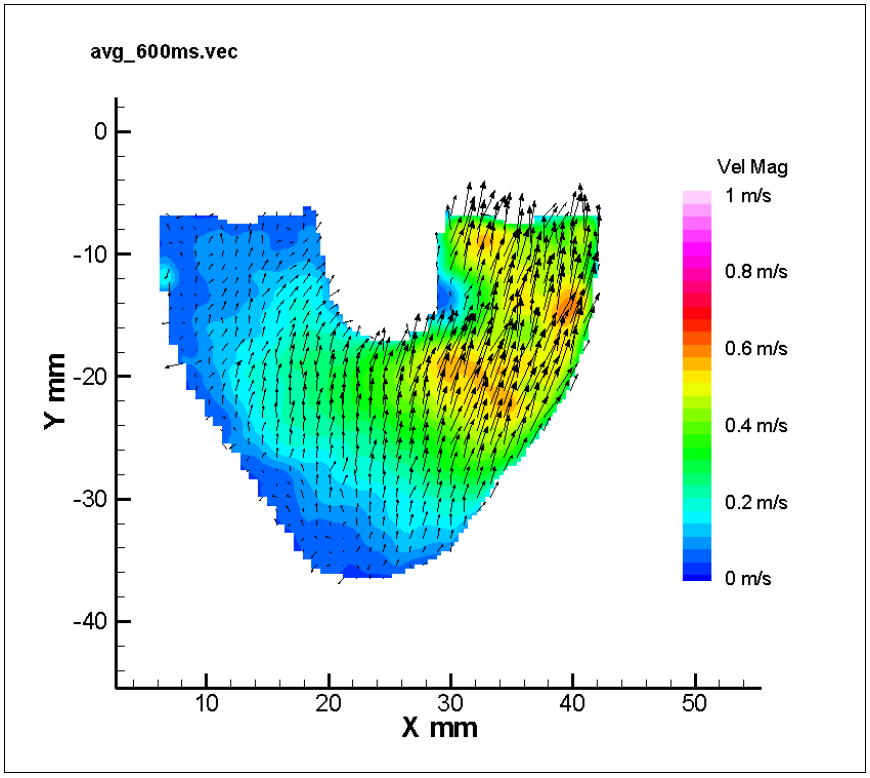
avg_600ms.vec
0
-10
-20
-30
-40
Y mm
10
20
30
40
50
X mm
Vel Mag
1 m/s
0.8 m/s
0.6 m/s
0.4 m/s
0.2 m/s
0 m/s

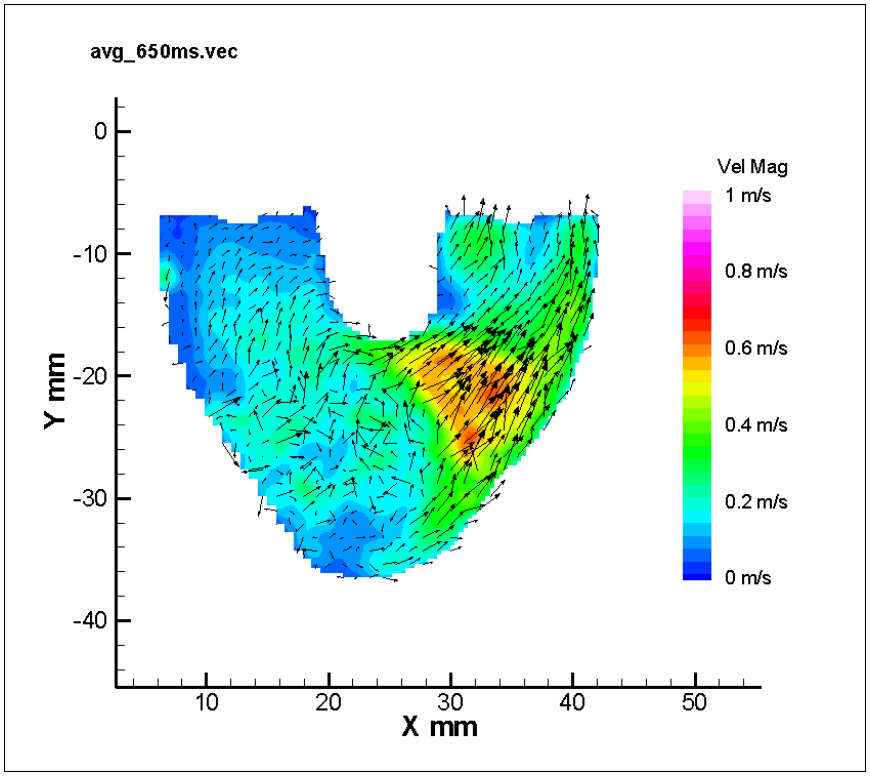
avg_650ms.vec
0
-10
-20
-30
-40
Y mm
10
20
30
40
50
X mm
Vel Mag
1 m/s
0.8 m/s
0.6 m/s
0.4 m/s
0.2 m/s
0 m/s

Appendix B-3. 8.2 mm Parallel Plane

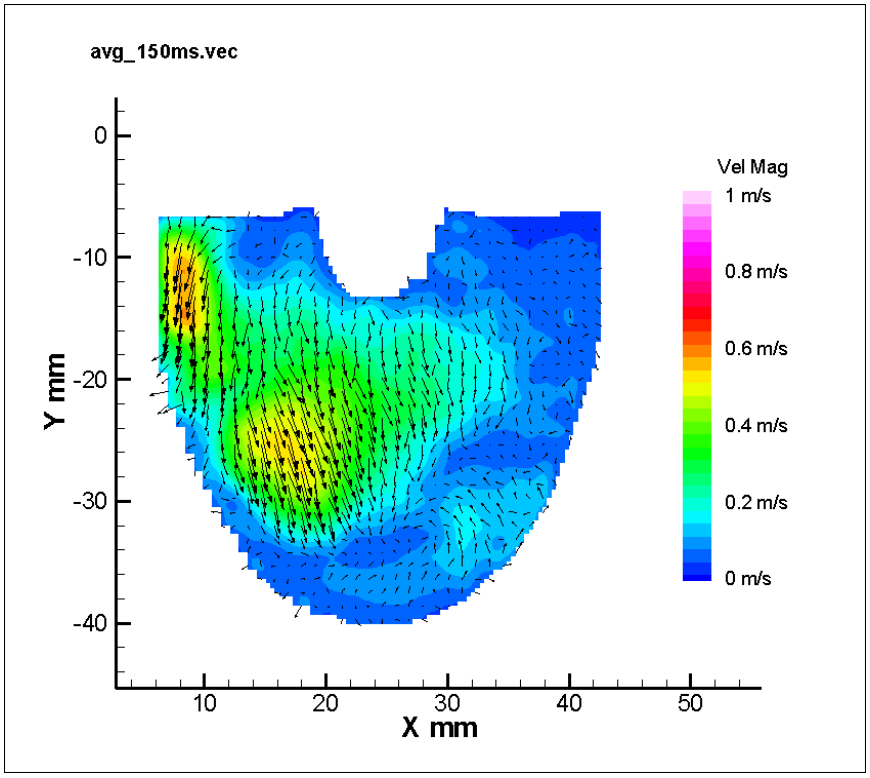

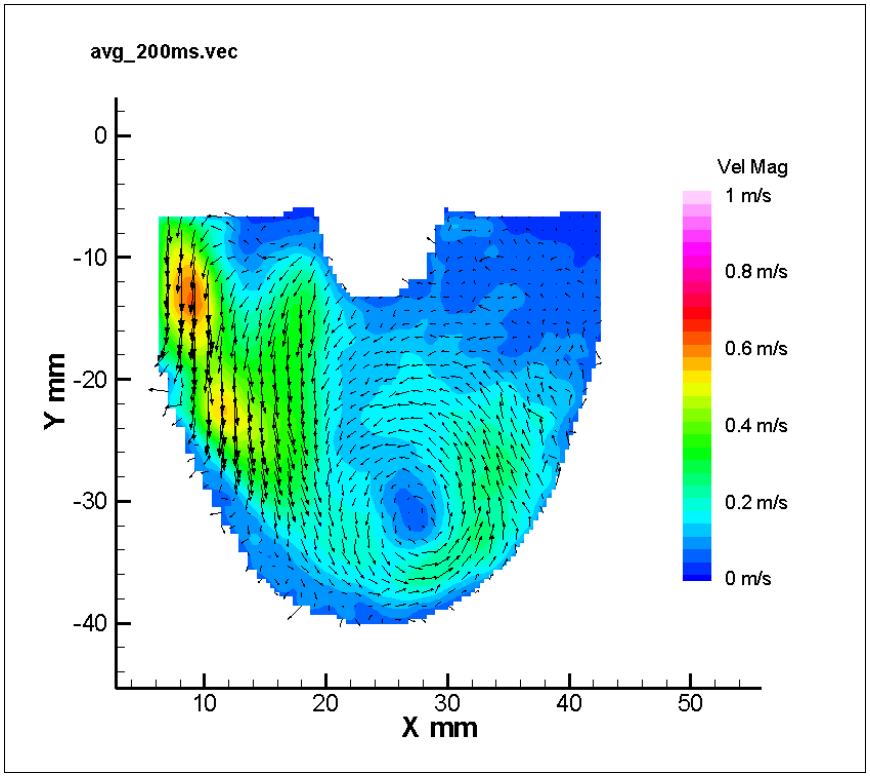

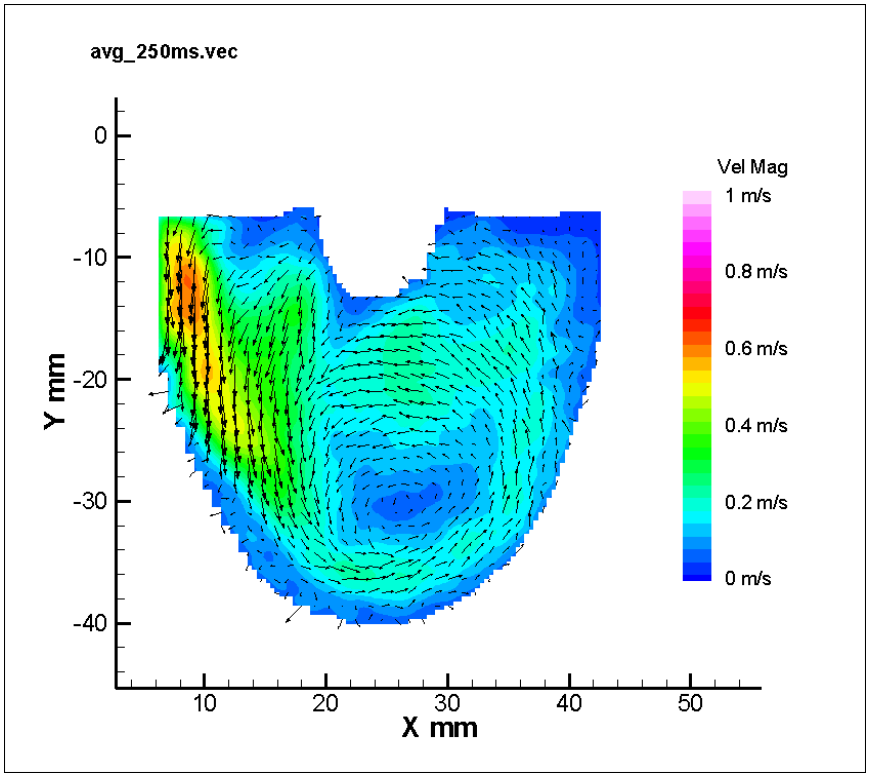
avg_250ms.vec
0
-10
-20
-30
-40
Y mm
10
20
30
40
50
X mm
Vel Mag
1 m/s
0.8 m/s
0.6 m/s
0.4 m/s
0.2 m/s
0 m/s

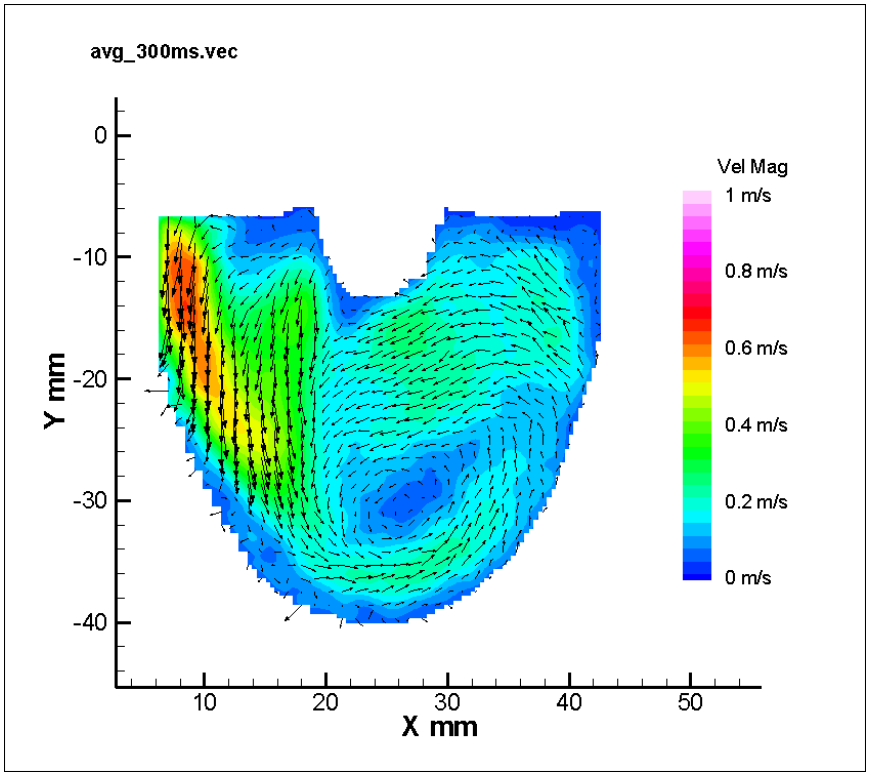
avg_300ms.vec
0
-10
-20
-30
-40
Y mm
10
20
30
40
50
X mm
Vel Mag
1 m/s
0.8 m/s
0.6 m/s
0.4 m/s
0.2 m/s
0 m/s

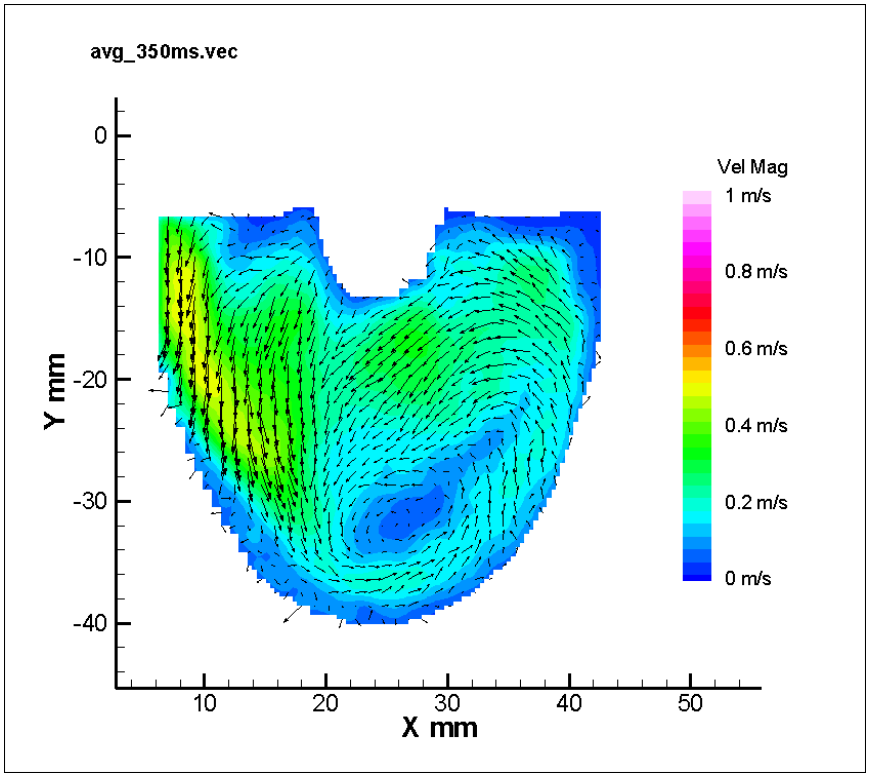
avg_350ms.vec
0
-10
-20
-30
-40
Y mm
10
20
30
40
50
X mm
Vel Mag
1 m/s
0.8 m/s
0.6 m/s
0.4 m/s
0.2 m/s
0 m/s

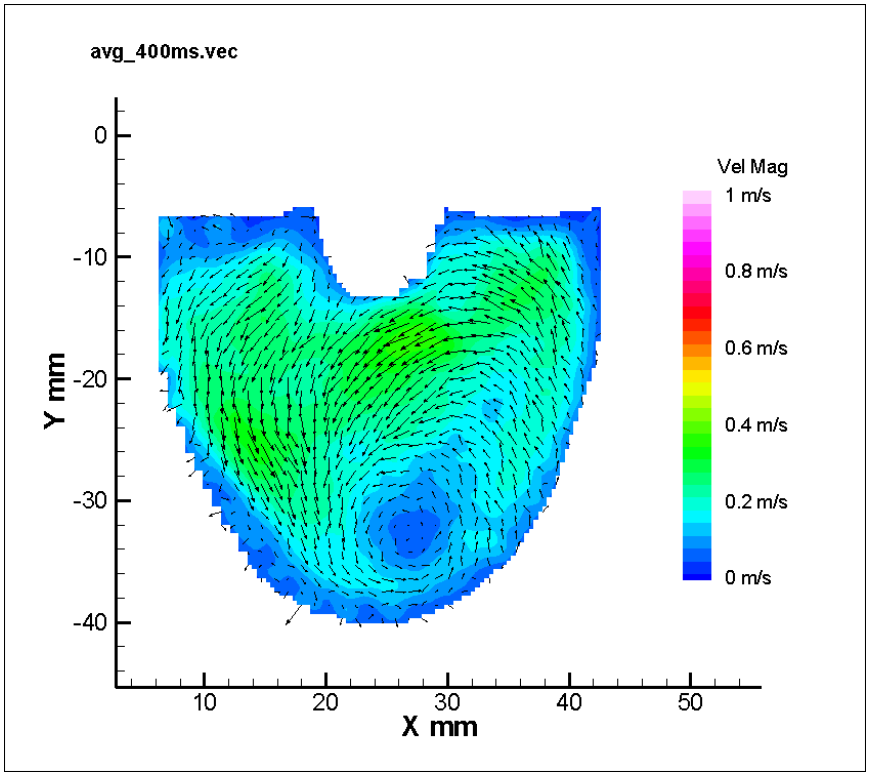
avg_400ms.vec
0
-10
-20
-30
-40
Y mm
10
20
30
40
50
X mm
Vel Mag
1 m/s
0.8 m/s
0.6 m/s
0.4 m/s
0.2 m/s
0 m/s

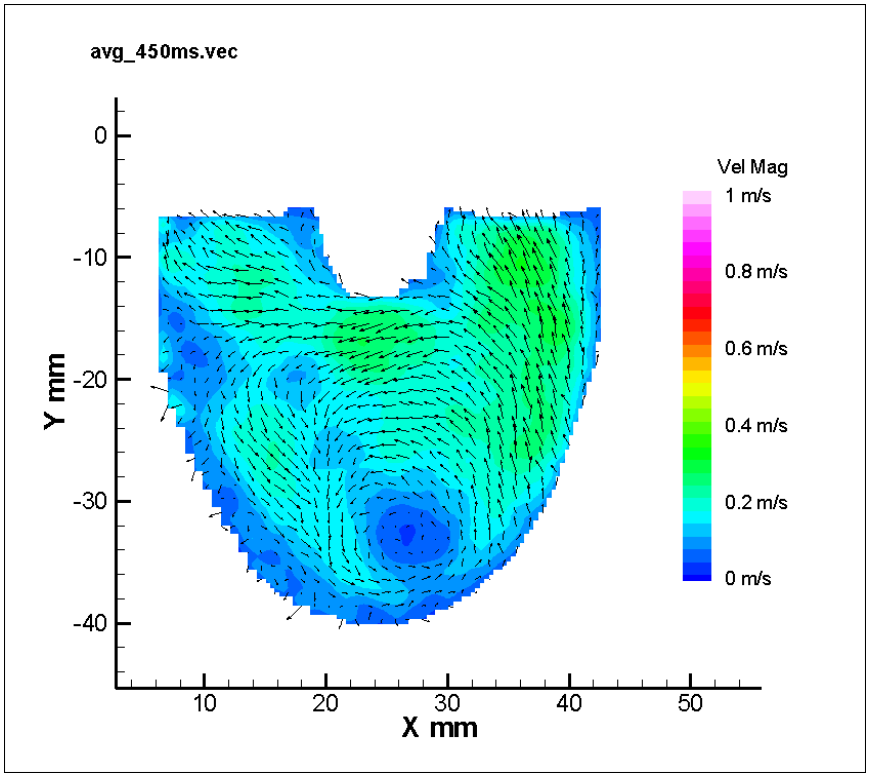
avg_450ms.vec
0
-10
-20
-30
-40
Y mm
10
20
30
40
50
X mm
Vel Mag
1 m/s
0.8 m/s
0.6 m/s
0.4 m/s
0.2 m/s
0 m/s

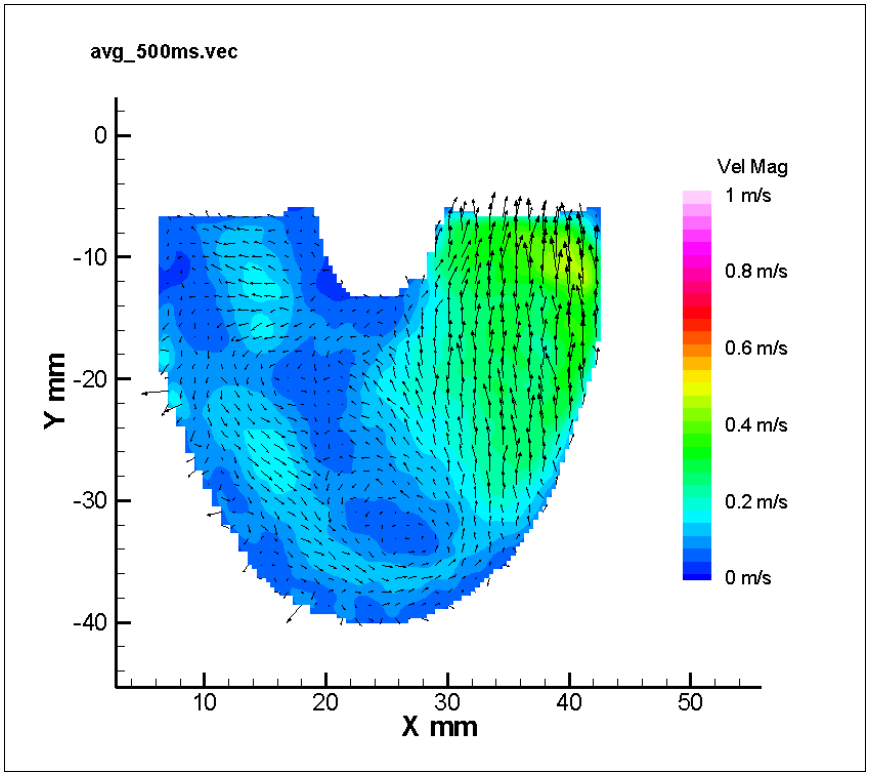
avg_500ms.vec
0
-10
-20
-30
-40
Y mm
10
20
30
40
50
X mm
Vel Mag
1 m/s
0.8 m/s
0.6 m/s
0.4 m/s
0.2 m/s
0 m/s

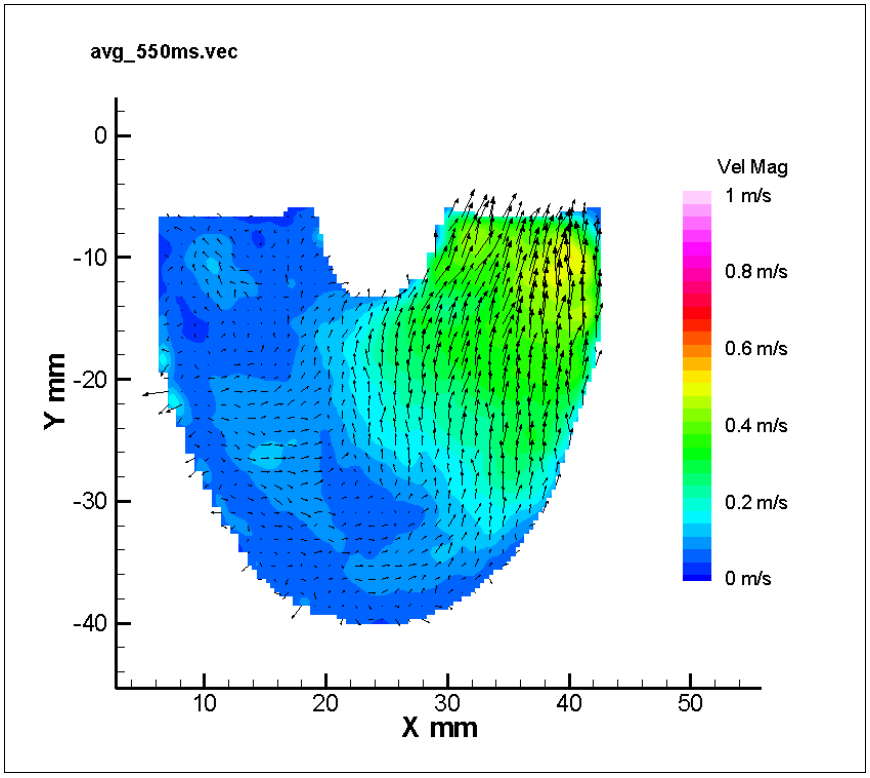
avg_550ms.vec
0
-10
-20
-30
-40
Y mm
10
20
30
40
50
X mm
Vel Mag
1 m/s
0.8 m/s
0.6 m/s
0.4 m/s
0.2 m/s
0 m/s

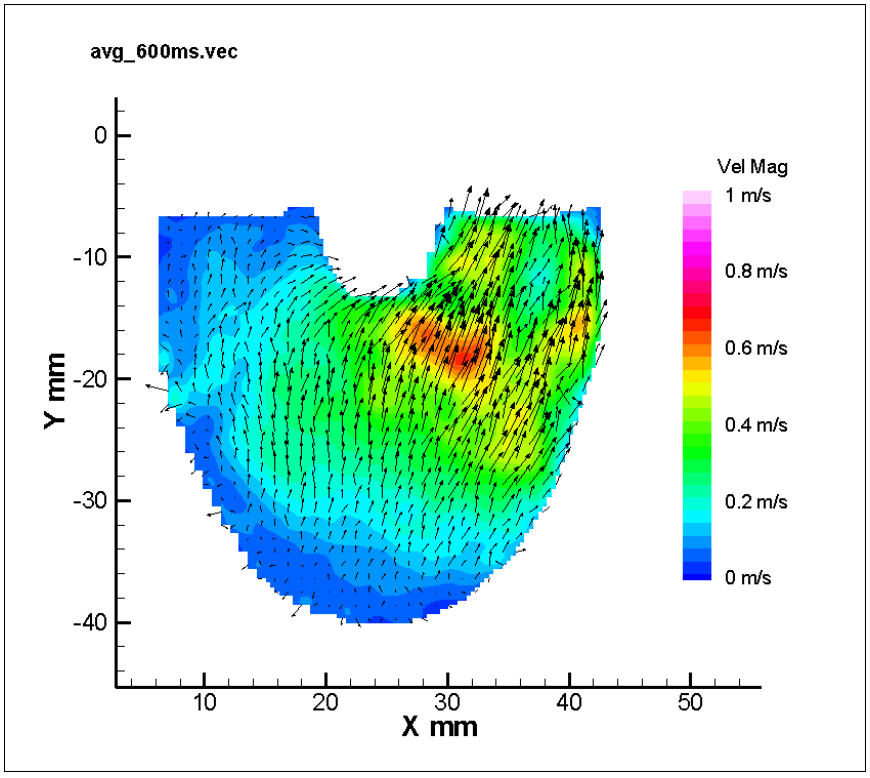
avg_600ms.vec
0
-10
-20
-30
-40
Y mm
10
20
30
40
50
X mm
Vel Mag
1 m/s
0.8 m/s
0.6 m/s
0.4 m/s
0.2 m/s
0 m/s

Appendix B-4. 11 mm Parallel Plane

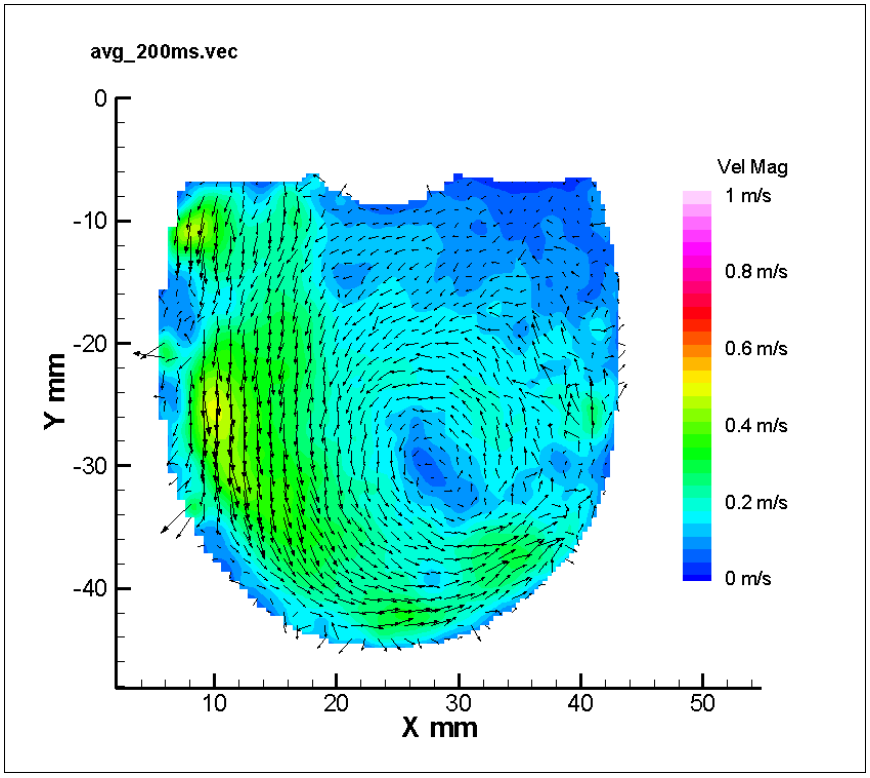

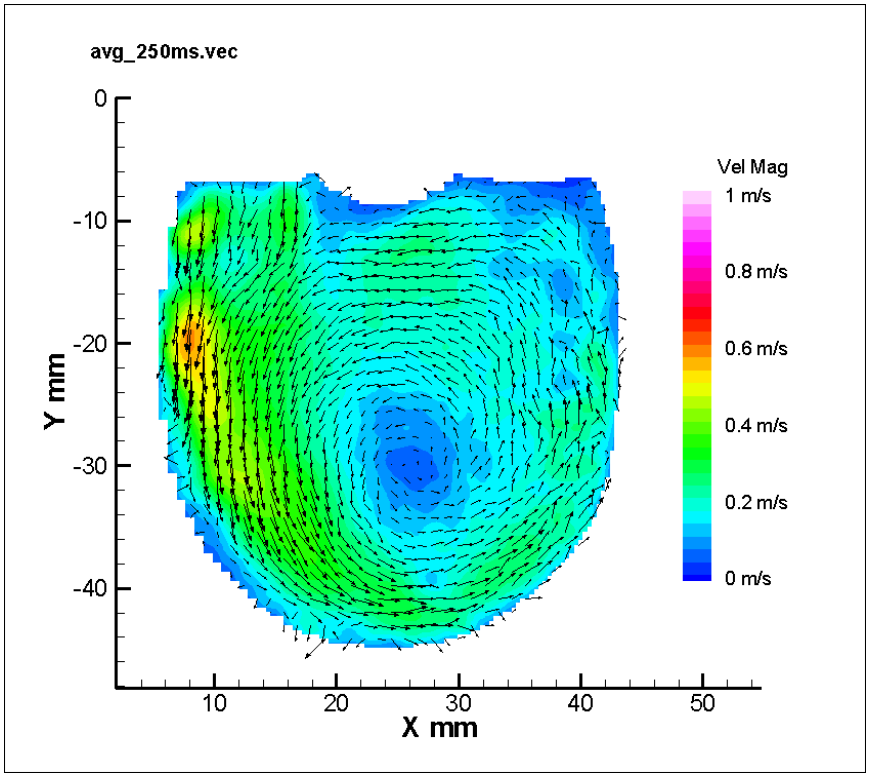

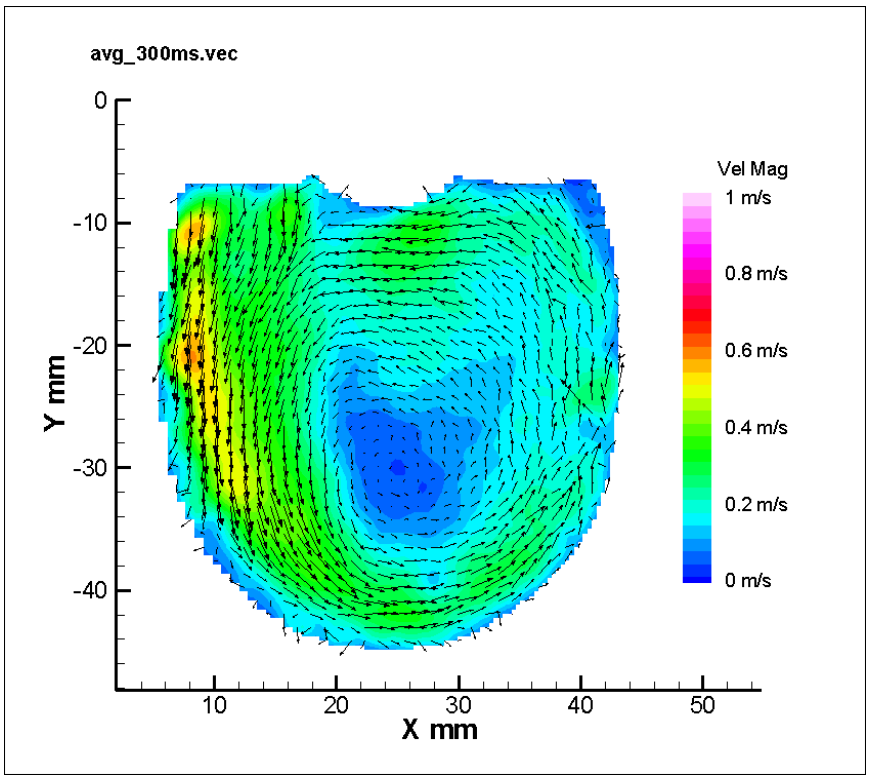
avg_300ms.vec
0
-10
-20
-30
-40
Y mm
10
20
30
40
50
X mm
Vel Mag
1 m/s
0.8 m/s
0.6 m/s
0.4 m/s
0.2 m/s
0 m/s

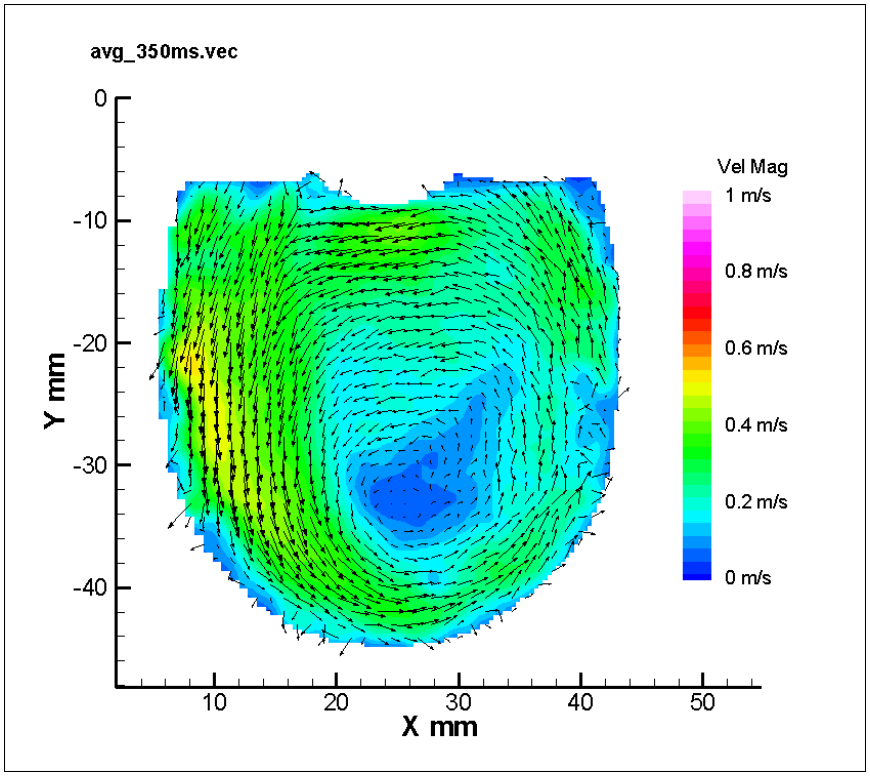
avg_350ms.vec
0
-10
-20
-30
-40
Y mm
10
20
30
40
50
X mm
Vel Mag
1 m/s
0.8 m/s
0.6 m/s
0.4 m/s
0.2 m/s
0 m/s

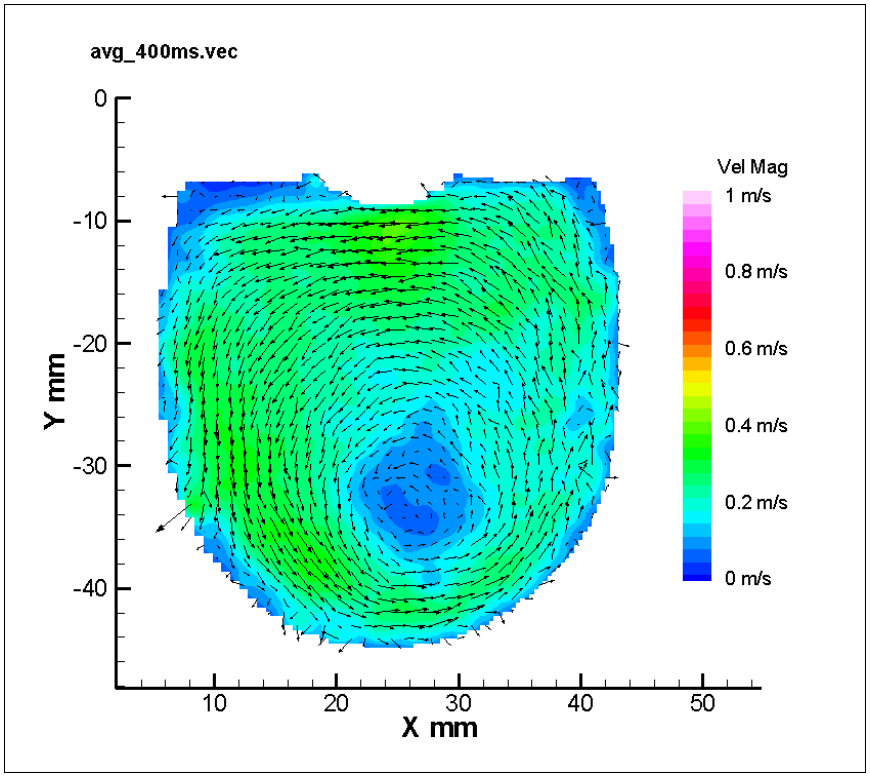
avg_400ms.vec
0
-10
-20
-30
-40
Y mm
10
20
30
40
50
X mm
Vel Mag
1 m/s
0.8 m/s
0.6 m/s
0.4 m/s
0.2 m/s
0 m/s

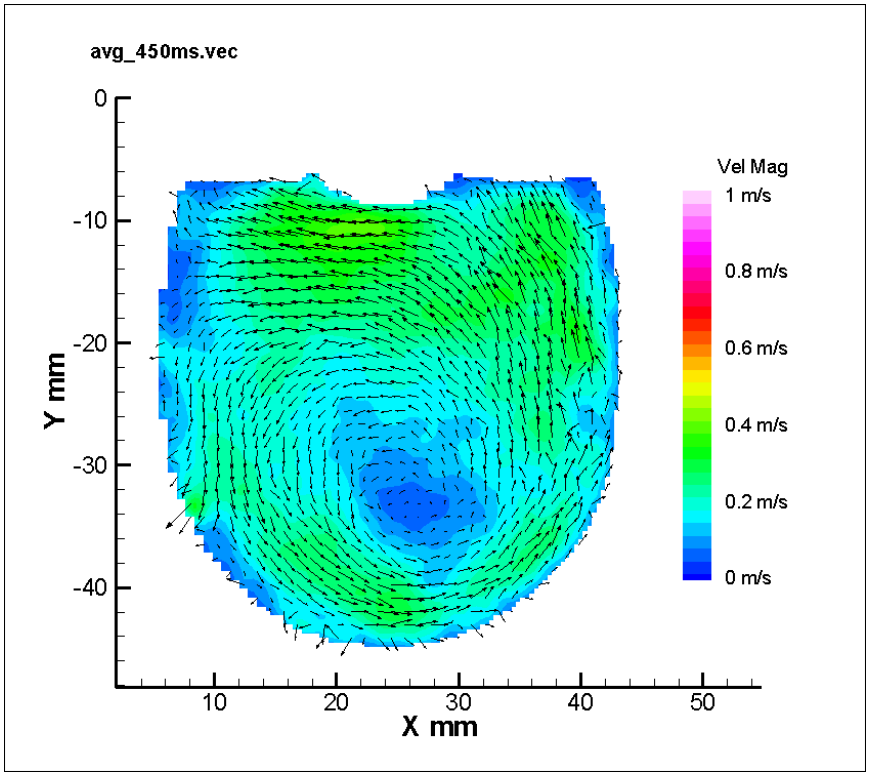
avg_450ms.vec
0
-10
-20
-30
-40
Y mm
10
20
30
40
50
X mm
Vel Mag
1 m/s
0.8 m/s
0.6 m/s
0.4 m/s
0.2 m/s
0 m/s

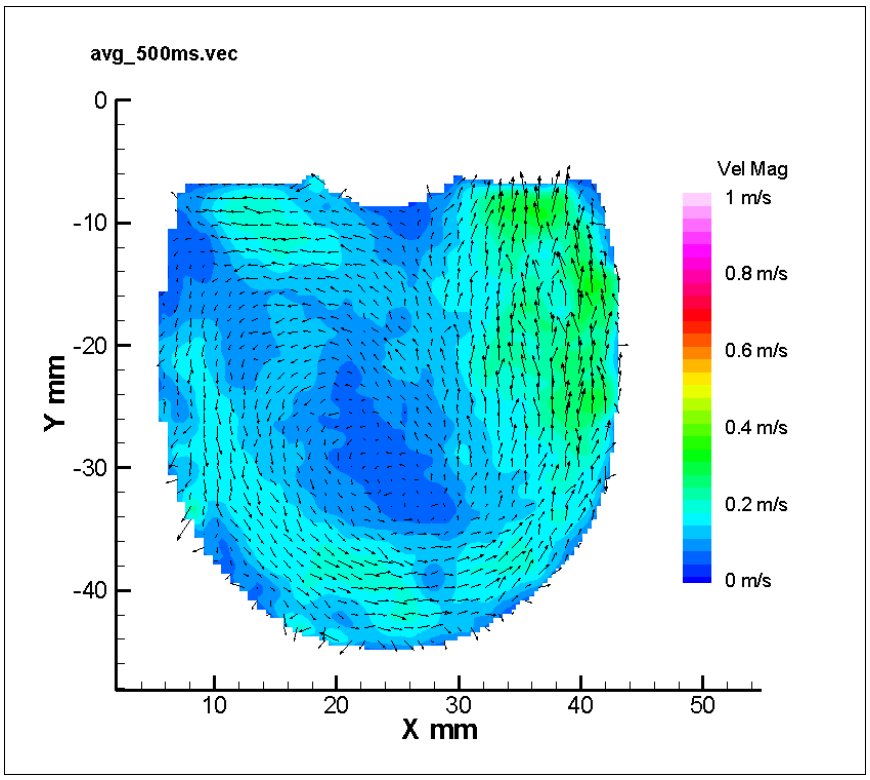
avg_500ms.vec
0
-10
-20
-30
-40
Y mm
10
20
30
40
50
X mm
Vel Mag
1 m/s
0.8 m/s
0.6 m/s
0.4 m/s
0.2 m/s
0 m/s

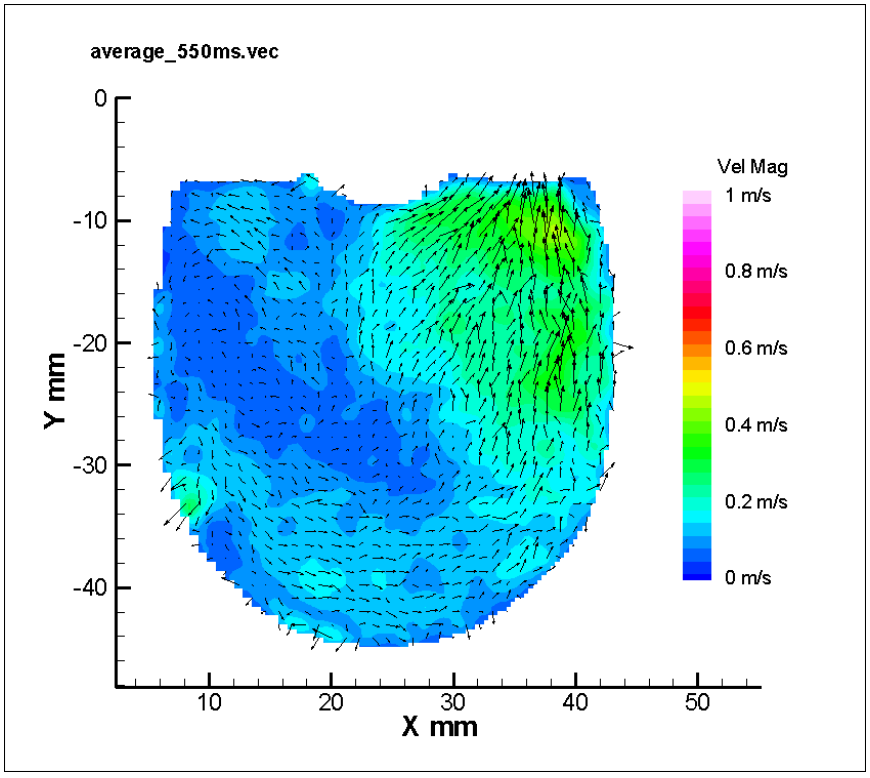
average_550ms.vec
0
-10
-20
-30
-40
Y mm
10
20
30
40
50
X mm
Vel Mag
1 m/s
0.8 m/s
0.6 m/s
0.4 m/s
0.2 m/s
0 m/s

Appendix C 60% HEMATOCRIT

Appendix C-1. 6.5 mm Parallel Plane

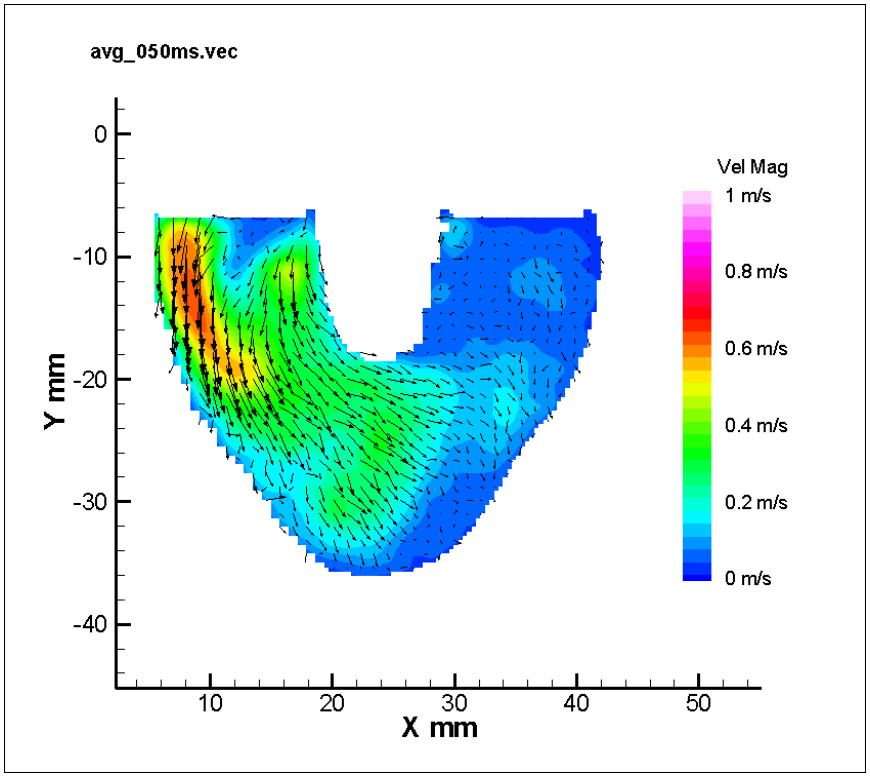

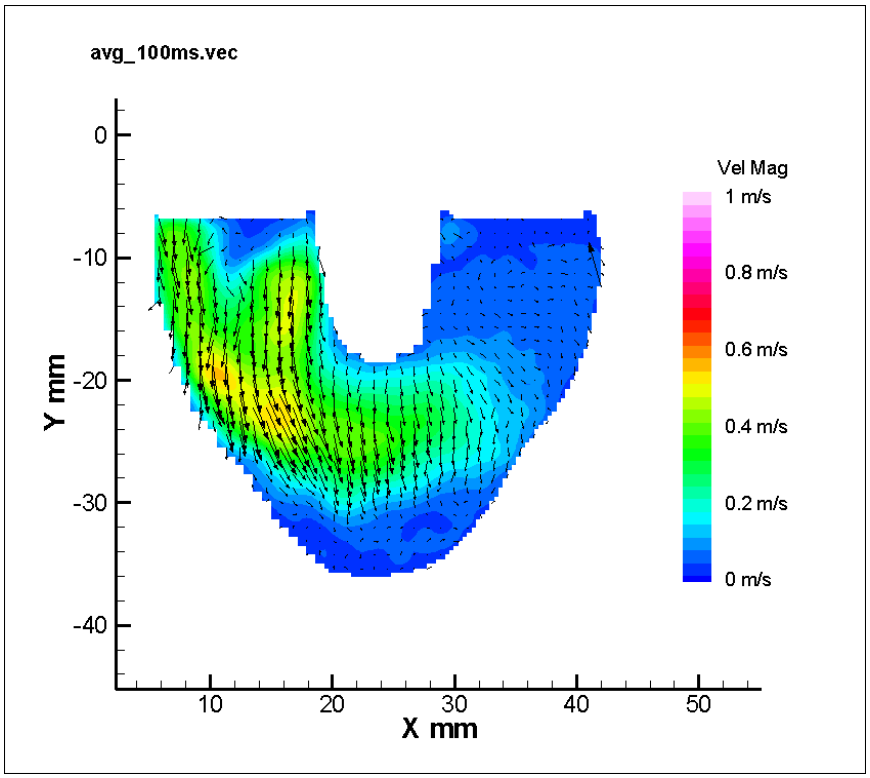

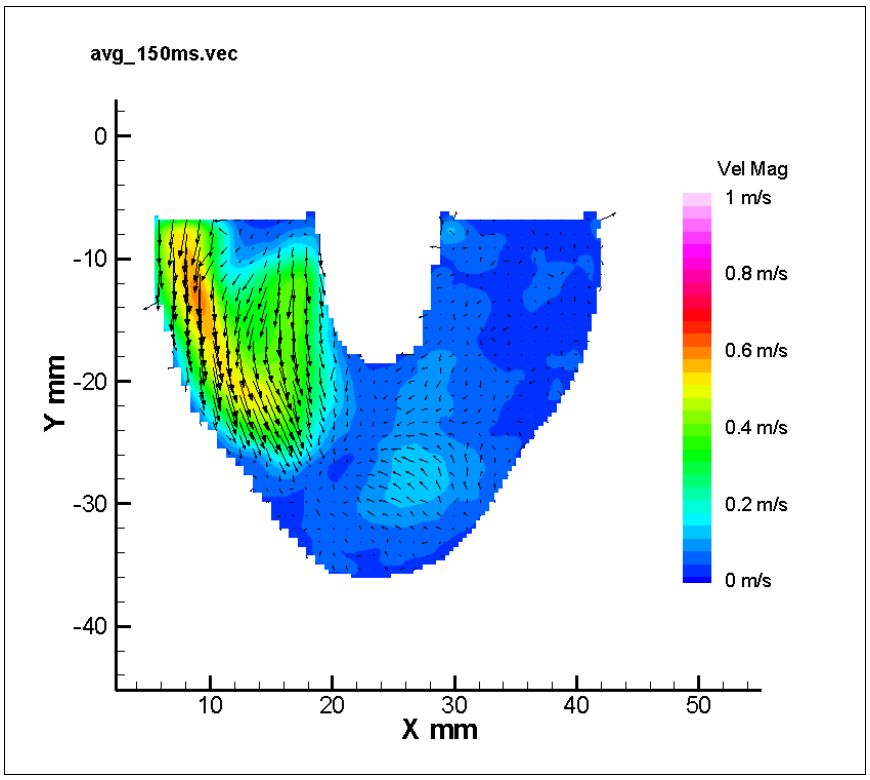
avg_150ms.vec
0
-10
-20
-30
-40
Y mm
10
20
30
40
50
X mm
Vel Mag
1 m/s
0.8 m/s
0.6 m/s
0.4 m/s
0.2 m/s
0 m/s

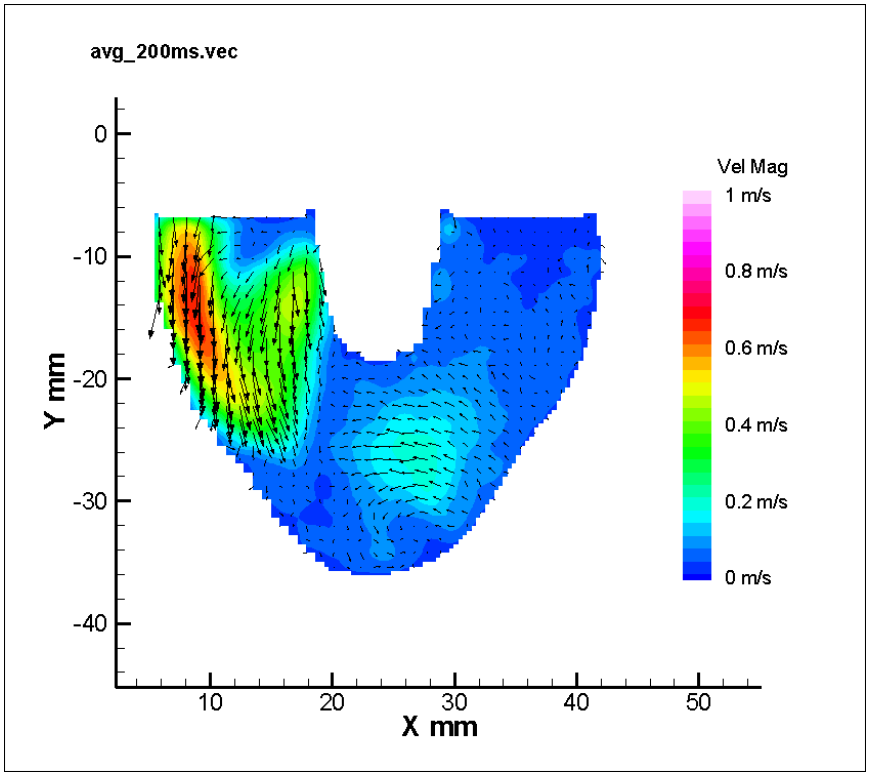
avg_200ms.vec
0
-10
-20
-30
-40
Y mm
10
20
30
40
50
X mm
Vel Mag
1 m/s
0.8 m/s
0.6 m/s
0.4 m/s
0.2 m/s
0 m/s

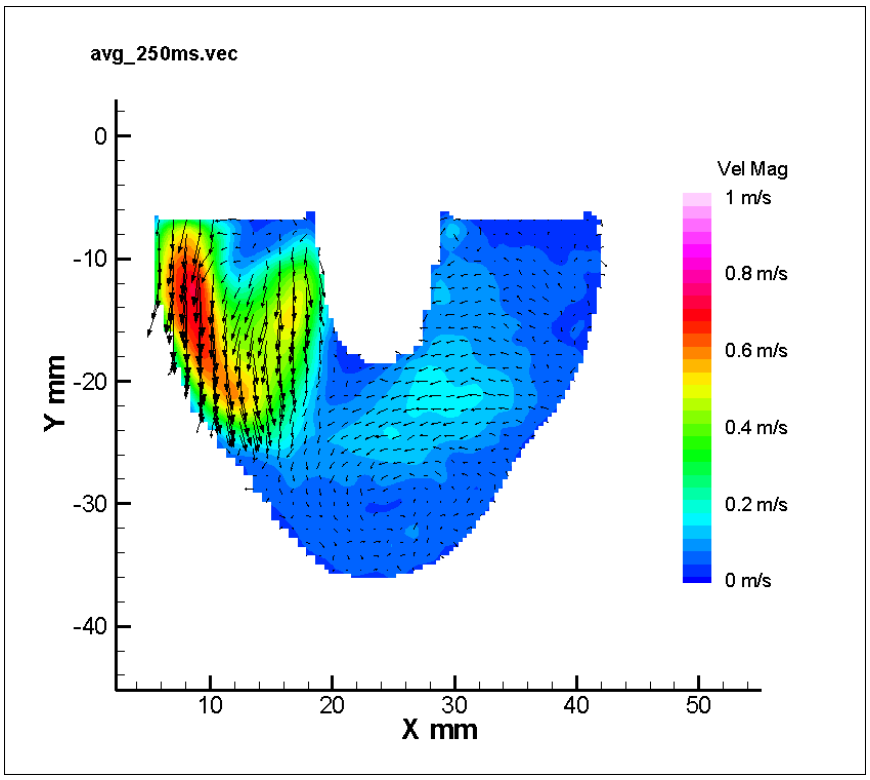
avg_250ms.vec
0
-10
-20
-30
-40
Y mm
10
20
30
40
50
X mm
Vel Mag
1 m/s
0.8 m/s
0.6 m/s
0.4 m/s
0.2 m/s
0 m/s

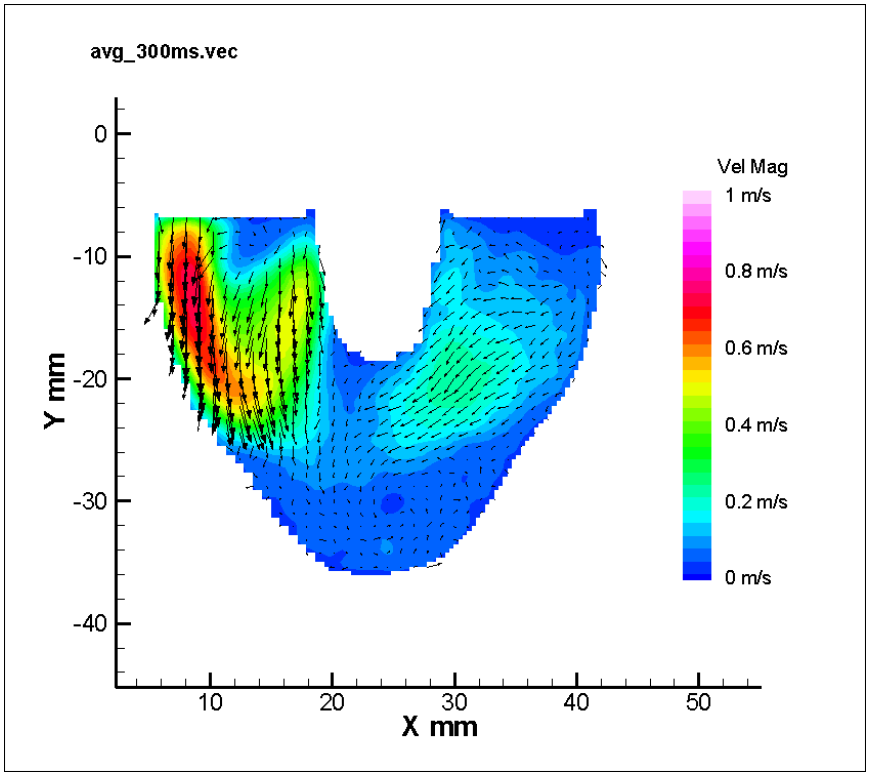
avg_300ms.vec
0
-10
-20
-30
-40
Y mm
10
20
30
40
50
X mm
Vel Mag
1 m/s
0.8 m/s
0.6 m/s
0.4 m/s
0.2 m/s
0 m/s

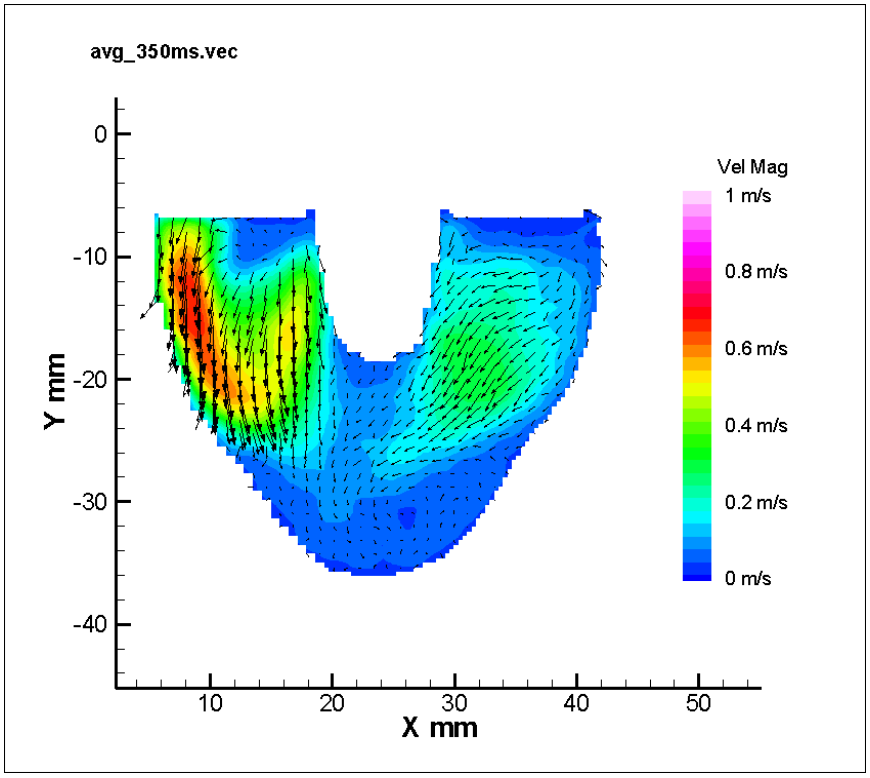
avg_350ms.vec
0
-10
-20
-30
-40
Y mm
10
20
30
40
50
X mm
Vel Mag
1 m/s
0.8 m/s
0.6 m/s
0.4 m/s
0.2 m/s
0 m/s

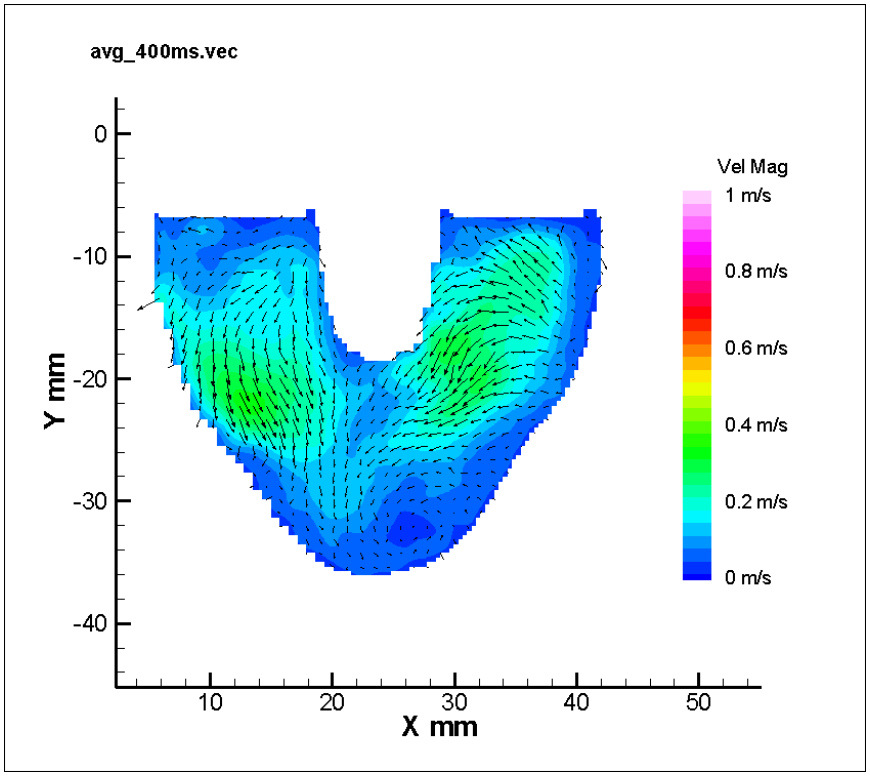
avg_400ms.vec
0
-10
-20
-30
-40
Y mm
10
20
30
40
50
X mm
Vel Mag
1 m/s
0.8 m/s
0.6 m/s
0.4 m/s
0.2 m/s
0 m/s

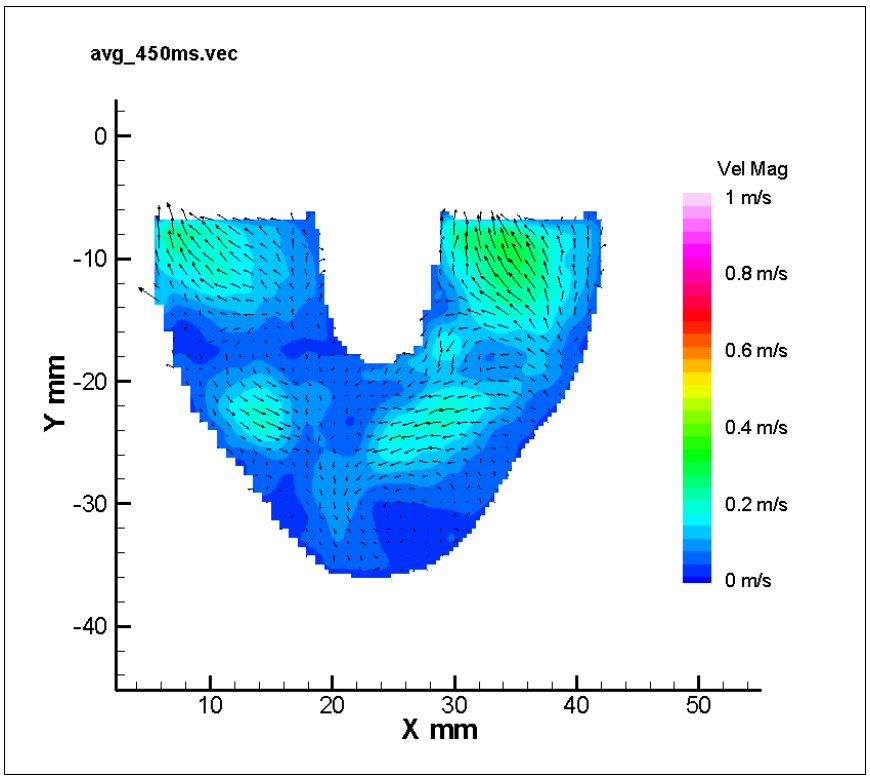
avg_450ms.vec
0
-10
-20
-30
-40
Y mm
10
20
30
40
50
X mm
Vel Mag
1 m/s
0.8 m/s
0.6 m/s
0.4 m/s
0.2 m/s
0 m/s

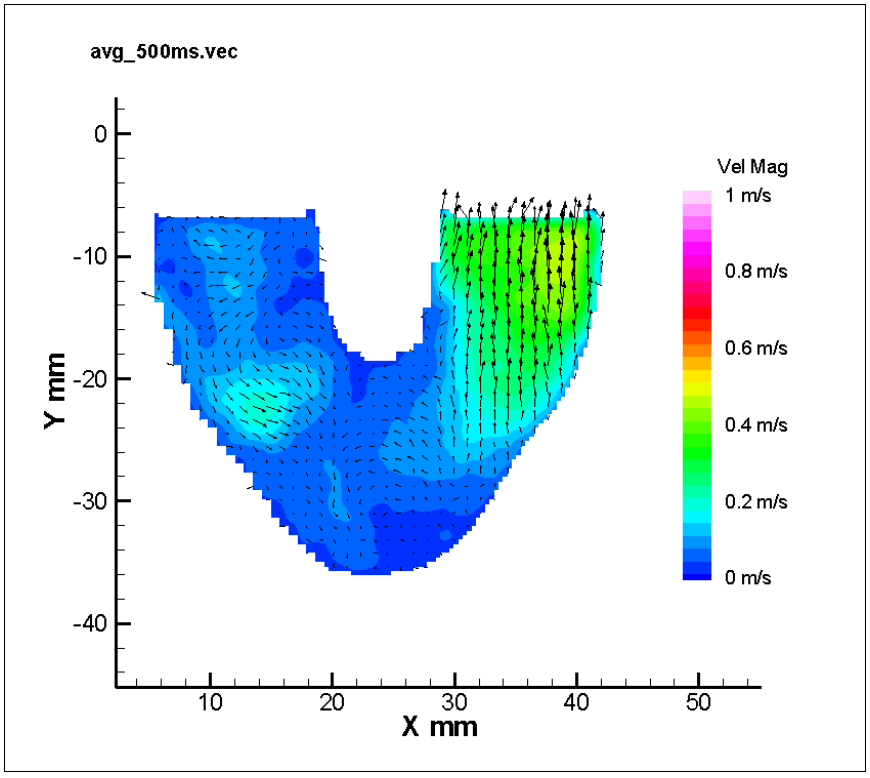
avg_500ms.vec
0
-10
-20
-30
-40
Y mm
10
20
30
40
50
X mm
Vel Mag
1 m/s
0.8 m/s
0.6 m/s
0.4 m/s
0.2 m/s
0 m/s

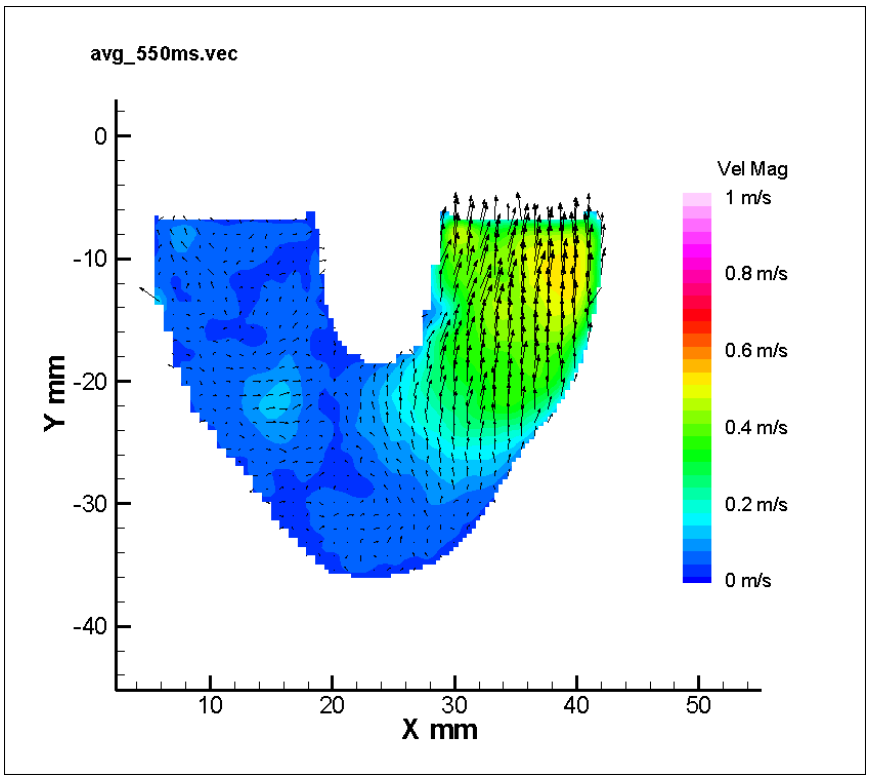
avg_550ms.vec
0
-10
-20
-30
-40
Y mm
10
20
30
40
50
X mm
Vel Mag
1 m/s
0.8 m/s
0.6 m/s
0.4 m/s
0.2 m/s
0 m/s

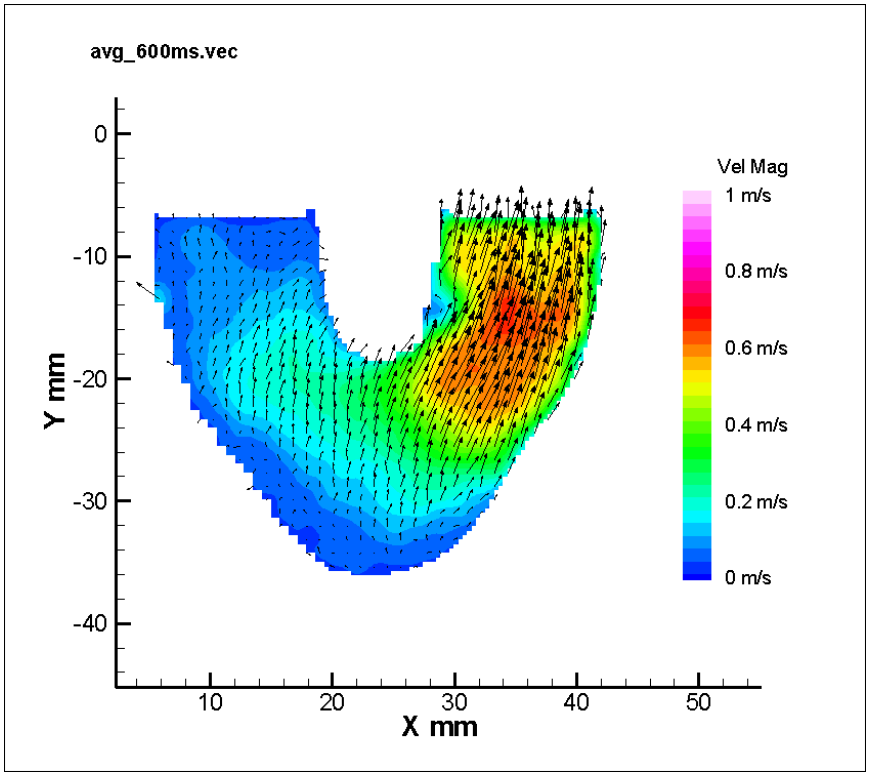
avg_600ms.vec
0
-10
-20
-30
-40
Y mm
10
20
30
40
50
X mm
Vel Mag
1 m/s
0.8 m/s
0.6 m/s
0.4 m/s
0.2 m/s
0 m/s

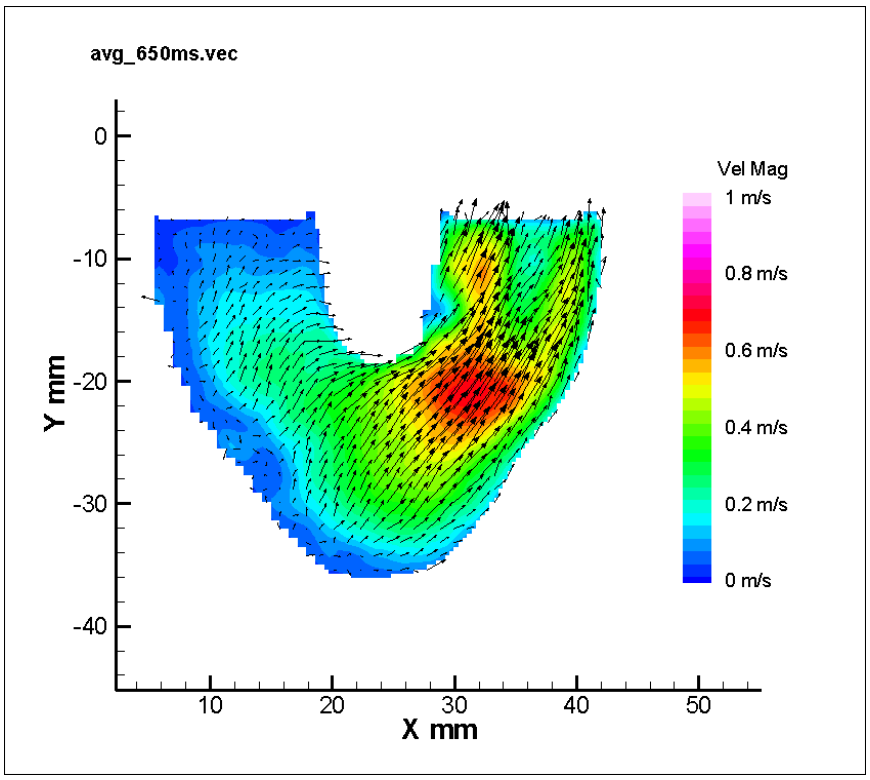
avg_650ms.vec
0
-10
-20
-30
-40
Y mm
10
20
30
40
50
X mm
Vel Mag
1 m/s
0.8 m/s
0.6 m/s
0.4 m/s
0.2 m/s
0 m/s

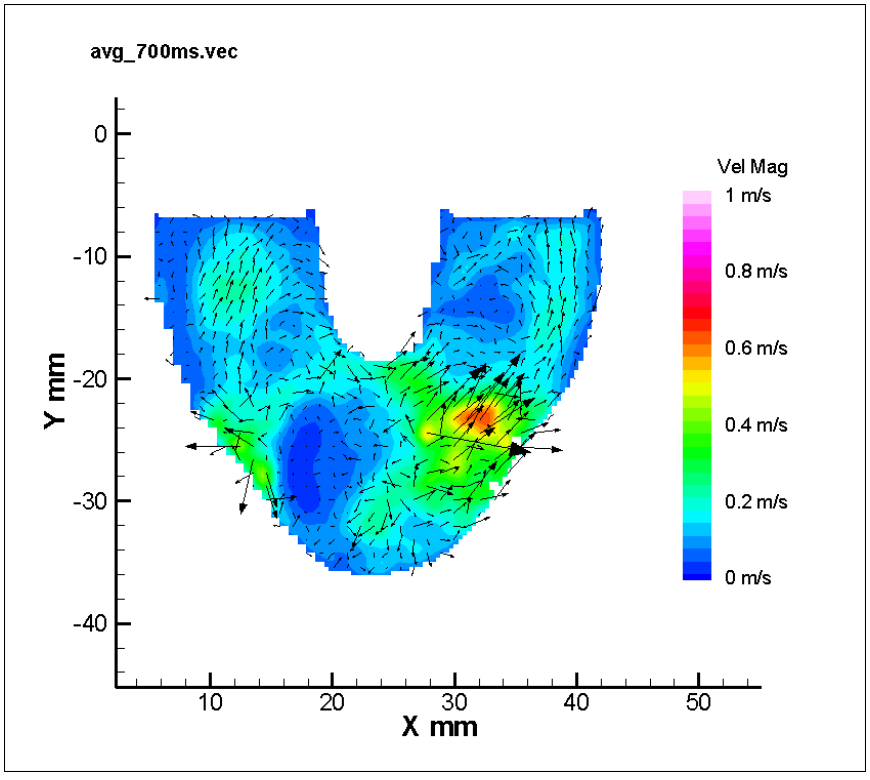
avg_700ms.vec
0
-10
-20
-30
-40
Y mm
10
20
30
40
50
X mm
Vel Mag
1 m/s
0.8 m/s
0.6 m/s
0.4 m/s
0.2 m/s
0 m/s

Appendix C-2. 7 mm Parallel Plane

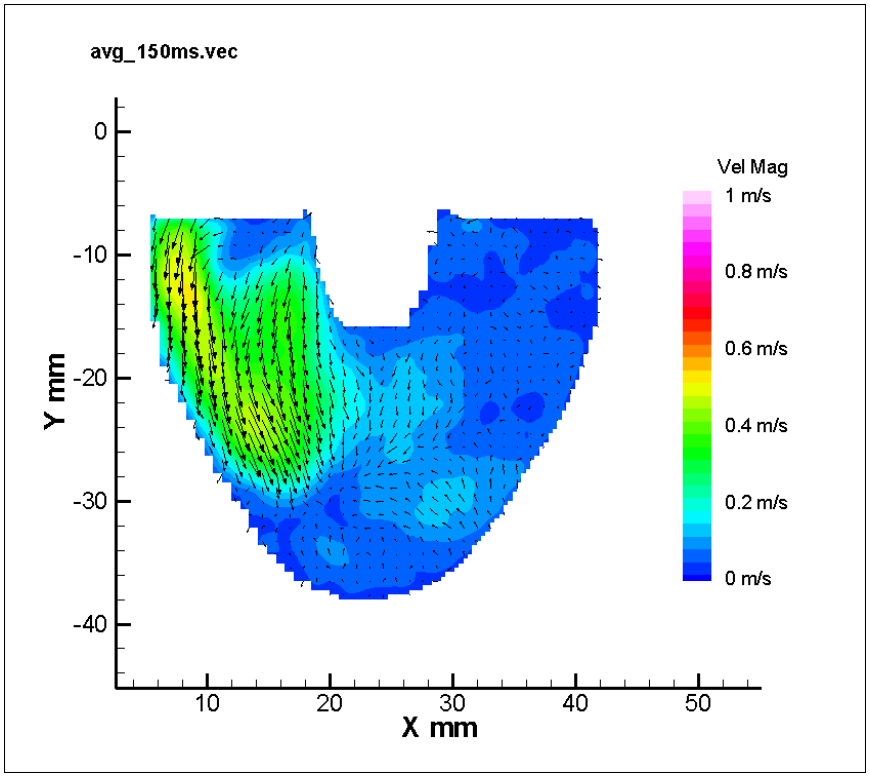

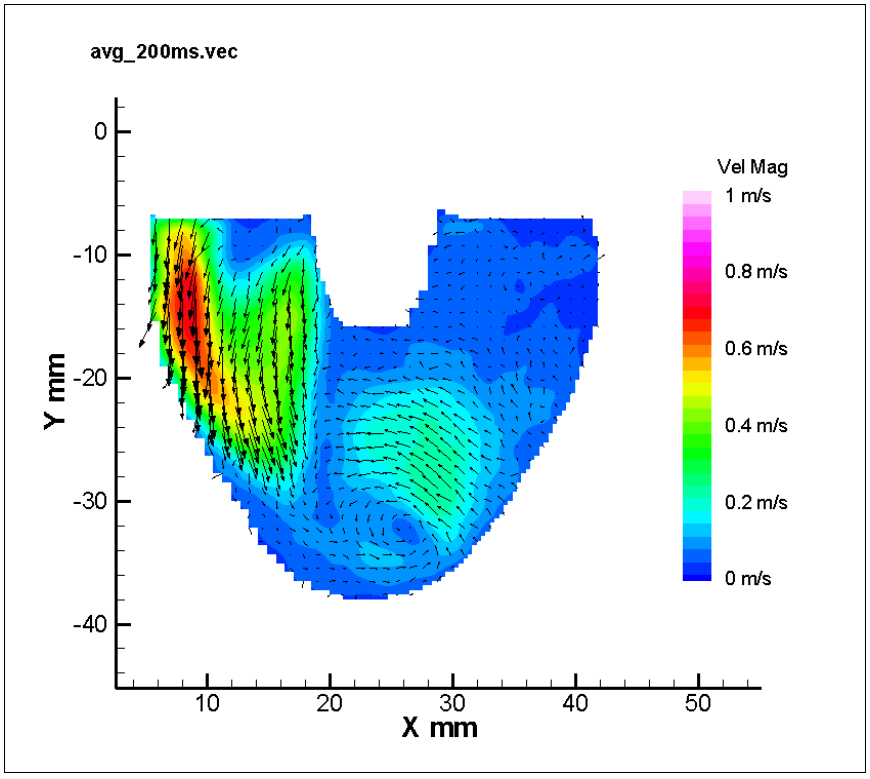

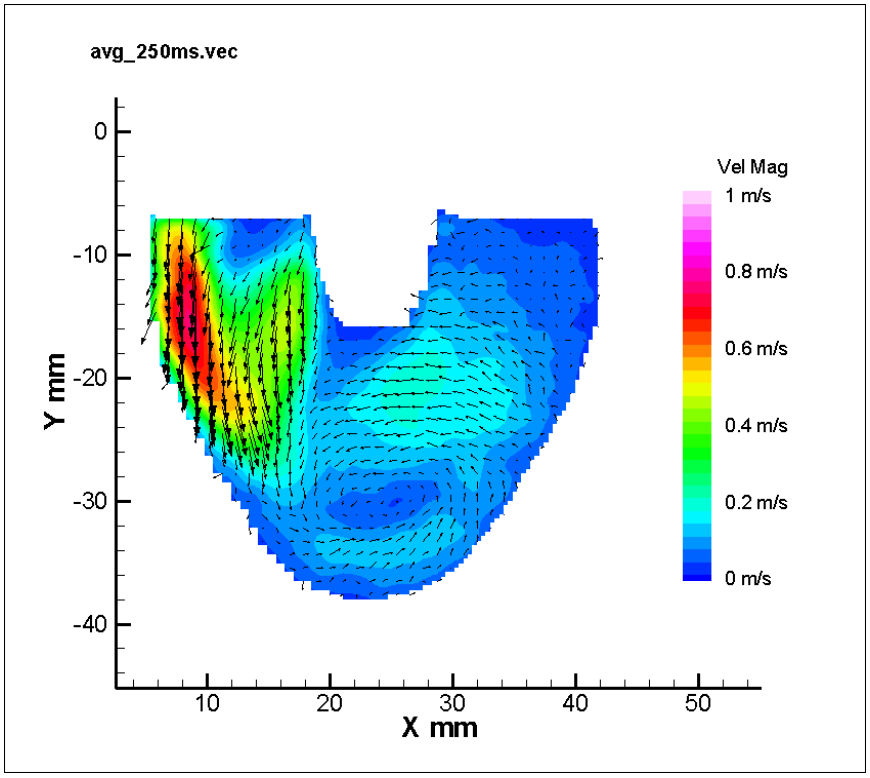
avg_250ms.vec
0
-10
-20
-30
-40
Y mm
10
20
30
40
50
X mm
Vel Mag
1 m/s
0.8 m/s
0.6 m/s
0.4 m/s
0.2 m/s
0 m/s

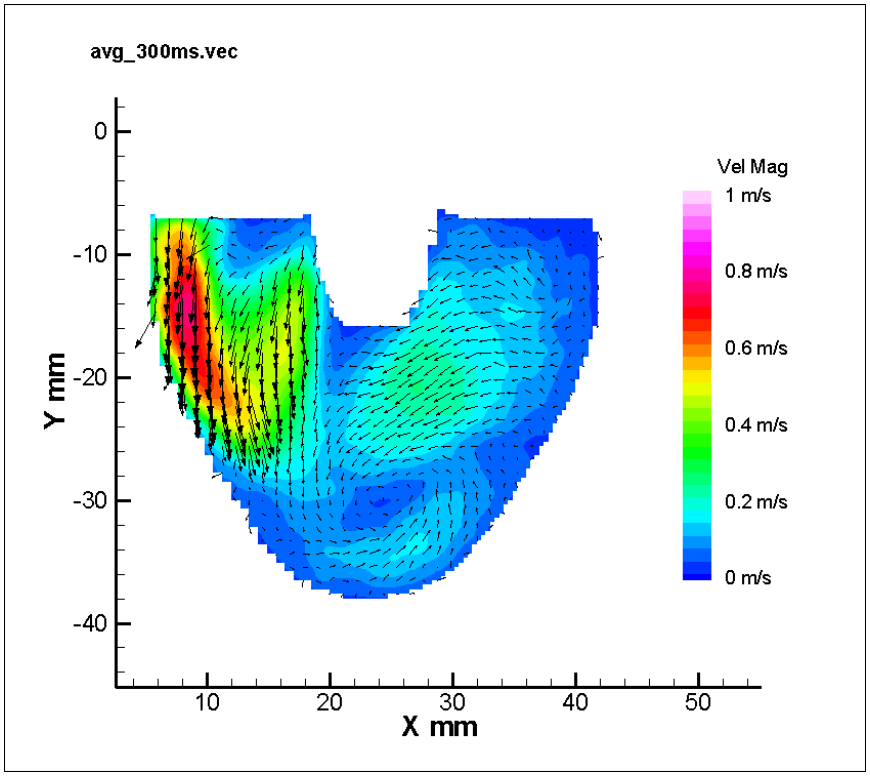
avg_300ms.vec
0
-10
-20
-30
-40
Y mm
10
20
30
40
50
X mm
Vel Mag
1 m/s
0.8 m/s
0.6 m/s
0.4 m/s
0.2 m/s
0 m/s

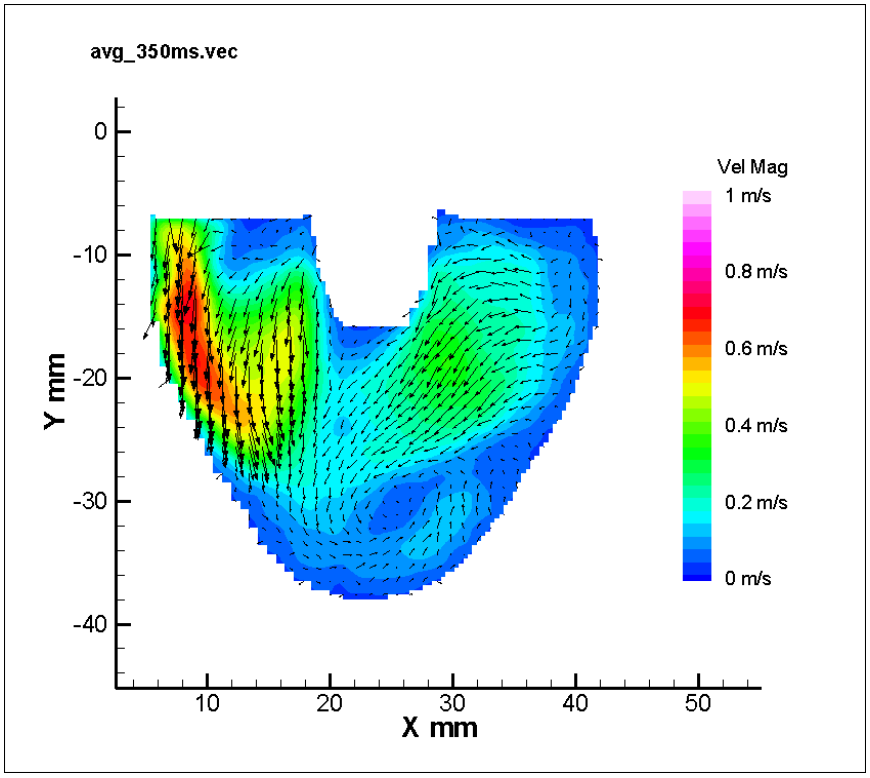
avg_350ms.vec
0
-10
-20
-30
-40
Y mm
10
20
30
40
50
X mm
Vel Mag
1 m/s
0.8 m/s
0.6 m/s
0.4 m/s
0.2 m/s
0 m/s

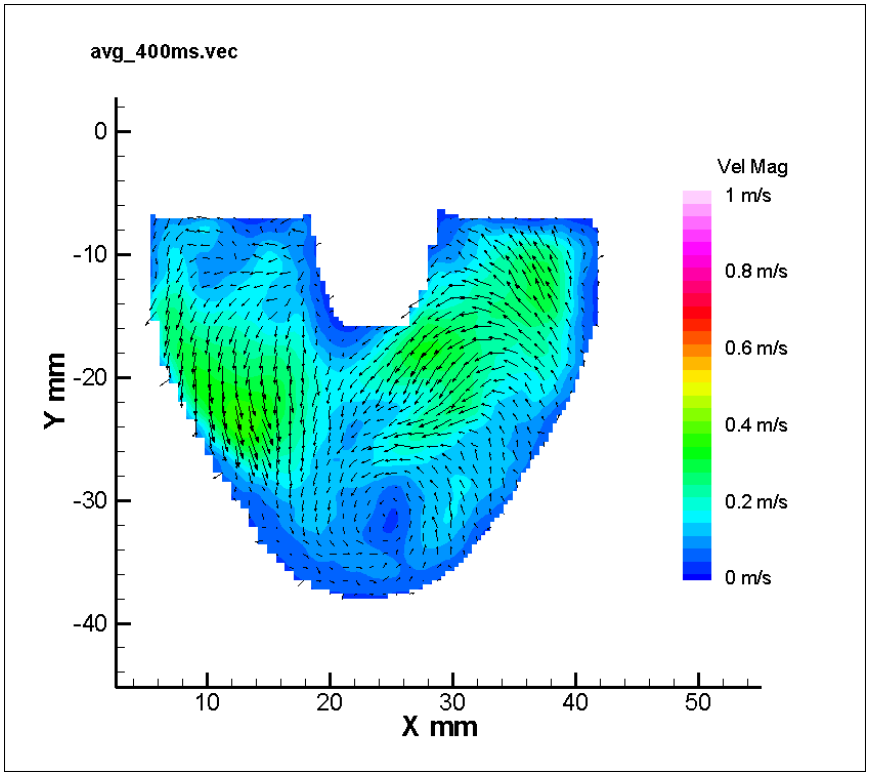
avg_400ms.vec
0
-10
-20
-30
-40
Y mm
10
20
30
40
50
X mm
Vel Mag
1 m/s
0.8 m/s
0.6 m/s
0.4 m/s
0.2 m/s
0 m/s

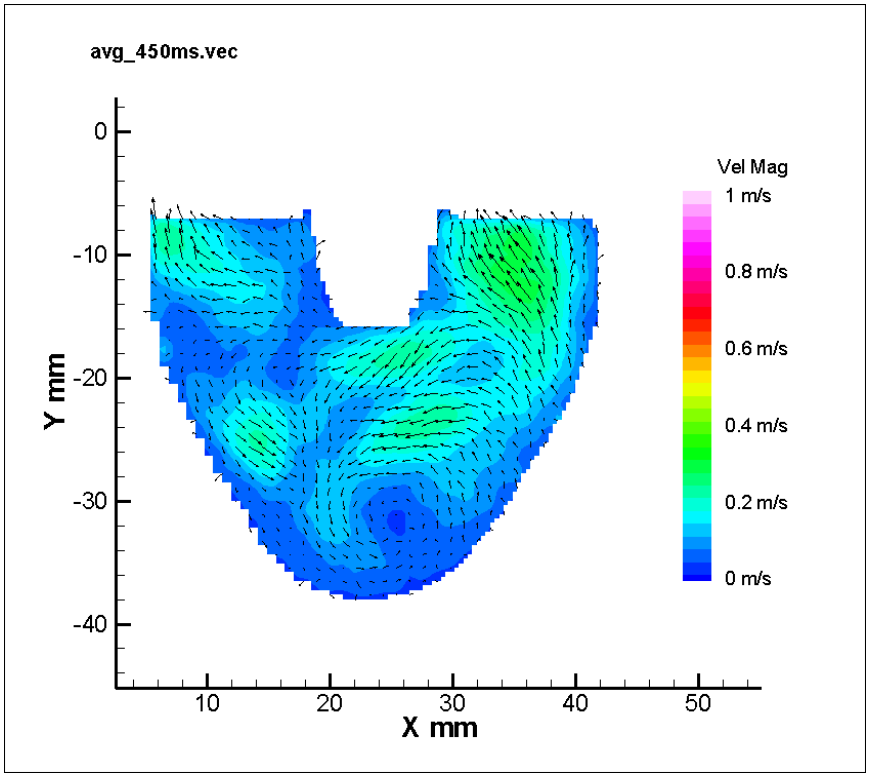
avg_450ms.vec
0
-10
-20
-30
-40
Y mm
10
20
30
40
50
X mm
Vel Mag
1 m/s
0.8 m/s
0.6 m/s
0.4 m/s
0.2 m/s
0 m/s

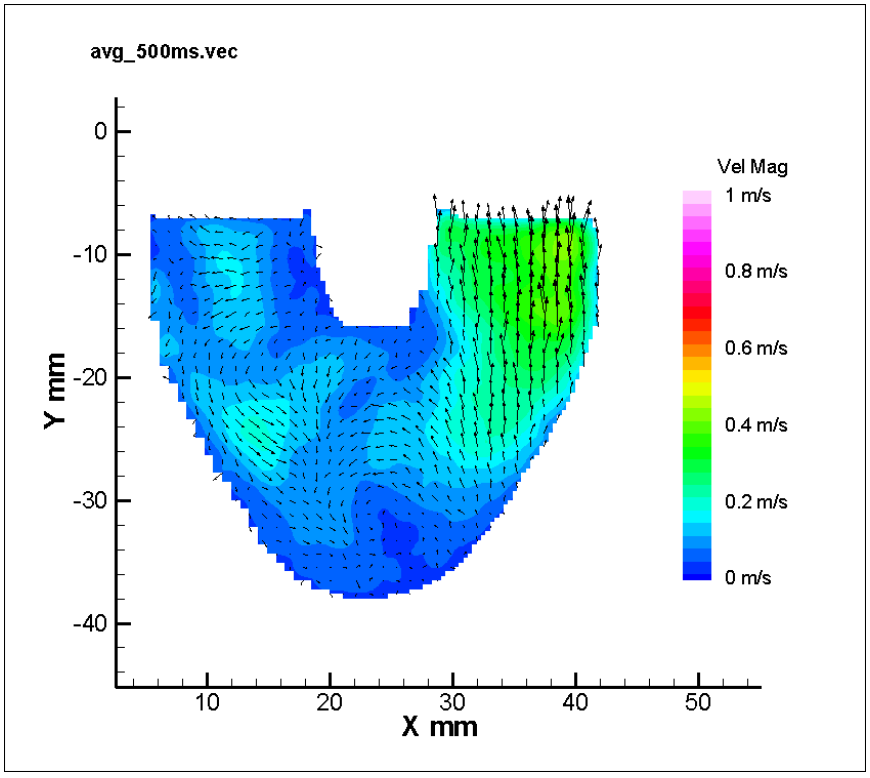
avg_500ms.vec
0
-10
-20
-30
-40
Y mm
10
20
30
40
50
X mm
Vel Mag
1 m/s
0.8 m/s
0.6 m/s
0.4 m/s
0.2 m/s
0 m/s

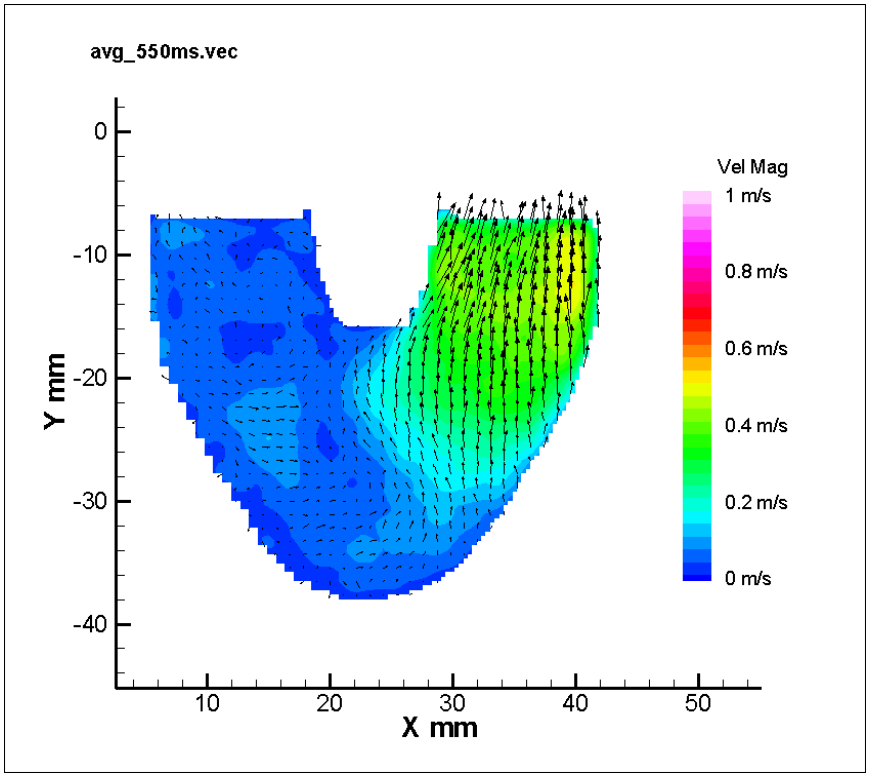
avg_550ms.vec
0
-10
-20
-30
-40
Y mm
10
20
30
40
50
X mm
Vel Mag
1 m/s
0.8 m/s
0.6 m/s
0.4 m/s
0.2 m/s
0 m/s

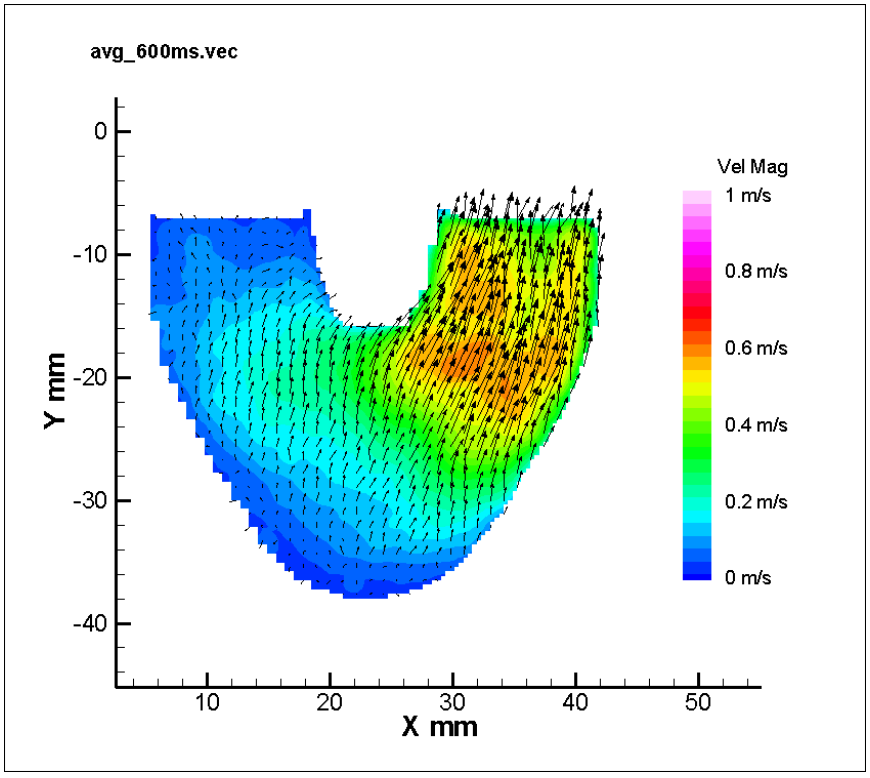
avg_600ms.vec
0
-10
-20
-30
-40
Y mm
10
20
30
40
50
X mm
Vel Mag
1 m/s
0.8 m/s
0.6 m/s
0.4 m/s
0.2 m/s
0 m/s

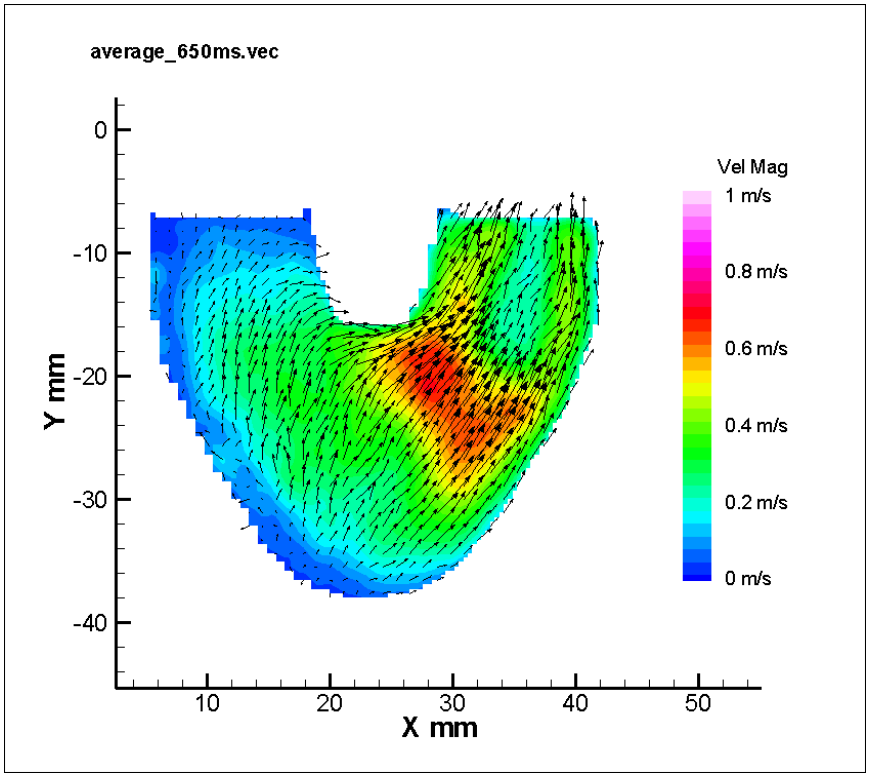
average_650ms.vec
0
-10
-20
-30
-40
Y mm
10
20
30
40
50
X mm
Vel Mag
1 m/s
0.8 m/s
0.6 m/s
0.4 m/s
0.2 m/s
0 m/s

Appendix C-3. 8.2 mm Parallel Plane

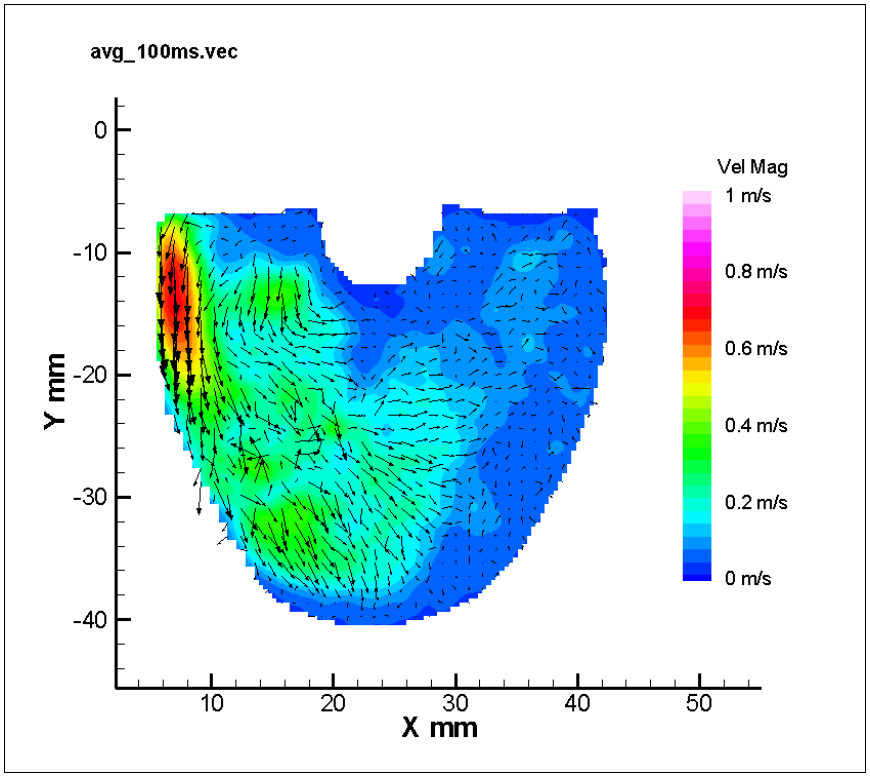

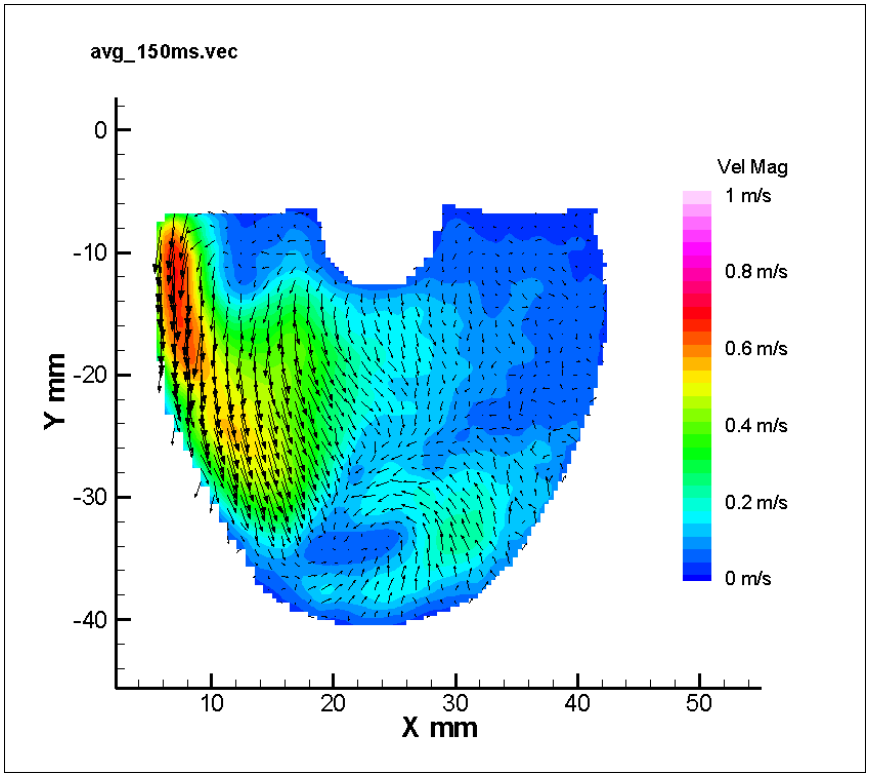

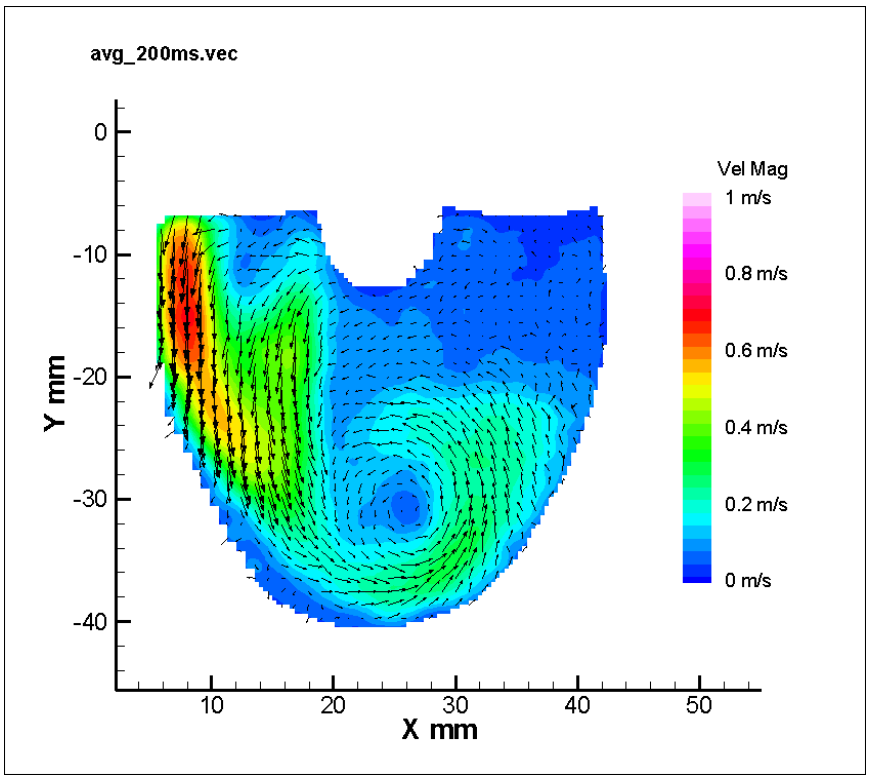
avg_200ms.vec
0
-10
-20
-30
-40
Y mm
10
20
30
40
50
X mm
Vel Mag
1 m/s
0.8 m/s
0.6 m/s
0.4 m/s
0.2 m/s
0 m/s

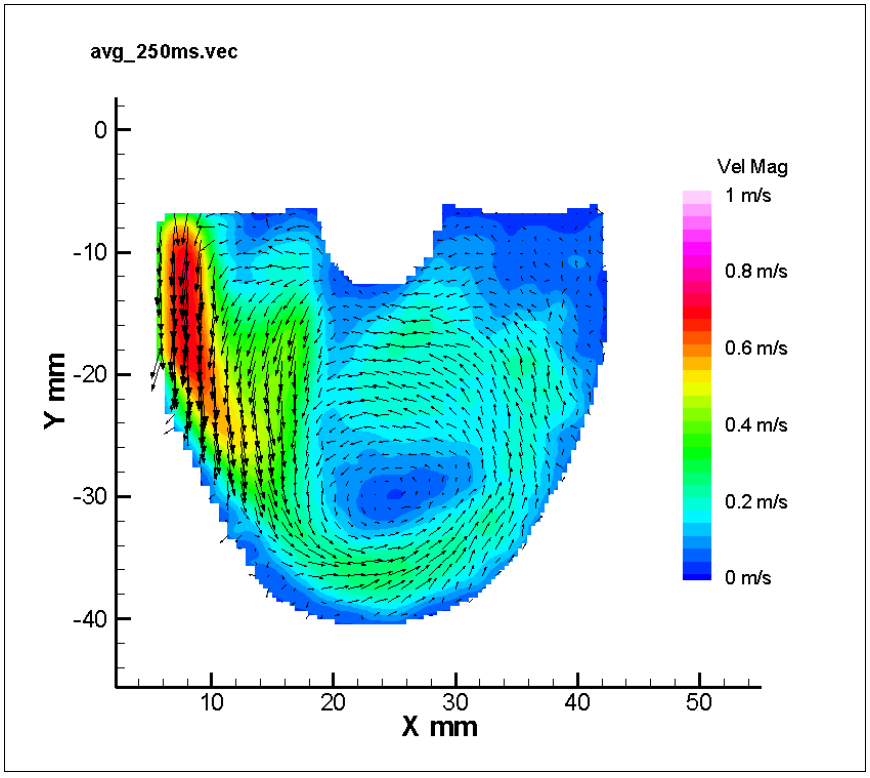
avg_250ms.vec
0
-10
-20
-30
-40
Y mm
10
20
30
40
50
X mm
Vel Mag
1 m/s
0.8 m/s
0.6 m/s
0.4 m/s
0.2 m/s
0 m/s

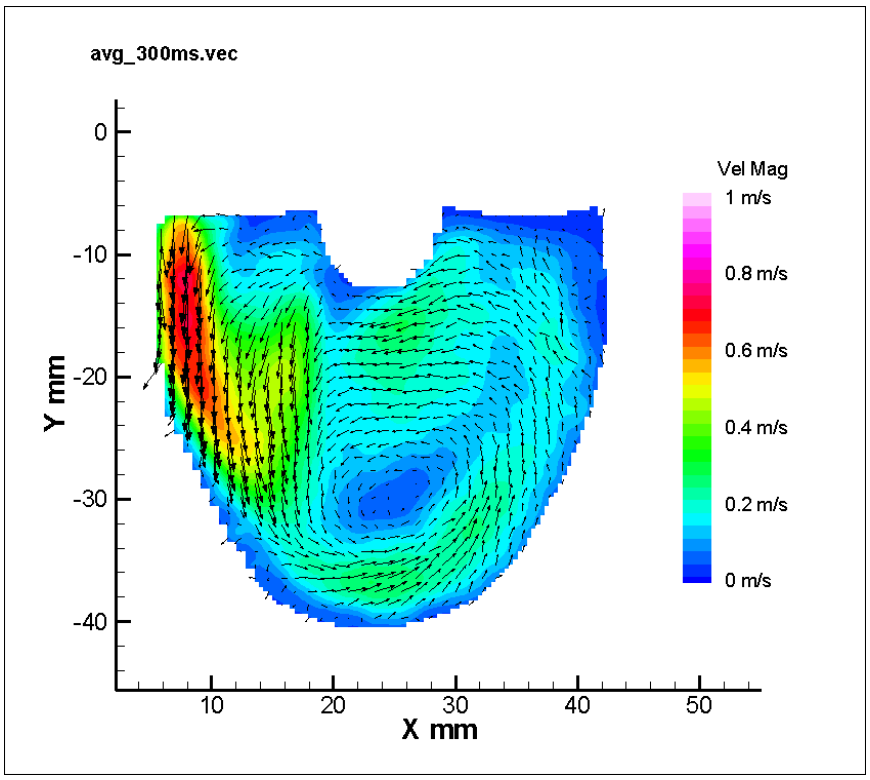
avg_300ms.vec
0
-10
-20
-30
-40
Y mm
10
20
30
40
50
X mm
Vel Mag
1 m/s
0.8 m/s
0.6 m/s
0.4 m/s
0.2 m/s
0 m/s

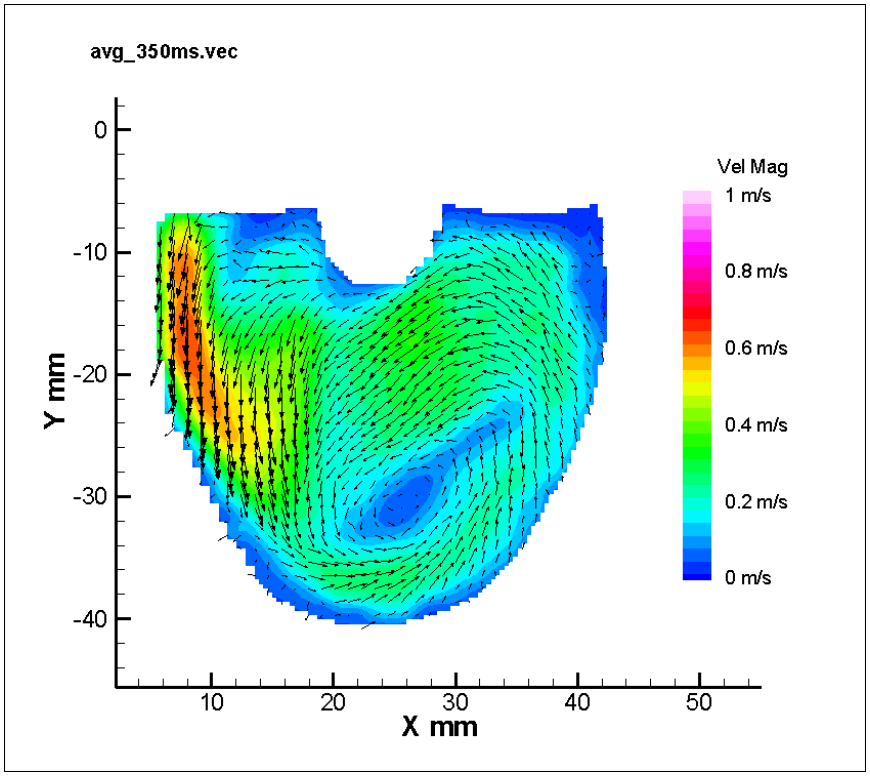
avg_350ms.vec
0
-10
-20
-30
-40
Y mm
10
20
30
40
50
X mm
Vel Mag
1 m/s
0.8 m/s
0.6 m/s
0.4 m/s
0.2 m/s
0 m/s

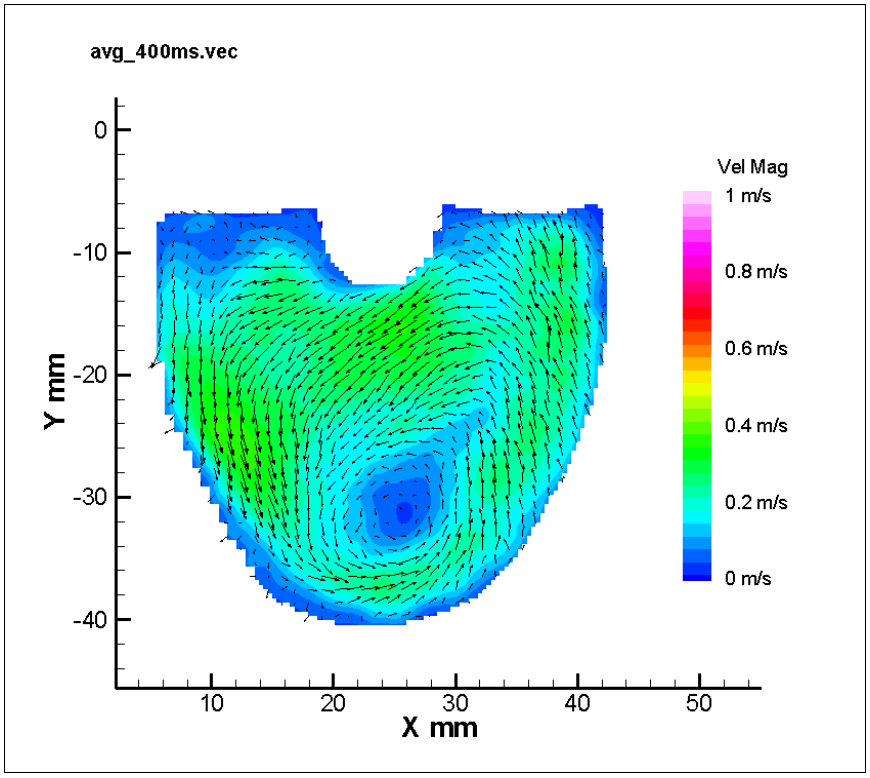
avg_400ms.vec
0
-10
-20
-30
-40
Y mm
10
20
30
40
50
X mm
Vel Mag
1 m/s
0.8 m/s
0.6 m/s
0.4 m/s
0.2 m/s
0 m/s

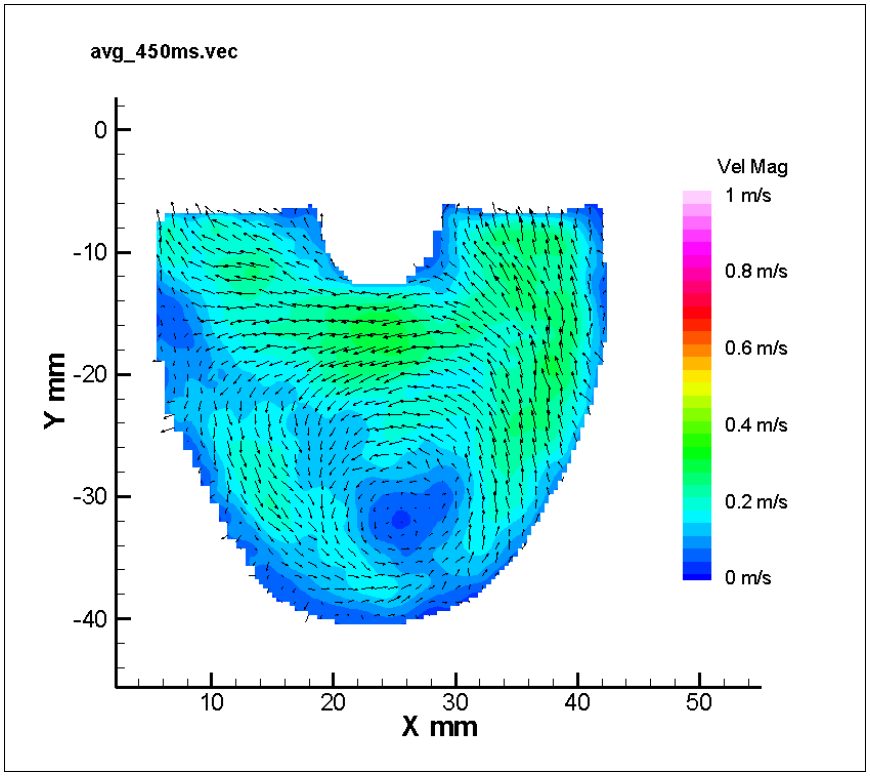
avg_450ms.vec
0
-10
-20
-30
-40
Y mm
10
20
30
40
50
X mm
Vel Mag
1 m/s
0.8 m/s
0.6 m/s
0.4 m/s
0.2 m/s
0 m/s

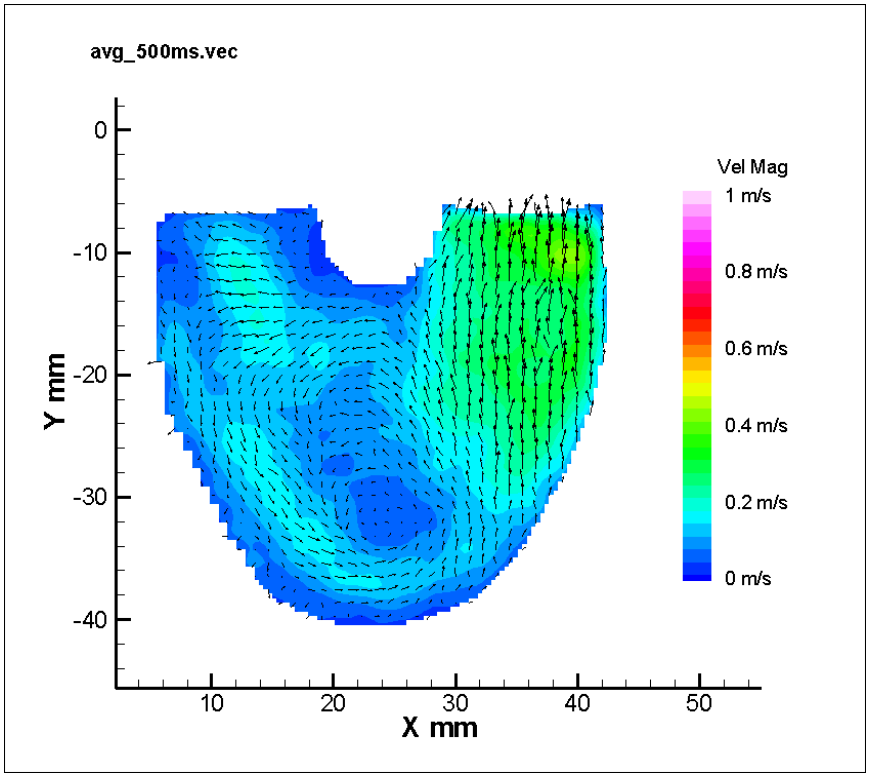
avg_500ms.vec
0
-10
-20
-30
-40
Y mm
10
20
30
40
50
X mm
Vel Mag
1 m/s
0.8 m/s
0.6 m/s
0.4 m/s
0.2 m/s
0 m/s

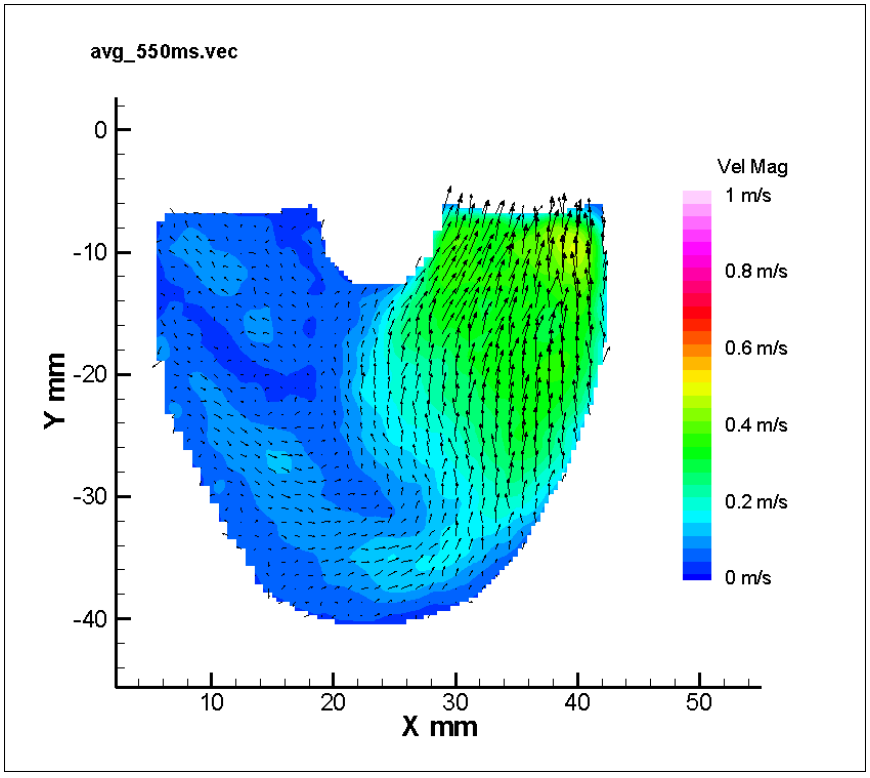
avg_550ms.vec
0
-10
-20
-30
-40
Y mm
10
20
30
40
50
X mm
Vel Mag
1 m/s
0.8 m/s
0.6 m/s
0.4 m/s
0.2 m/s
0 m/s

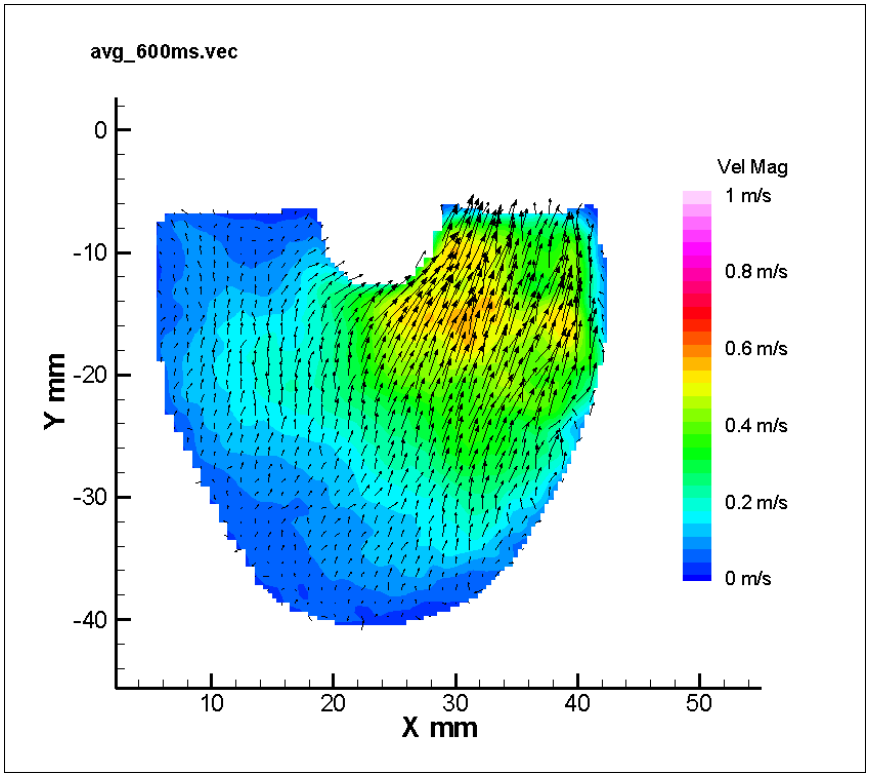
avg_600ms.vec
0
-10
-20
-30
-40
Y mm
10
20
30
40
50
X mm
Vel Mag
1 m/s
0.8 m/s
0.6 m/s
0.4 m/s
0.2 m/s
0 m/s

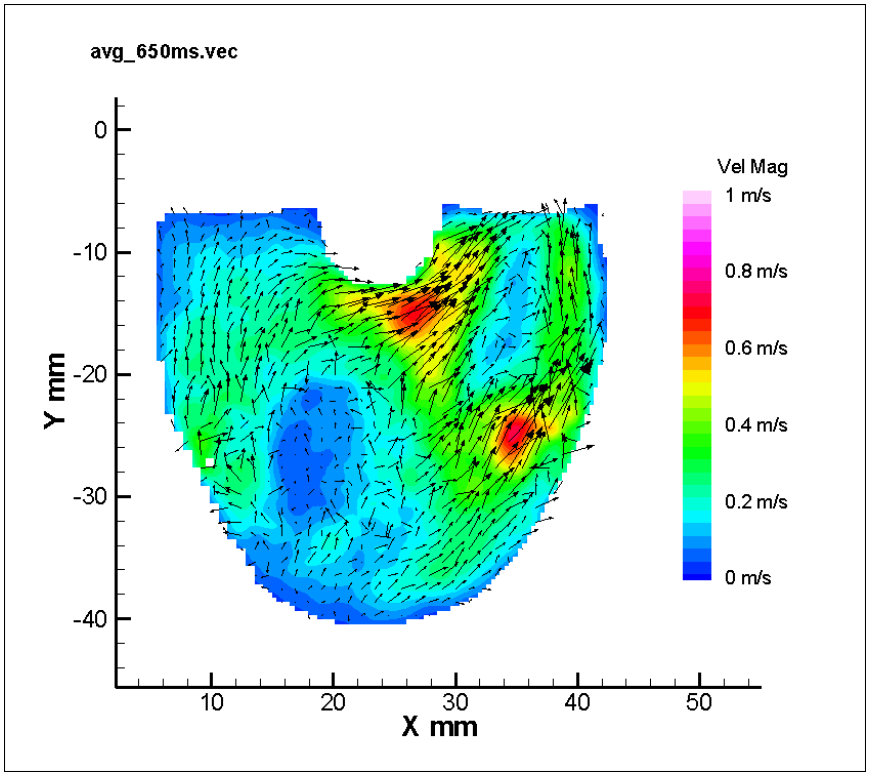
avg_650ms.vec
0
-10
-20
-30
-40
Y mm
10
20
30
40
50
X mm
Vel Mag
1 m/s
0.8 m/s
0.6 m/s
0.4 m/s
0.2 m/s
0 m/s

Appendix C-4. 11 mm Parallel Plane

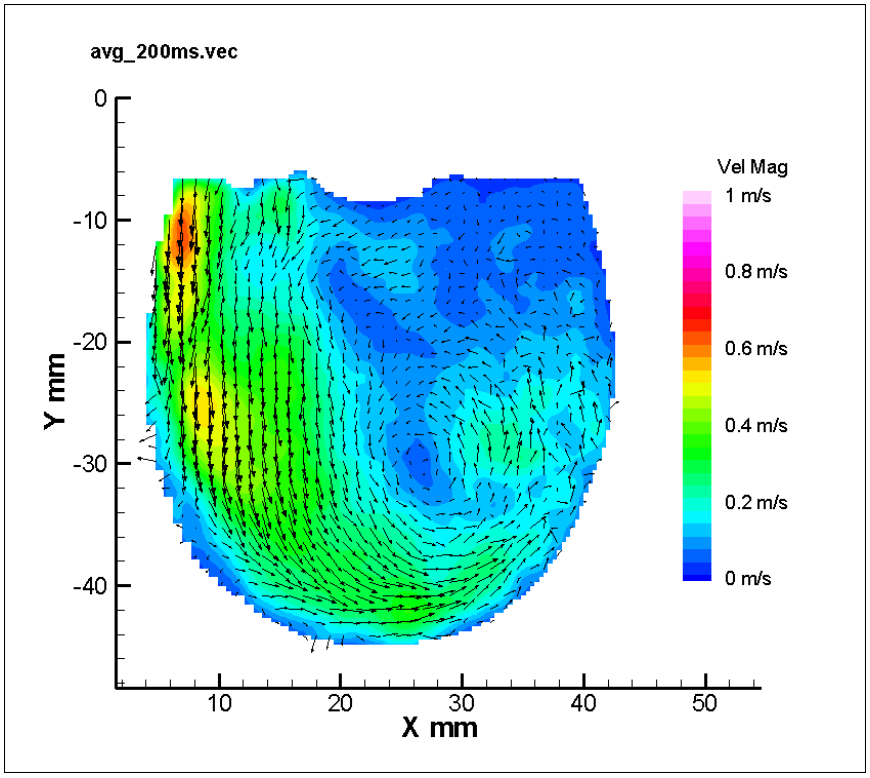

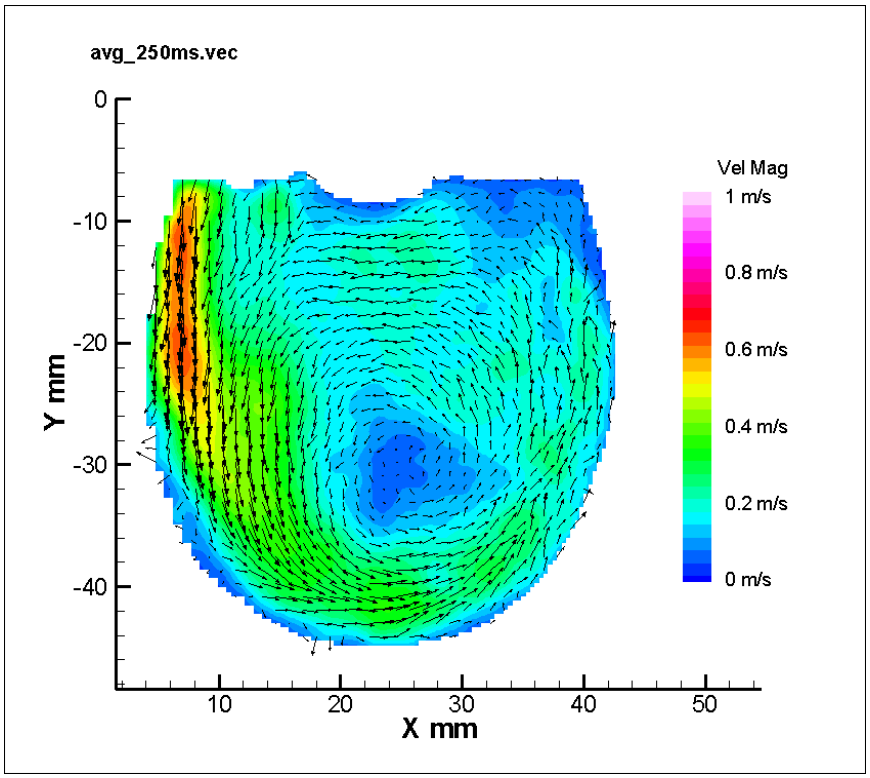

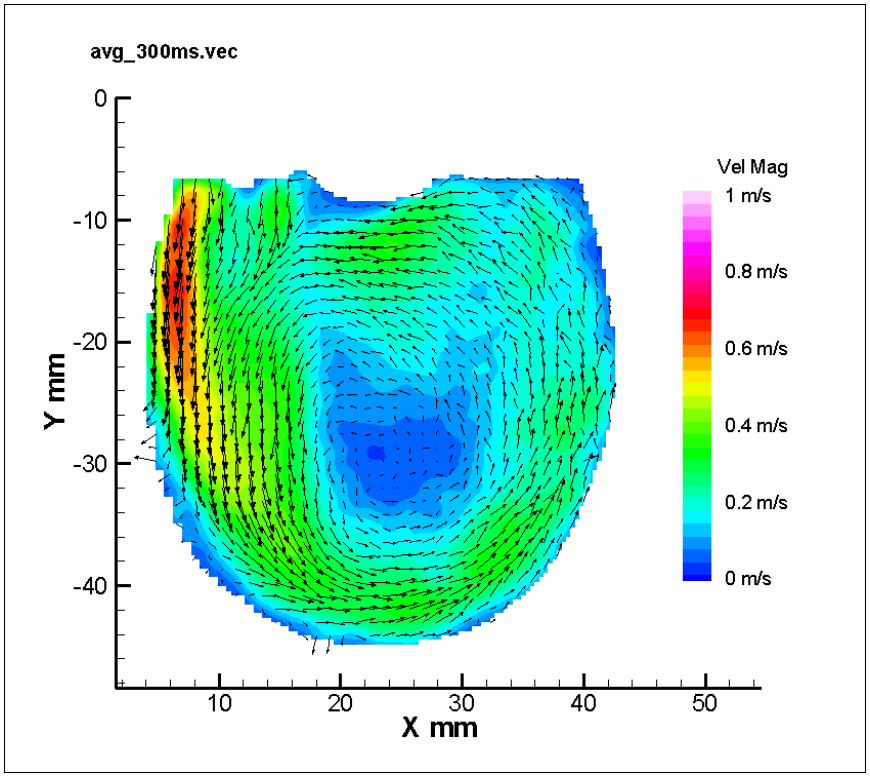
avg_300ms.vec
0
-10
-20
-30
-40
Y mm
10
20
30
40
50
X mm
Vel Mag
1 m/s
0.8 m/s
0.6 m/s
0.4 m/s
0.2 m/s
0 m/s

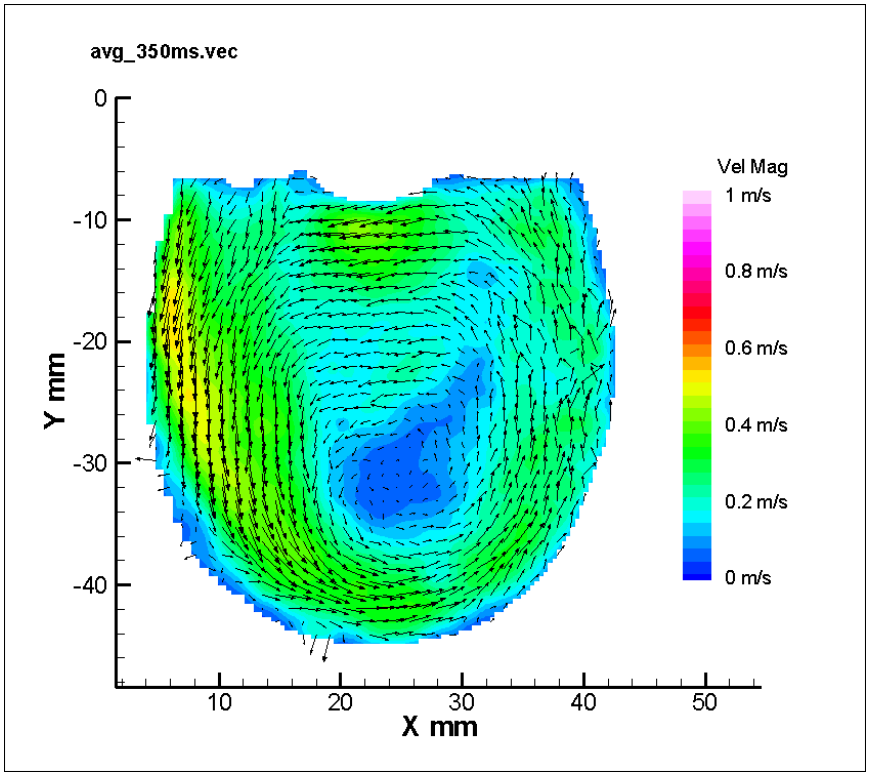
avg_350ms.vec
0
-10
-20
-30
-40
Y mm
10
20
30
40
50
X mm
Vel Mag
1 m/s
0.8 m/s
0.6 m/s
0.4 m/s
0.2 m/s
0 m/s

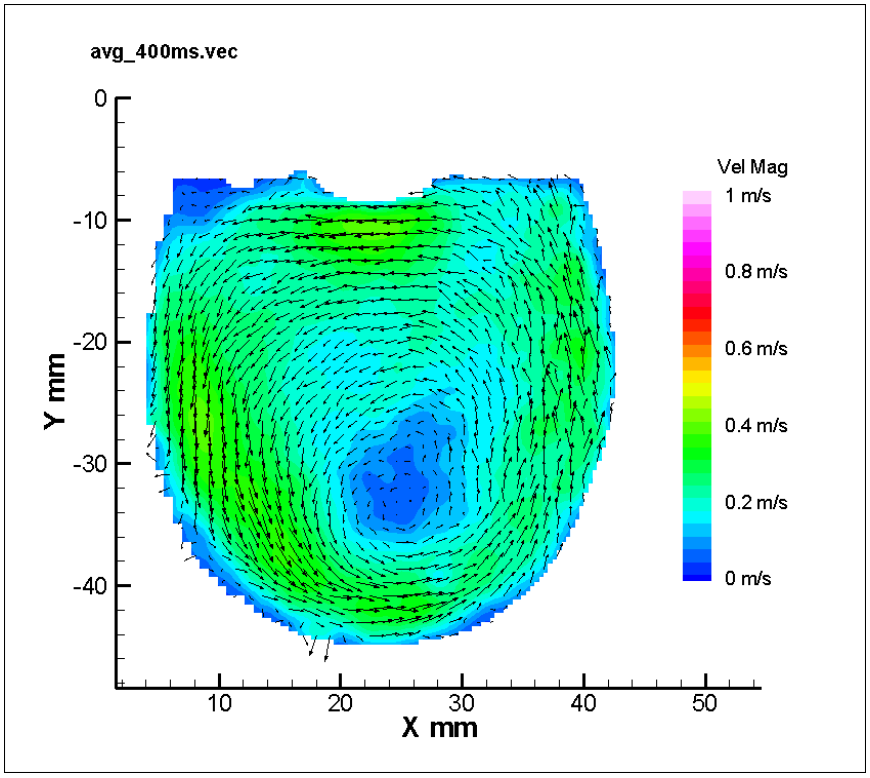
avg_400ms.vec
0
-10
-20
-30
-40
Y mm
10
20
30
40
50
X mm
Vel Mag
1 m/s
0.8 m/s
0.6 m/s
0.4 m/s
0.2 m/s
0 m/s

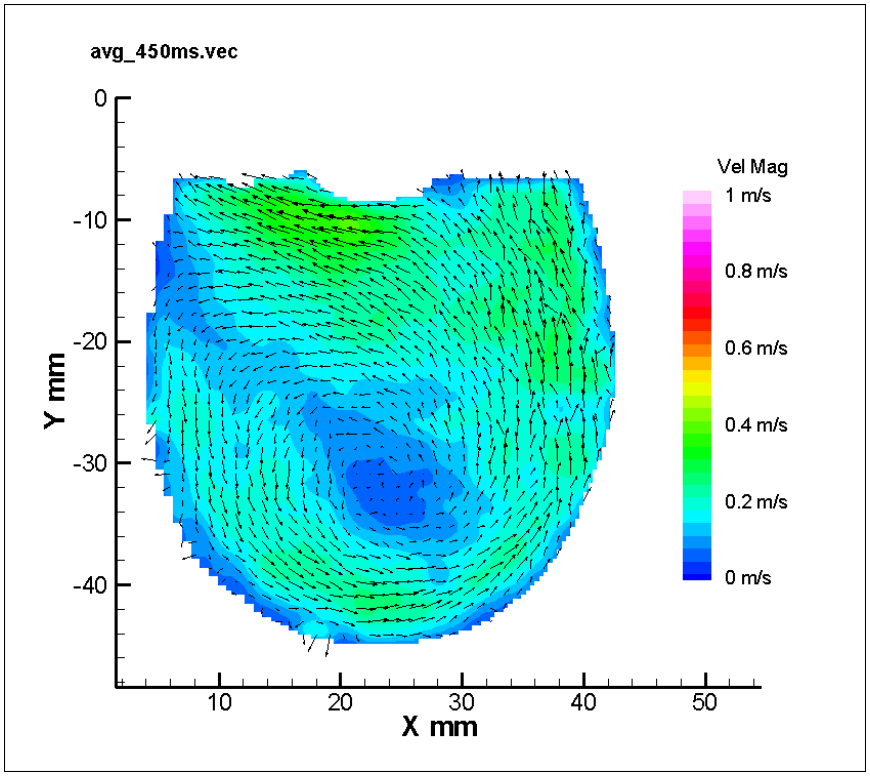
avg_450ms.vec
0
-10
-20
-30
-40
Y mm
10
20
30
40
50
X mm
Vel Mag
1 m/s
0.8 m/s
0.6 m/s
0.4 m/s
0.2 m/s
0 m/s

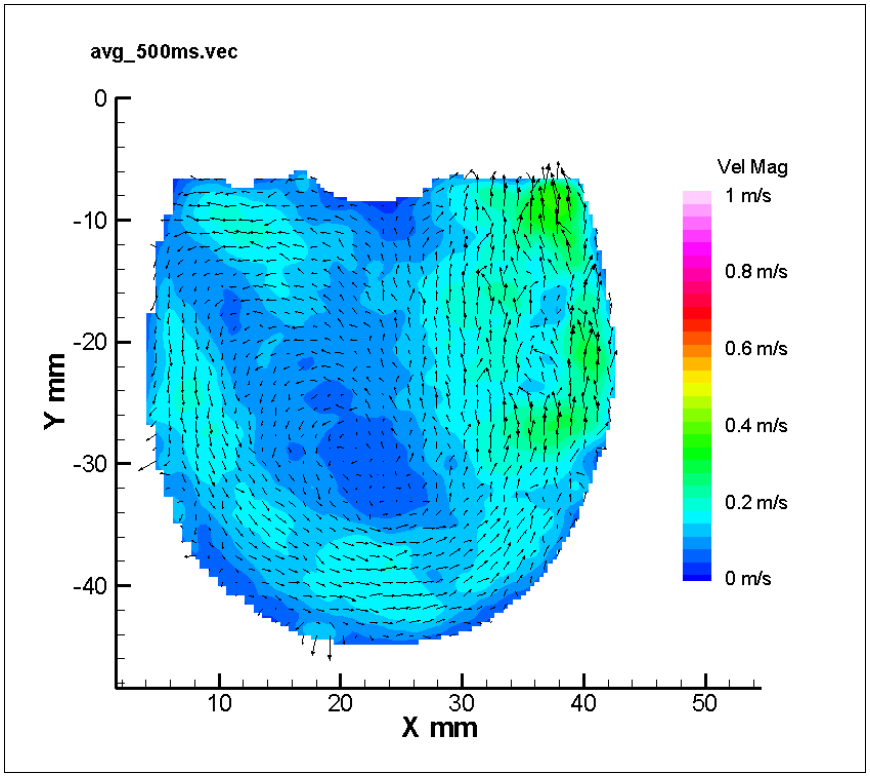
avg_500ms.vec
0
-10
-20
-30
-40
Y mm
10
20
30
40
50
X mm
Vel Mag
1 m/s
0.8 m/s
0.6 m/s
0.4 m/s
0.2 m/s
0 m/s

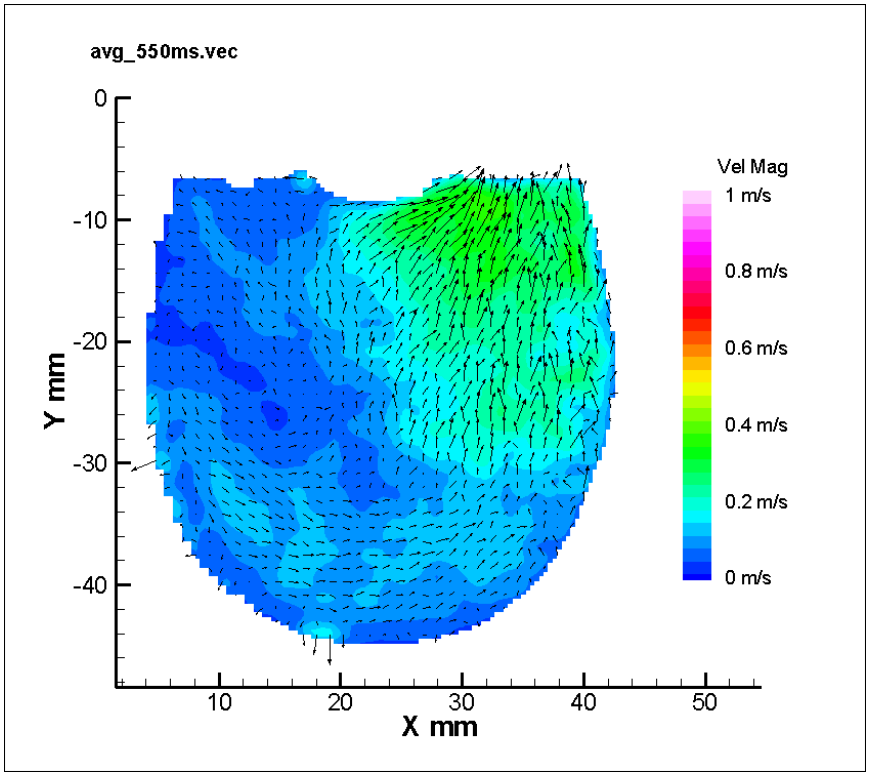
avg_550ms.vec
0
-10
-20
-30
-40
Y mm
10
20
30
40
50
X mm
Vel Mag
1 m/s
0.8 m/s
0.6 m/s
0.4 m/s
0.2 m/s
0 m/s

REFERENCES

[1] "FASTSTATS: Leading causes of death," 2009.

[2] "Statistical Fact Sheet Update," 2012.

[3] "Statistical Reference Book," 2005.

[4] C. S. Almond, R. R. Thiagarajan, G. E. Piercey, K. Gauvreau, E. D. Blume, H. J. Bastardi, F. Fynn-Thompson and T. P. Singh, "Waiting list mortality among children listed for heart transplantation in the United States," *Circulation,* vol. 119, pp. 717-727, 2009.

[5] "Report of the U.S. Organ Procurement and Transplantation Network and the Scientific Registry of Transplant Recipients: transplant data 1999-2008," Rockville, MD, 2009.

[6] M. D. Black, J. G. Coles, W. G. Williams, I. M. Rebeyka, G. A. Trusler, D. Bohn, C. Gruenwald and R. M. Freedom, "Determinants of success in pediatric cardiac patients undergoing extracorporeal membrane oxygenation," *Ann Thoracic Surgery,* vol. 60, no. 1, pp. 133-138, 1995.

[7] S. Kawahito, T. Maeda, T. Motomura, H. Ishitoya, T. Takano, K. Nonaka, J. Linneweber, S. Ichikawa, M. Kawamura, K. Hanazaki, J. Glueck and Y. Nose, "Hemolytic characteristics of oxygenators during clinical extracorporeal membrane oxygenation," *ASAIO J,* vol. 48, no. 6, pp. 636-639, 2002.

[8] A. Jeewa, C. Manlhiot, B. W. McCrindle, G. Van Arsdell, T. Humpl and A. I. Dipchand, "Outcomes with ventricular assist device versus extracorporeal membrane oxygenation as a bridge to pediatric heart transplantation," *Artif Organs,* vol. 34, no. 12, pp. 1087-1091, 2010.

[9] B. L. Short, "Extracorporeal membrane oxygenation," in *Neonatology, the Pathophysiology and Management of the Newborn, 5th ed.*, Baltimore, MD, Lippincott, Williams & Wilkins, 1999, pp. 557-568.

[10] E. A. Rose, A. C. Gelijns, A. J. Moskowitz, D. F. Heitjan, L. W. Stevenson, W. Dembitsky, J. W. Long, D. D. Ascheim, A. R. Tierney, R. G. Levitan, J. T. Watson, P. Meier, P. A. Shapiro, R. M. Lazar, L. W. Miller, L. Gupta, O. H. Frazier, P. Desvigne-Nickens, M. C. Oz and V. L. Poirier, "Randomized evaluation of mechanical assistance for the treatment of congestive heart failure (REMATCH) study group. Long-term use of a left ventricular assist device for end-stage heart failure," *N Engl J Med,* vol. 345, pp. 1435-1443, 2001.

[11] O. Reinhartz, B. Stiller, R. Eilers and D. J. Farrar, "Current clinical status of pulsatile pediatric circulatory support," *ASAIO J,* vol. 48, pp. 455-459, 2002.

[12] "Ventricular assist devices in children," Department of Cardiothoracic Surgery, Washington University School of Medicine, [Online]. Available: http://www.cardiothoracicsurgery.wustl.edu.

[13] "Berlin Heart EXCOR: Option for children awaiting heart transplant," McGowan Institute for Regenerative Medicine, UPMC, [Online]. Available: http://www.mirm.pitt.edu.

[14] D. L. Morales, C. S. Almond, R. D. Jaquiss, D. N. Rosenthal, D. C. Naftel, M. P. Massicotte, T. Humpl, M. W. Turrentine, J. S. Tweddell, G. A. Cohen, R. Kroslowitz, E. J. Devaney, C. E. Canter, F. Fynn-Thompson, O. Reinhartz, M. Imamura, N. S. Ghanayem, H. Buccholz, S. Furness, R. Mazor, S. K. Gandhi and C. D. Fraser Jr., "Bridging children of all sizes to cardiac transplantation: the initial multicenter North American experience with the Berlin Heart EXCOR ventricular assist device," *J Heart Lung Transplant,* vol. 30, no. 1, pp. 1-8, 2011.

[15] C. D. Fraser Jr., R. D. Jaquiss, D. N. Rosenthal, T. Hump, C. E. Canter, E. H. Blackstone, D. C. Naftel, R. N. Ichord, L. Bomgaars, J. S. Tweddell, M. P. Massicotte, M. W. Turrentine, G. A. Cohen, E. J. Devaney, F. B. Pearce, K. E. Carberry, R. Kroslowitz and C. S. Almond, "Prospective trial of a pediatric ventricular assist device," *N Engl J Med,* vol. 367, pp. 532-541, 2012.

[16] A. L. Throckmorton, P. E. Allaire, H. P. Gutgesell, G. P. Matherne, D. B. Olsen, H. G. Wood, J. H. Allaire and S. M. Patel, "Pediatric circulatory support systems," *ASAIO J,* vol. 48, no. 3, pp. 216-221, 2002.

[17] J. T. Baldwin, H. S. Borovetz, B. W. Duncan, M. J. Gartner, R. K. Jarvik, W. J. Weiss and T. R. Hoke, "The national heart, lung, and blood institute pediatric circulatory support program," *Circulation,* vol. 113, no. 1, pp. 147-155, 2006.

[18] J. A. Magovern, J. L. Pennock, D. B. Campbell, W. E. Pae, W. S. Pierce and J. A. Waldhausen, "Bridge to heart transplantation: the Penn State experience," *J Heart Transplantation,* vol. 5, pp. 196-202, 1986.

[19] "Pierce-Donachy Ventricular Assist Device," ASME, [Online]. Available: http://www.asme.org.

[20] S. Deutsch, J. M. Tarbell, K. B. Manning, G. Rosenberg and A. Fontaine, "Experimental fluid mechanics of pulsatile artificial blood pumps," *Ann Rev of Fluid Mechanics,* vol. 38, pp. 65-86, 2006.

[21] B. T. Cooper, B. N. Roszelle, T. C. Long, S. Deutsch and K. B. Manning, "The 12cc Penn State pulsatile pediatric ventricular assist device: fluid dynamics associated with valve selection," *J Biomech Eng,* vol. 130, no. 4, 2008.

[22] R. W. Colman, "Mechanisms of thrombus formation and dissolution," *Cardiovasc Pathology,* vol. 2, pp. 23S-31S, 1993.

[23] S. R. Hanson, "Device thrombosis and thromboembolism," *Cardiovascular Pathology,* vol. 2, pp. 157S-165S, 1993.

[24] P. Hochareon, K. B. Manning, A. A. Fontaine, J. M. Tarbell and S. Deutsch, "Correlation of in vivo clot deposition with the flow characteristics in the 50cc Penn State artificial heart: a preliminary study," *ASAIO J,* vol. 50, pp. 537-542, 2004.

[25] J. A. Hubbell and L. V. McIntire, "Visualization and analysis of mural thrombogenesis on collage, polyurethane, and nylon," *Biomaterials,* vol. 7, pp. 354-363, 1986.

[26] B. B. Daily, T. W. Pettitt, P. S. Salvatore and W. S. Pierce, "Pierce-Donachy pediatric VAD: progress in development," *Ann Thoracic Surg,* vol. 61, pp. 437-443, 1996.

[27] C. Bachmann, G. Hugo, G. Rosenberg, S. Deutsch, A. A. Fontaine and J. M. Tarbell,

"Fluid dynamics of a pediatric ventricular assist device," *Artificial Organs,* vol. 5, pp. 362-372, 2000.

[28] K. B. Manning, B. D. Wivholm, N. Yang, A. A. Fontaine and S. Deutsch, "Flow behavior within the 12-cc Penn State pulsatile pediatric ventricular assist device: an experimental study of the initial design," *Artificial Organs,* vol. 32, no. 6, pp. 442-452, 2008.

[29] B. N. Roszelle, S. Deutsch and K. B. Manning, "A parametric study of valve orientation on the flow patterns of the Penn State pulsatile pediatric ventricular assist device," *ASAIO J,* vol. 56, no. 4, pp. 356-363, 2010.

[30] B. N. Roszelle, S. Deutsch and K. B. Manning, "Flow visualization of three-dimensionality inside the 12cc Penn State pulsatile pediatric ventricular assist device," *Ann Biomed Eng,* vol. 38, no. 2, pp. 439-455, 2010.

[31] B. N. Roszelle, S. Deutsch, W. J. Weiss and K. B. Manning, "Flow visualization of a pediatric ventricular assist device during stroke volume reductions related to weaning.," *Ann Biomed Eng,* vol. 39, no. 7, pp. 2046-2058, 2011.

[32] B. T. Cooper, B. N. Roszelle, T. C. Long, S. Deutsch and K. B. Manning, "The influence of operational protocol on the fluid dynamics in the 12cc Penn State pulsatile pediatric ventricular assist device: the effect of end-diastolic delay," *Artif Organs,* vol. 34, no. 4, pp. E122-E133, 2010.

[33] J. A. Long, A. Undar, K. B. Manning and S. Deutsch, "Viscoelasticity of pediatric blood and its implications for the testing of a pulsatile pediatric blood pump," *ASAIO J,* vol. 51, no. 5, pp. 563-566, 2005.

[34] S. G. Greenberg, R. S. Baker, D. Yang and K. E. Clark, "Effects of continuous infusion of endothelin-1 in pregnant sheep," *Hypertension,* vol. 30, pp. 1585-1590, 1997.

[35] G. B. Thurston, "Effects of hematocrit on blood viscoelasticity and in establishing normal values," *Biorheology,* vol. 15, pp. 239-249, 1978.

[36] "Particle Image Velocimetry (PIV)," Institute of Aerodynamics and Flow Technology, [Online]. Available: http://www.dlr.de.

[37] M. Raffel, C. Willert and J. Kompenhans, Particle Image Velocimetry, Berlin: Springer, 1998.

[38] "PIV Image Evaluation," La Vision, [Online]. Available: http://www.piv.de.

[39] G. Rosenberg, W. M. Phillips, D. Landis and W. S. Pierce, "Design and evaluation of the Pennsylvania State University mock circulatory system," *ASAIO J,* vol. 4, pp. 41-49, 1981.

ACADEMIC VITA

Jeremy M. Silver

jeremysilver4@gmail.com
1150 Folkstone Drive, Pittsburgh, PA 15243

EDUCATION

The Pennsylvania State University, University Park, PA **Fall 2009-Fall 2014**

- Schreyer Honors College
- Integrated Undergraduate/Graduate Program (IUG)
- Bachelor of Science and Master of Science in Bioengineering
- Chemical Engineering Option

National University of Singapore, Singapore **Summer 2010**

- Study abroad engineering design course led by faculty from The National University of Singapore, Brigham Young University, and Penn State
- Collaborated with three students from Singapore, China, and India to develop a portable umbrella/chair apparatus for Singaporeans

THESIS

The Pennsylvania State University, University Park, PA **Fall 2014**

Artificial Heart & Cardiovascular Fluid Dynamics Lab

- "A Fluid Dynamic Study of the Effect of Hematocrit in the 12 cc Penn State Pediatric Ventricular Assist Device"
- Supervised by Dr. Keefe Manning

RESEARCH

Penn State Artificial Heart Lab, University Park, PA **Fall 2011-Fall 2014**

Undergraduate & Graduate Research Assistant

- Used particle image velocimetry (PIV) to study fluid flow in cardiovascular devices
- Penn State Pediatric Ventricular Assist Device (PVAD)
- Ension Pediatric Cardiopulmonary Assist System (pCAS)
- FDA Critical Path Initiative: Computational Fluid Dynamics/Blood Damage Project

HONORS & AWARDS

The Pennsylvania State University, University Park, PA **Fall 2009-Fall 2014**

Undergraduate Research Exhibition *Spring 2013*

- Awarded 2nd place in the engineering division for outstanding undergraduate research for work on the Ension pCAS

Leonhard Center Speaking Contest *Spring 2013*

- Awarded 1st place in the audience vote for talk about the current state of pediatric heart transplantation and my research on the Penn State PVAD

Undergraduate Summer Discovery Grant *Summer 2012*

- Awarded $3,500 to pursue my research on the Penn State PVAD

President's Freshman Award *Spring 2010*

- Awarded for 4.0 GPA

PRESENTATIONS

ASAIO Conference, Washington, D.C. **Summer 2014**

American Society of Artificial Internal Organs Poster Presentation

- Presented my thesis research at the 60th Annual ASAIO International Conference

Penn State Department of Bioengineering, University Park, PA **Spring 2013-Summer 2014**

Bioengineering Symposium *Spring 2013 & Spring 2014*

- Conducted both oral and poster presentations about my research

Spend a Summer Day *Summer 2014*

- Student presenter to answer questions and talk to prospective high school students and their families about Penn State

LEADERSHIP

Graduate Teaching Assistant & Grader, University Park, PA **Spring 2013-Fall 2013**

- Teaching Assistant for the bioengineering section of Capstone senior design course
- Grader for bio-continuum mechanics and bio-fluid mechanics

Penn State Club Golf Team, University Park, PA **Fall 2010-Spring 2013**

President *Fall 2011-Spring 2013*

- Increased membership from 20 to over 100 active members in 2 years
- Organized tournaments, travel arrangements, fundraisers, and THON events for the club
- Joined the National Collegiate Club Golf Association (NCCGA)

Home Events Coordinator *Fall 2010-Spring 2011*

- Arranged tee times, golf course payments, and membership paperwork for the club

WORK EXPERIENCE

ZOLL LifeVest, Pittsburgh, PA **September 2014**

Associate Regulatory Affairs Engineer

- Worked with the ZOLL LifeVest Wearable Cardioverter Defibrillator
- Prepared documentation for premarket approval (PMA) supplements, complaint handling, adverse event reporting, and other associated reports necessary for an FDA approved Class III medical device
- Performed risk analysis and failure mode analysis associated with the LifeVest